PERFORMANCE STUDIES OF OIL LUBRICATED HELICAL GROOVE JOURNAL BEARING

531

by

Muhammad Zubair Khan, M.Phil

Thesis Submitted for the Degree of Doctor of Philosophy

Department of Mechanical Engineering

Brunel, The University of West London

May 1992

Dedicated to my Children

Sanna and Usman

CONTENTS

ABSTRACT

The provision of helical grooves on the surface of a plain journal bearing can improve the stability of a rotor-bearing system. However, the improvement depends on the arrangement of the grooves along the axial length of the bearing. In order to verify this improved stability three types of helical groove bearing and a reference plain journal bearing were investigated. The helical groove journal bearings were: a symmetrical, an asymmetrical and a partial grooved bearing. The bearing test rig was used to measure the oil flow rate, load carrying capacity, power losses, bearing surface temperatures, and stability characteristics. A theoretical model was developed to calculate the load carrying capacity, stiffness and damping coefficients, and stability characteristics of the various types of bearing.

The experimental and theoretical results show that at the expense of a reduced load capacity the helical groove bearings are more stable particularly at low eccentricity ratios. However, the experimental observations showed that the partial helical groove bearing is not a practical bearing because the bearing becomes misaligned above certain load.

For a given eccentricity ratio and speed the symmetrical bearing ran hotter and with greater power losses in comparison to the other three bearings. At the same eccentricity ratio and speed, the asymmetrical bearing ran at about the same temperature as the plain journal bearing.

Acknowledgements

First of all I would like to express my appreciation to those who have given me their support and cooperation during the course of my work.

My supervisor Dr.T.A. Stolarski, for his guidance and encouragement.

Professor A.W. Crook, for his help and suggestions.

Dr Andrew Harangozo, for his help and suggestions.

I am grateful to the Government of Pakistan for providing me with financial support.

I would like to thank to the inter library loan section of the university library for its efficient assistance in obtaining the references.

My thanks go to the Computer Advisory Section for help with my computational problems.

List of Figures

NOTATION

X	Circumferential coordinate	m
Y	Horizontal coordinate	m
Z	Axial coordinate	m
H	Film thickness	m
C	Mean radial clearance	m
L	Bearing length	m
R_b	Bearing radius	m
R_j	Journal radius	m
D	Diameter of the bearing	m
μ	Viscosity	N sec/m^2
P	Film pressure	N/m^2
N	Rotational speed	RPM
ω	Angular speed of the shaft	radian /sec
$T=\omega t$	Reference time	
U	Surface velocity	m/sec
α	Groove angle	radians
$u_x = \frac{U}{\omega R_b}$	Component of velocity in X direction	

$u_y = \frac{U}{\omega R_b}$	Component of velocity in Y direction	
H_g	Groove depth	m
B_r	Ridge width	m
B_g	Groove width	m
V_o	Motion of the shaft centre	m /sec
R	Axis along the longitudinal direction of the groove	m
S	Axis perpendicular to the longitudinal direction of the groove	m
F_x	Components of the oil film forces along X axis	N
F_y	Component of oil film force along Y axis	N
w_b	Bearing load	N
M	Mass of the bearing housing	kg
Ω	Whirl speed	radians/sec
$\bar{\Omega} = \frac{\Omega}{\omega}$	Whirl speed ratio	
θ	Angle measured from the X axis	radians
ϕ	Attitude angle	radians

$A_{x\,x}$		Principal stiffness coefficients along X axis	N/m
A_{yy}		Principal stiffness coefficients along Y-axis	N/m
A_{xy}		Crosscoupled stiffness	N/m
A_{yx}		Crosscoupled stiffness	N/m
B_{xx}		Principal damping coefficient along X axis	N-sec/m
B_{yy}		Principal damping coefficient along Y-axis	N sec/m
B_{xy}		Crosscoupled damping coefficients	N
B_{yx}		Crosscouple damping coefficients	N sec / m
A_e		Area of the triangular element	m^2
N_{ij}		Interpolation function	
∇		Gradient operator	
$\nabla.$		Divergence operator	
Qo	$\omega R_b C$	Reference flow per unit length	m^3 /sec
Fo	$\frac{12\ \mu\omega^2 R_b^4}{C^2}$	Reference force per unit length	

e	E/C	Eccentricity ratio
ex	Ex/C	X-Component of eccentricity
ey	Ey/C	Y-Component of eccentricity
x	X/R_b	Dimensionless x-coordinates
z	Z/R_b	Dimensionless z-coordinates
f	F/Fo	Dimensionless load capacity
f_x	F_x /Fo	Dimensionless x components of oil film forces
f_y	F_y /Fo	Dimensionless z-component of oil film forces
hg	Hg/C	Dimensionless groove depth
h	H/C	Dimensionless film thickness
hr	Hr/C	Dimensionless film thickness at ridge
P_o	$\frac{12\mu\omega R_b^2}{C^2}$	Reference pressure per unit length
p	$\frac{P}{P_o}$	Dimensionless pressure
q_x	$\frac{Q_x}{Q_o}$	Dimensionless flow in x direction
q_z	$\frac{Q_z}{Q_o}$	Dimensionless flow in z direction

S_p		Stability parameter or dimensionless critical mass
K_{xx}	$\frac{A_{yy} * C}{W_b}$	Dimensionless stiffness coefficient
K_{yy}	$\frac{A_{yy} * C}{W_b}$	
K_{xy}	$\frac{A_{xy} * C}{W_b}$	
K_{yx}	$\frac{Ayx * C}{W_b}$	
C_{xx}	$\frac{B_{xx} * \omega C}{W_b}$	Dimensionless damping coefficient
C_{yy}	$\frac{C_{xy} * \omega C}{W_b}$	
C_{xy}	$\frac{B_{xy} * \omega C}{W_b}$	
C_{yx}	$\frac{B_{xy} * \omega C}{W_b}$	

CHAPTER 1

INTRODUCTION

1.1 General Background

The rotor of any turbomachinery running in journal bearings, is prone to two types of well known vibration [1,2]. The first is synchronous vibration due to the runout or forces resulting from unbalance of the shaft. The second and more serious is a self excited non synchronous vibration, also known as "low frequency whirl". This latter phenomenon is usually associated with the oil film forces of the journal bearing and occurs particularly at low journal eccentricities.

In turbomachinery the parameters characterizing operation such as, power losses, vibration amplitude and frequency are dependent on the type of bearings used, specific loads, bearing clearance, and load orientation. There are several types of journal bearing design in common use in turbomachinery [3,4]. They include the circular bore plain journal bearings which is easy to manufacture and inexpensive but, operating at low eccentricity, prone to be unstable. To improve the stability of a rotor, a geometrically pre-loaded bearing is often used in which two or more circular bearing arcs are set eccentric relative to the bearing centre such as elliptical bore bearings and three lobe bearings. Journal bearings with dams, steps, and pockets are also often used to improve stability. A pressure dam bearing is basically a plain journal bearing in which a dam is cut in its top half. As the fluid is dragged into the dam region hydrodynamic pressure is created at the

top half of the journal. The resulting downward acting hydrodynamic force adds to the static load and the shaft assumes a greater eccentricity and hence becomes more stable. Another bearing which can increase stability though has a more complex geometry is the tilting pad journal bearing. In this type of bearing the number of pads can usually vary from three to seven. Each pad is pivoted at a point located on its back. Tilting pad bearings induce greater stability and exciting crosscouple forces are reduced due to the ability of the pad to tilt.

There are also other types of bearing designs used in engineering applications such as, spiral groove or helical groove bearings [5,6]. The spiral groove bearing has been widely used as a thrust journal bearing in small devices using gas, grease, or oil as a lubricating medium. In the helical groove bearing shallow grooves are cut in the surface of the bearing or in the surface of the journal. The grooves are inclined at a certain angle to the direction of rotation. As the journal rotates, due to the self-pumping action of the grooves, additional pressure is developed inside the bearing. This pressure preloads the bearing and causes an increase in stability. The performance of the helical groove bearing is affected by the depth of the groove, its width, angle, and the arrangement of the grooves along the bearing length. There are various types of helical groove journal bearing although only three of them will be described here. In the "symmetrical helical groove bearing", the grooves are of equal length about the mid axial plane of the bearing, but have opposite directions. In such a bearing the rotation of the journal pumps lubricant toward the centre of the bearing and there is no net flow of lubricant out of the bearing except the flow due to leakage. A bearing in which an axial flow of lubricant is achieved due to the grooves on one side of the bearing

being slightly longer than those on its other side, is called an "asymmetrical bearing". A third type of a bearing is a "partially grooved bearing", in which only half of the bearing surface is grooved while the rest of the surface is left plain. Asymmetrical and partially grooved journal bearings have the ability to pump the lubricant axially through the bearing. This pumping ability is important because a large part of the heat energy produced within can be dissipated by the outflow of the lubricant. This can be of importance in the case of high speed bearings. However, there is no published work in which measured bearing surface temperatures of helical groove bearings have been reported. Similarly experimental work regarding the steady state and dynamic characteristics of partial and asymmetrical helical groove bearing has not been reported.

1.2 Review of Spiral Groove Bearing Design

The distribution of pressure in the lubricating film of a plain journal bearing is well known and governed by the Reynolds equation [8,9]. In spiral groove bearings, however, the pressure profile in the circumferential direction has a saw tooth shape. Basic hydrodynamic theory was applied for the first time to a spiral groove thrust bearing by Wipple [5]. He adopted certain assumptions similar to those commonly used in the analysis of a smooth bearing, i.e the groove could be considered narrow and the pressure distribution across the groove could be regarded as linear.

Muijderman [6,7] also addressed the problem of lubrication in spiral groove bearings. He considered many important aspects of their operation and analysed load capacity and frictional losses. He has also considered the effect of various

groove parameters on the performance of the bearing.

In a spiral groove journal bearing operating eccentrically, a variation in pressure in the circumferential direction takes place. Solution of the Reynolds equation for this type of bearing was not available till 1965 when Vohr and Chow [10] and also Hirs [11] put forward a theoretical model. They proposed that in order to find the load capacity and stability it is not necessary to know the actual pressure profile but, instead, it is sufficient to know the mean pressure across the width of a groove and ridge pair. This pressure profile is known as a smoothed pressure profile and is valid provided that the number of grooves on the surface of the bearing or on the surface of the journal is infinite. In practical terms the provision of an infinite number of grooves on the surface of a bearing or on the surface of a journal is not possible. However, the theoretical analysis proved to be quite accurate when applied to bearings having only a finite number of grooves. The experimental verification of this approach was carried out by Hirs [11] and Bootsma [12,13].

The differential equation for the smoothed pressure profile, was solved by Castelli [14] and Smally [15] using the finite difference method. In their analysis they assumed a constant viscosity across the film. The results of their analysis were in a good agreement with experimental data. A finite element analysis of the helical groove journal bearing was conducted by Reinhoudt [16] and Yavelov [17]. However, they did not compare their theoretical results with experimental data.

In order to maximize the load carrying capacity and radial stiffness, Yavelov [18], Fleming [19,20] tried to optimize the various parameters characterising groove geometry.

There are two methods to inscribe grooves in the surface of a bearing or in the surface of a journal. The first method consists of chemical etching the surface as described by Hirs [21]. The other method produces grooves by milling [22].

There are also a number of known applications of the gas lubricated helical groove bearing. A stability analysis of the gas lubricated herring-bone bearing was carried experimentally by Cunning and Fleming [23]. They tested six rotors with grooves cut into the surface of the rotor. The rotors were tested in a vertical position and supported by plain bearings. Speeds of up to 60000 rpm were attained without applying any radial load. No instability was observed. Beside speed they also varied the bearing clearance in order to observe its effect on the stability. It was seen that the stability could improved by reducing the bearing clearance.

Malanoski [24] carried out an experimental study of an ultra stable gas bearing of 40 mm in diameter. A rotor with grooves was mounted in two air lubricated plain bearings. No instability developed up to the speed of 60000 rpm while the rotor was loaded up to an eccentricity ratio of 0.3.

A recent industrial application of a 9 mm spiral groove journal bearing was reported by Molyneaux [25]. The bearing supported a stainless steel rotor running at a speed of 350000 rpm. In another application a helical groove journal bearing supported a rotor of an expansion turbine [26].

The load capacity of air lubricated helical groove bearings is too small for most engineering applications. To obtain a bearing with a sufficient load capacity a lubricant with a substantially higher viscosity needs to be used. Grease is the preferred lubricant in applications where a self sealing action for the bearing is needed. The application of a spiral groove bearing system with grease as a

lubricant has been reported by Bos [27]. Theoretical and experimental analysis of a grease lubricated spiral groove bearing was conducted by Dewar [28]. Muijderman [29] published work regarding the application of grease lubricated herringbone journal bearings in video cassette recoders.

Experiments on a series of hydrodynamic journal bearings lubricated with sodium at a temperature from 500 °F to 800 °F were conducted by Fredrick and Schuller [30,]. Four different bearings were tested, that is, a cylindrical bearing with two and three axial grooves, a plain journal bearing with a herringbone grooved journal and a tilting pad bearing with three pads. The bearings in all tests were 40 mm in diameter and the test speed was 12000 rpm. The conclusion was that the tilting pad bearing was the most stable bearing and was followed by the plain journal bearing with a herringbone grooved journal, and then the axial groove bearing.

Using water as a lubricant Fredrick and Schuller [31] conducted a series of stability tests on grooved rotors running in plain journal bearings. Three different sets of grooves were machined on three rotors: complete herringbone, partial herringbone with twenty grooves and another partial herringbone journal with forty grooves. The tests were conducted at a speed of 12000 rpm. The results of the test indicated that the number of grooves had no effect on the stability of the rotor. Similarly, a complete herringbone or a partial herringbone pattern was found to have no effect on stability. In experiments the effect of varying clearance on stability was also studied. It was found that the stability threshold is very sensitive to changes in clearance. The stability can be improved by reducing the clearance. However, their theoretical work predicted higher stability threshold in comparison

to those measured experimentally.

A theoretical analysis of a turbulent flow journal bearing with helical grooves of different configurations was conducted by Vohr and Chow [32]. Their analysis predicted the steady state and dynamic properties of the bearing. The grooves in all cases were machined into the surface of the journal. However, results indicated that the performance of the bearing in the case of an incompressible lubricant is not affected regardless whether the grooves are on the surface of the bearing or on the surface of the journal.

The majority of theoretical models of spiral groove bearings are based on isoviscous analysis. Bootsma [33] considered the effect of variation in viscosity on the performance of a thrust bearing. Thermodynamic analysis of a grease lubricated spiral groove thrust bearing was carried out by Dewar [29]. In order to reduce the power losses of a plain journal bearing a floating ring bearing is a preferred solution in some applications. However, the floating ring plain journal bearing is inherently unstable. To improve the stability, Chow [34] proposed a helical groove floating ring journal bearing. The steady state and dynamic analyses was based on a smoothed pressure concept, and a finite difference method was used.

Yavelov [35,36] reported the use of spiral groove journal bearings to support the spindle of a milling machine running at 24000 rpm. The diameter of the bearing was 52 mm and water was used as a the lubricant.

Helical groove bearings are effective only in one direction of rotation. However, Nobuyoshi and Yasumi [37] have recently published theoretical work on a reversible type herringbone journal bearing. This type of bearing was shown

to have load capacity slightly less than that of a conventional herringbone journal bearing.

There are several other applications outside the bearing field where spiral grooves have found use e.g, in shaft seals and viscous screw pumps [38,39,40].

1.3 Objective and Scope of Present Work.

The main objective of the present study was to assess, through experimental testing and computer modelling, the suitability of oil lubricated helical groove journal bearings for turbomachinery application.

In order to accomplish the objective three helical groove journal bearings namely, a symmetrical helical groove journal bearing,, an asymmetrical helical groove journal bearing and a partial helical groove journal bearing have been studied and their performance compared with that of a plain journal bearing. The results of the investigation are presented in the following chapters. In chapter 2, the experimental apparatus, including the bearings, and experimental procedure are described. The experimental results are presented in chapter 3. In chapter 4, the theoretical model is described and the governing equations for both the steady state and dynamic properties are given. In chapter 5, computational and experimental results are compared. Finally, conclusions and recommendations for further work are presented in chapter 6.

CHAPTER 2

EXPERIMENTAL APPARATUS AND PROCEDURE

2.1 Introduction

The steady state properties and stability characteristics of the journal bearings tested were obtained experimentally using an existing bearing test rig [41]. In rotor-bearing systems the stability is determined both by the dynamic characteristics of the rotating parts and the dynamic characteristics of the journal bearings. In order to focus attention on the stability characteristics of the bearing and eliminate the other factors which may influence the stability, the test rig incorporated a movable test bearing and a rigid shaft mounted on fixed rolling contact bearings. The bearing test rig, Figure 2.1, consisted of a number of systems. These systems and the experimental procedure will be described.

2.2 The Test Bearings

Four bearings with different geometries were tested, a plain journal bearing, a partial helical groove journal bearing, a symmetrical helical groove journal bearing and an asymmetrical helical groove journal bearing. All the bearings were made of phosphor bronze. The nominal diameter of the bore was 127 mm and the radial clearance was 0.125 mm. These dimensions were chosen in accordance with the existing bearing rig.

A plain journal bearing was selected as a reference bearing. For the purpose of consistency of comparison, the plain bearing was tested first and was then converted subsequently into helical groove bearings.

The plain journal bearing is presented in Figures 2.2 to 2.5. Oil was supplied to the bearing through a hole in the top of the bearing. The bearing was manufactured from a hollow phosphor bronze cylinder. The manufacturing accuracy was checked and revealed that the variation in the clearance was 0.02 mm to 0.03 mm. The roundness error was found to be within 0.024 mm. The surface roughness measured on the Talysurface was found to be 0.5 to 1 μm .

The partial helical groove bearing is shown in Figures 2.6 to 2.8. The groove was cut by a cutter held in the right angle head of a pneumatic grinder. The cutting and its indexing was performed by a universal miller as shown in Figure 2.8a. The variation in the groove depth was about 6 to 8 μm . The groove parameters are listed below;

Groove angle = 33 degrees

Groove width = 2 mm

Ridge width = 2 mm

Groove depth = 0.13 mm

Calculations regarding the groove pitch and lead angle of the groove are given in Appendix A. Oil was admitted to the bearing through an inlet hole which was located in the top centre plane of the main bearing housing, Figure 2.15. The circumferential groove in the main bearing housing distributed oil to a number of holes in the bearing, for example, oil was distributed to the bearing through an

axial groove in the bearing housing and a hole as illustrated in Figure 2.8b. The instrumented partial helical groove bearing is shown in Figure 2.8c.

The symmetrical helical groove bearing assembled in the mild steel housing is shown in Figure 2.9. The detail drawings are shown in Figures 2.10 and 2.11. Oil was supplied to the bearing through two inlets as shown in Figure 2.9. These oil inlets were connected to the axial groove of the bearing housing via connectors. The groove parameters were the same as in the case of the partial groove bearing.

The asymmetrical helical groove bearing bush is shown in Figure 2.12 and details are shown in Figures 2.13 to 2.14. The groove parameters are the same as those described earlier in the case of the partial groove bearing with the exception that in this case the grooves on one side of the bearing are slightly longer than those on the other side of the bearing. Oil was supplied to the bearing through an oil inlet hole which flooded the end of the bearing which had the longer grooves.

2.3 The Main Bearing Housing and Seals

The main housing which contained the seals is shown in Figure 2.15. The purpose of the housing was to hold the bearing assembly firmly to enable the bearing to be loaded. It also distributed supply oil to the inlets of the test bearing. Supply oil entered the housing via an oil inlet hole and was then distributed via an annular groove. Oil exiting the bearing flowed to the sump via two drain pipes. Oil leakage from the housing was controlled by floating ring seals. The floating rings were made of a phosphor bronze and had an inside diametral clearance of 0.152 mm and an outside diametral clearance of 0.203 mm. The rings were free to move radially and could therefore accommodate a relatively large amount of

shaft/bearing misalignment.

2.4 Bearing Surface Temperature Measurements

The bearing surface was instrumented with a number of thermocouples as shown in Figure 2.16. All the thermocouples were cemented in place with araldite to within 2 mm of the bearing surface. The location of thermocouples in the circumferential and axial directions was the same in all bearings tested. Type 'T' thermocouples were used to measure the temperatures. A data acquisition system was used to provide signal conditioning and multiplexing for the thermocouples. The thermocouples were calibrated at two known temperatures, the freezing point and the boiling point of water. On calibration, the thermocouple cards were found to be within 0.3 °C to 0.5 °C of each other. A data acquisition programme was installed on a BBC computer to send commands to the various instruments and receive back data over an RS232c serial port. In the program the temperatures measured by the thermocouple system were corrected by using the formula described in Appendix B. The corrected temperatures were displayed on the screen or stored on disc.

2.5 Shaft Displacement Measurements

In order to obtain the displacements in x and y direction of the journal centre relative to the bearing centre, it is necessary to measure the position of the shaft in two perpendicular planes on either side of the bearing. Inductive displacement transducers were used in this respect. The positions of the transducers are shown in Figure 2.17. The outputs from the probes mounted

directly opposite to each other were combined to cancel the effects of thermal expansion and to give the average shaft position at each end of the bearing. Each pair of transducers was connected to a carrier frequency amplifier. The output from the carrier frequency amplifier was connected to a channel of a storage oscilloscope and a u-v recorder. As load was applied to the bearing the displacements in x and y direction were read from each respective channel of the oscilloscope. Using the x-y axis display of the oscilloscope, the shaft motion was displayed in the form of an orbit. The output signal for a given displacement depends upon the initial gap between the shaft and transducer and upon the gain of the amplifier which is preset. Each pair of transducers was calibrated as a unit before installation. A typical calibration chart is given in Figure 2.18. The distance between the transducers and the shaft was 1 mm, and the radial clearance between the shaft and bearing was 0.125 mm.

The calibration of the transducers after installation in the test rig was not possible. However, displacements measured by the transducers were compared with dial gauge readings and they were in good agreement. The eccentricity ratio was calculated from x and y displacements.

2.6 Shaft and Support Bearings

Figure 2.19 shows the shaft and its support structure. One end of the shaft was supported by a double row spherical bearing, while the other end was supported on a system of ball bearings. The support bearings were mist lubricated.

2.7 Oil Supply System

The oil supply system is shown in Figure 2.20. It was designed to operate

in two modes. In one mode the oil in the tank is heated to the required supply temperature. The filtered oil is then supplied to the test bearing. Oil leaving the bearing is returned to the tank. The oil supply pressure can be set to any value between 34 and 480 kN/m^2 by suitable adjustment of the by-pass valve in the supply line. Flexible hose is used immediately prior to the test bearing housing to isolate the housing from vibration generated by the oil pump. The oil inlet pressure was measured using a calibrated bourdon tube pressure gauge. The second mode of oil supply system allows longer test runs. In this mode, oil that has passed through the bearing is returned to the supply tank and the supply oil temperature is held constant by adjusting the cooling system.

In practice, however, the heating of the oil and hence the oil supply temperature could not be controlled to the required accuracy without the use of a cooler. Therefore the second mode of oil supply was used for the tests. The required inlet temperature was set at 40 °C and the temperature variation was held to within $\pm$ 1 °C. The oil used in the experiments was Shell Tellus 37. The viscosity of the oil measured over the range of temperatures using a suspended level viscometer is shown in figure 2.20a. The measured value of pH is 6. Which points to a neutral character of the oil. It was according to Shell specifications with following features.

a) Improved thermal stability

b) Excellent oxidation resistance

c) Low friction

d) Good water separation

2.8 Flow Rate Measurement

A flow meter was provided to measure the flow rate of the oil through the bearing. The calibration chart taken from reference [41] is given in Appendix C. However, in most of the test runs the oil flow rate was too small to be measured accurately by the rotameter. Instead the flow rate was measured directly using a calibrated container and a stop watch.

2.9 Power Loss Measurement

The power absorbed by a bearing was estimated from the measurements of the oil flow rate and oil temperature rise resulting from its passage through the bearing.

2.10 Loading System

The loading system is shown in Figure 2.21. The bearing is loaded vertically upward by two 6mm multi- strand wire ropes. Load is applied by a hydraulic jack which is fed from a hand pump. Each wire rope incorporated a turn-buckle so that its length could be adjusted to facilitate alignment of a bearing. The wire ropes were attached to a mild steel carrier which cradled the bearing housing. The system could apply a load of up to 25 kN to the bearing. The system incorporated a safety feature, in the form of a solenoid valve built-in into the hydraulic system which normally remained closed. However, in an emergency the solenoid valve could be opened via the data acquisition system to release the load on the bearing. The load was calculated using the measured jacking oil pressure and jack cylinder diameter. The jacking oil pressure was measured in the

loading system hydraulic line by a standard bourdon tube type gauge. In order to compensate for pressure losses in the system, a gas charged hydraulic accumulator was installed. This kept the pressure stable in the hydraulic line.

2.11 Drive System

The drive to the test shaft was provided by a petrol engine, Figure 2.22, via a propshaft and heavy pitch timing belt and pulley set. Shaft speed was measured by a tachometer consisting of a shaft mounted sprocket which interrupted an opto-switch connected to the counter/timer card of the data acquisition system. The speed was controlled by throttling the engine. With a pulley ratio of 40:27 and shaft diameter of 0.127m a shaft speed of up to 7000 rpm could be attained. The shaft speed once set, remained constant to within $\pm$ 30 rpm. However, the use of a belt drive directly connected to the end of the test shaft inevitably introduced some vibrations. However, those were not excessive up to 4000 rpm, though above 4000 rpm displacement measurements became unreliable. In the drive system an engine cut-out device was installed and could be operated in an emergency via the data acquisition system.

2.12 Data Acquisition System

The main role of the data acquisition system was to collect, display and store data from the various instruments used and to control certain aspects of rig operation. The system shown in Figure 2.23, comprised of a 64k BBC microcomputer interfaced with a "3D Thinklab" data logger. The data logger

contained its own microprocessor and all the cards to interface with the instrumentation. The BBC microcomputer was programmed to send commands to the thinklab controller card and to receive data back over the RS232c serial communication card. Data received could either be displayed or stored on a disc.

There were a number of cards within the system, each one having its own specific function. Five R-16TACJC cards provided signal conditioning and multiplexing for the type T thermocouples. An R-10MUCS counter/timer card connected to the opto-switch measured shaft speed and an R-8CTA transducer amplifier card provided amplification for the outputs which were then converted to digital form by the R-12ADS 12 bit integrating A-D converter card. The digitised information was then sent to the BBC microcomputer. The maximum rate of data capture was dictated by the conversion speed of the A-D converter and for this card it was approximately 10 channels/sec.

The data acquisition system also contained an R-8CDR relay card which, programmed from the BBC, could operate the relay system shown in Figure 2.23, [41] and control the engine ignition, oil heaters and solenoid valve. The capture, display, storage of data and control of the rig were all programmed options that could be chosen systematically from a menu. These options included:-

1 **Relay Control** - by controlling relays, the engine and oil heater could be switched on or off and the loading system solenoid valve opened or closed.

2 **Safety Control** - if chosen, the system monitored the hottest bearing temperature every other channel. If the temperature exceeded the trip value, the bearing was unloaded and the engine stopped. Excessive bearing temperatures

could be caused by lubricant failure, engine failure, overloading, etc.

3 Start Up Display - load, speed, power losses, oil flow rate, bearing minimum film region temperatures and supply groove temperature, outlet and return temperature and relay status were all displayed. Oil supply temperatures were also monitored and the oil heaters controlled accordingly.

4 Temperature Display - temperature readings for all the thermocouples used were displayed together with oil inlet, supply and outlet temperatures. Engine coolant and oil supply temperatures were also monitored.

5 Data Entry - this option allowed the readings from mechanical instruments such as pressure gauges and the flow meter to be input.

6 Data to Disc - after inputing a file name, time and date, experimental rig data could then be stored on the disc.

An important keyboard option, rather than screen option, was the emergency stop button, which, if pressed, immediately shut down the rig.

2.13 The Experimental Procedure

In order to established actual bearing clearance and alignment, it was necessary to established a datums at which the axis of the journal and the axis of the bearing bore were collinear. The datums was established with the shaft stationary by moving the bearing from side to side and vertically up and down into hard contact with the journal. The bearing was first moved vertically by use of the turn buckles and then side to side, the datums was established with the bearing set

in its mid vertical position. The nominal diametral clearance was 0.25 mm. The diametral clearance indicated by moving the bearing across from hard contact to hard contact was between 0.2 mm and 0.22 mm. At the beginning of an experiment, the bearing was run under zero load in order to check that the shaft centre coincided with the bearing centre and that was taken as a reference. During experiments, frequent checks for zero drift were made.

Before the test, the oil in the tank and the bearing were brought up to a temperature just above the required oil supply temperature of 40 °C. This was achieved by using the tank oil heaters and circulating the oil through the bearing. Once the desired supply temperature was reached, the engine was started. Load was applied to the bearing after the required shaft speed was attained. Oil supply temperature was controlled by occasionally adjusting the cooling. The bearing required 30 minutes to reach thermal equilibrium. Data were recorded only after thermal equilibrium of the bearing had been achieved. Thermal equilibrium was judged to have been attained when the bearing temperatures were seen to vary with the supply temperature. At equilibrium condition a data file name was selected and bearing temperatures, power losses, oil flow rate, load, speed, date and time were stored on the disc. After recording the steady state parameters, the static load applied to the bearing housing was reduced by small increments until the first indication of instability was observed. During this process the unstable whirl orbit was observed on the oscilloscope and recorded photographically. The load at which the instability began to grow, was taken as the instability load.

Four series of test were run for each bearing, with each series consisting of various combinations of shaft speed and load.

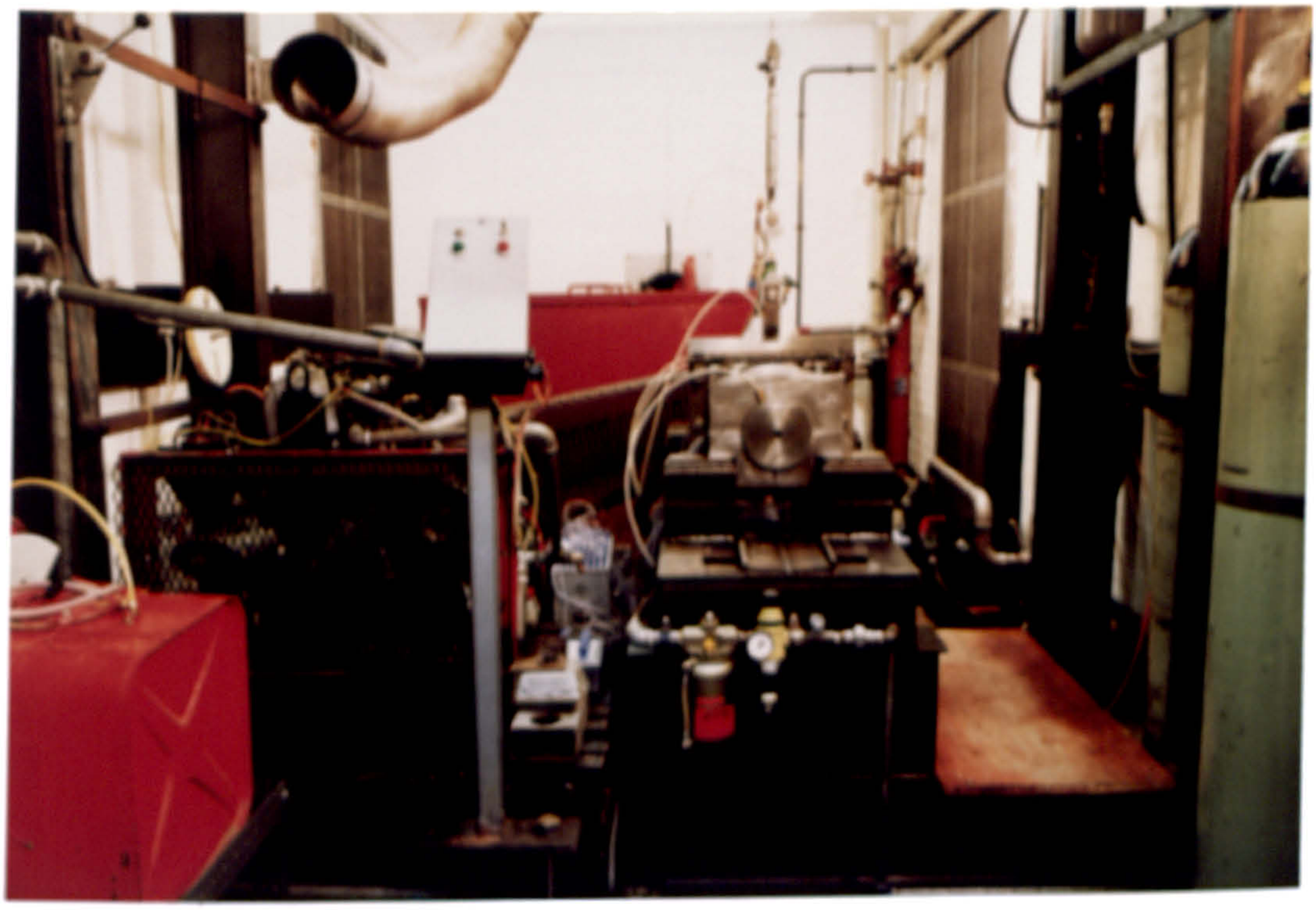

Figure 2.1 Bearing test rig

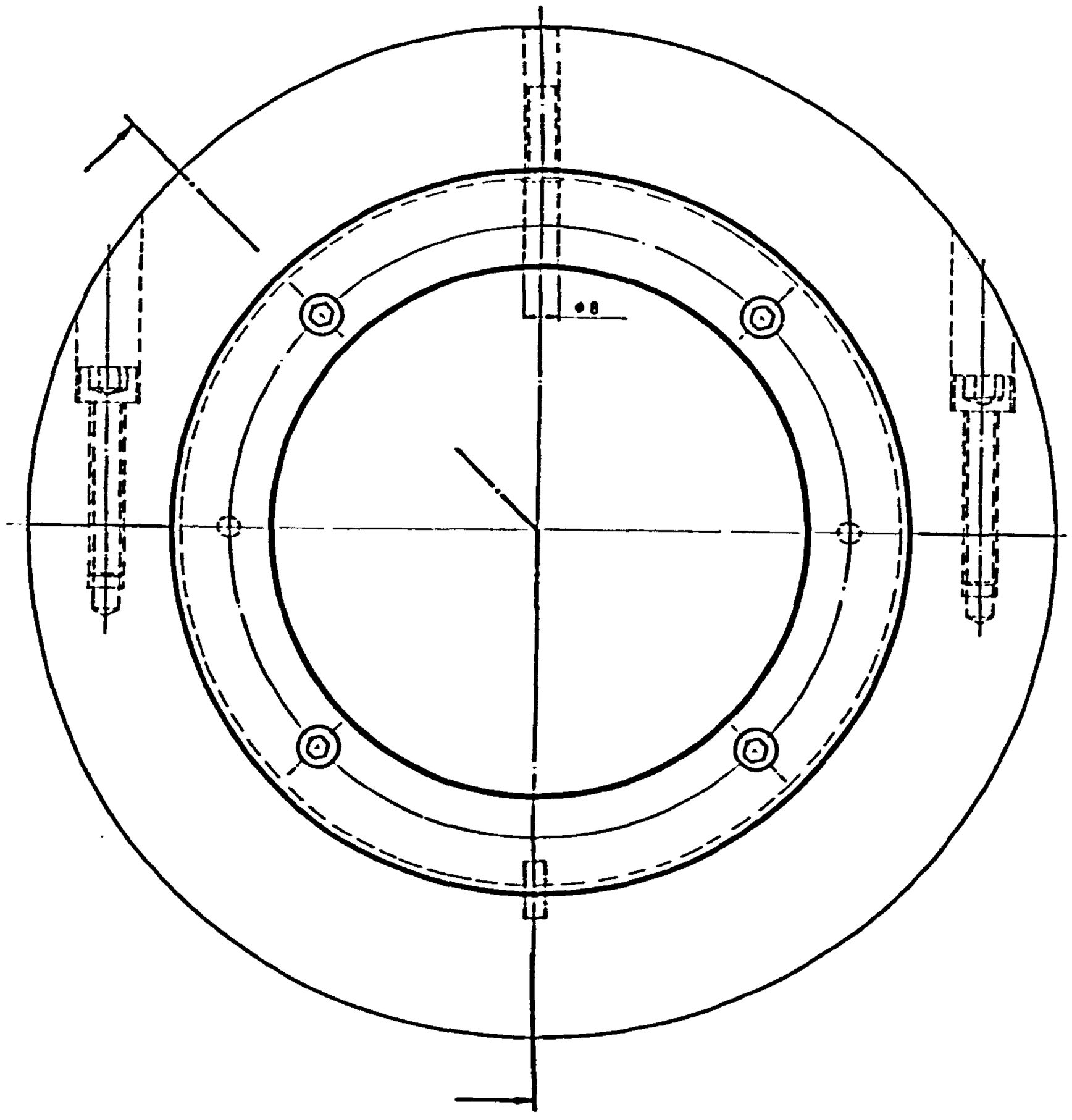

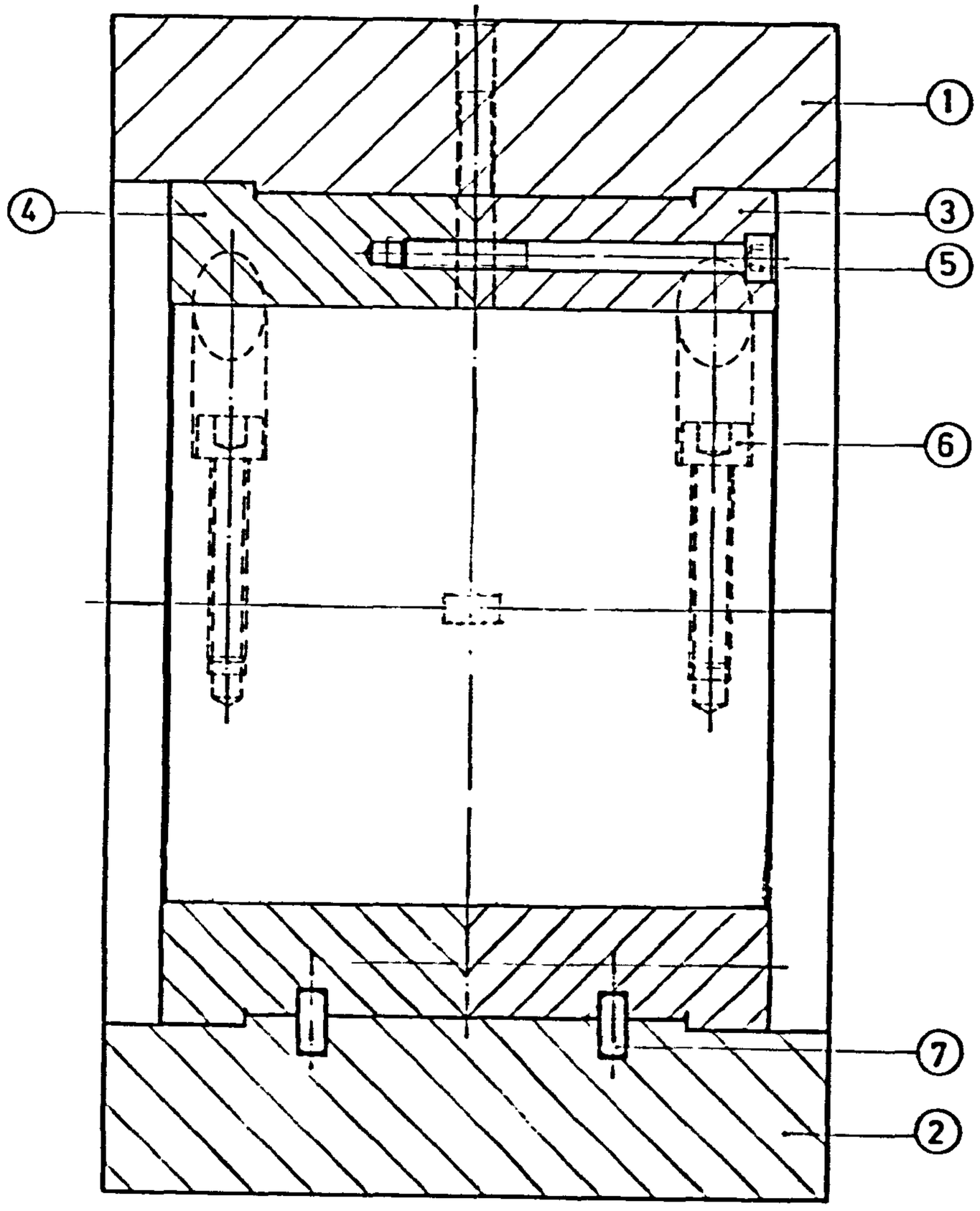

S.No.	Part Name.	Material.	Qty.
7	Dowel Pin ø5 × 10	M S	2
6	Socket Head Screw M8 × 42		4
5	Socket Head Screw M5 × 72		4
4	Right Part of Bush		1
3	Left Part of Bush		1
2	Lower Part of Bush Housing	M S	1
1	Upper Part of Bush Housing	M S	1

Figure 2.2 Plain journal bearing

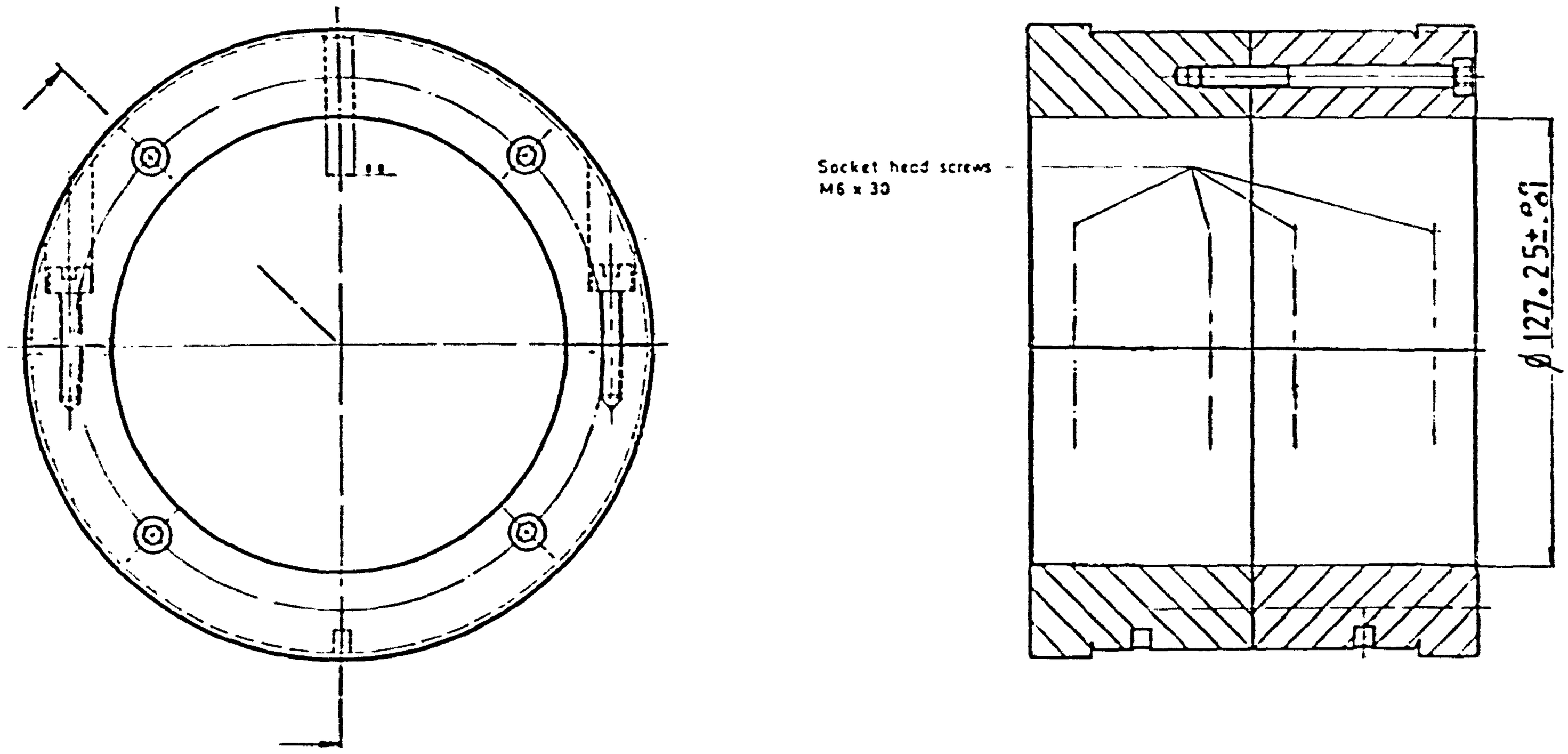

Figure 2.3 Plain bearing bush

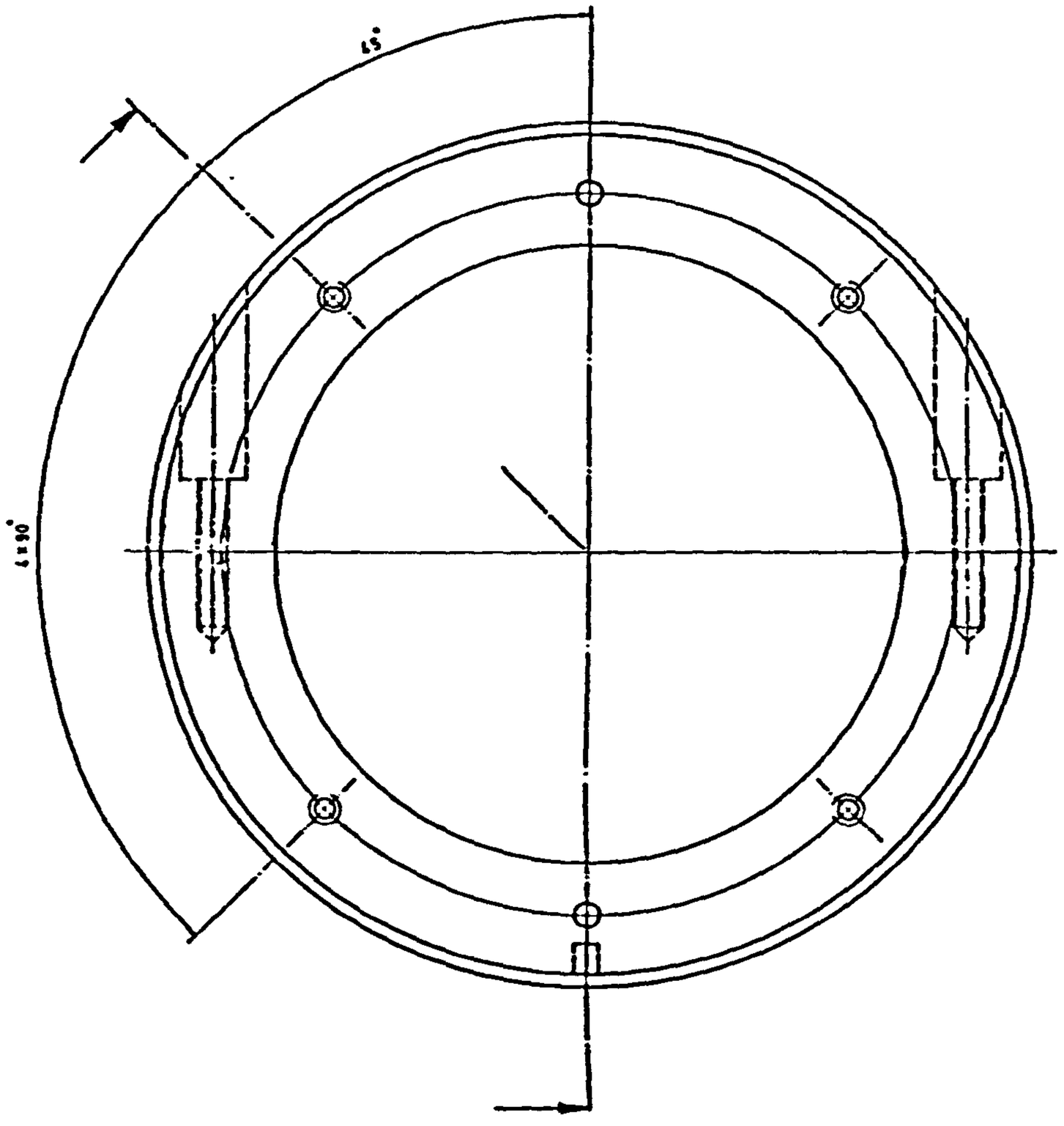

Figure 2.4 Left half of the plain bearing bush

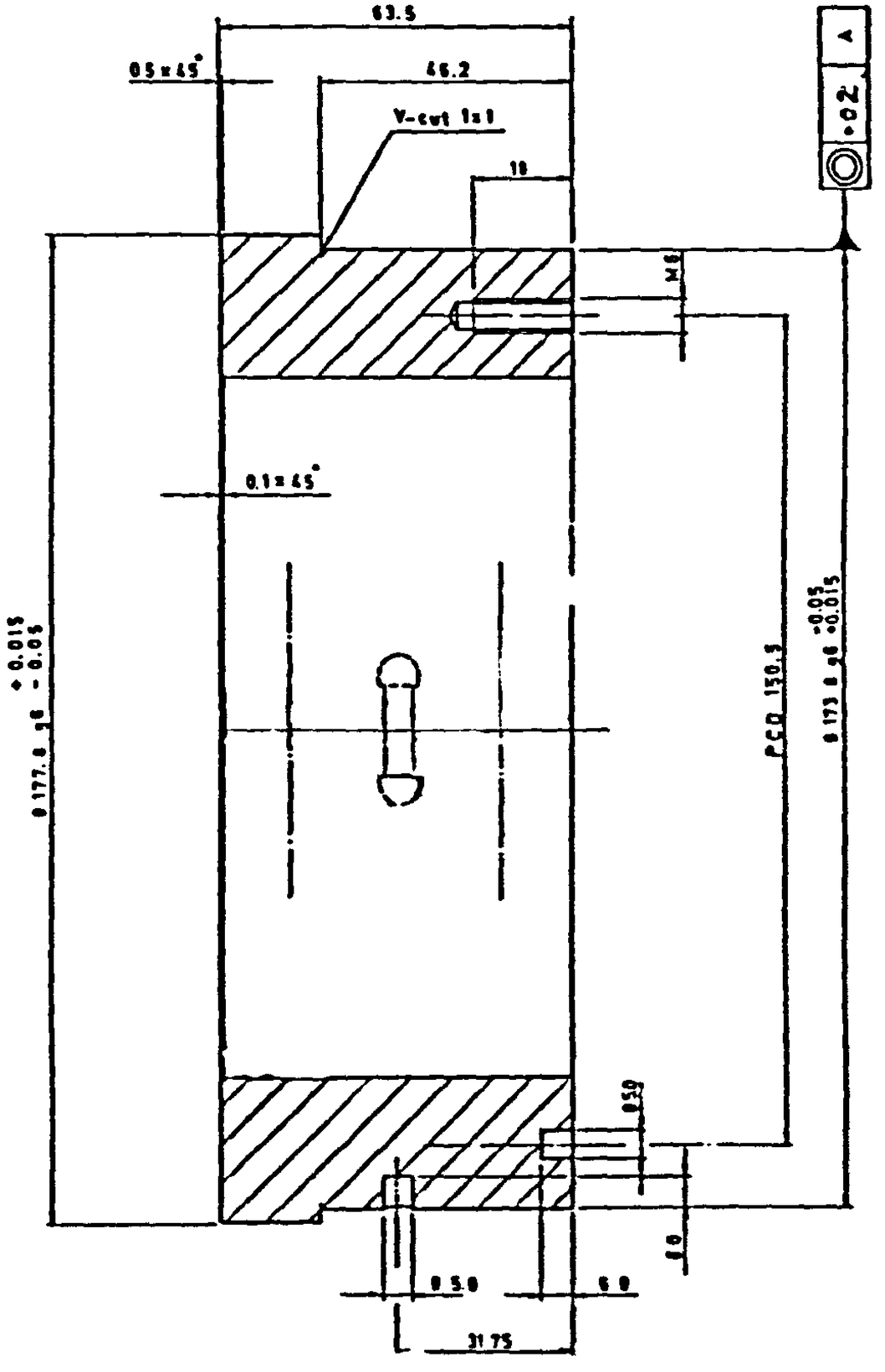

Designed		Material — BRONZE			
Drawn					
Checked					
Traced			Wt	Scale 1:1	
Approved		BUSH HALF (LEFT PART)	Qty		

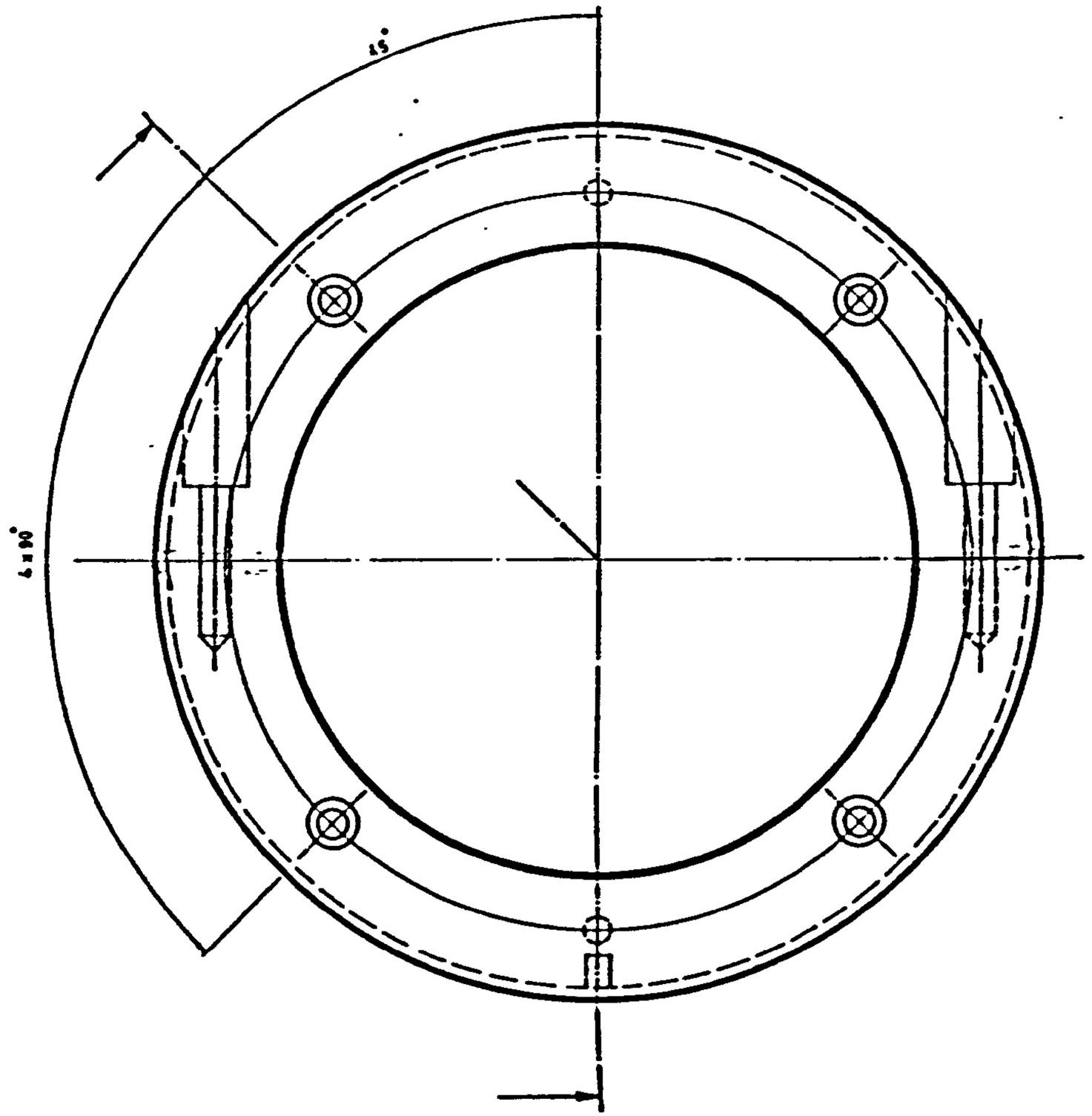

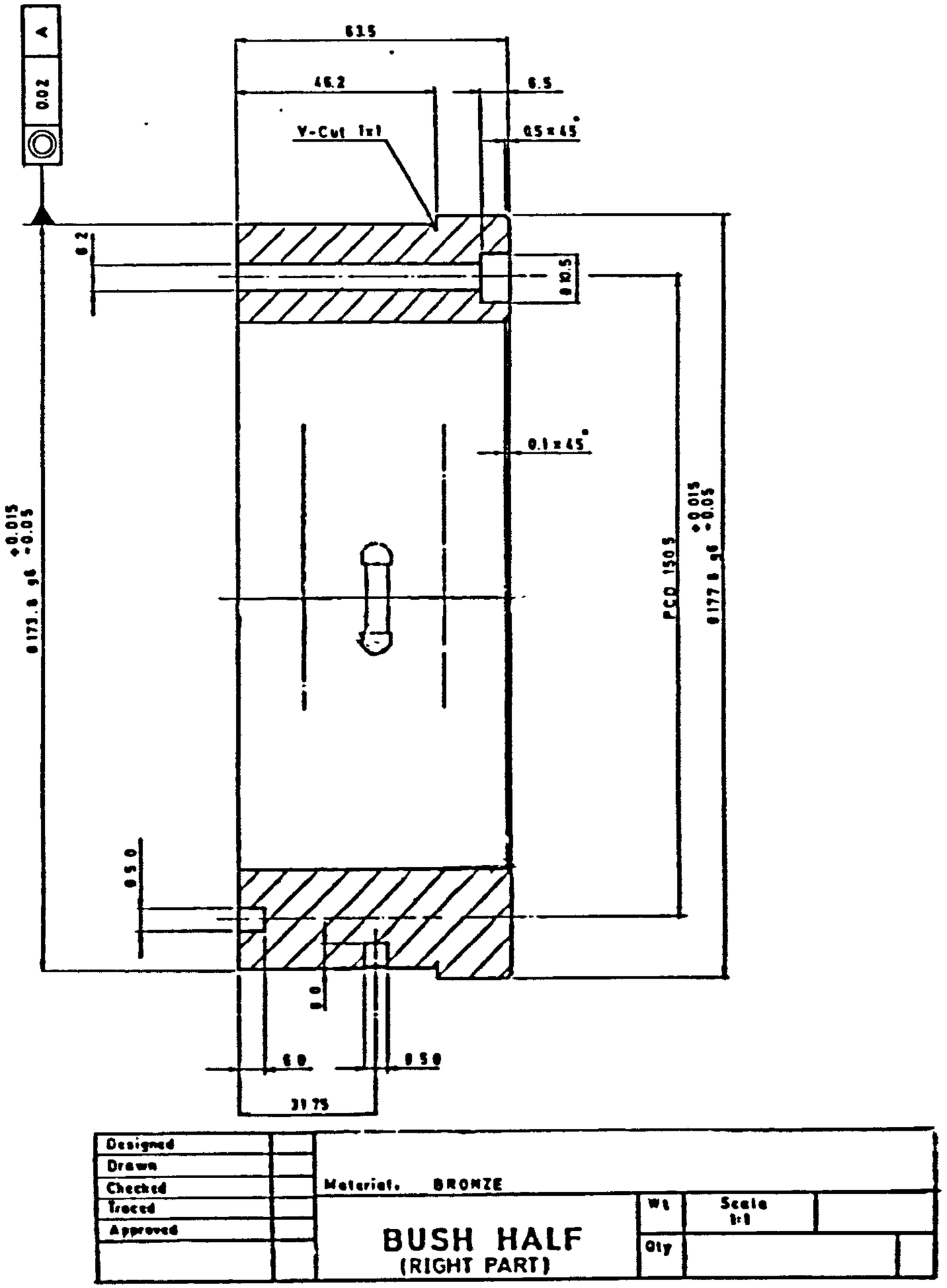

Figure 2.5 Right half oi the plain bearing bush

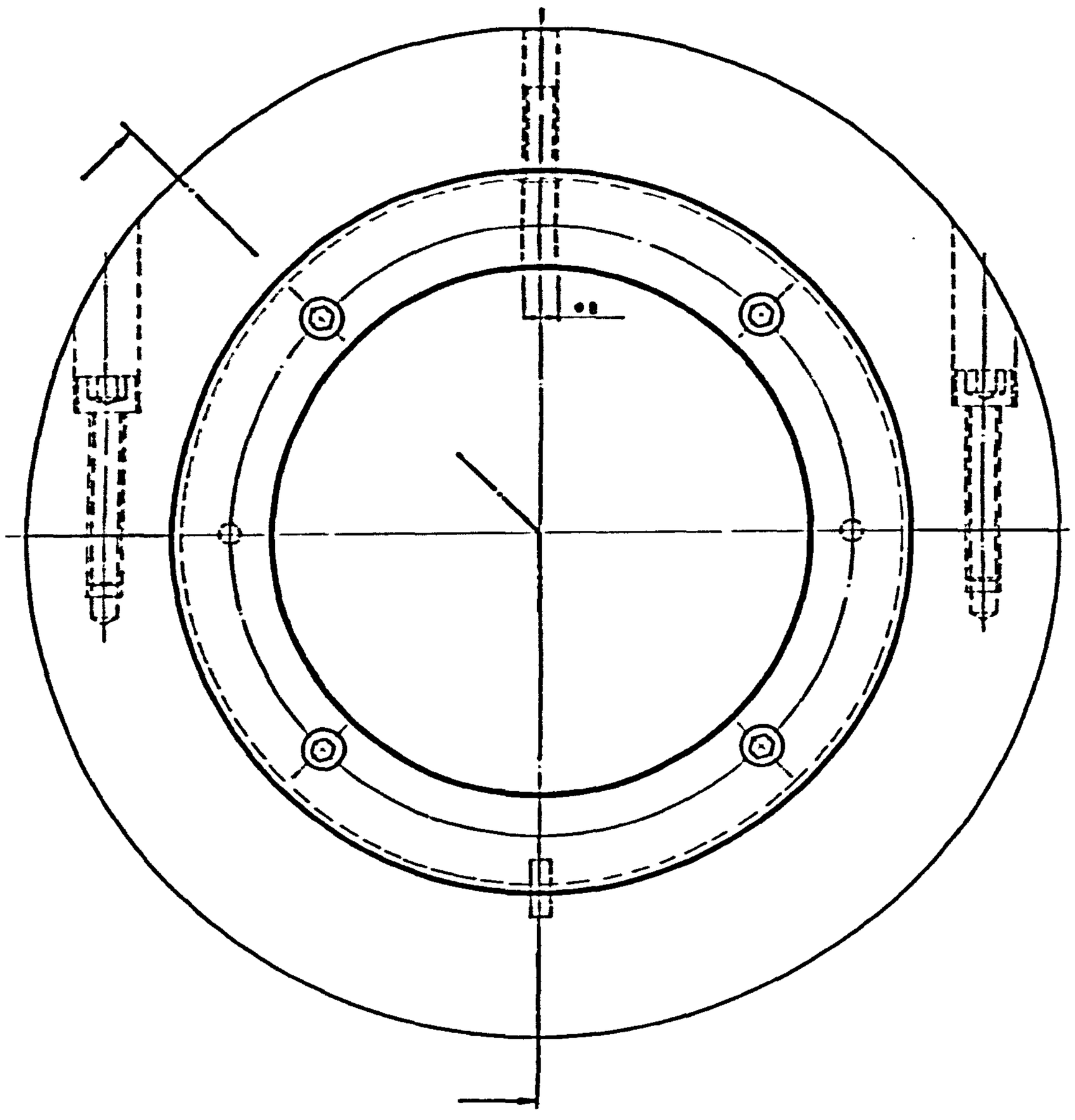

Figure 2.6 Partial helical groove journal bearing

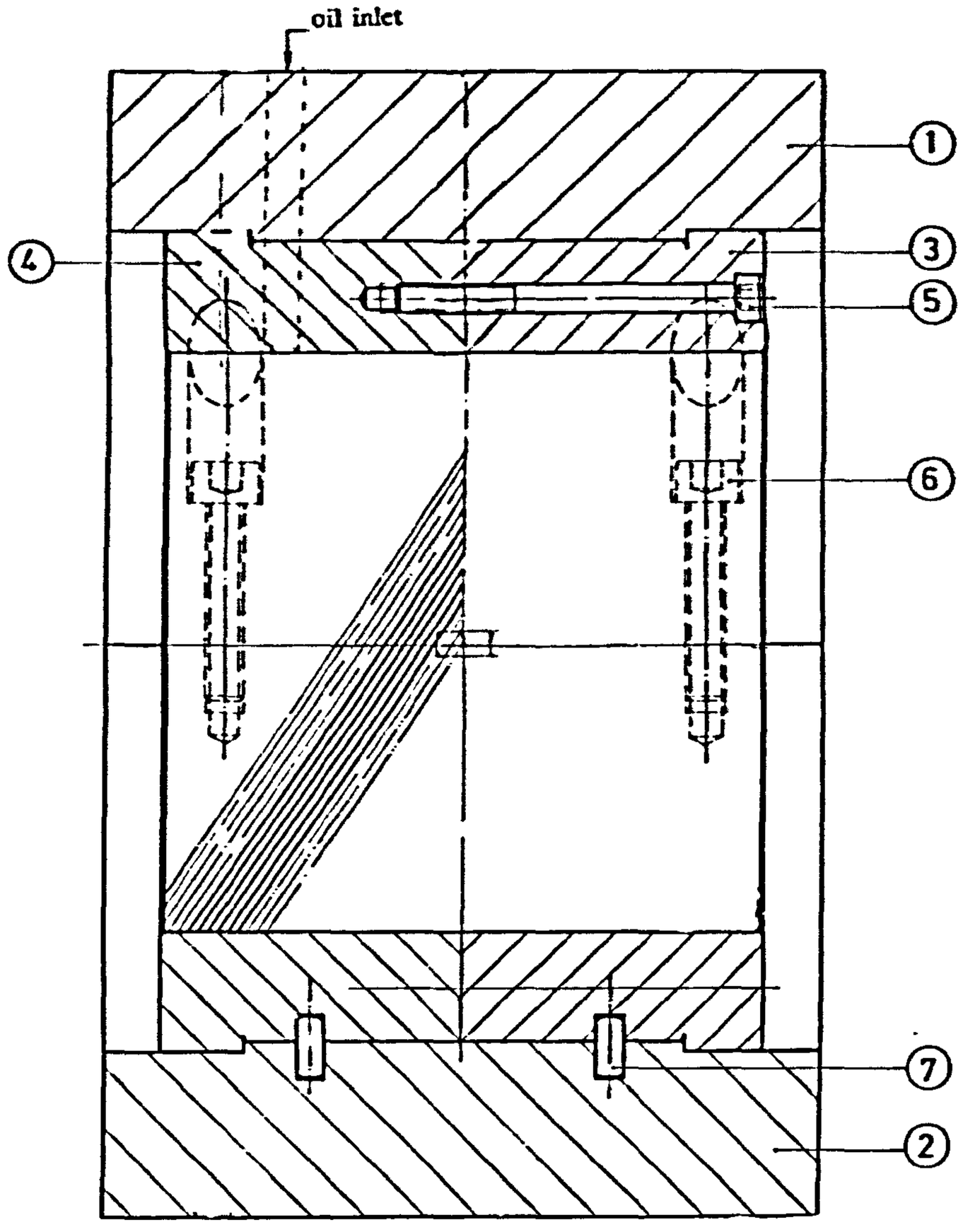

S.No	Part Name.	Material.	Qty
7	Dowel Pin ϕ5×	M S	4
6	Socket Head Screw M8×42		4
5	Socket Head Screw M6×72		4
4	Right Part of Bush		1
3	Left Part of Bush		1
2	Lower Part of Bush Housing	M S	1
1	Upper Part of Bush Housing	M S	1

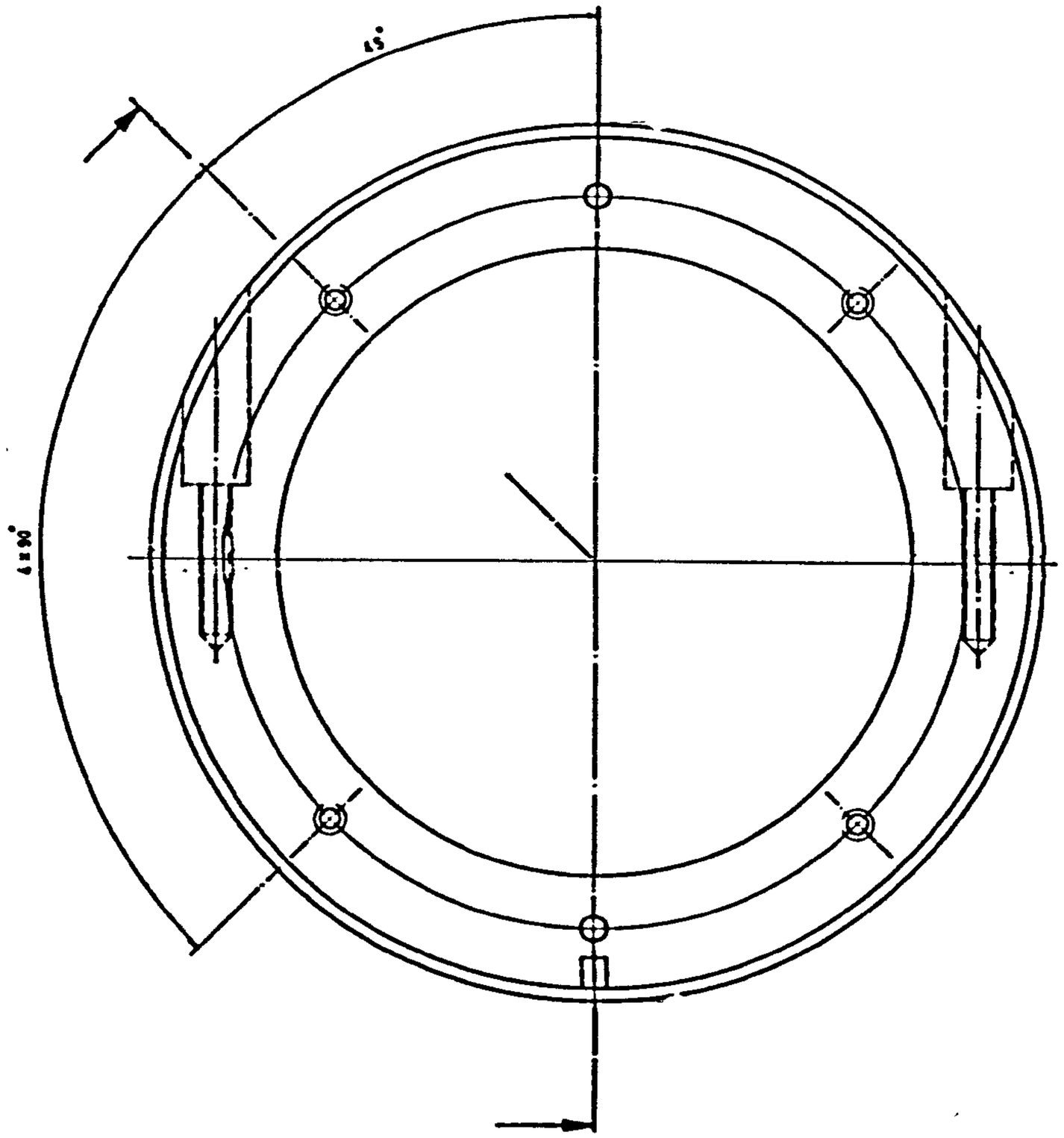

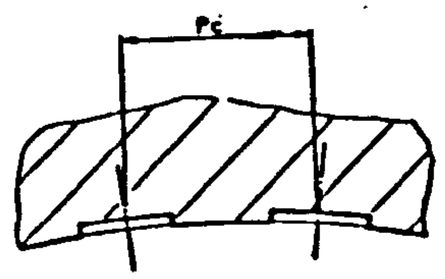

DETAIL OF 'Y'

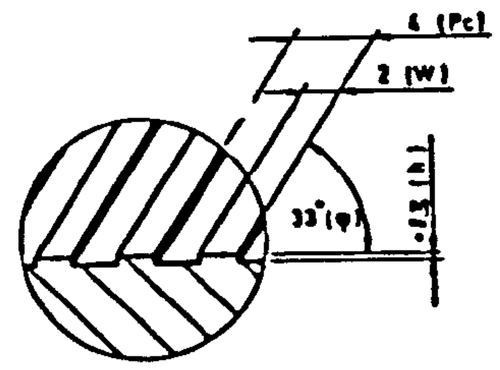

DETAIL OF 'Z'

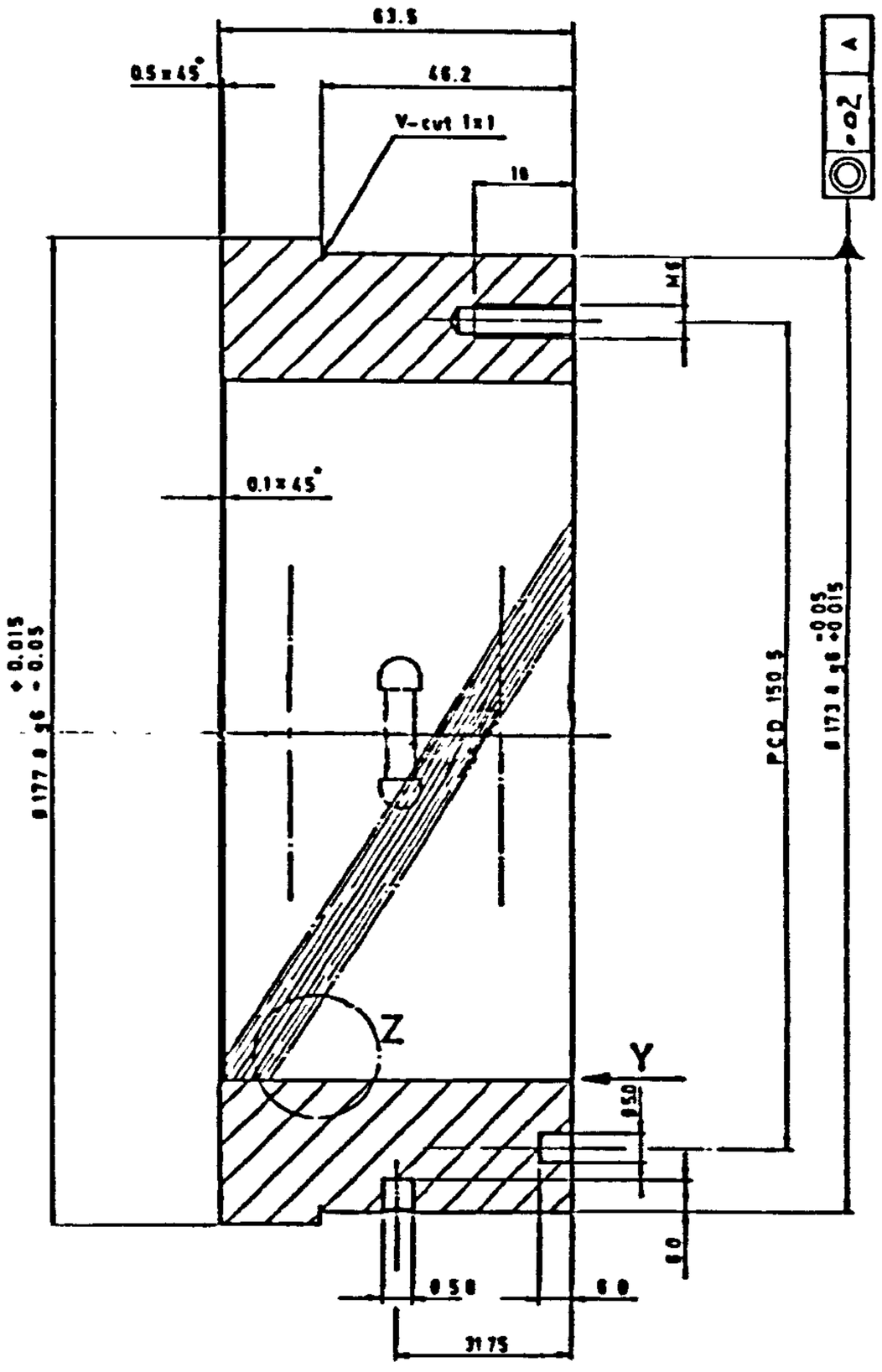

Figure 2.7 Detailes of the groove portion of the partial bearing bush

Pc = Circular pitch.
Pn = Normal pitch.
ψ = Helix angle.
W = Width of groove.
h = Depth of groove.
N = Number of grooves.
L = Lead.

Pc	Pn	ψ	W	h	N	L
7.352	4	33°	2	1.3	54	268

Designed	
Drawn	
Checked	
Traced	
Approved	

Material – BRONZE

BUSH HALF
(LEFT PART)

Wt.
Scale 1:1
Qty

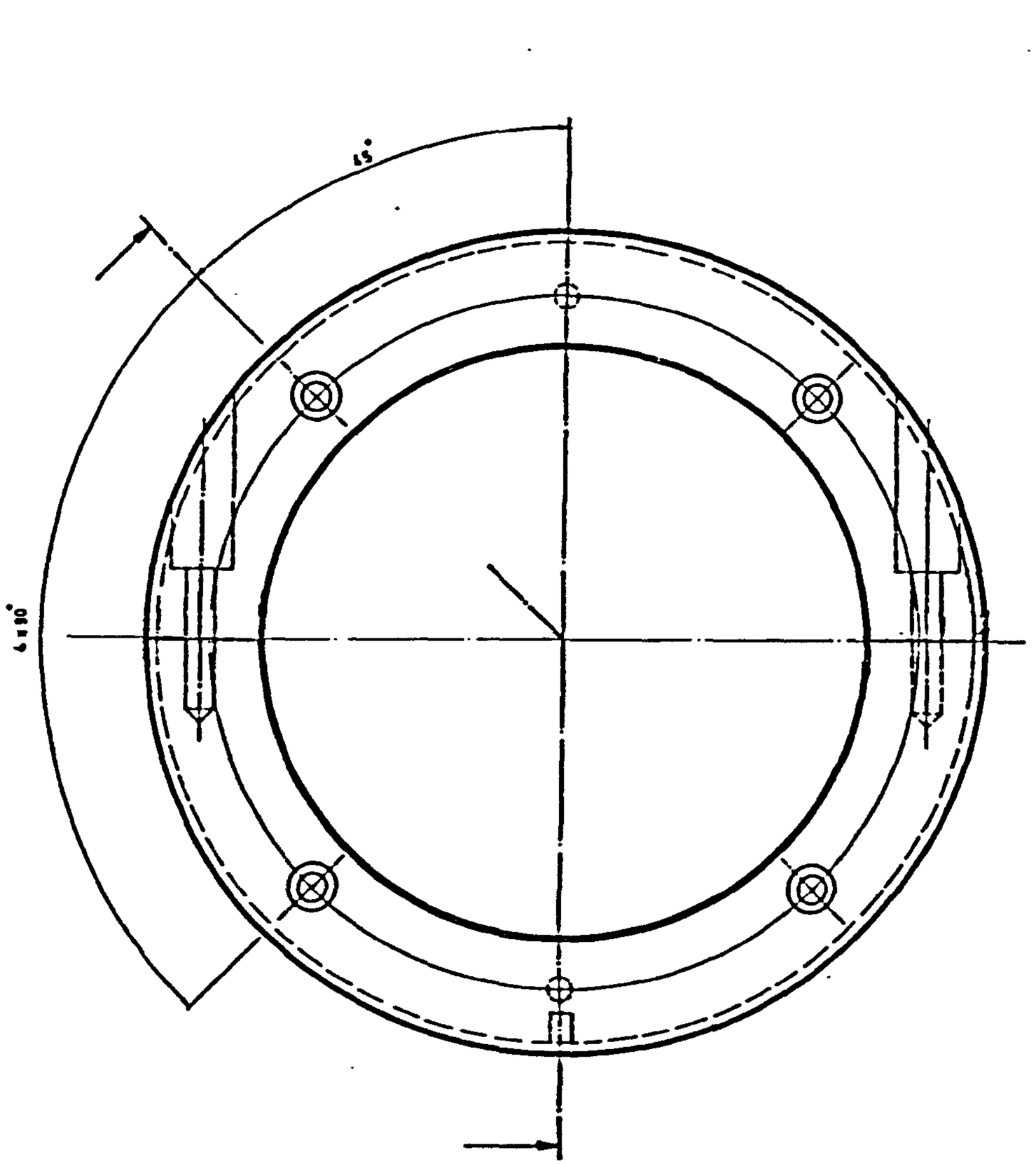

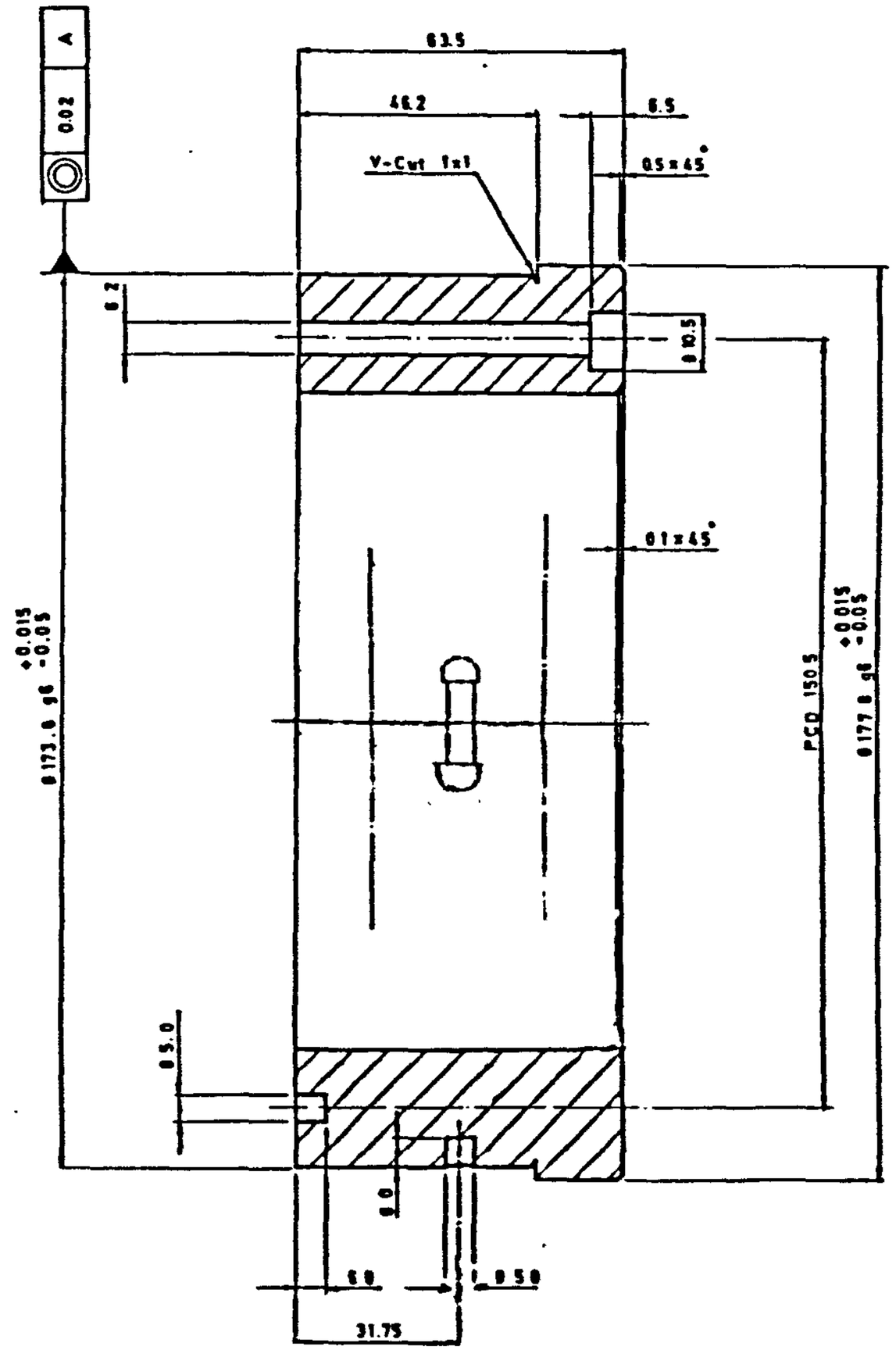

Figure 2.8 Details of the plain portion of the partial bearing bush

Designed		Material. BRONZE		
Drawn				
Checked			Wt	Scale 1:1
Traced		BUSH HALF (RIGHT PART)		
Approved			Qty	

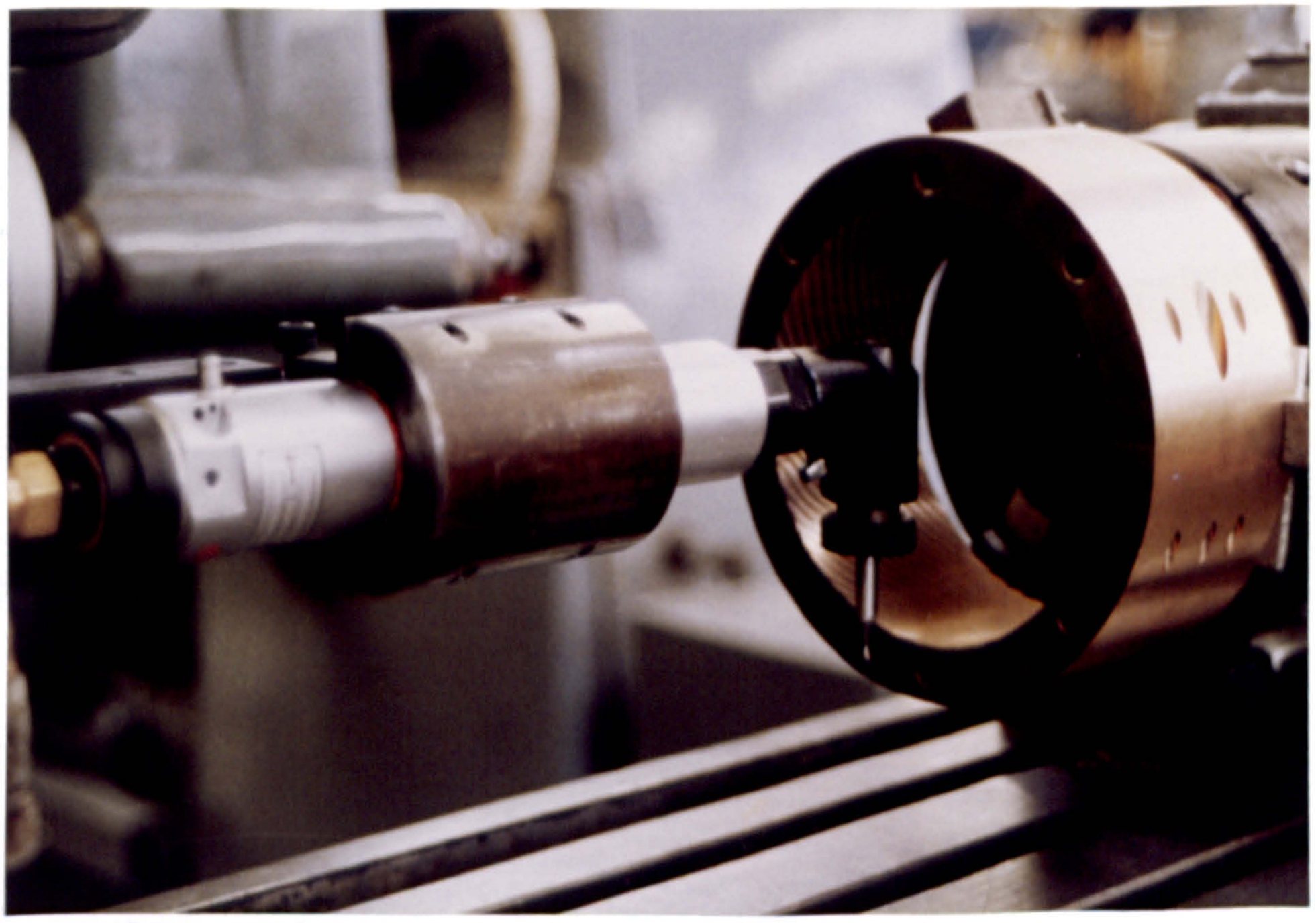

Figure 2.8a Machining of the helical groove by the milling machine

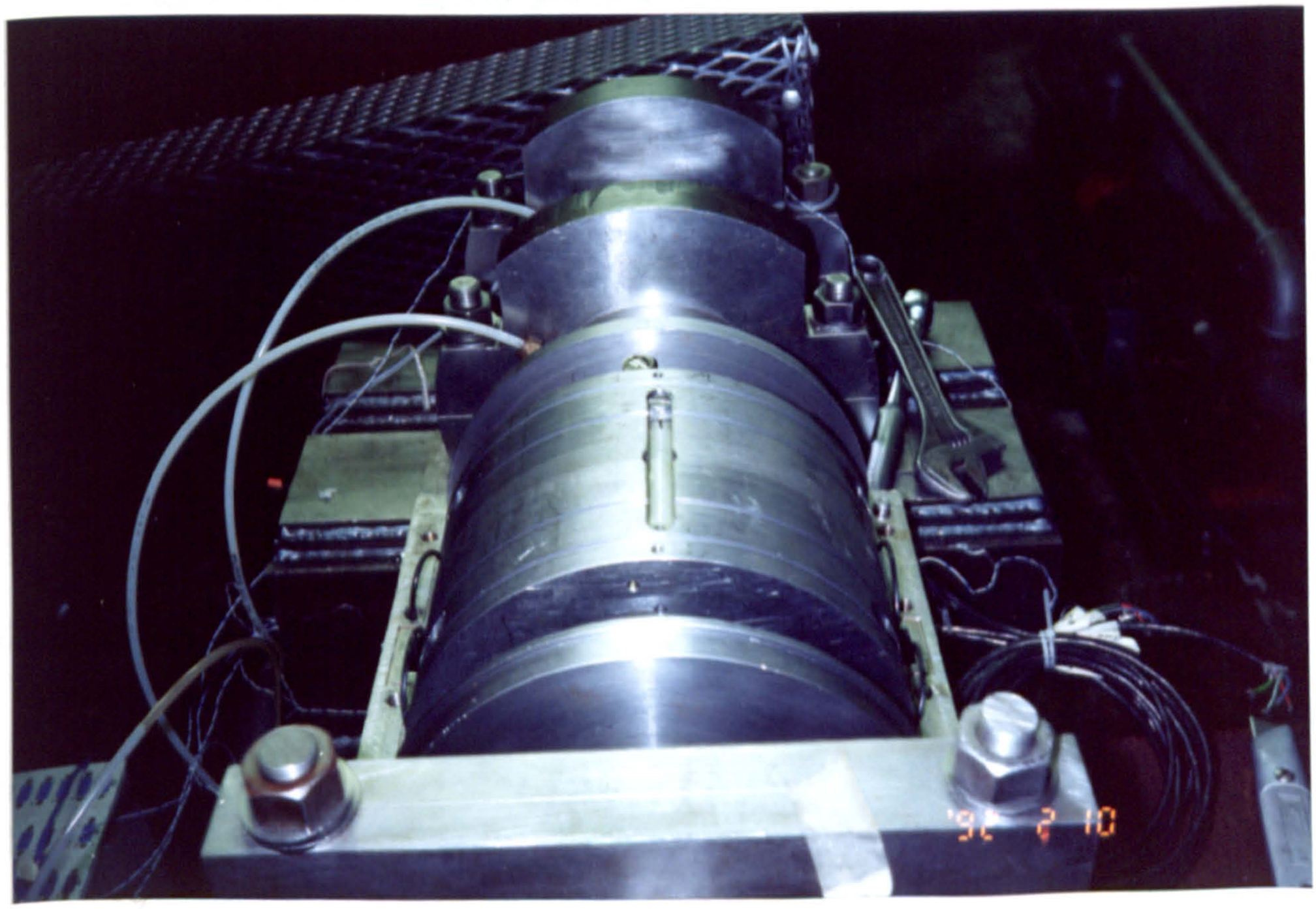

Figure 2.8b Shows axial groove in bearing housing

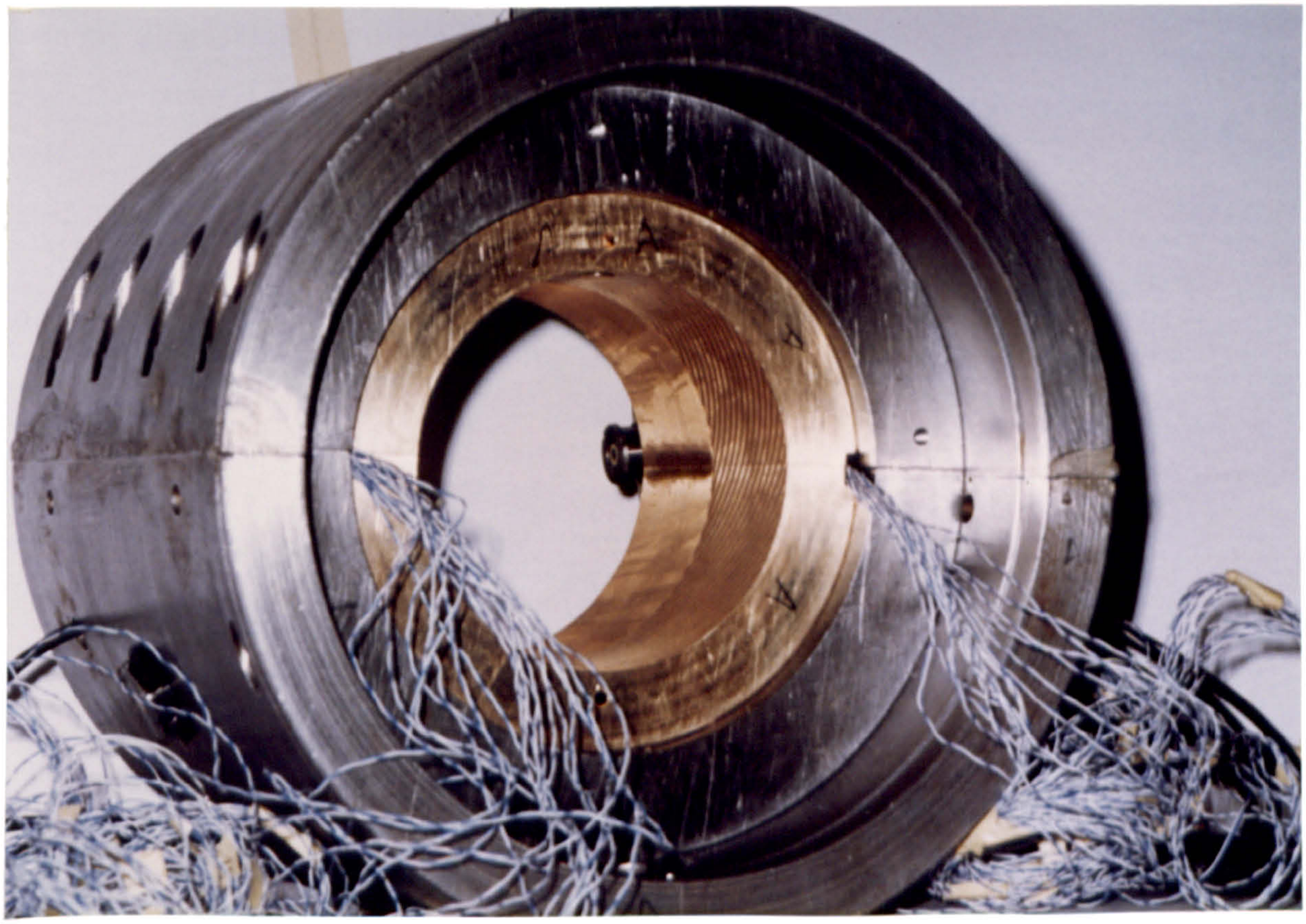

Figure 2.8c Completely assembled partial bearing with instruments

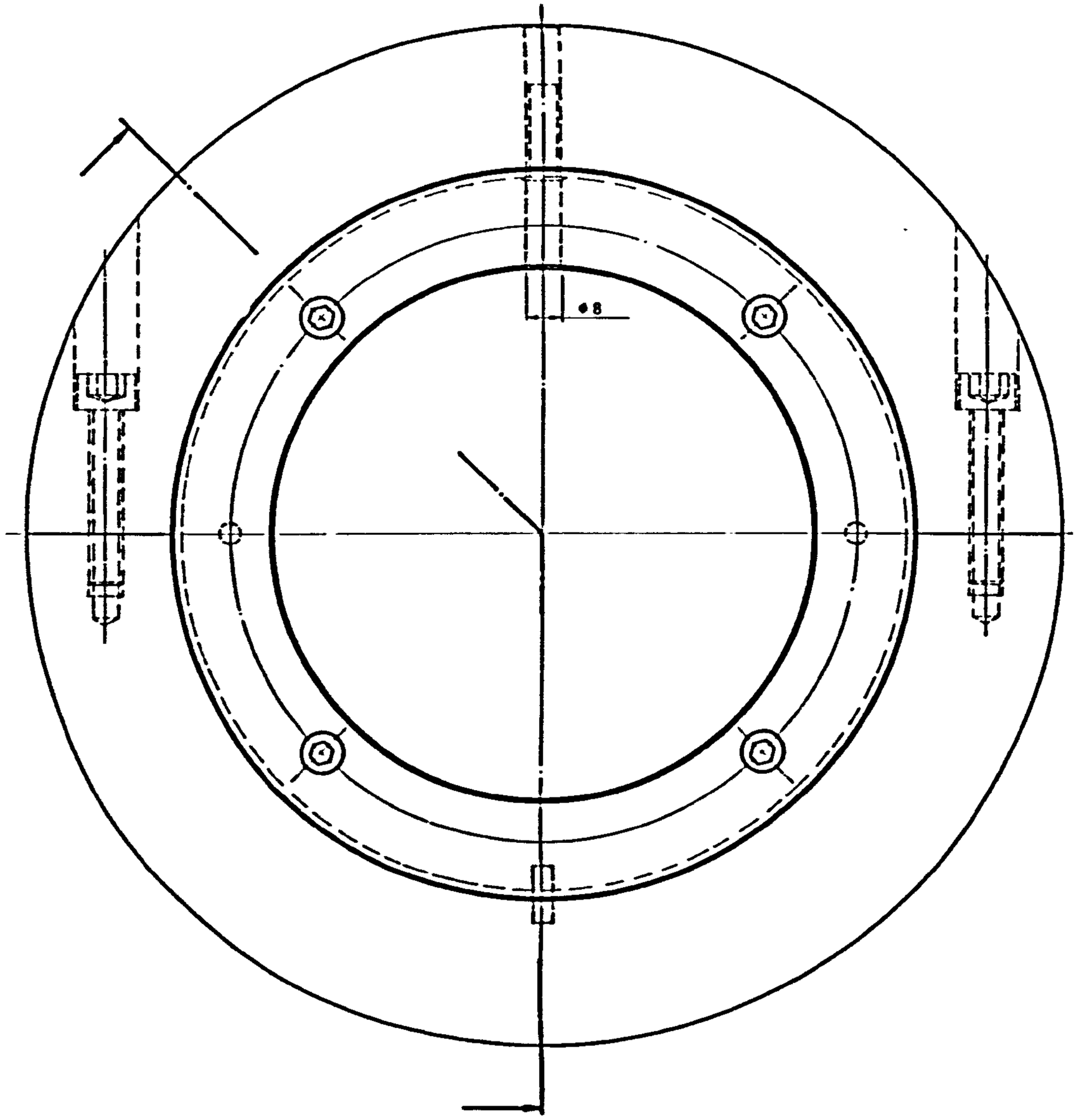

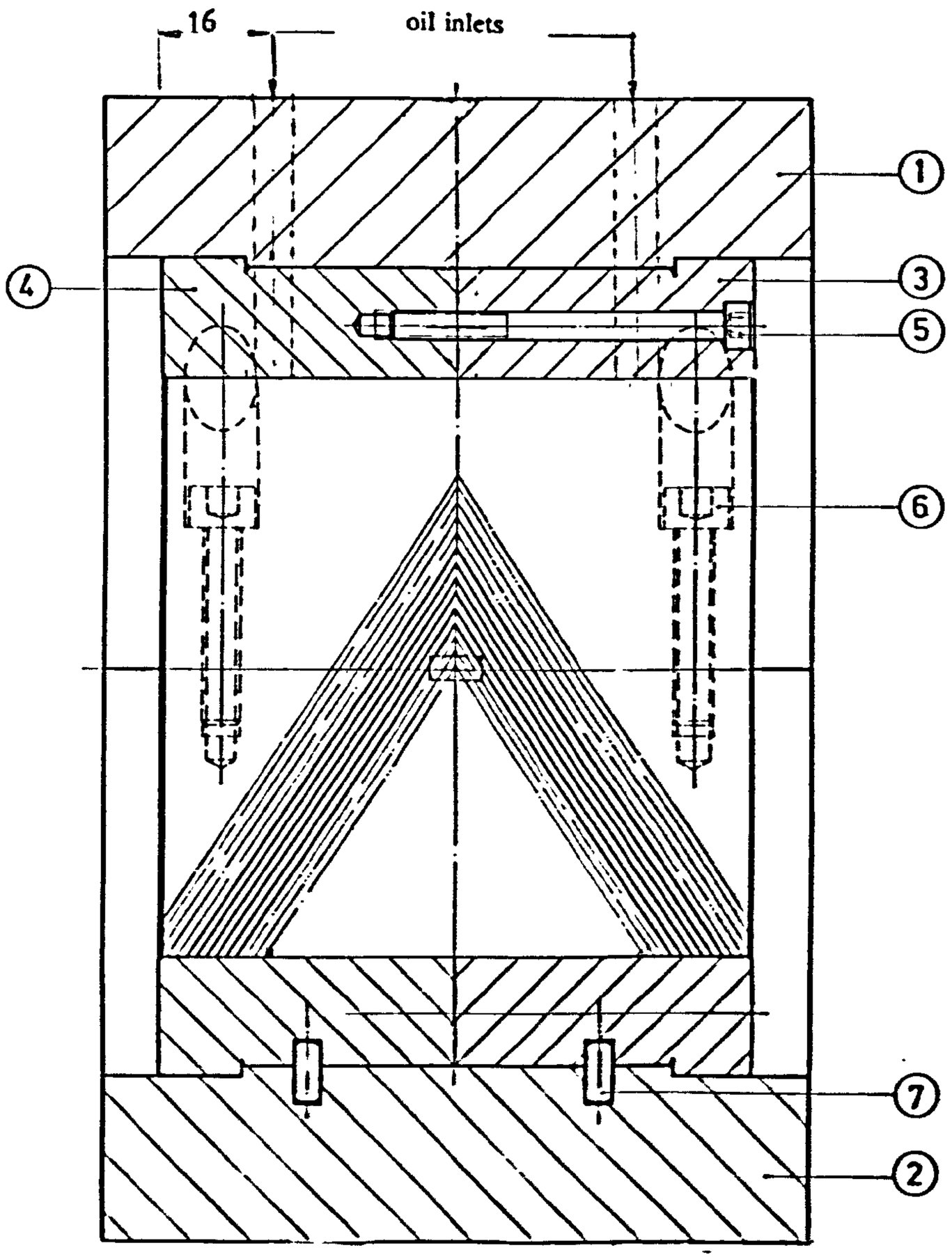

S.No.	Part Name.	Material.	Qty.
7	Dowel Pin ø5×30	MS	4
6	Socket Head Screw M8×42		4
5	Socket Head Screw M6×72		4
4	Right Part of Bush		1
3	Left Part of Bush		1
2	Lower Part of Bush Housing	MS	1
1	Upper Part of Bush Housing	MS.	1

Figure 2.9 Symmetrical helical helical groove bearing

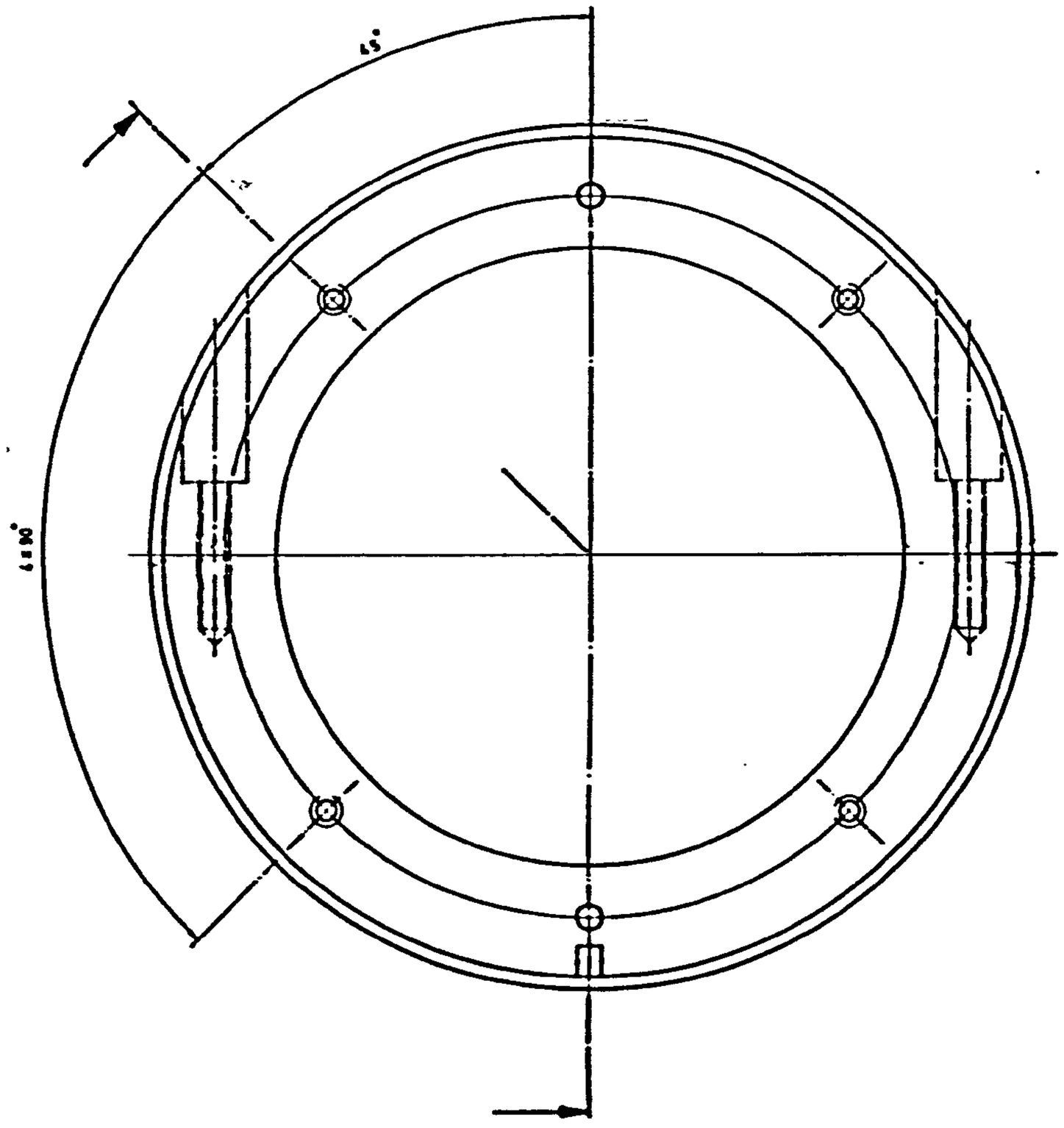

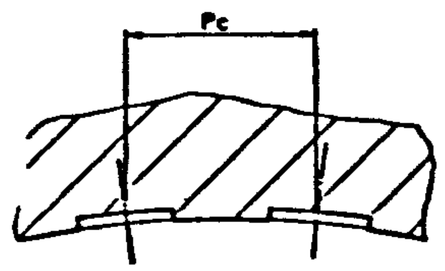

DETAIL OF 'Y'

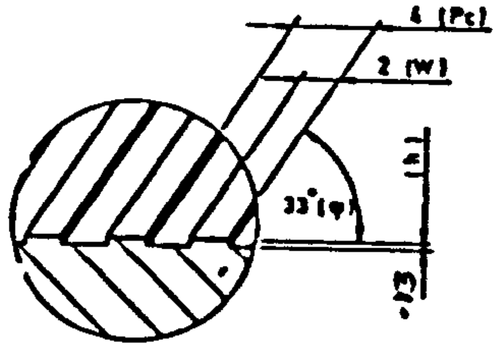

DETAIL OF 'Z'

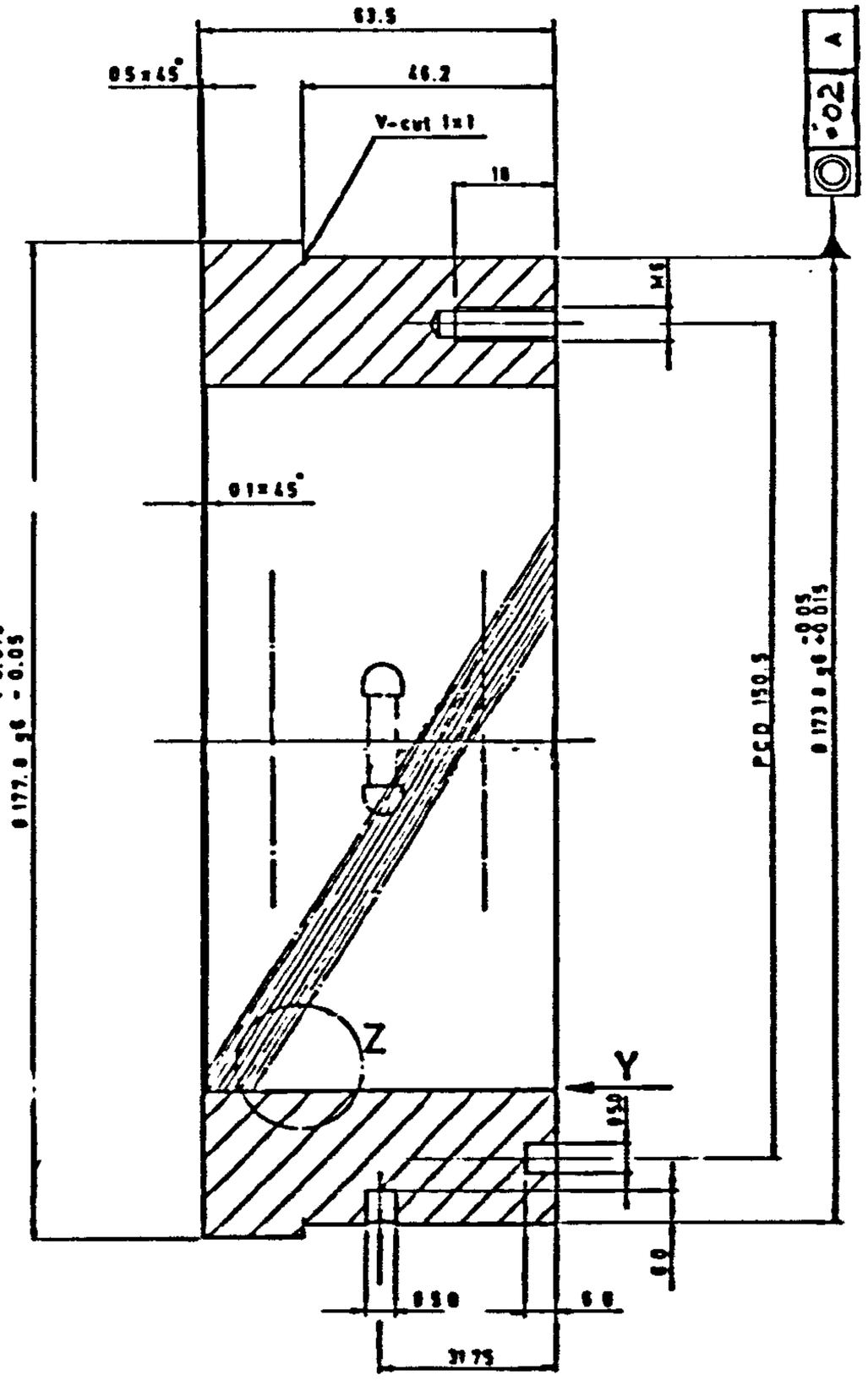

Figure 2.10 Details of the left half of symmetrical bearing bush

Pc = Circular pitch
Pn = Normal pitch.
φ = Helix angle.
W = Width of groove.
h = Depth of groove.
N = Number of grooves.
L = Lead.

Pc	Pn	φ	W	h	N	L
7.352	6	33°	2	1.3	54	268

Designed	
Drawn	
Checked	
Traced	
Approved	

Material — BRONZE

BUSH HALF
(LEFT PART)

Wt.
Scale 1:1
Qty

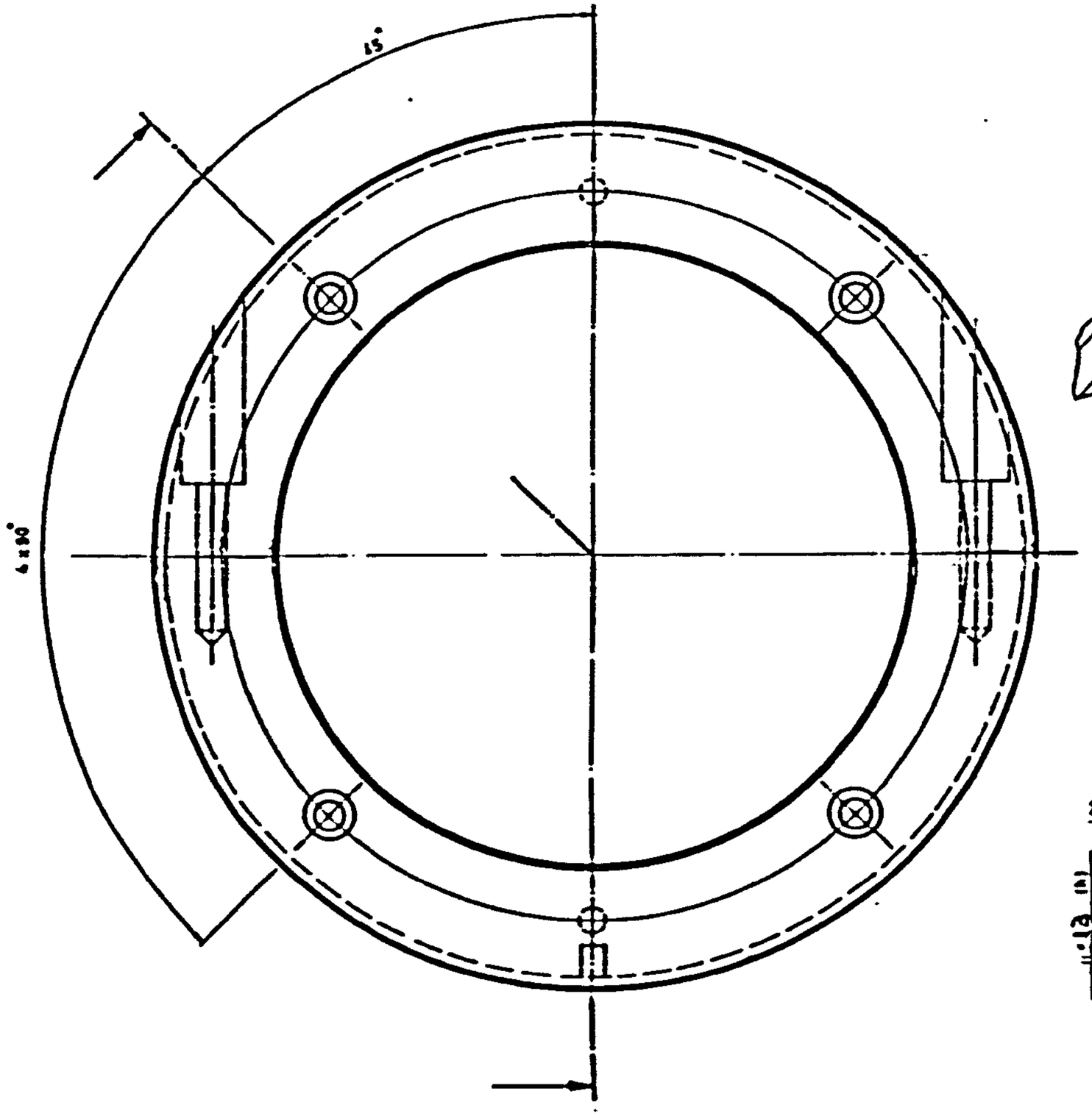

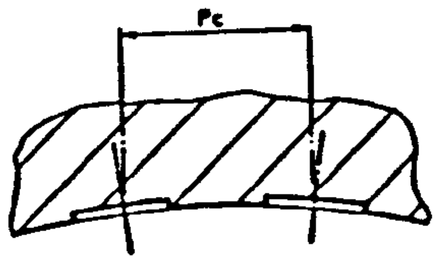

DETAIL OF 'Y'

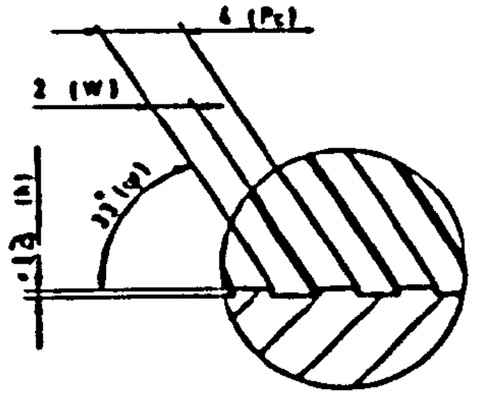

DETAIL OF 'Z'

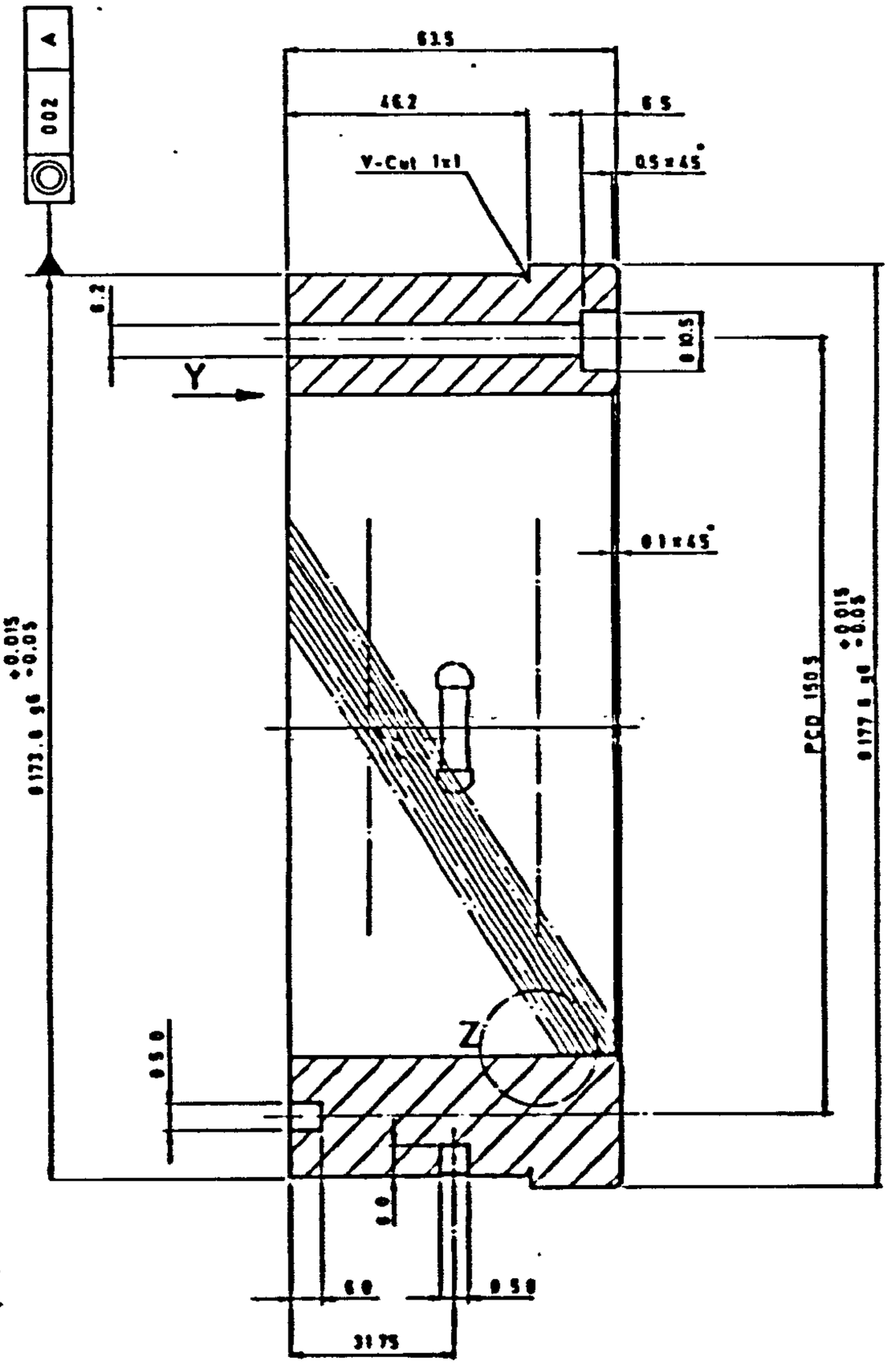

Figure 2.11 Details of the right half of the symmetrical bearing

Pc = Circular pitch.
Pn = Normal pitch.
ψ = Helix angle.
W = Width of groove.
h = Depth of groove.
N = Number of grooves.
L = Lead.

Pc	Pn		W	h	N	L
7.352	6	35°	2	-13	54	268

Designed		Material. BRONZE		
Drawn				
Checked				
Traced			Wt	Scale 1:1
Approved		BUSH HALF (RIGHT PART)	Qty	

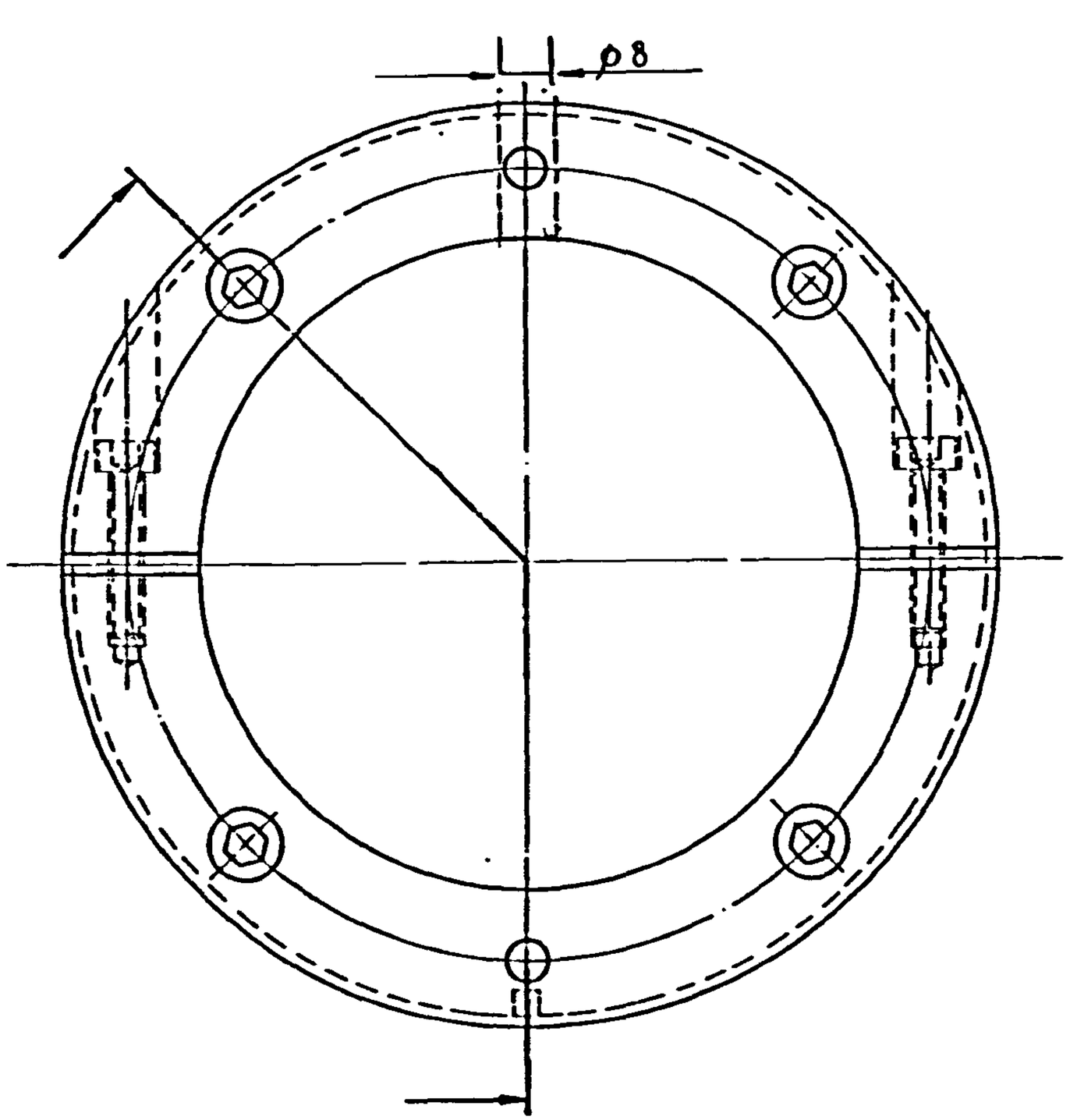

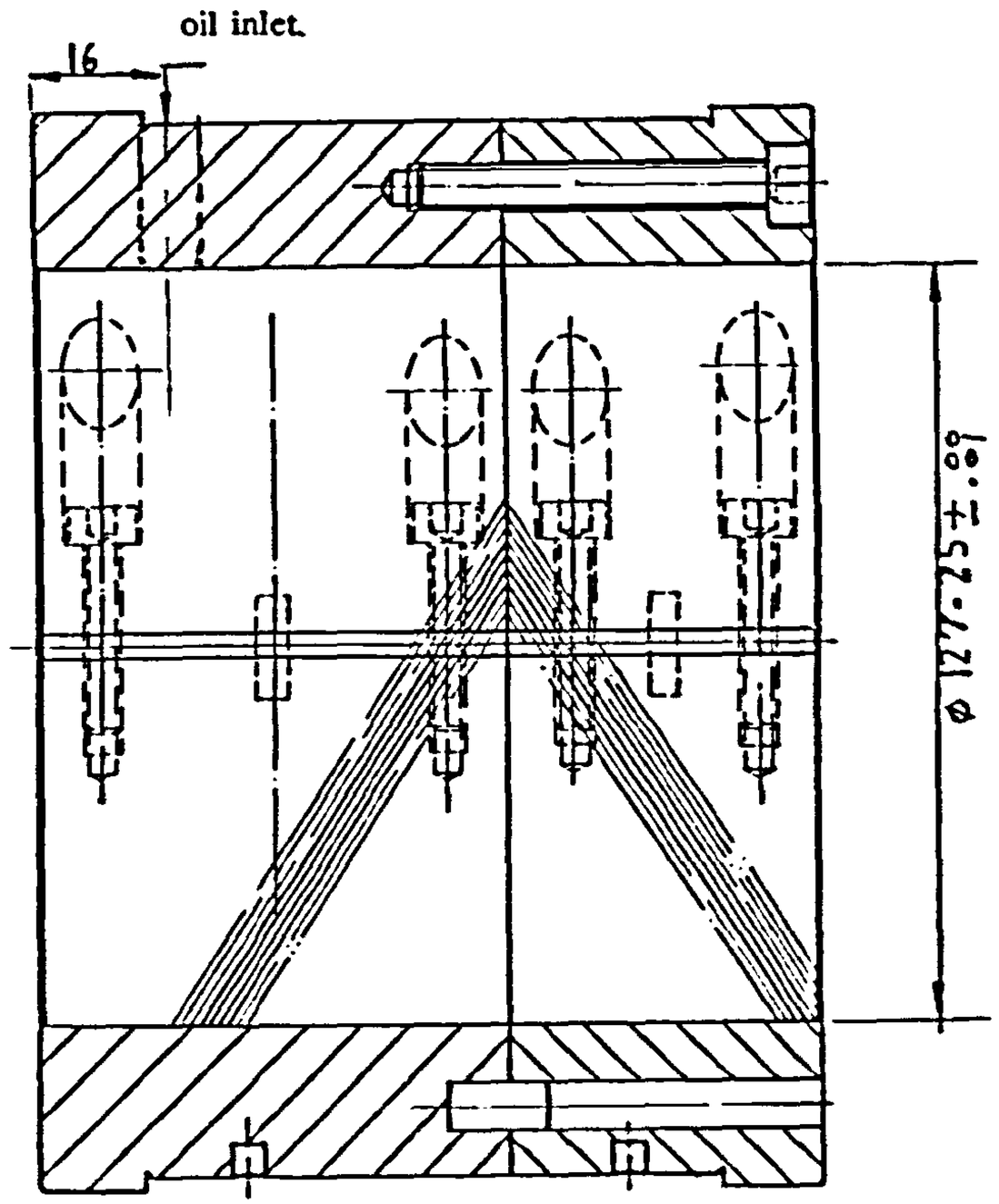

Designed		Material:-		
Drawn				
Checked				
Traced				
Approved		BUSH (ASSEMBLY)	Wt	Scale
			Qty	

Figure 2.12 Asymmetrical helical groove journal bearing bush

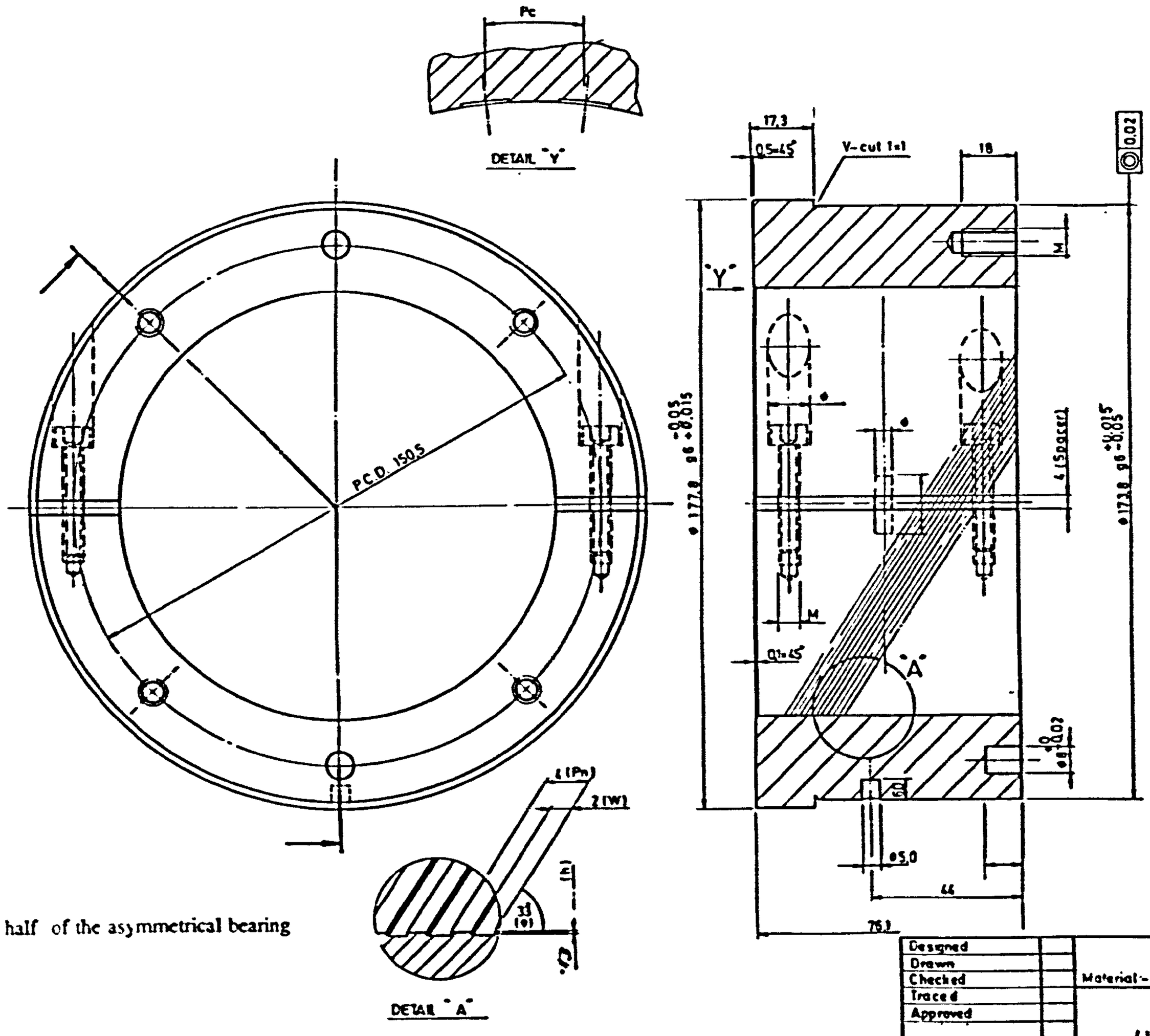

Figure 2.13 Left half of the asymmetrical bearing bush

Pc	Pn	θ	W	h	N	L
7.352	6	33	2	13	54	260

Designed		Material:- BRONZE	
Drawn			
Checked			
Traced			
Approved		BUSH (LEFT PART)	Wt. / Scale 1:1 / Qty.

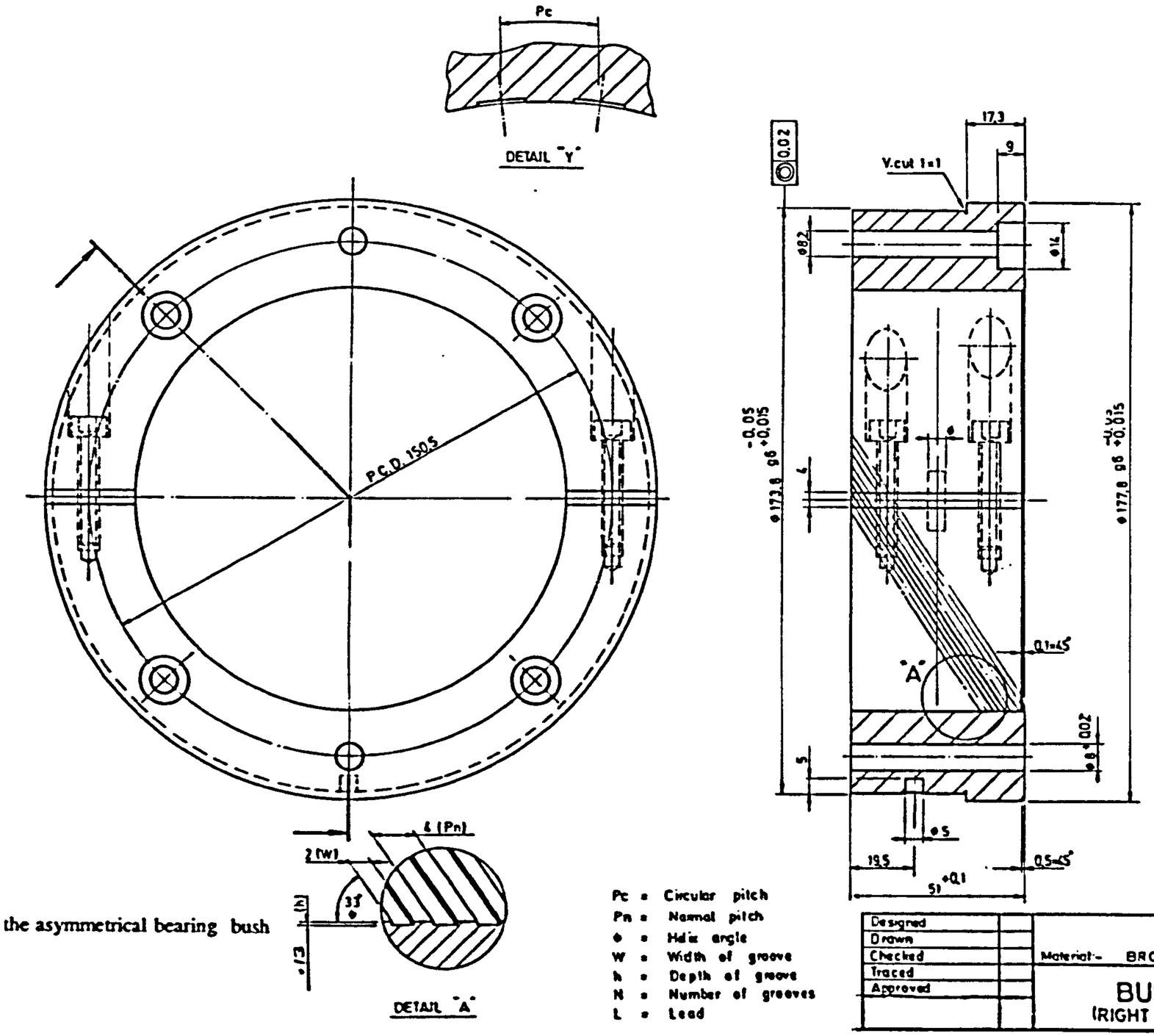

Figure 2.14 Right half of the asymmetrical bearing bush

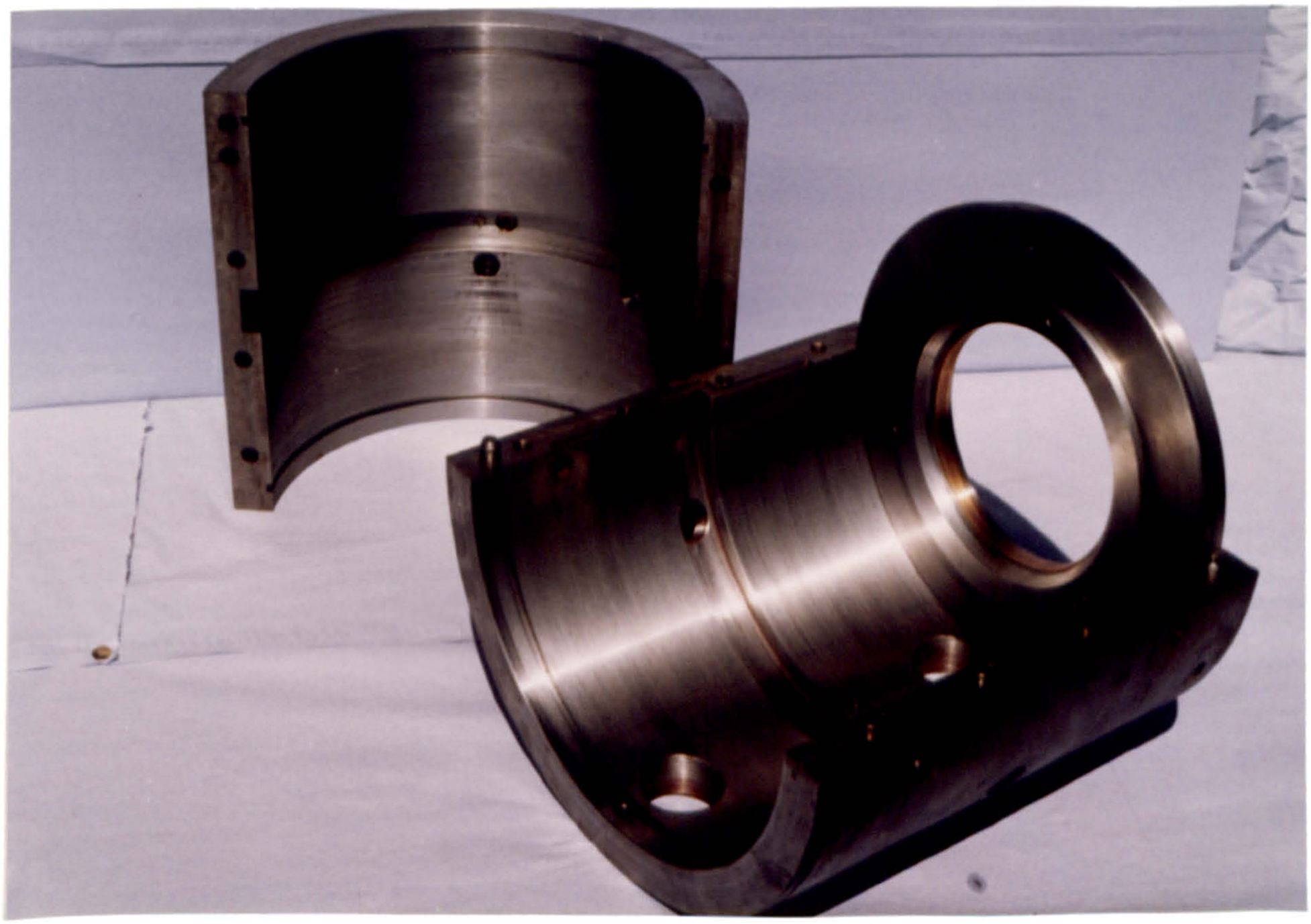

Figure 2.15 Main bearing housing

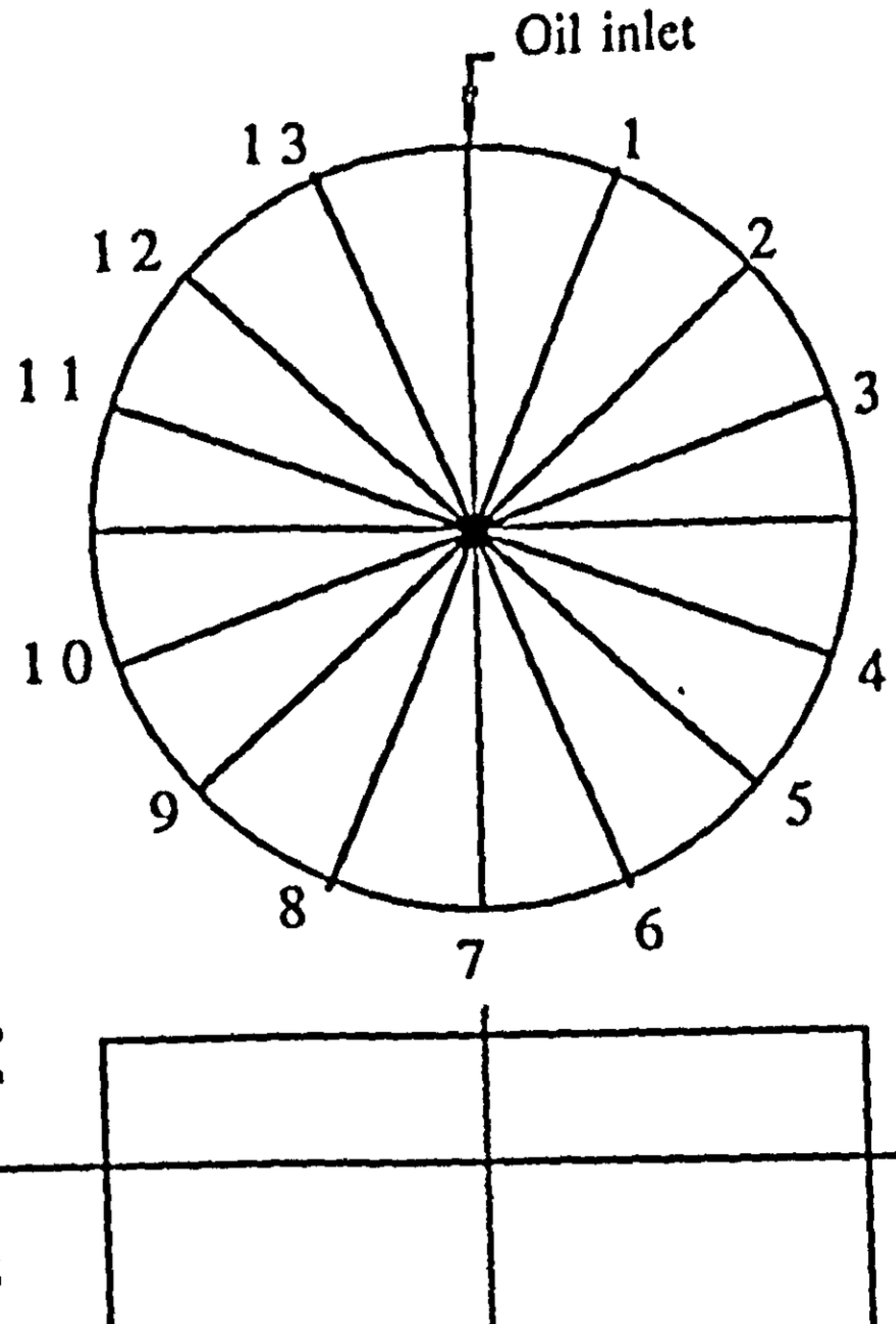

Angular position of thermocouples at locations 2 and 3

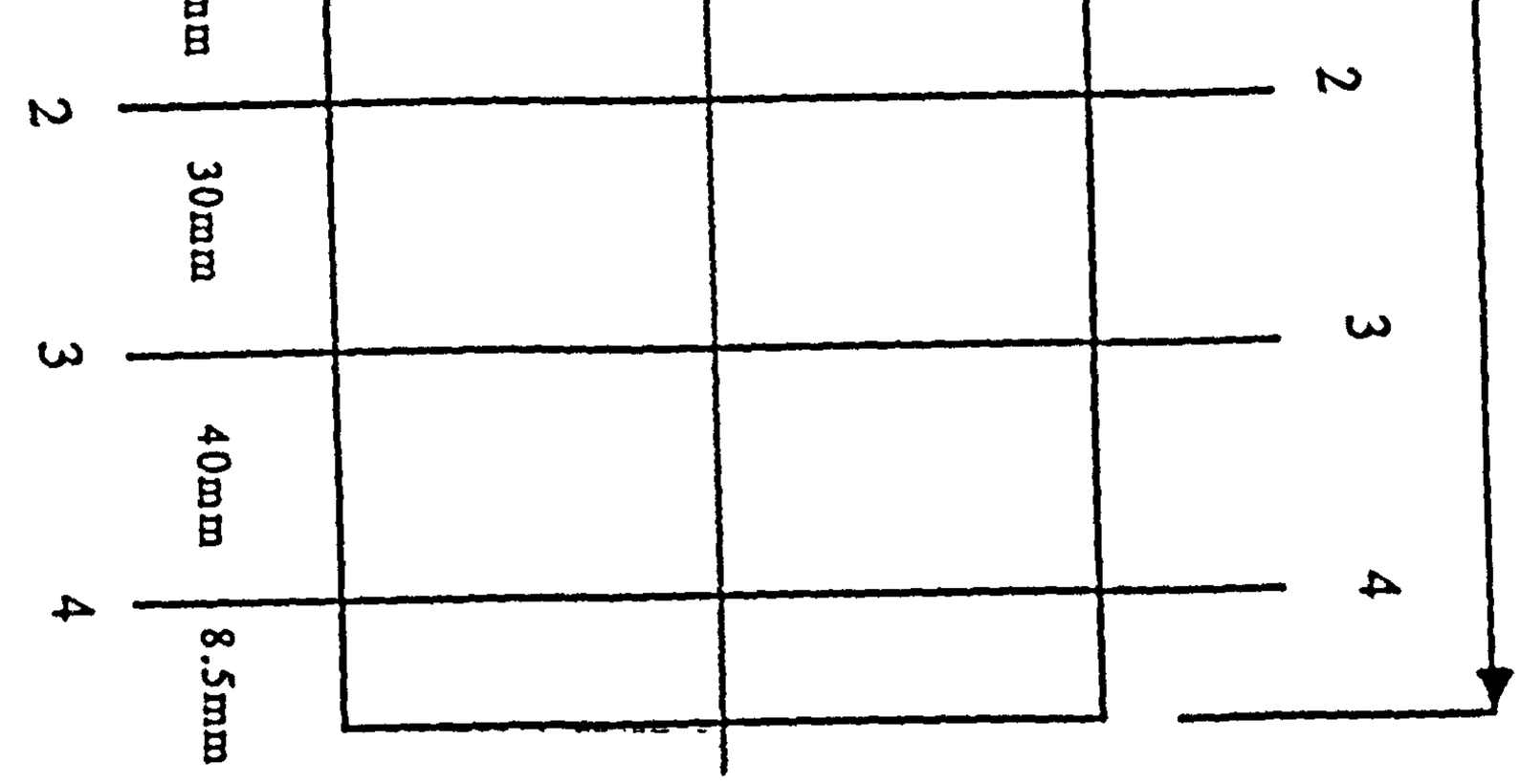

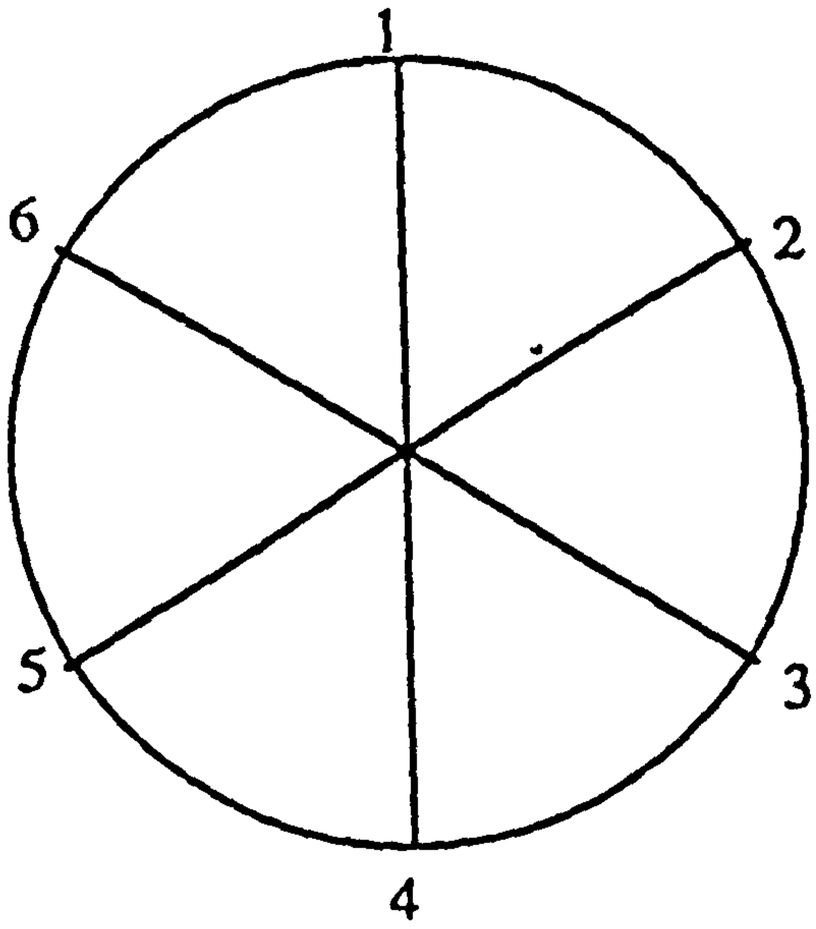

Angular position of thermocouple at location 1 and 4

Figure 2.16 Locations of thermocouples in four planes along the axial length of the bearing

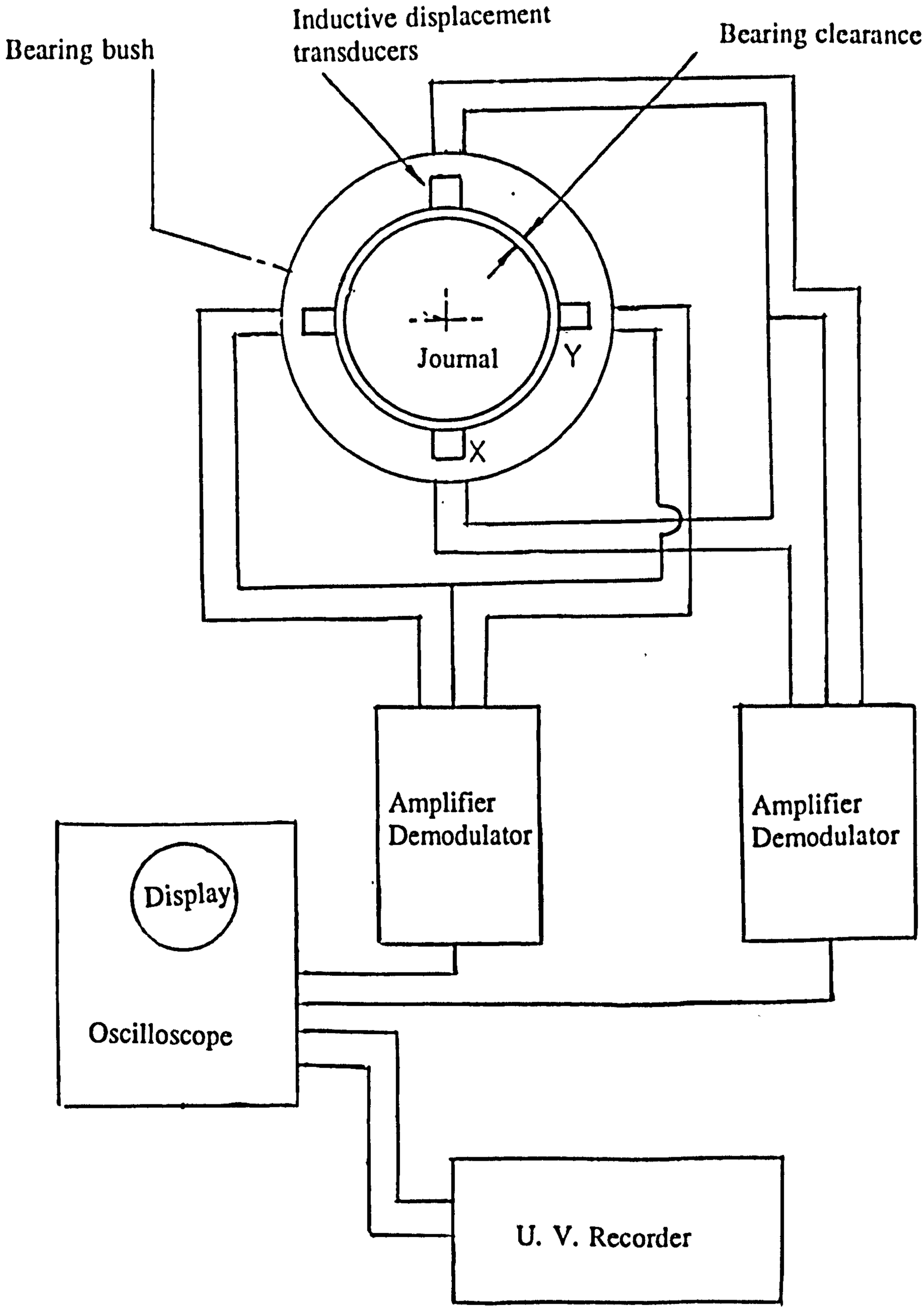

Figure 2.17 Displacement measuring system

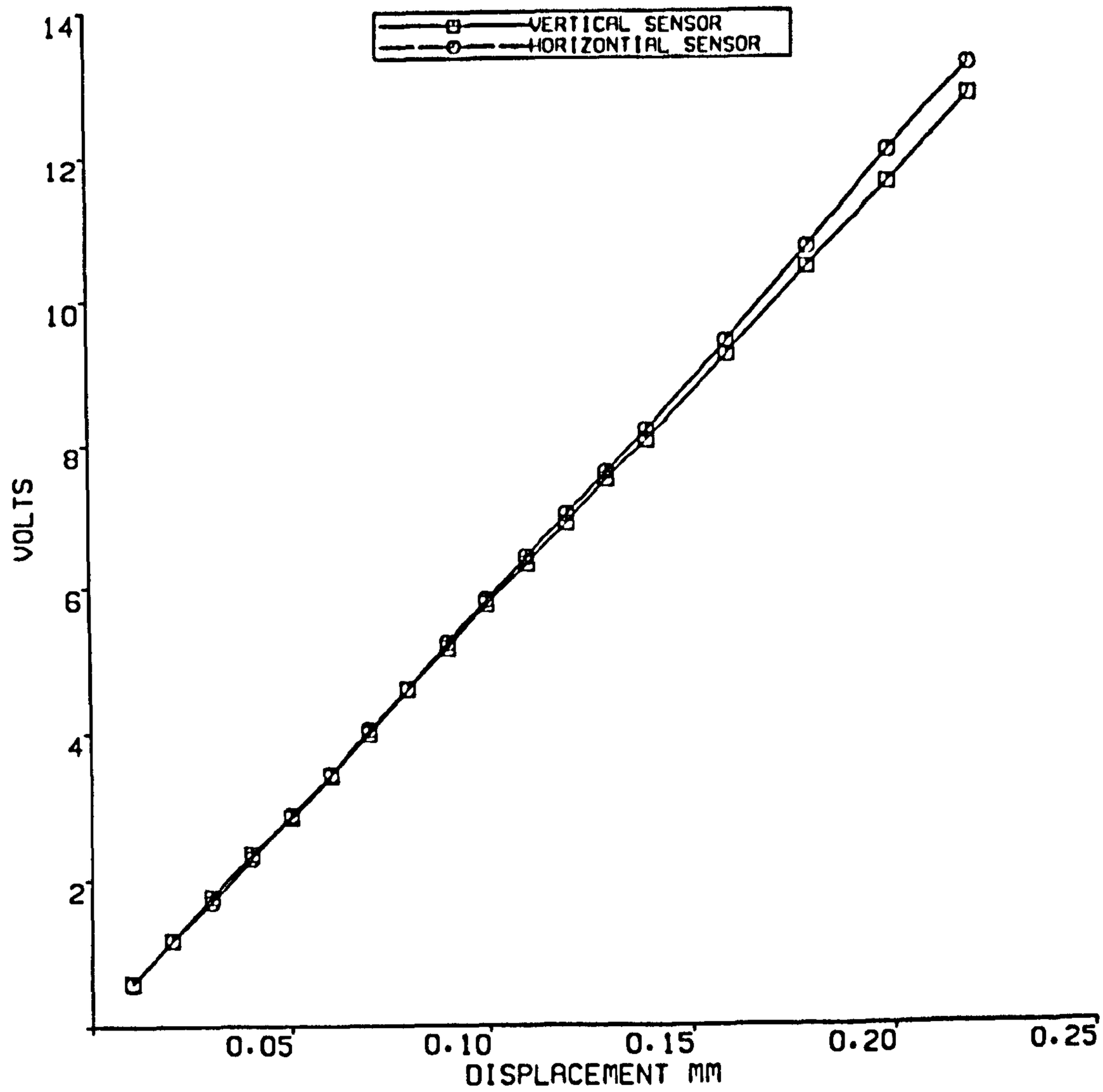

FIGURE 2.18 SENSOR CALIBRATION CHART
INITIAL DISTANCE OF 1 MM
PUSH PULL ARRANGEMENT

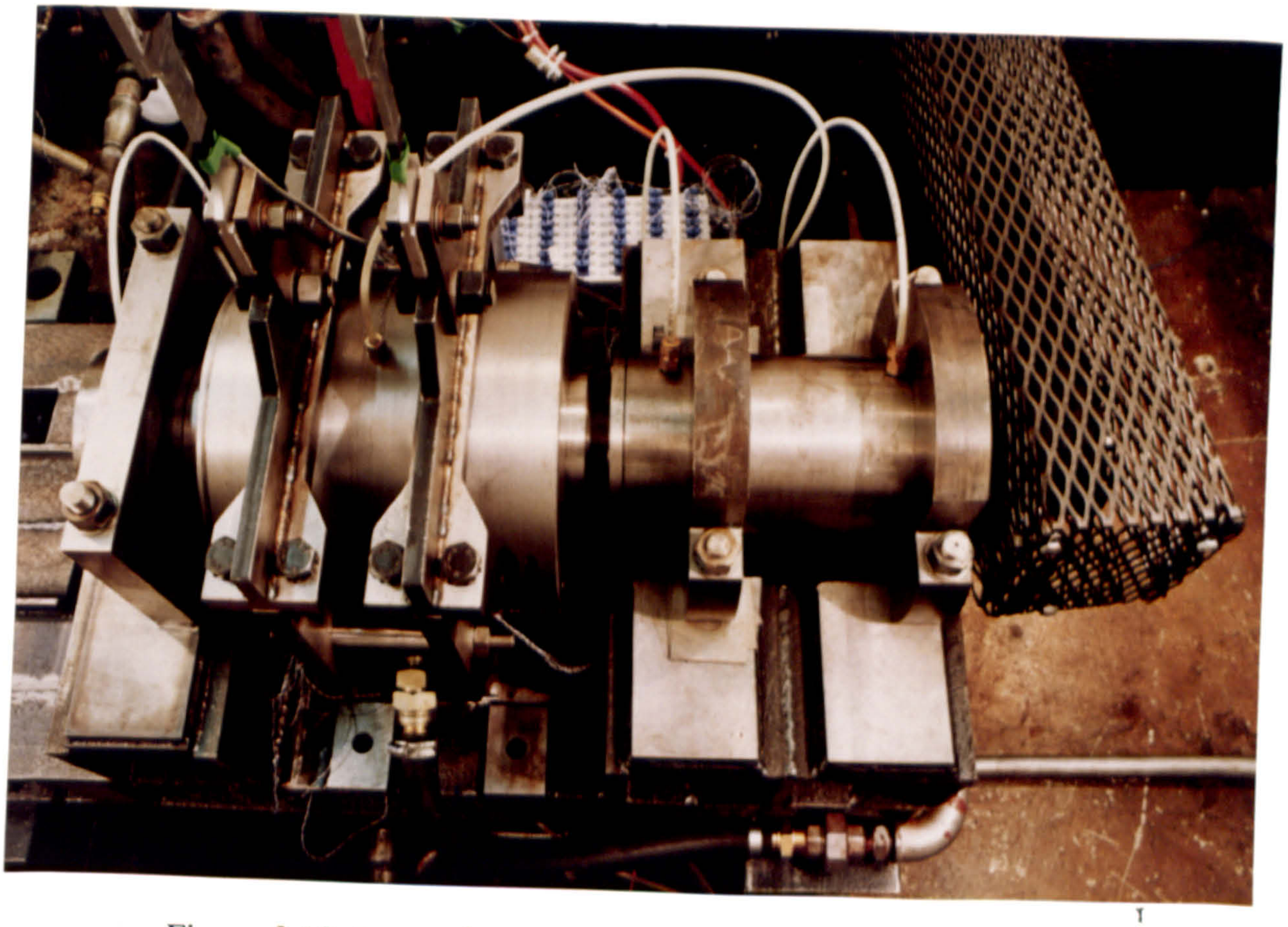

Figure 2.19 Overview of Shaft and support bearing

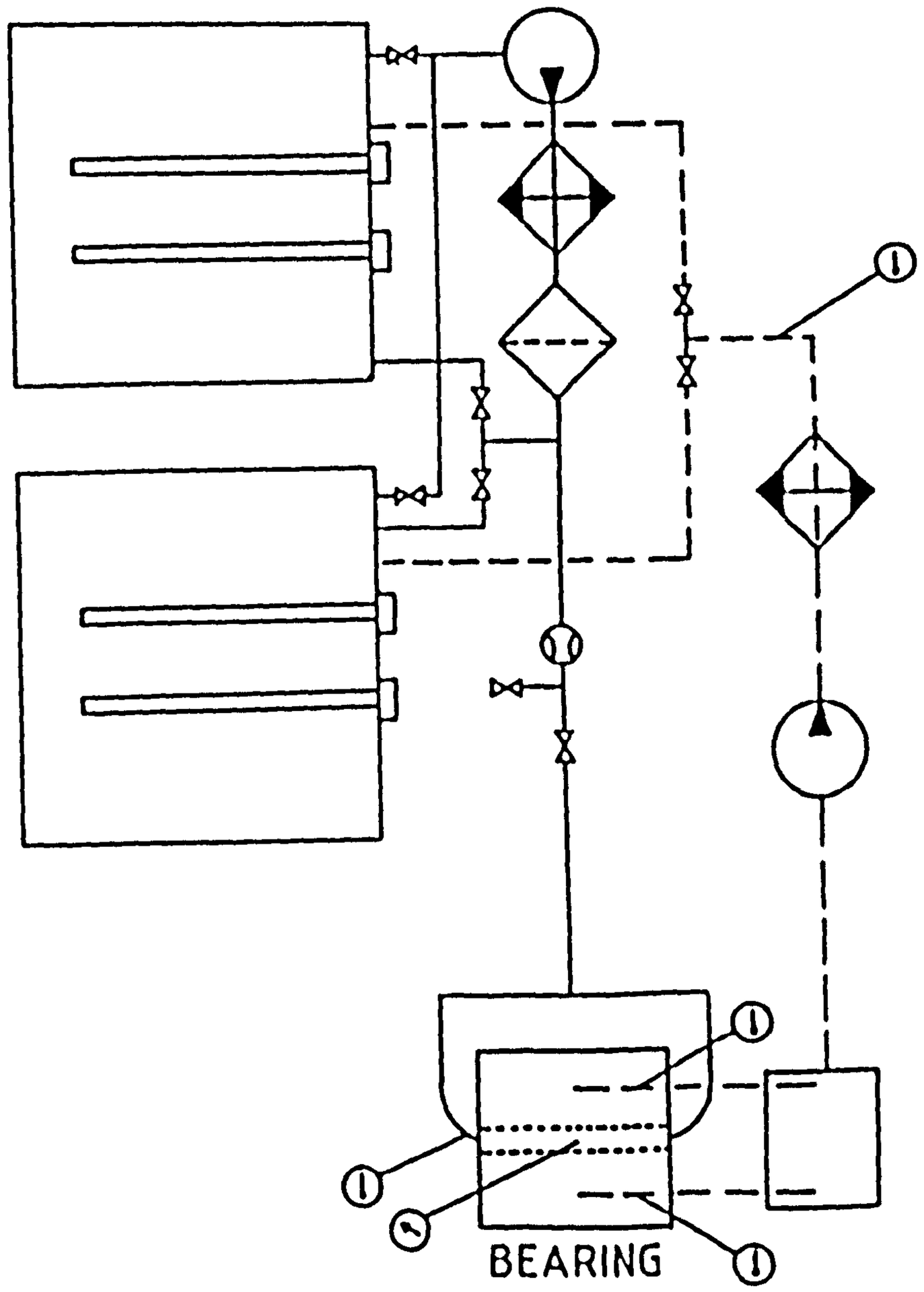

Figure 2.20 Oil supply system

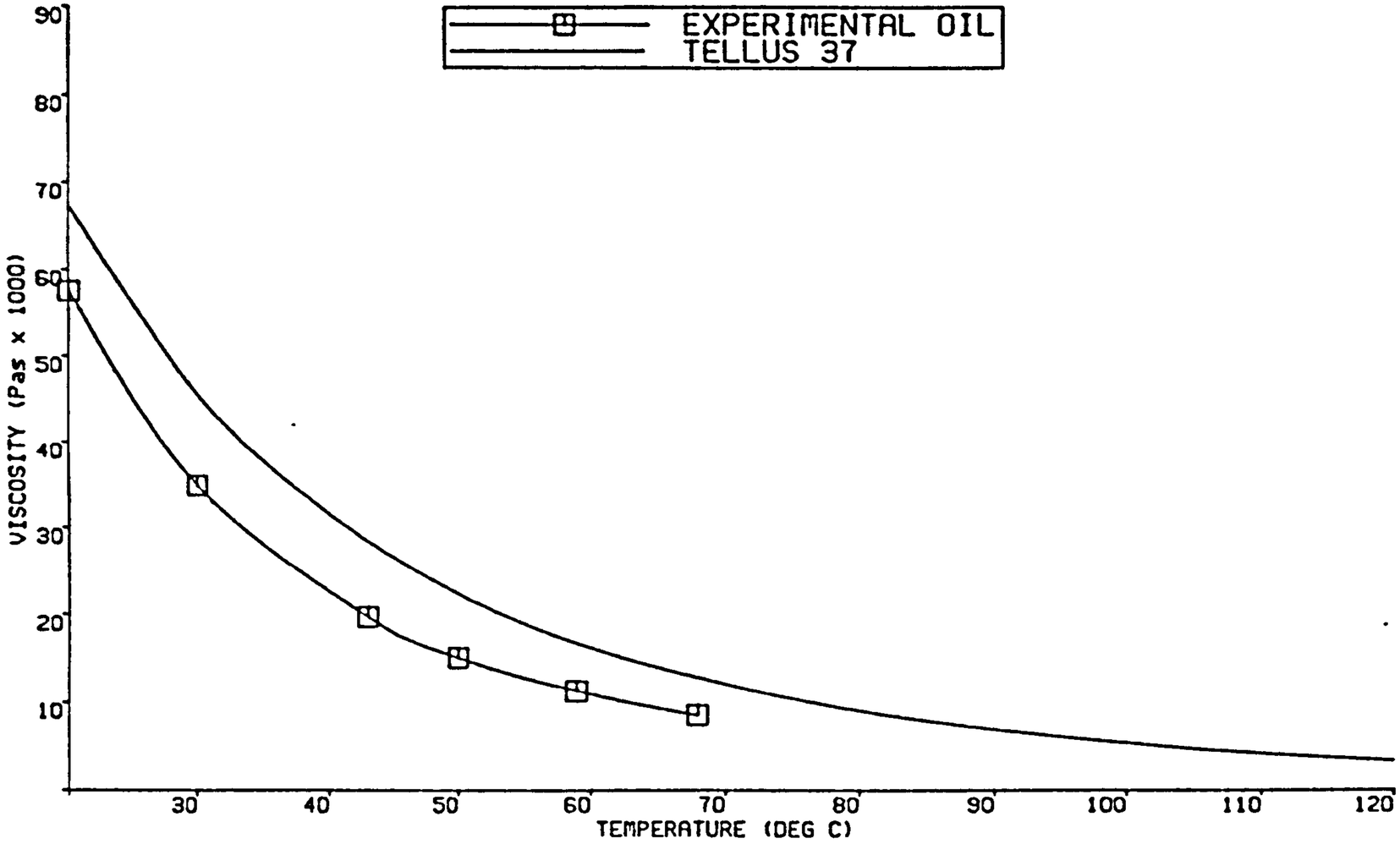

Figure 2.20a Lubricant Calibration Curve

Lubricant : Experimental Oil
Density : 865 kg/m**3

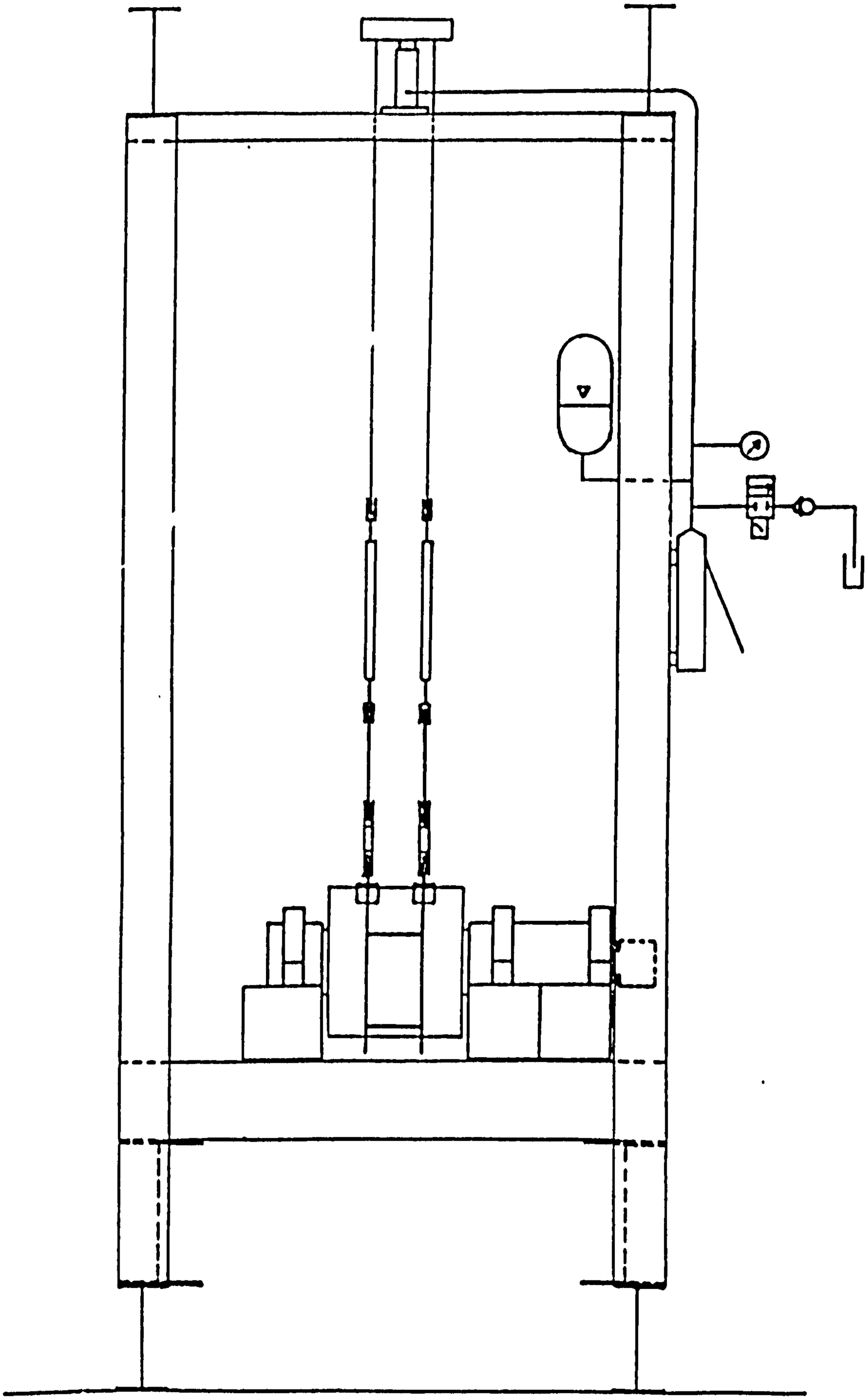

Figure 2.21 Schematic diagram of loading system [41]

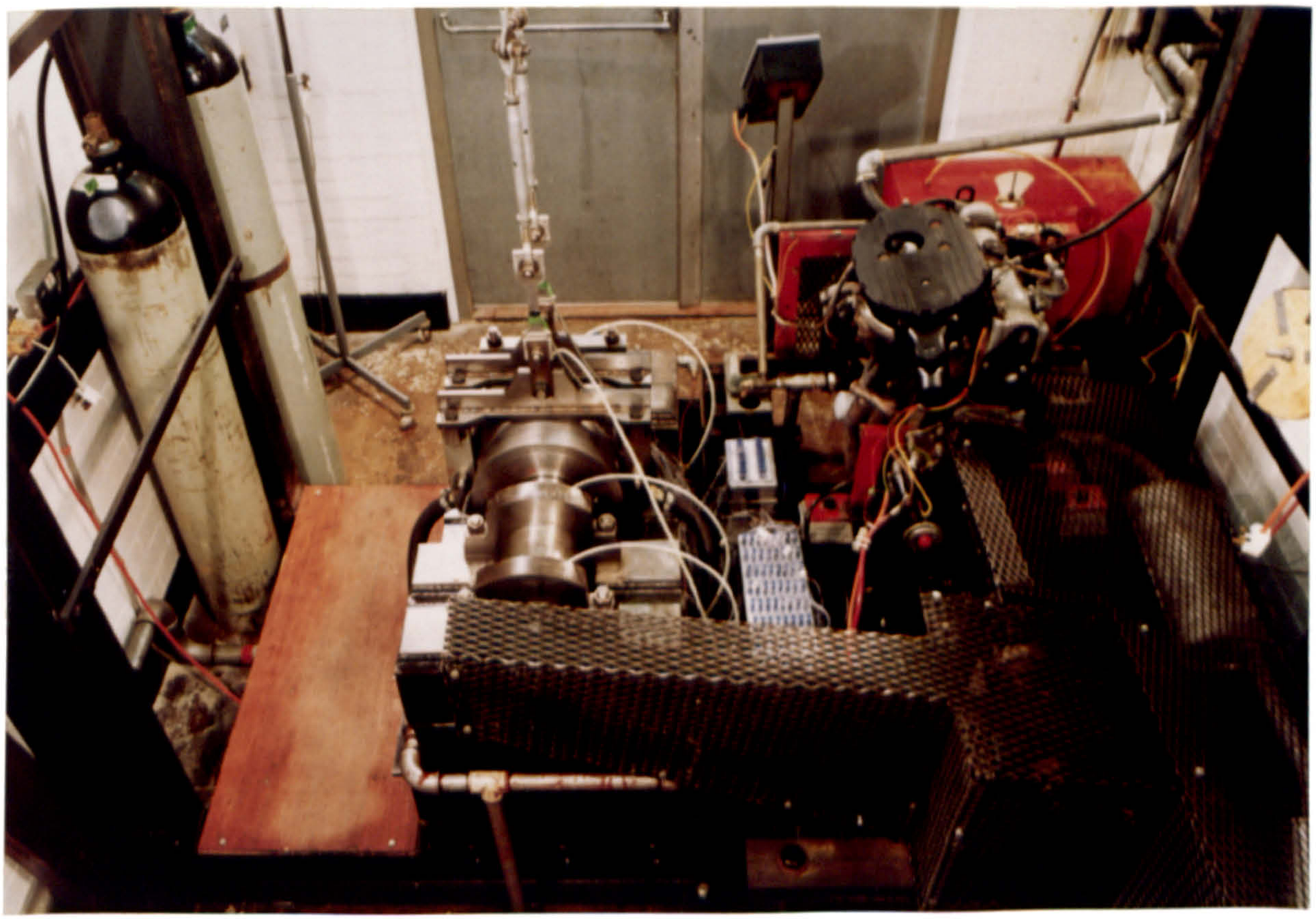

FIGURE 2.22 Overview of drive system

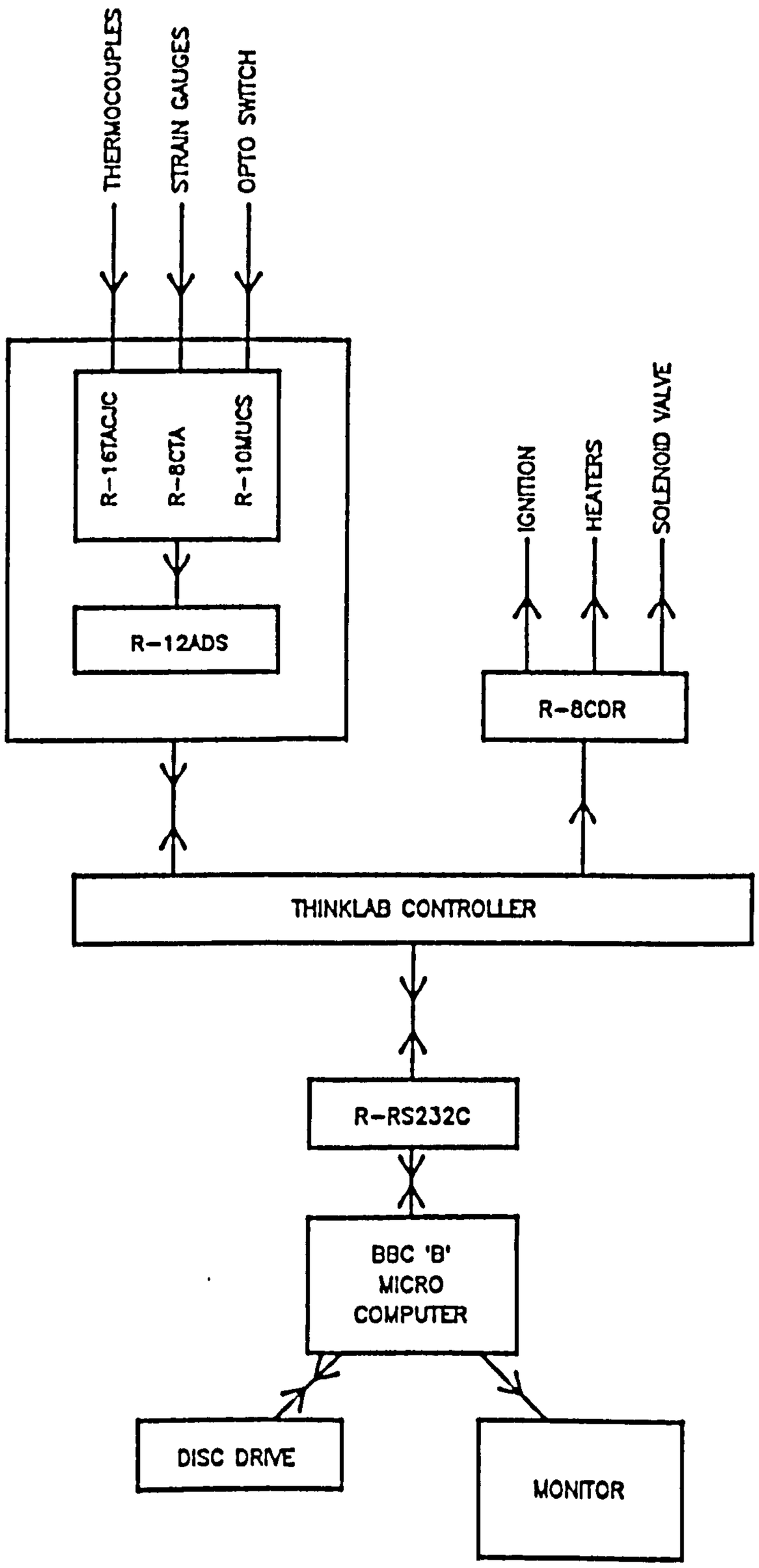

Figure 2.23 Data acquisition system [41]

CHAPTER 3

EXPERIMENTAL RESULTS

3.1 INTRODUCTION

Test were carried out on the following four types of bearings:-

a) A plain journal bearing, as a reference bearing.

b) A symmetrical helical groove journal bearing.

c) An asymmetrical helical groove journal bearing.

d) A partial helical groove journal bearing.

In each instance the following measurements were made:-

i) Bearing temperatures measured by thermocouples.

ii) Oil flow rate.

iii) Power loss.

iv) Eccentricity ratio as derived from the position transducers.

v) Stability as measured by the load and eccentricity ratio below which vibration of the bearing rises rapidly.

All the bearings were tested with the oil inlet temperature held at 40 ± 1 °C. The temperature of the oil was measured by a thermocouple positioned in oil supply annulus just before the oil entered in to the bearing. Similarly, the oil supply pressure of 257.7 kN/m^2 is the oil pressure in the oil supply annulus.

All the tests were carried out in a speed range of 2000 rpm to 4000 rpm (see section 2.11 page 16) and were conducted at steps of 1000 rpm. The direction of the force applied to the bearing, attitude angle and direction of rotation are

indicated in Figure 3.1.

3.2 Plain Journal Bearing

3.2.1 Bearing Surface Temperature Measurements

The temperature profiles at fixed load and different speeds are shown in Figure 3.2 and 3.3. Whilst the temperature profiles at fixed speed and different loads are shown in Figures 3.4. These temperature profiles were constructed from the output of the thermocouples positioned circumferentially near the mid axial plane at location 2, Figure 2.16. In general bearing temperature increases gradually in the direction of rotation from its value at the inlet and reaches a maximum at the angle of about 225 to 250 degrees, i.e in the region of minimum film thickness. After this position there is a gradual decrease in temperature. The maximum temperature at minimum gap results from the gap reduction which, at minimum film thickness location results in the highest shear rate within the film.

The increase in temperature was more dependent on an increase in speed rather than an increase in load. This was because the heat generated by viscous shearing is proportional to speed. The increase in temperature at fixed load was about 7°C per 1000 rpm. The increase in temperature when the load was increased from 11120 N to 13344 N was about 3 to 4°C.

The axial variation of temperature was determined by measurement from the thermocouple at location 1 to 4 along the axial length of the bearing at angle of 180 degrees with respect to the oil inlet, Figure 2.16. The temperatures measured by the four thermocouples are plotted in Figure 3.5. The variation of temperature along the axial length of the plain journal bearing is small approximately 2 to 3°C.

If there is no misalignment, the axial variation of temperature is expected to be small.

3.2.3 Oil Flow Rate Measurements

The oil flow rate as a function of speed at a load of 13344 N is given in Figure 3.6. The flow rate as a function of load at a speed of 3000 rpm is given in Figure 3.7. It appears that the flow rate increases more significantly with an increase in load. This is because, the increase in the eccentricity results in increased specific pressures and so greater leakage of oil from the sides of the bearing occur.

3.2.4 Power Losses Measurements

The power losses as a function of rotational speed at a load of 13344 N are given in Figure 3.8, whilst the power losses as function of load at a speed of 3000 rpm are given in Figure 3.9. The power losses were obtained by estimating the convected heat flow rate from the bearing. This was achieved by measuring the oil flow rate and oil temperatures at the bearing oil inlet and exit. The method of calculating the power losses is described in more detail in Appendix D.

3.2.5 Bearing Load

The variation of journal eccentricity with load at a speed of 3000 rpm is given in Figure 3.10. The displacement of the bearing housing was measured as described in chapter 2, section 2.5. The eccentricity was calculated from these measurements. The displacement readings were taken after thermal equilibrium

had been attained.

3.2.6 Stability Characteristics

The bearing stability characteristics were determined experimentally by running the shaft at various speeds and varying the load on the bearing. At each speed, and after thermal equilibrium had been established, the static load on the bearing was progressively reduced by small decrements whilst the motion of the bearing housing was observed on the oscilloscope. The value of the load below which the housing motion started to grow was taken as the critical load or the load at the threshold of instability. In Figure 3.11 is shown the stability curve in which the critical load is plotted against rotational speed. In the area above the curve, stable operation can be expected, whilst in the area below the curve vibration at a frequency of about half of the rotational speed is likely. The amplitude of the whirling motion was observed in the form of orbits. The whirling motion at an early stage of instability is shown in Figure 3.12a, speed 3000 rpm and load 11120 N. As the load was decreased to just below the stability threshold, the bearing started to whirl around the equilibrium position. The form of the orbit at the onset of instability at 4040 rpm is shown in Figure 3.13. The final stage of the instability would be at the no load condition, and the motion would then develop to full clearance whirling. The whirling motion at 3000 rpm is shown in the time domain in Figure 3.12b. The lower curve is from the displacement transducers on the vertical diameter and the upper curve from the transducers on the horizontal diameter. The frequency of whirl indicated by the plot is close to half of the rotational speed.

The bearing was unstable below an eccentricity ratio of about 0.4. Once the bearing became unstable a higher load than the critical load was required in order to stop the instability. When there is a hysteresis in the whirl extra load is required to recover the instability, this is due to inertia forces which opposes the motion when it starts and then tends to keeps it. The detailed explanation for this phenomena is given in reference [3].

3.3 Symmetrical Helical Groove Bearing

3.3.1 Bearing Surface Temperature Measurements

It is well known that heat is generated in a lubricating oil film because of the shearing that it undergoes. For the safe operation of a bearing the amount of heat generated must be dissipated. The mechanisms of heat dissipation from the bearing are, conduction across the oil film, conduction along the axial length of the journal and heat convection by the lubricating oil. In a plain bearing oil escapes from the ends of the bearing and so heat is convected away. This is one of the principal mechanisms for the dissipation of heat in a plain bearing. With the symmetrical helical groove bearing the effect of the grooves are to return the axial flowing oil to the mid plane of the bearing. The end leakage is reduced and it is expected that the bearing will run hotter than the plain bearing. Under certain circumstances the bearing can even be self sealing.

In order to observe the circumferential temperature profile at different loads and different speeds, temperatures were measured near the mid axial plane at location 2, Figure 2.16. The temperature profiles are plotted in Figures 3.14 to 3.16. These graphs show that the lubricant increases in temperature as it progresses

through the bearing. The maximum temperature was observed at an angle of approximately 250 degrees, in the vicinity of the minimum film thickness region. It was also observed that the variation of temperature in the circumference temperature profile of the symmetrical helical groove bearing was less than that in the plain journal bearing. As there was no through flow of oil, the heat convected by the oil was circulated around the bearing, as result the difference in temperature in the case of symmetrical groove bearing was reduced. The increase in temperature was about 8°C per 1000 rpm. As can be seen from Figure 3.15, the temperature increases more with the speed than with load.

The variation in temperature along the axial length of the bearing was measured at locations 1 to 4 at an angle of 180 degrees with respect to the oil inlet, Figure 2.16. The temperatures measured along the length of the bearing are plotted in Figure 3.17. It is observed that one axial half of the bearing is about 5°C higher in temperature the than other half. It could have been due to slight misalignment.

3.3.2 Oil Flow Rate Measurements

Oil flow rates at constant load and variable speeds are given in Table 3.1. An increase in flow rate indicates that the leakage from the sides of the bearing is compensated by external supply. Oil flow rates at constant speed and variable loads are given in Table 3.2. It was observed that as the load was reduced the side leakage was also reduced.

Table 3.1 Flowrate at constant Load and variable Speed

speed [rpm]	Load [N]	Flowrate l/s
2000	6672	.165
3000	6672	.168
3000	8896	.18

Table 3.2 Flow Rate at Constant Speed and Variable Load

Speed [rpm]	Load [N]	Flowrate l/sec
2000	4448	0.158
2000	6672	0.165
3000	6672	0.168
3000	8896	0.180

3.3.3 Power Loss Measurements

The power losses were estimated by measuring the convected heat flow rate. This was achieved by measuring the oil temperature at the inlet and the outlet of the bearing and also the oil flow rate.

Power losses at constant load and variable speed are given in Table 3.3. Whilst power losses at constant speed and variable loads are presented in Table 3.4.

Table 3.3 Power Losses at Constant Load and Variable Speed

Speed [rpm]	Load [N]	Power losses [kW]
2000	6672	1.13
3000	6672	2.033
3000	8896	2.542
4000	8896	4.177

Table 3.4 Power Losses at Variable Loads and Constant Speed

Speed [rpm]	Load [N]	Power losses [kW]
2000	4448	0.347
2000	6672	1.13
3000	6672	2.033
3000	8896	2.542

An increase in power loss compare to plain bearing of 0.9 kW was observed when the speed was changed from 2000 rpm to 3000 rpm at a load of 6672 N. Similarly, an increase in power loss compared to plain bearing of .409 kW was noted when the load on the bearing was changed from 6672 N to 8896 N whilst a speed of 3000 rpm was maintained.

3.3.4 Bearing Load

The variation of journal eccentricity with load at constant speed is given in Figure 3.18. The displacements of the bearing housing were measured in two direction as discussed in chapter 2 section 2.5. However, it was observed that the bearing had maximum displacement in the direction of applied load, because of reduced crosscoupling. The displacement in horizontal direction at high eccentricities was very small. The displacement measurements were taken after thermal equilibrium was achieved.

3.3.5 Stability Characteristics

The stability curve for the symmetrical helical groove bearing is shown in Figure 3.19. A speed of 1645 rpm was attained without any external stabilizing load being required on the bearing. At 1645 rpm the motion of the bearing housing started to grow and load was applied. The critical load at the onset of instability was determined in the same way as described in section 3.2.5. This was achieved by testing the bearing at each speed and load. The speeds and loads used in the test were, at 2000 rpm and 4448 N, at 3000 rpm and 8896 N and finally at a speed of 4000 rpm and the static load applied to the bearing was 8896 N. For each speed and static load the corresponding value of the critical load is plotted in

Figure 3.19. Having determined the onset of instability, the trajectory of the whirl motion was observed in the form of an orbit. Typical whirl orbits are shown in Figure 3.20 to 3.21. The speed and static load at equilibrium eccentricity are also given in each figure. The whirl amplitude in the time domain is also shown in Figure 3.20b and the frequency ratio calculated from the time period is about 0.5. It was noticed that when the load was reduced below the critical value the rate of increase of load dependent amplitude was not so rapid as compared with the plain bearing. Because the plain bearing loses its load capacity as the instability grows the hydrodynamic forces move the journal toward the wall of the bearing. In the helical groove bearing due to groove pumping action, hydrodynamic forces around the journal restrict the journal movement. However, like the plain bearing, once the motion starts to grow greater load than the critical load is required to control it. The reason for this could be the same as that described in section 3.2.6. Above a speed of 1645 rpm the bearing was unstable below an eccentricity of 0.65.

3.4 Asymmetrical Helical Groove Journal Bearing

3.4.1 Bearing Surface Temperature Measurements

The circumferential temperature profiles were measured at location 2, Figure 2.16 and at each speed and load used during testing are shown in Figures 3.22 to 3.24. Because the asymmetrical bearing was unstable below an eccentricity ratio of 0.7, data plotted in Figures 3.22 to 3.24 are limited to a single load and speed such that the bearing was operating at a high enough eccentricity ratio. It is seen from the graphs that the temperatures increases in the direction of rotation from its value at the oil inlet. The maximum rise in temperature was observed in the

minimum film thickness region, i.e. between 150 to 250 degrees from the inlet. A gradual decrease in temperature follows as the bearing gap diverges. The temperature curves in Figures 3.22 to 3.24 show no prominent peaks. This appears to be because in the asymmetrical bearing the heat generated in the minimum film region is removed more by convection than by conduction across the film. This is mainly due to the axial flow of lubricant in the bearing.

The variation of temperature along the axial length of the bearing positions 1 to 4 in Figure 2.16 at 180 degrees with respect to oil inlet, is shown in Figure 3.25. The graph shows a temperature difference of 8°C between the two ends of the bearing. This is due to the fact that oil at 40°C was supplied to the bearing from only one end.

3.4.2 Oil Flow Rate Measurements

Oil was supplied to the bearing through a hole which flooded the end of the bearing with the longer grooves. The axial flow rate of the oil was measured at an outlet hole located at the other end of the bearing. A summary of the flow rate measurements is given in Table 3.5.

Table 3.5 Asymmetrical Bearing Oil Flow Rate

speed [rpm]	Load [N]	Supply end flow l/s	Outlet end flow l/s
2000	6672	.0876	.013
3000	8896	.0876	.015
4000	11120	.0876	.019

3.4.3 Power Losses Measurements

The power losses at each speed and load were calculated on the basis of measured oil flow rate and oil temperature at the bearing inlet and outlet. The power losses are given in Table 3.6.

Table 3.6 Asymmetrical Bearing Power Losses

Speed [rpm]	Load [N]	Power losses [kW]
2000	6672	0.76
3000	8896	1.39
4000	11120	2.7

3.4.4 Bearing Load

The eccentricity ratio measured at each speed and load is given in Table 3.7. During experiments, it was noticed that the asymmetrical bearing operated cooler than the symmetrical bearing. However, no effect of this on the bearing load as compared to the symmetrical bearing load was observed. The bearing load was nearly the same as that of the symmetrical bearing.

Table 3.7 Bearing Load and Eccentricity Measurements

Speed [rpm]	Load [N]	Eccentricity ratio
2000	6672	.72
3000	8896	.85
4000	11120	.9

3.4.6 Stability Characteristics

In order to determine the stability characteristics of the bearing the shaft was gradually accelerated until a speed of 1280 rpm was reached at which whirl instability started to grow and load was required to stabilize the bearing. At each

speed and equilibrium eccentricity the bearing was tested in order to determine the critical load below which the onset of instability starts. The values of critical load for each speed used are plotted in Figure 3.26. The motion of the bearing housing at various speeds and loads below the threshold of instability is shown in Figures 3.27 to 3.28. It was observed that the bearing was unstable below an eccentricity ratio of 0.7.

3.5 Partial Helical Groove Journal Bearing

It was observed during the experiment that when a load greater than 2240 N was applied to the bearing the bearing became misaligned. Due to the difference in clearance,between the plain and grooved portion of the bearing, the stiffness of the plain portion of the bearing was greater than the grooved portion. The difference in stiffness had caused the bearing misalignment under load. In order to measure bearing surface temperatures, power losses, oil flow rate and stability characteristics the bearing was tested unloaded.

3.5.1 Bearing Surface Temperature Measurements

Circumferential temperatures were measured at position 3, Figure 2.16. It was observed that the temperatures measured at position 3 were higher than those at location 2. This could have been due to the difference in clearance at the two positions, as at position 3 the bearing surface was completely plain. The measured temperature profiles at each speed are plotted in Figure 3.29. The variation in circumferential surface temperature around the unloaded bearing seems to reflect the associated change in film thickness.

The variation of temperature along the axial length of the bearing is shown in Figure 3.30. The graph shows a temperature difference of 16°C between the two ends of the bearing. The difference in temperature can be explained in terms of the different geometry of the load supporting surface in this type of bearing and oil at an inlet temperature of 40° C being supplied to end of the bearing the with the groove.

3.5.2 Oil Flow Rate Measurements

Oil was supplied to the bearing through an inlet hole positioned at the end of the bearing provided with the helical grooves. The axial flow rate measured at the outlet hole near the end seal, at different speeds, is shown in Figure 3.31. The axial flow rate is seen to vary linearly with speed.

3.5.3 Power Losses Measurements

The convected power losses were estimated from the total oil flow rate through the bearing and the temperature rise of the oil as it passed through the bearing. The power losses at different speeds are shown in Figure 3.32.

3.5.4 Stability Characteristics

The partial helical groove bearing was tested up to 4000 rpm. The motion of the bearing housing was observed on an oscilloscope in the form of an orbit. It was found that there was no substantial increase in the size of the orbit up to 4000 rpm. However, the significant predominant misalignment was observed. It is therefore, difficult to interpret the stability results. The display of the bearing

housing motion is shown in Figures 3.33 and 3.34.

3.6 Comparison of the Performance of the Bearings Tested

3.6.1 Bearing Surface Temperature.

The surface temperature of each bearing at a load of 8896 N and speed of 3000 rpm is shown in Figure 3.35. It is seen that the plain bearing operated with the lowest surface temperatures in comparison to the other bearings. The asymmetrical helical groove bearing ran at a temperature approximately 2°C above the maximum temperature of the plain bearing. The symmetrical bearing as expected ran with the highest surface temperature amongst the bearings tested. This is understandable as in the symmetrical bearing there was no net axial flow of lubricant. At a load of 8896 N and speed of 3000 rpm, both of the helical groove bearings ran at an eccentricity ratio higher than 0.7. On the other hand, the plain journal bearing ran at an eccentricity ratio of about 0.46.

3.6.2 Axial Temperature

The variation in surface temperature in the axial direction, for each bearing is shown in Figure 3.36. It is seen that for the plain bearing and the asymmetrical bearing the maximum axial variation in temperature was about 3°C and 8°C respectively. As regards the symmetrical bearing the axial variation in temperature was about 5°C. All three bearings were with a shaft speed of 3000 rpm and a load, of 8896 N. The variation of axial temperature in the partial helical groove bearing, tested without load was about 16°C.

3.6.3 Power Losses

The power losses of all the bearings tested are shown in Table 3.8. The power consumed by the symmetrical helical groove bearing was the highest amongst the bearings tested. However, the plain bearing ran cooler than the helical groove bearing, which implies that it should have produced higher power losses This apparent contradiction can be explained by the fact that the symmetrical groove bearing ran with a much thicker lubricating film and therefore the losses due to the shearing of the film were greater.

Table 3.8 Power Losses Comparison

Bearing	Speed [rpm]	Load [N]	Power Loss [kW]
Plain	3000	8896	1.49
Symmetrical*	3000	8896	2.54
Asymmetrical*	3000	8896	1.39
Partial*	3000	8896	1.57

* Helical Groove Journal Bearing

3.6.4 Bearing Load Characteristics.

The bearing load capacity was assessed by measuring the position of the journal centre at each load and speed. This was done for all the bearings tested, except the partial bearing. The results are given in Table 3.9. The load capacity of the helical groove bearings were about half that of the plain bearing.

Table 3.9 Comparison of Bearing Load Capacity

Bearing	Load [N]	Speed [rpm]	Eccentricity ratio
Plain	8896	3000	0.46
Symmetrical*	8896	3000	0.94
Asymmetrical*	8896	3000	0.85

* Helical Groove Journal Bearing

3.6 Stability Characteristics

The stability curves of the three bearings tested are shown in Figure 3.37. However the stability curve of the partial helical groove bearing is not given in Figure 3.37. This is because, it was observed the bearing become misaligned as load was applied. The result was not reliable. It is seen from Figure 3.37 that the Symmetrical helical groove bearing was more stable up to speed of 1625 rpm than the other two bearings tested, and symmetrical bearing rquired no external stabilizing load up to 1625 rpm. The plain bearing showed good stability but only above an eccentricity ratio of 0.4. The asymmetrical bearing was unstable below an eccentricity ratio of approximately 0.7.

3.7 Discussion of Results

The bearing parameters such as, bearing surface temperature, power losses, load capacity, and critical load for stability have been presented.

The film thickness profile around the circumference of the helical groove journal bearing has saw tooth shape. The effect of this on the circumferential surface temperature profiles of the bearing was not observed, as these profiles are smooth and without distortion. However, it was not possible to position thermocouples in exactly equivalent positions regarding the groove and ridge geometry.

It was observed that for the symmetrical bearing the difference between the minimum surface temperature near the bearing inlet and maximum surface temperature near the minimum film thickness was not more than about 10 °C. For the asymmetrical helical groove bearing this difference was about 7°C

The stability characteristics of the symmetrical groove bearing are not so encouraging as compared to published work on similar configurations using air and gas as a lubricant. For fluid film bearing with groove surface, the stability of the bearing depends not only on the groove geometry but also upon other factors such as, bearing radial clearance. It is known that a decrease in the clearance can improve the stability. In addition variation in groove depth, i.e an increase in depth can lead to less stable bearing.

The partial helical groove bearing was tested without any load imposed on the bearing. The whirl amplitude, observed in the form of whirl orbit did not increase substantially which, apparently, shows that bearing is providing improvement in the stability. However, there are many variables involved in the experimental

verification of stability such as misalignment. The partial helical groove bearing showed tendency to misalignment. This was due to difference in stiffness between the plain and groove portion of this bearing. The groove portion has more clearance and due to this fact less stiffness in comparison to the plain portion of the bearing.

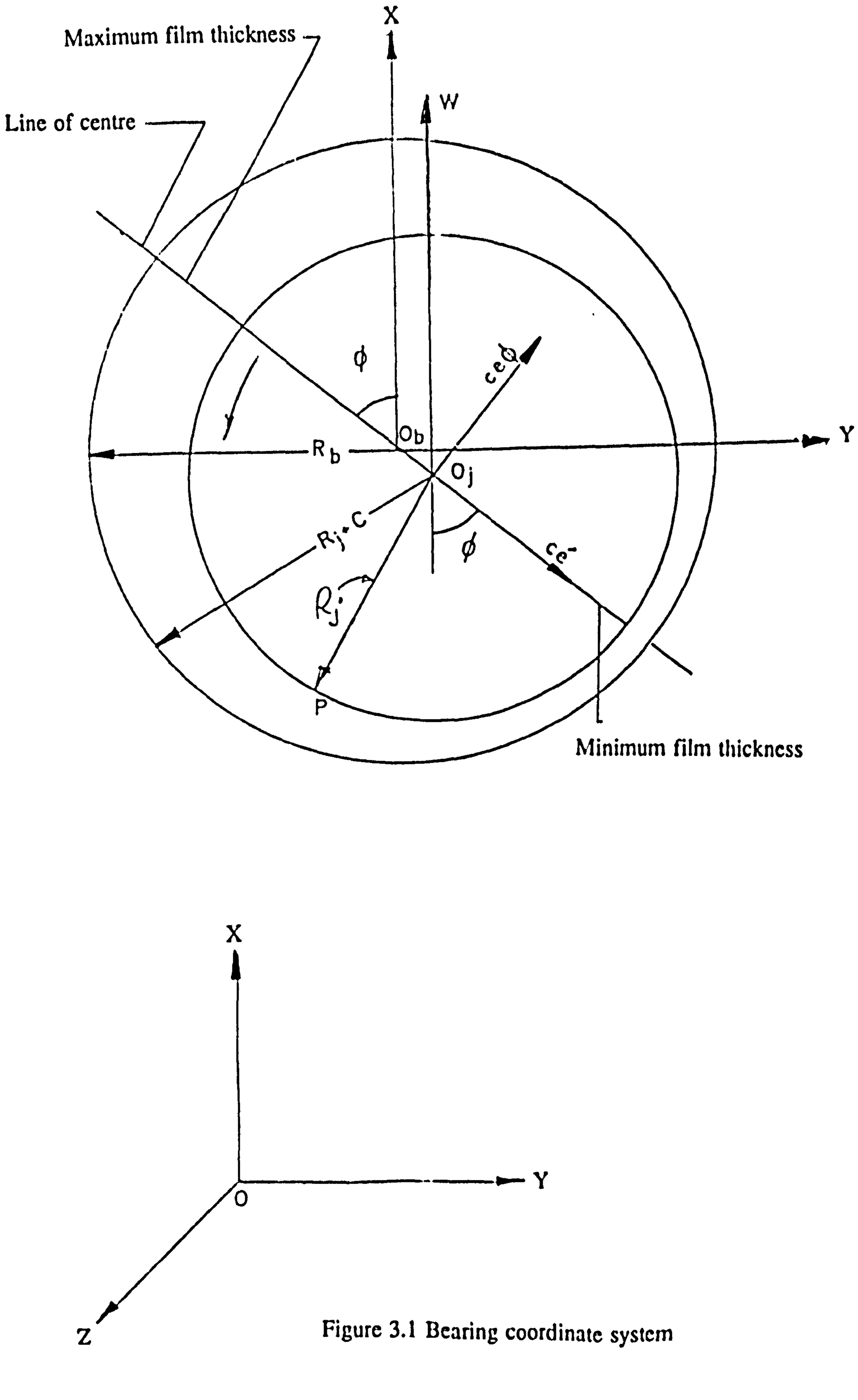

Figure 3.1 Bearing coordinate system

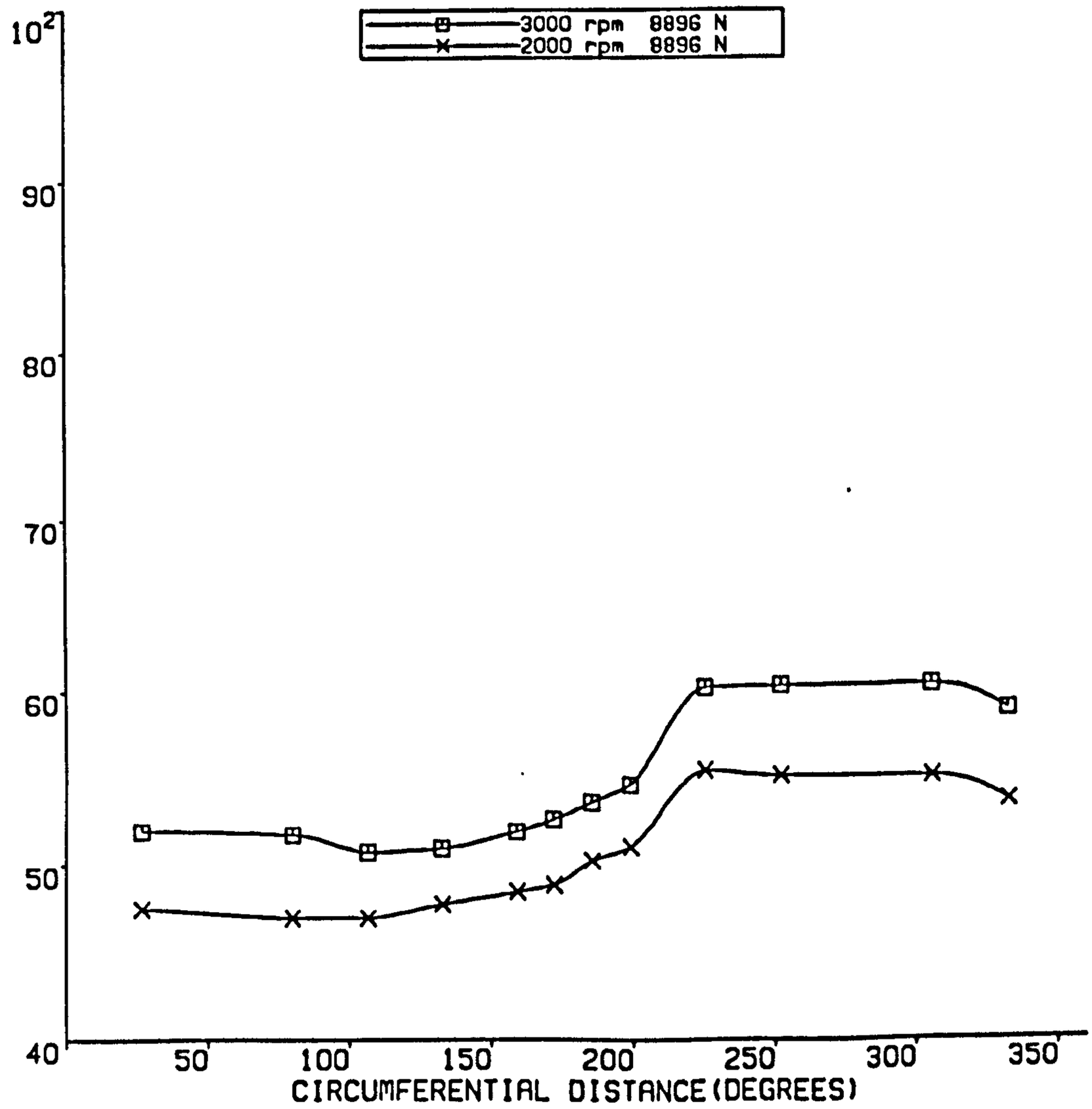

FIGURE 3.2 TEMPERATURE PROFILES FOR DIFFERENT SPEEDS

PLAIN JOURNAL BEARING

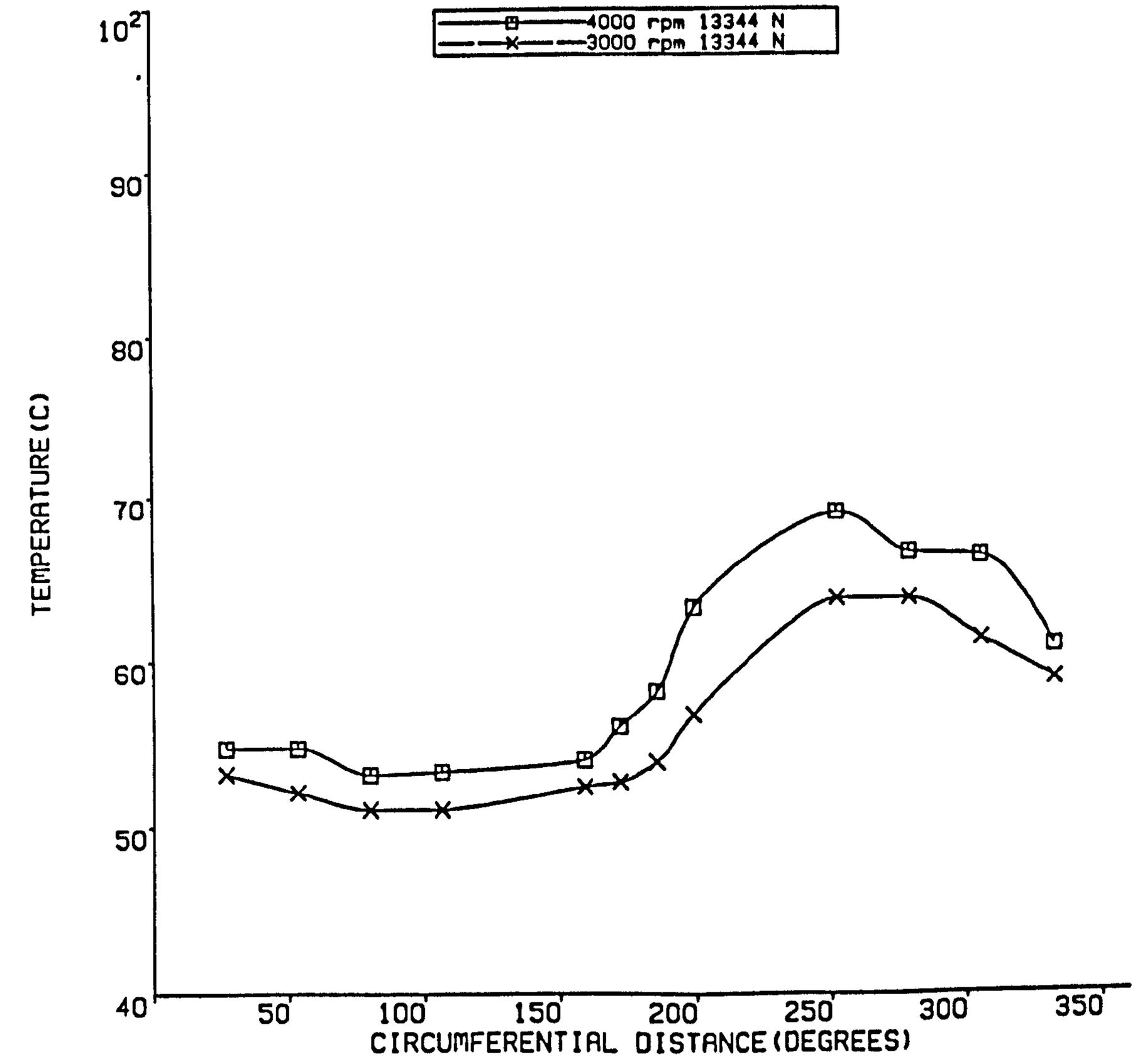

FIGURE 3.3 TEMPERATURE PROFILES FOR
DIFFERENT SPEEDS
PLAIN JOURNAL BEARING

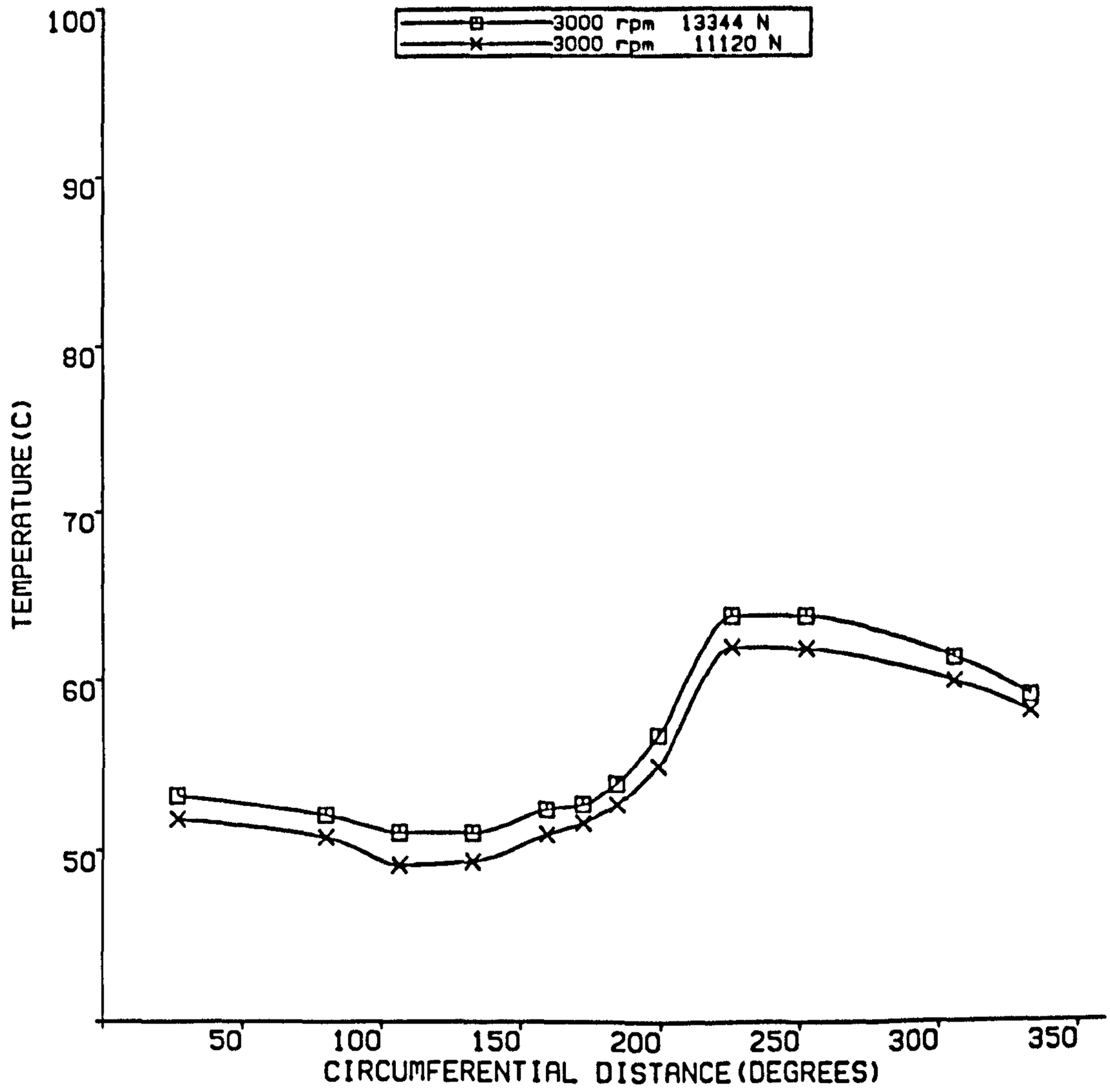

FIGURE 3.4 TEMPERATURE PROFILES AT DIFFERENT LOADS

PLAIN JOURNAL BEARING

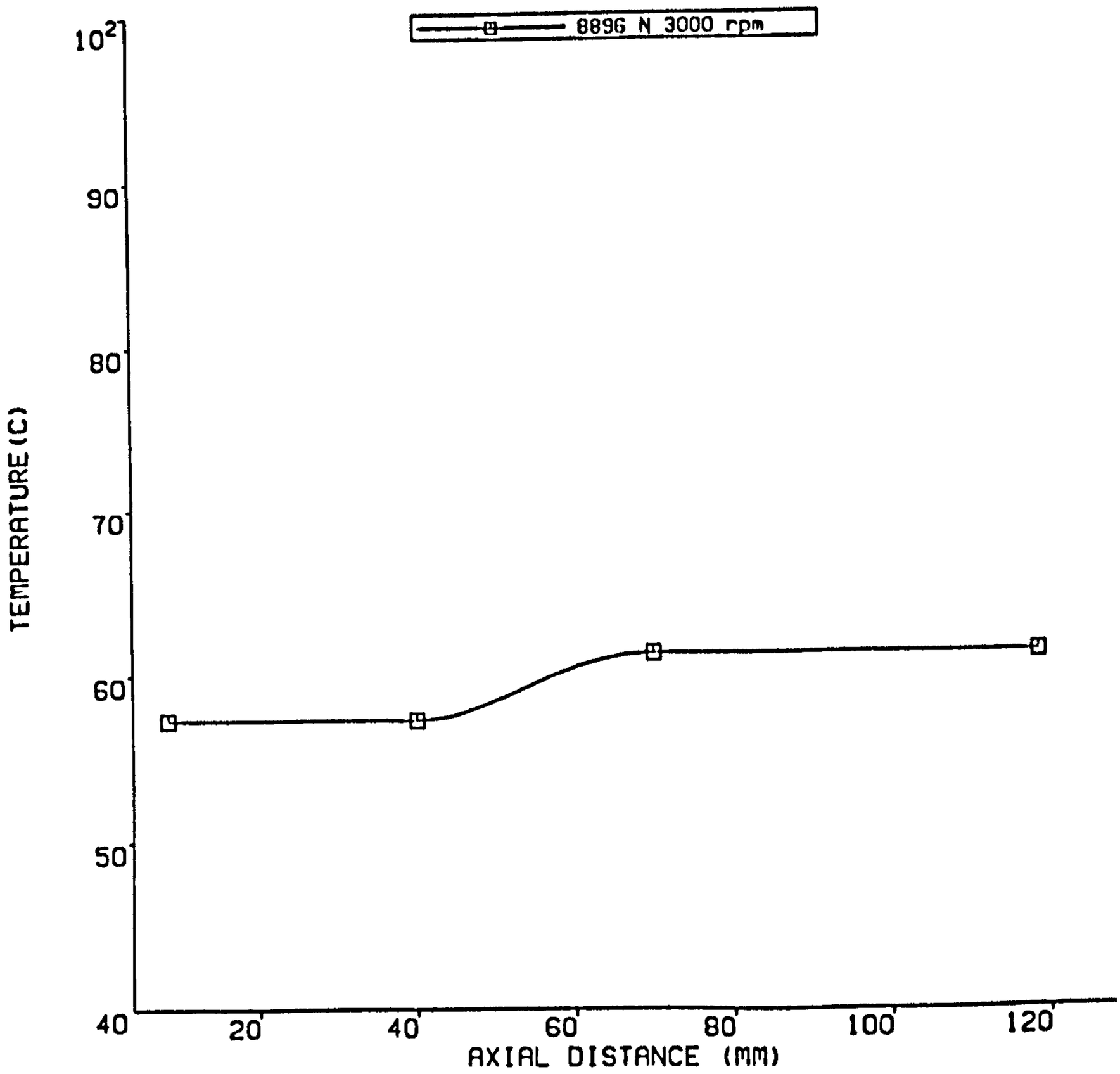

FIGURE 3.5 AXIAL TEMPERATURE VARIATION
OF PLAIN JOURNAL BEARING

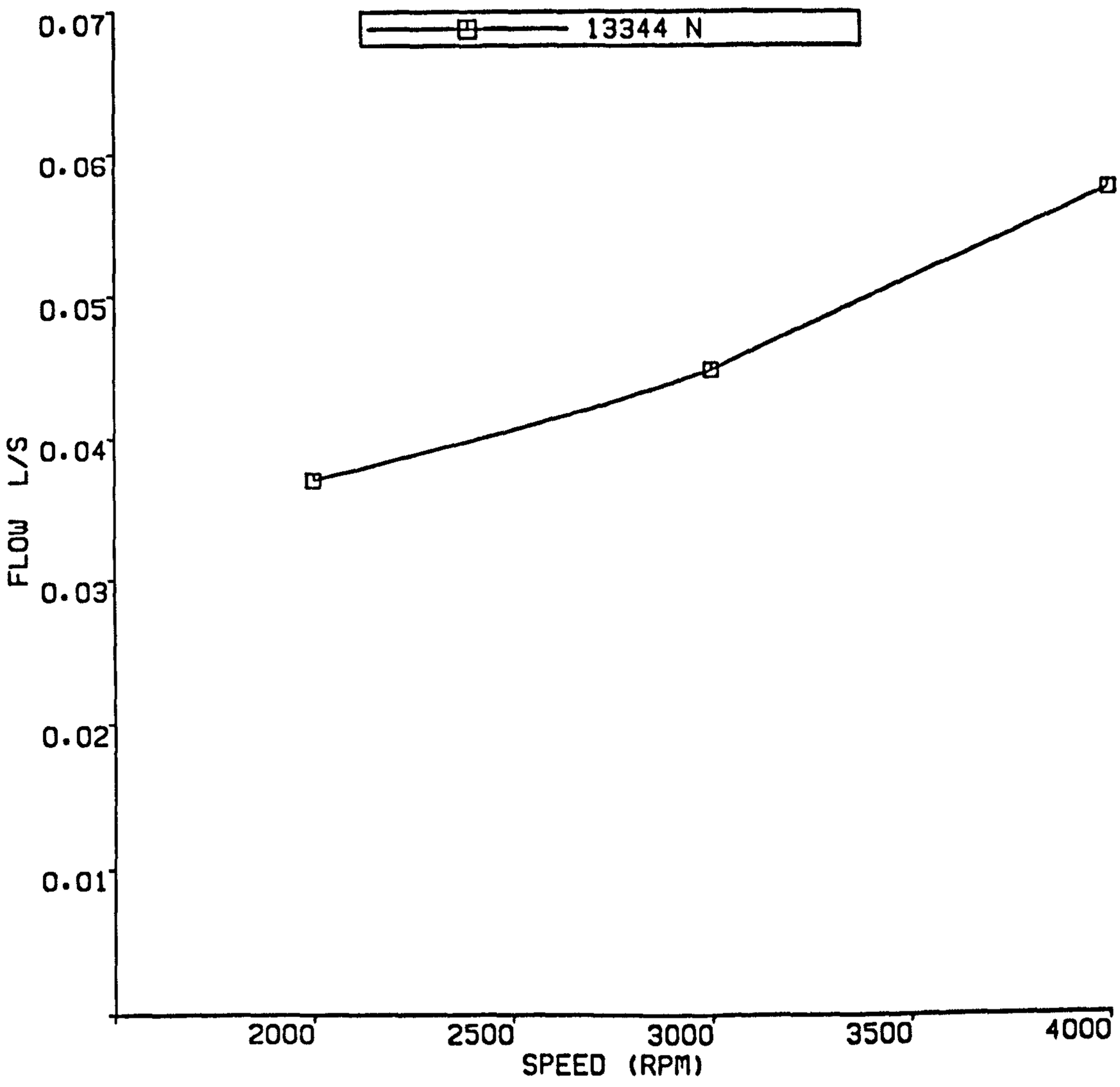

FIGURE 3.6 FLOW RATE VS SPEED

PLAIN JOURNAL BEARING

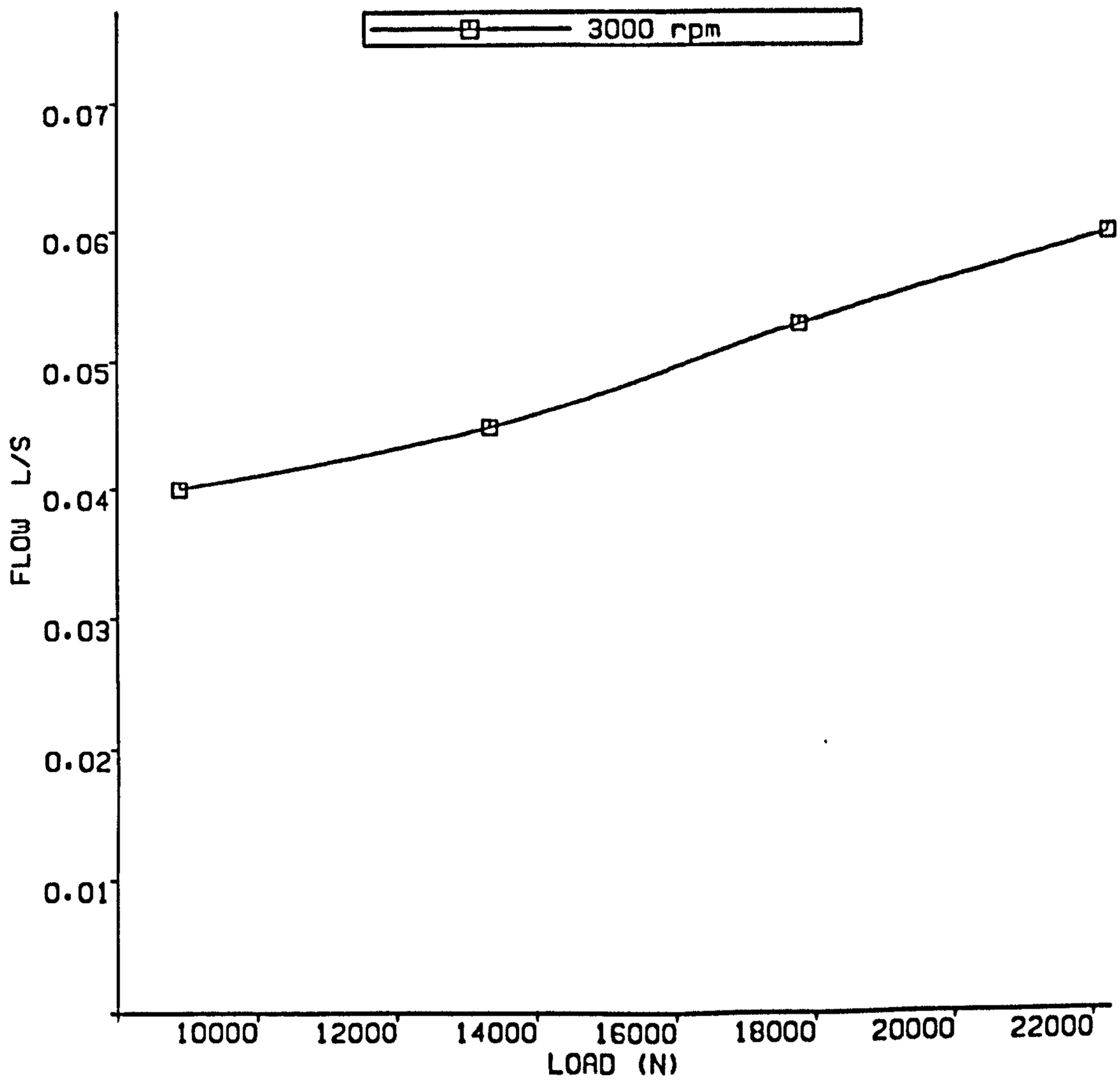

FIGURE 3.7 FLOW RATE VS LOADS

PLAIN JOURNAL BEARING

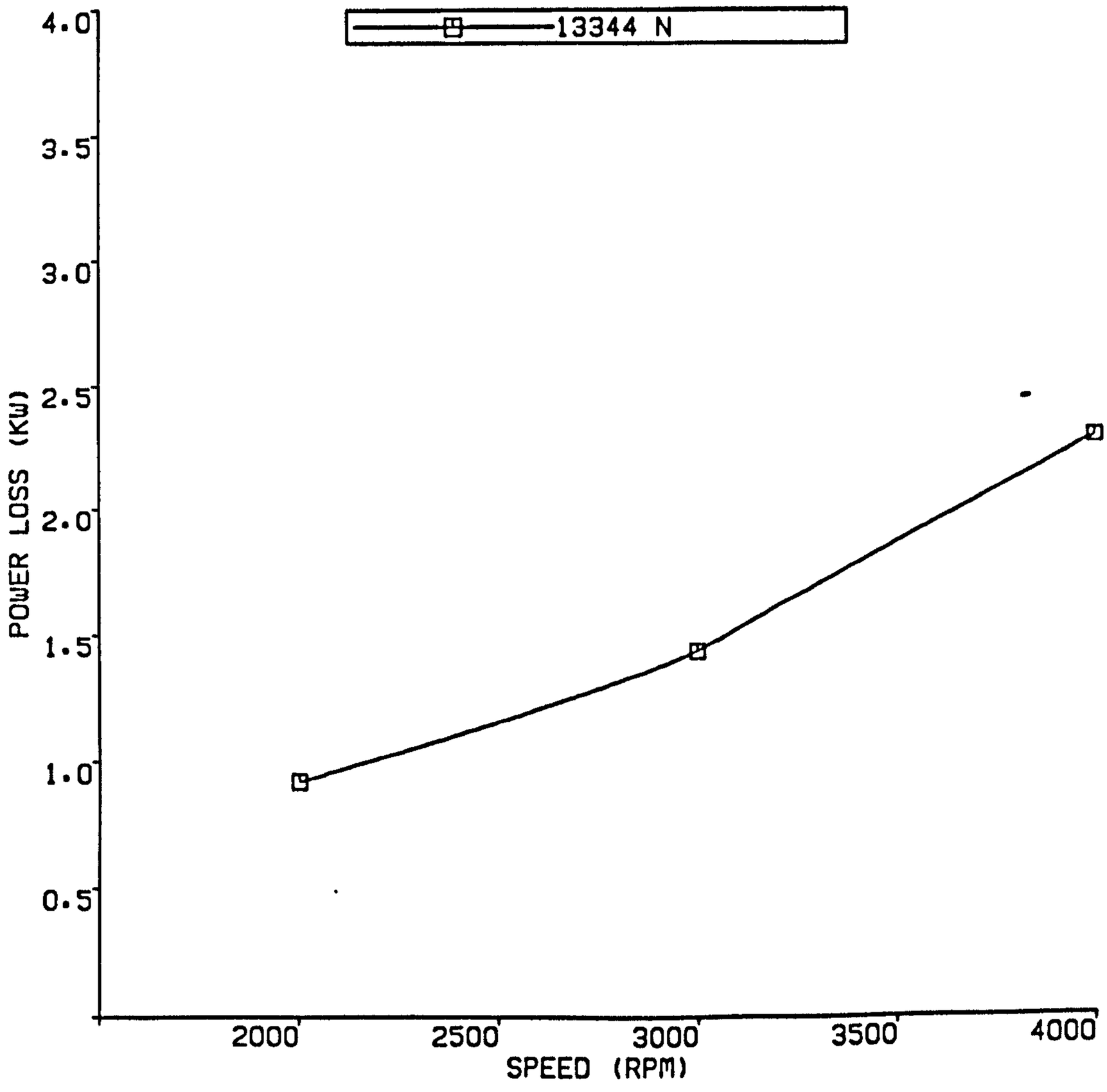

FIGURE 3.8 POWER LOSSES VS SPEED

PLAIN JOURNAL BEARING

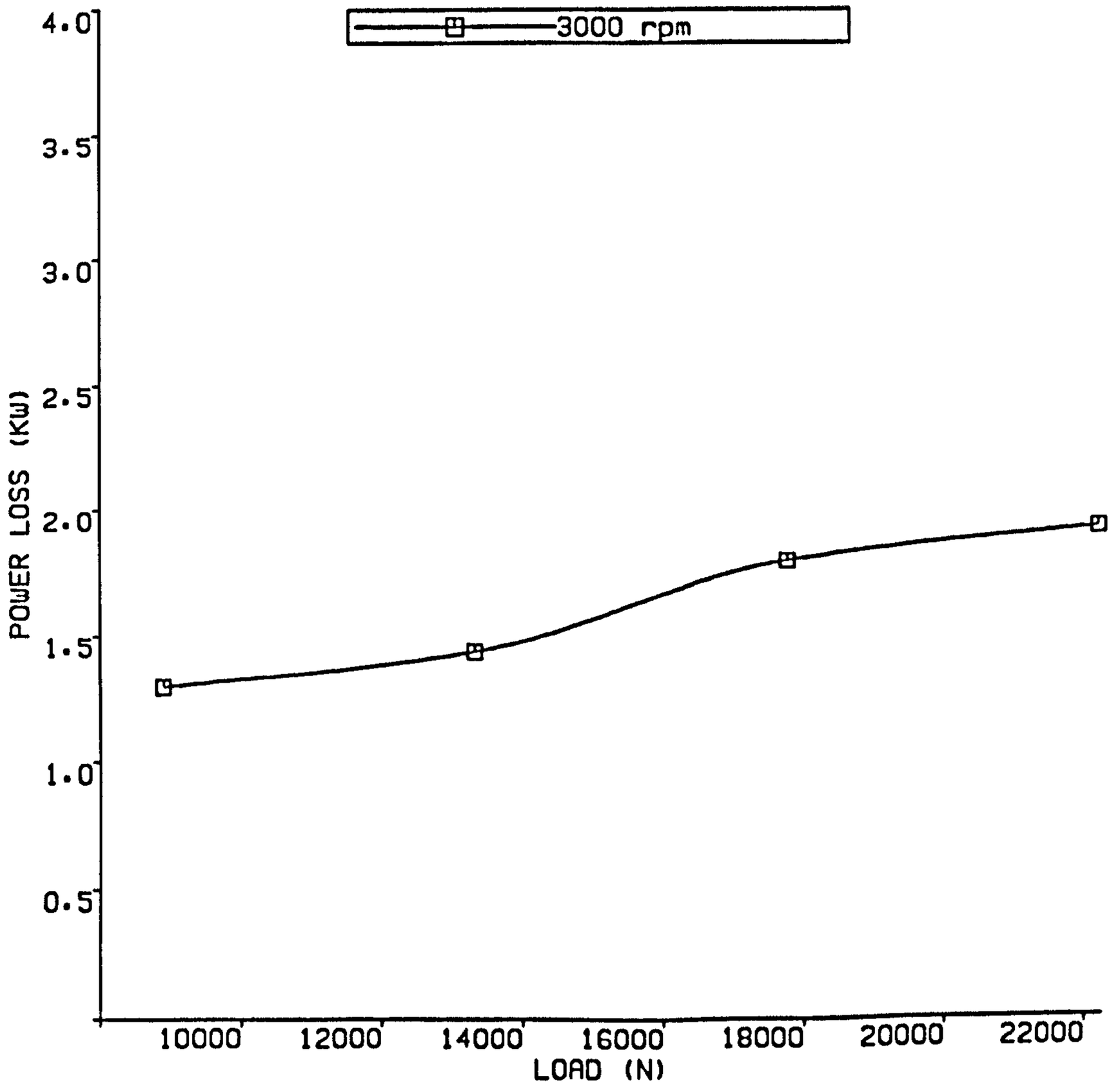

FIGURE 3.9 POWER LOSSES VS LOAD

PLAIN JOURNAL BEARING

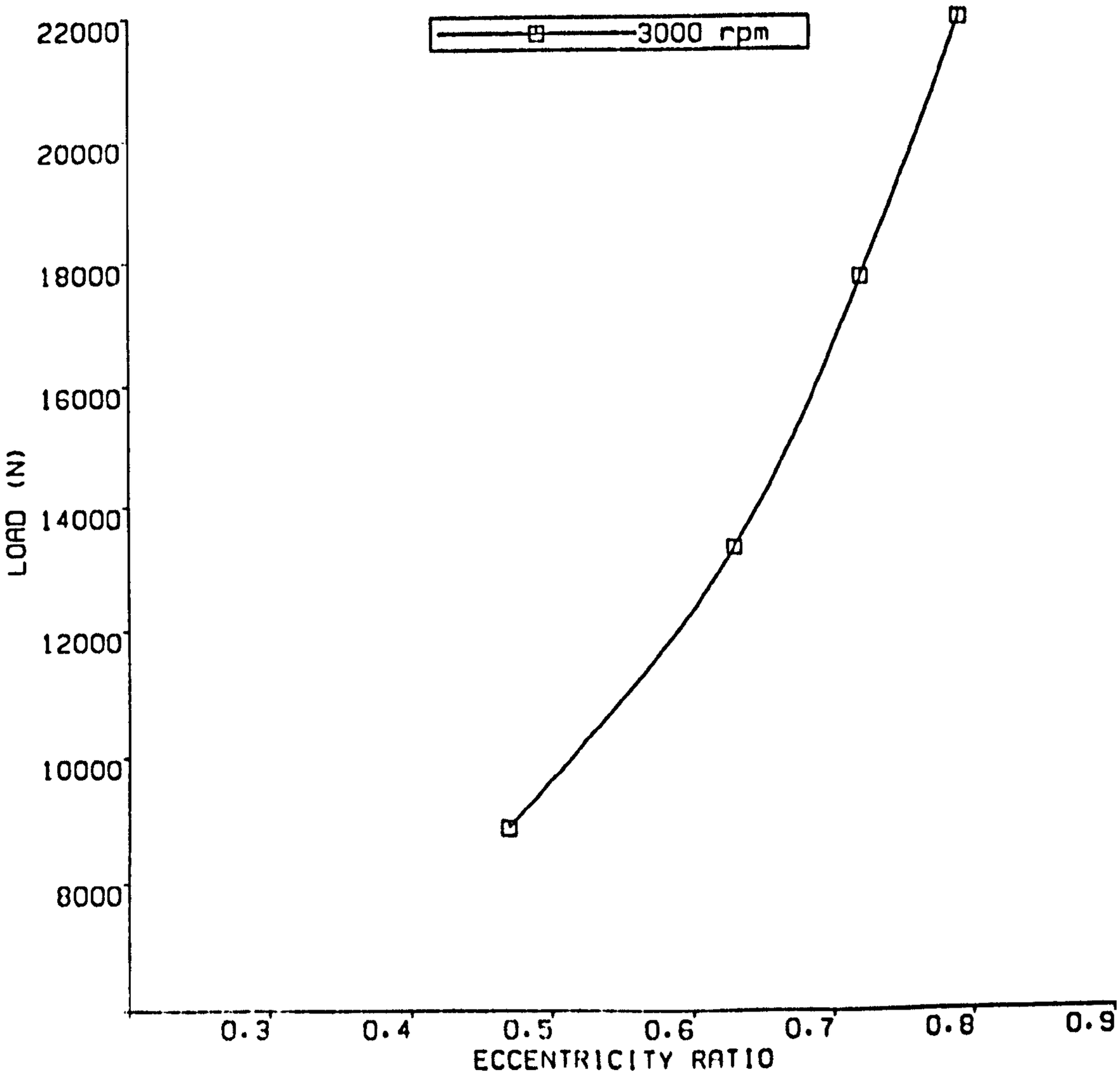

FIGURE 3.10 ECCENTRICITY VS LOAD

PLAIN JOURNAL BEARING

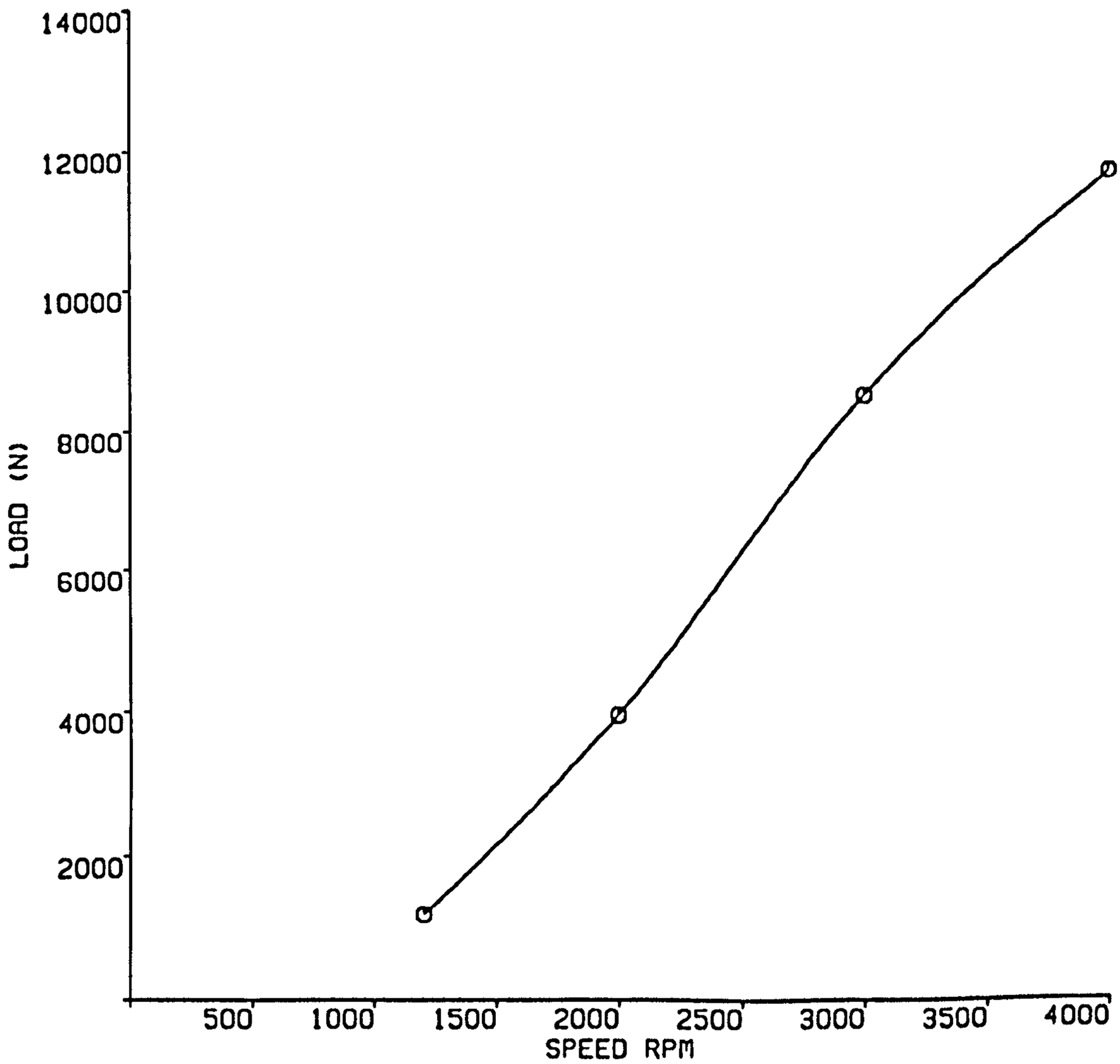

FIGURE 3.11 STABILITY DIAGRAM

PLAIN JOURNAL BEARING

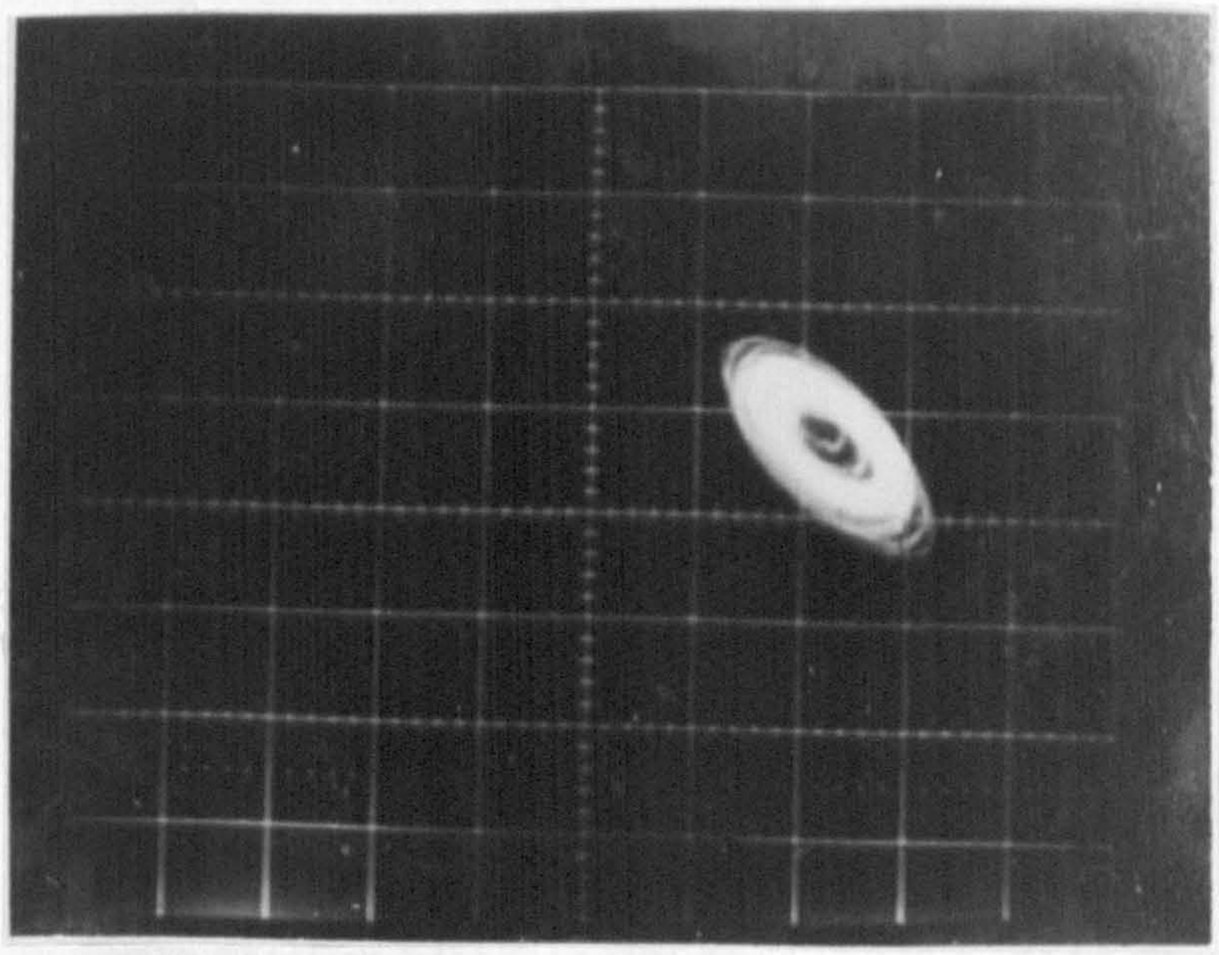

a) *Scale* 36.36 μ*m per centimeter*

Load 11200 N
Speed 3000 rpm

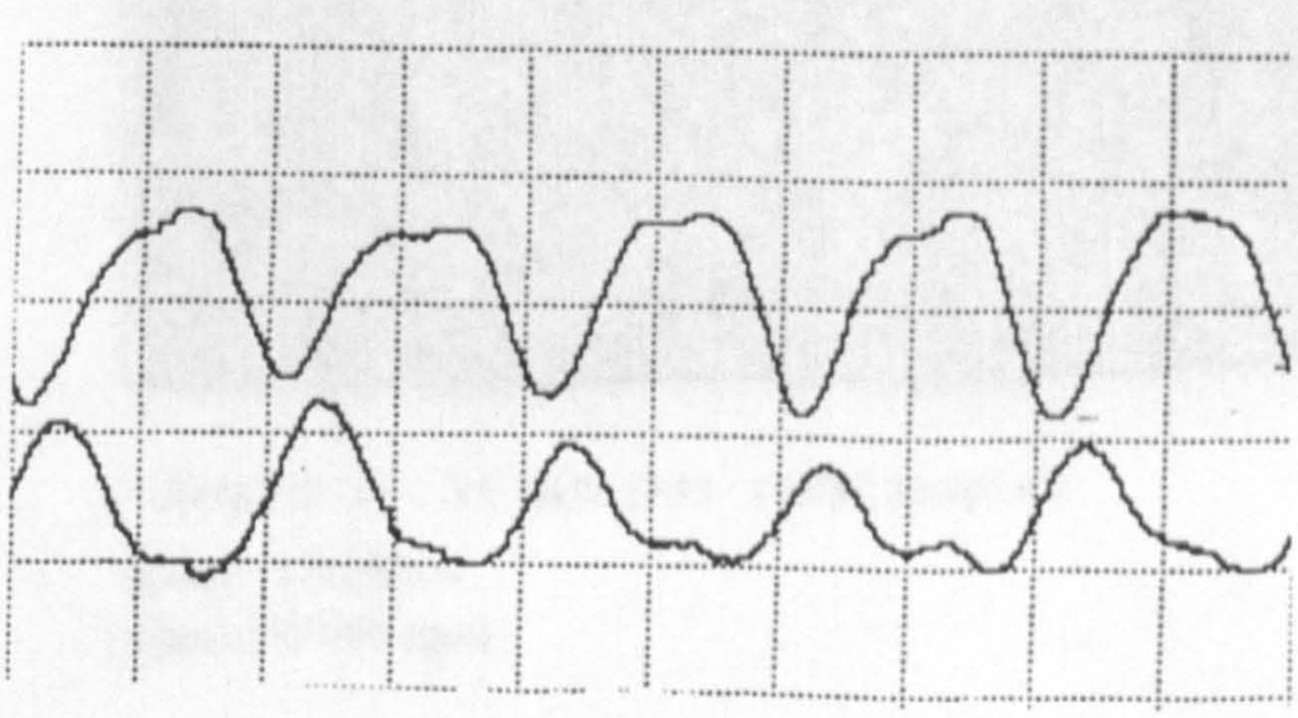

b) *Vertical axis scale* 36.36 μ*m per cm*

Horizontial axis scale 20 ms per centimeter
Load 11200 N
Speed 3000 rpm

Figure 3.12 Orbit of plain journal bearing
below threshold of instability

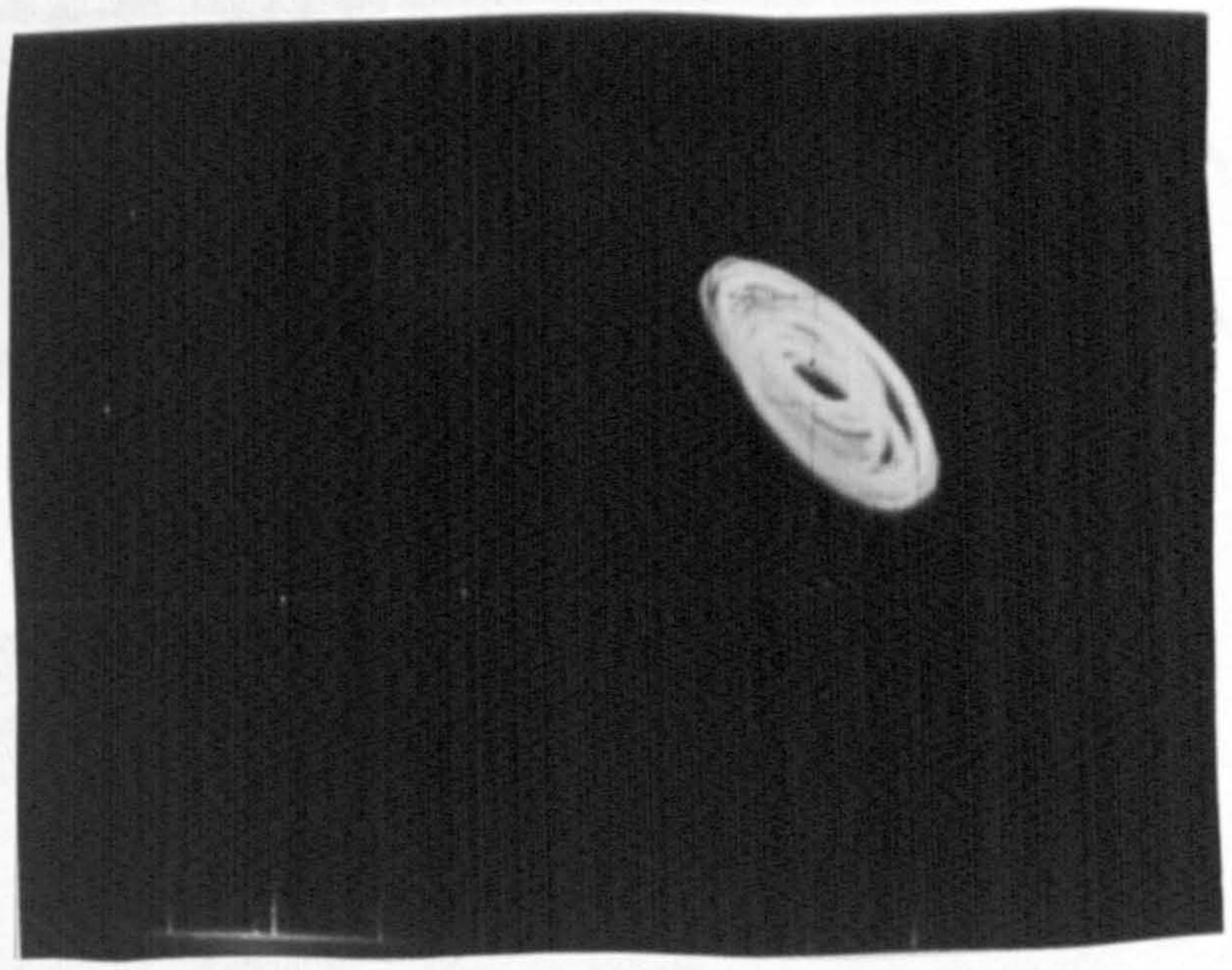

Scale 36.36 μm *per centimeter*

Load 15680 N
Speed 4040 rpm

Figure 3.13 Orbit of plain journal bearing
below threshold of instability

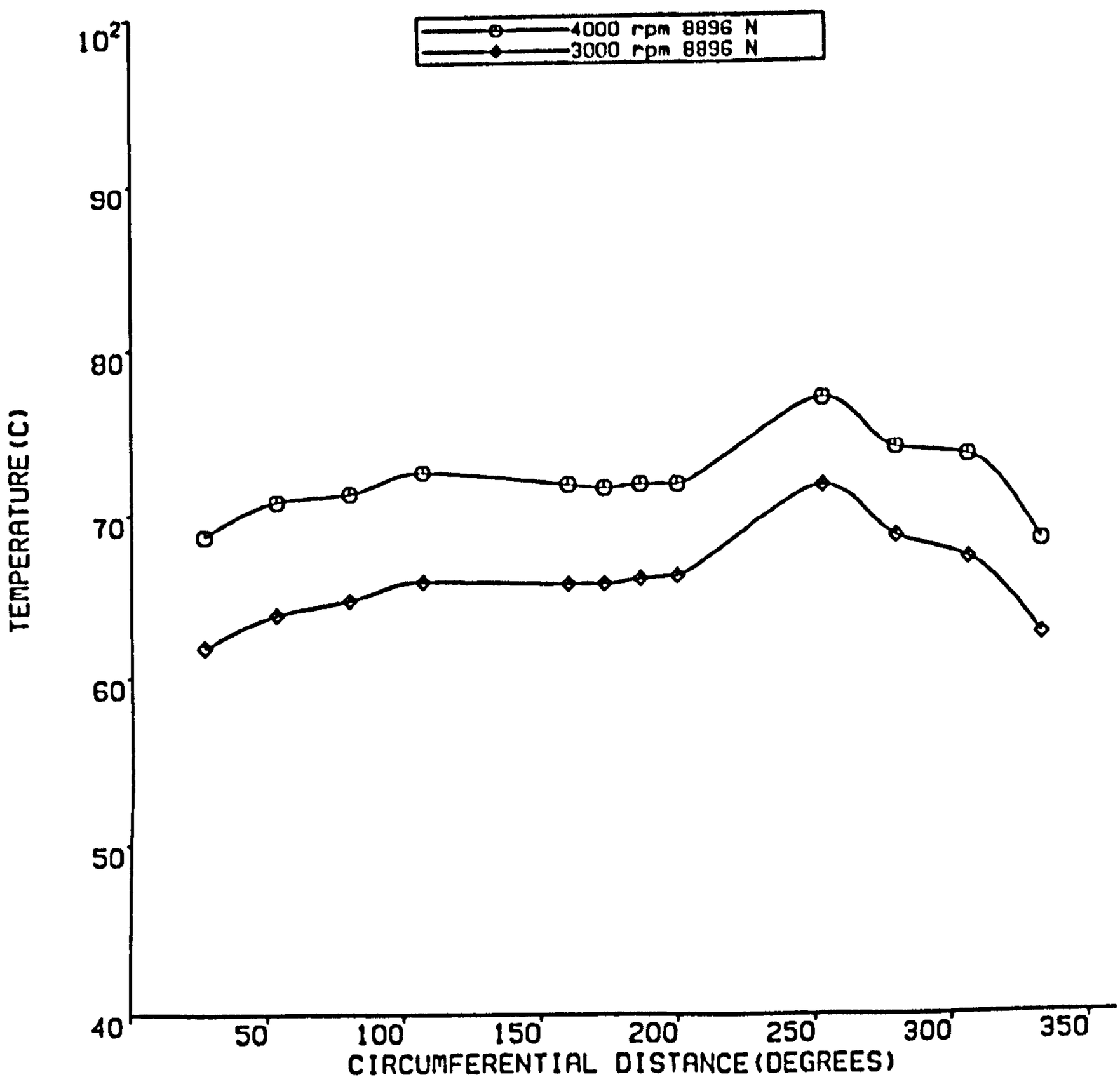

FIGURE 3.14 TEMPERATURE PROFILES FOR DIFFERENT SPEEDS

SYMMETRICAL HELICAL GROOVE JOURNAL BEARING

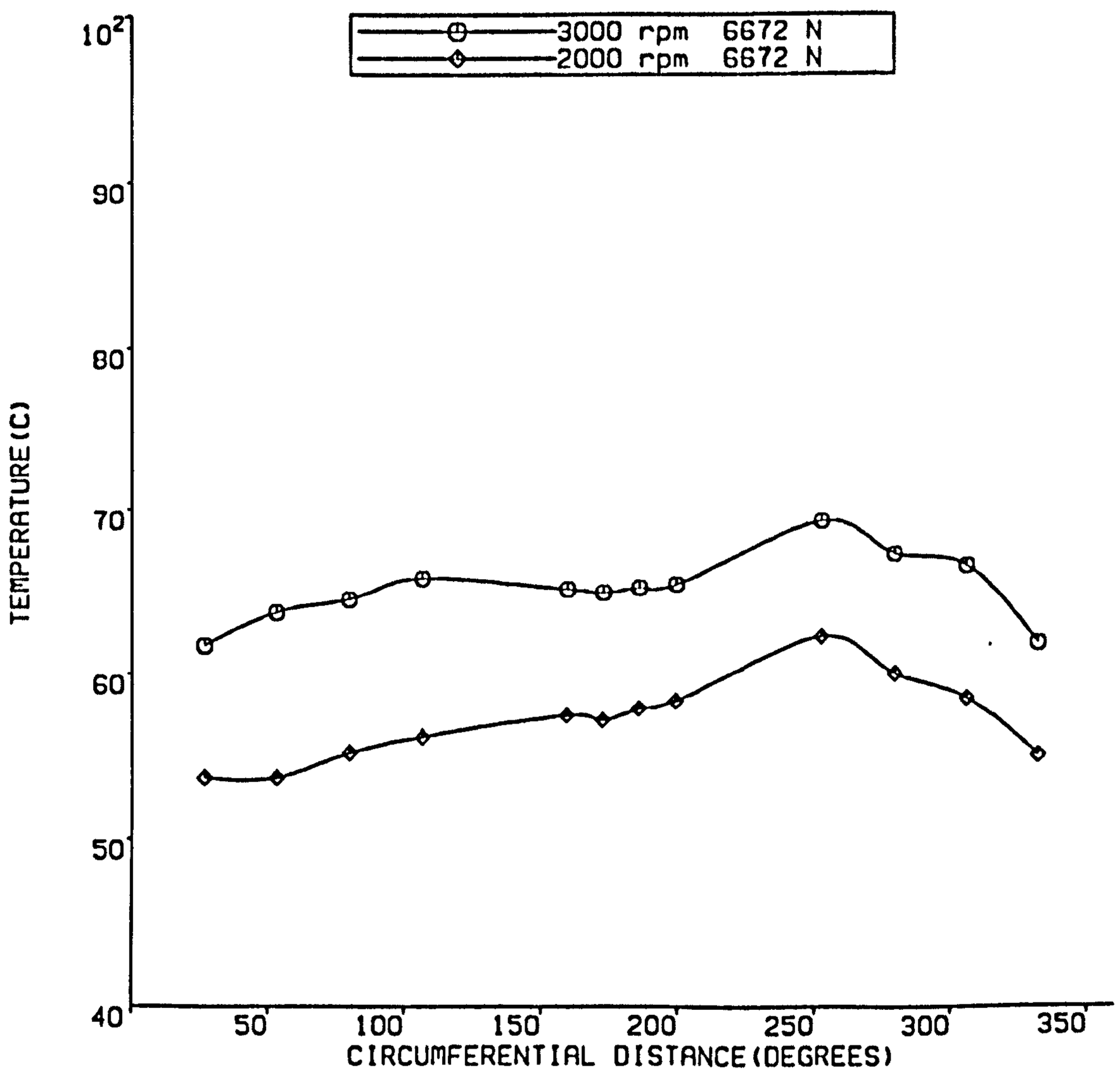

FIGURE 3.15 TEMPERATURE PROFILES FOR DIFFERENT SPEEDS

SYMMETRICAL HELICAL GROOVE JOURNAL BEARING

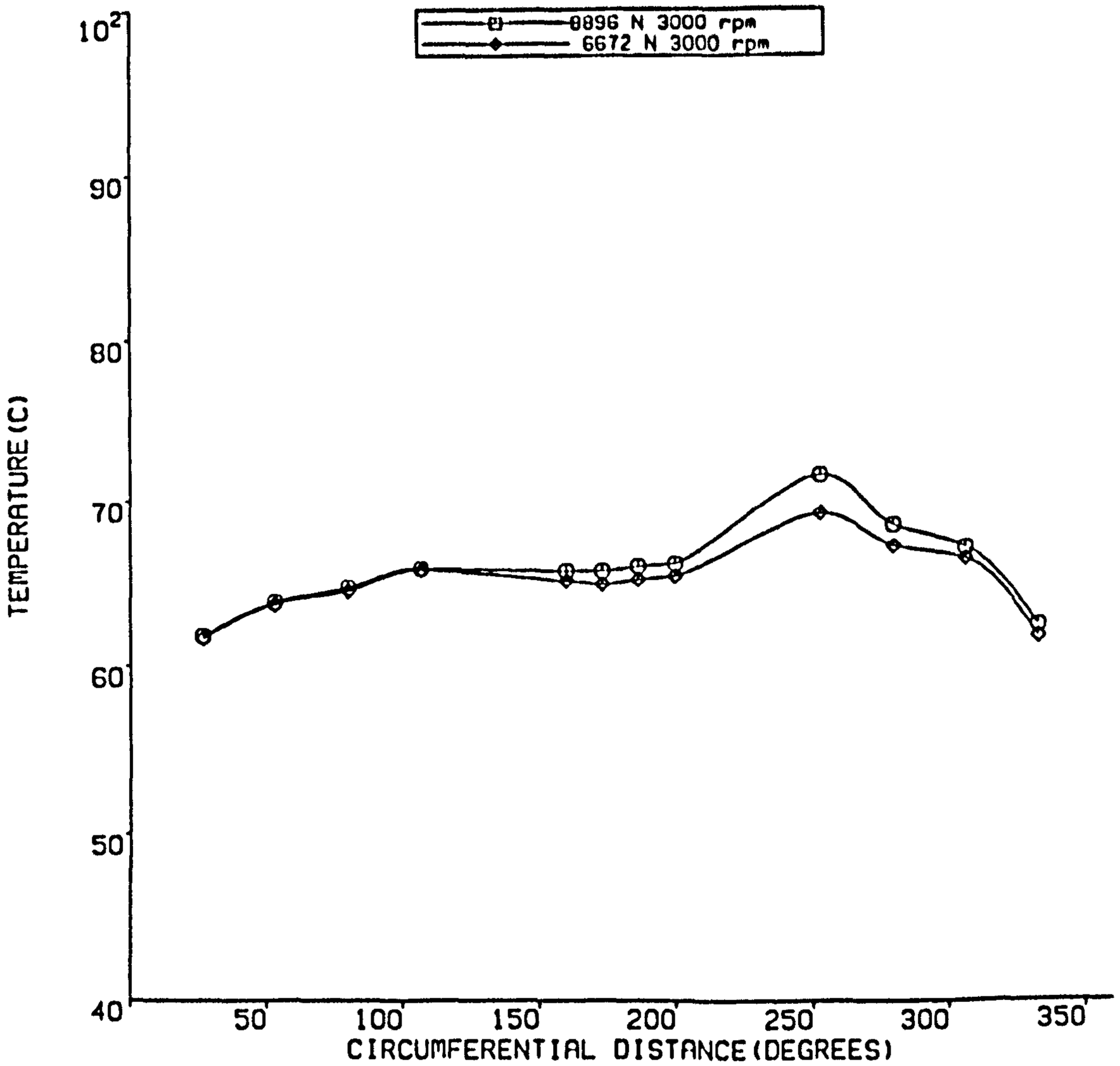

FIGURE 3.16 TEMPERATURE PROFILES AT DIFFERENT LOADS
SYMMETRICAL HELICAL GROOVE JOURNAL BEARING

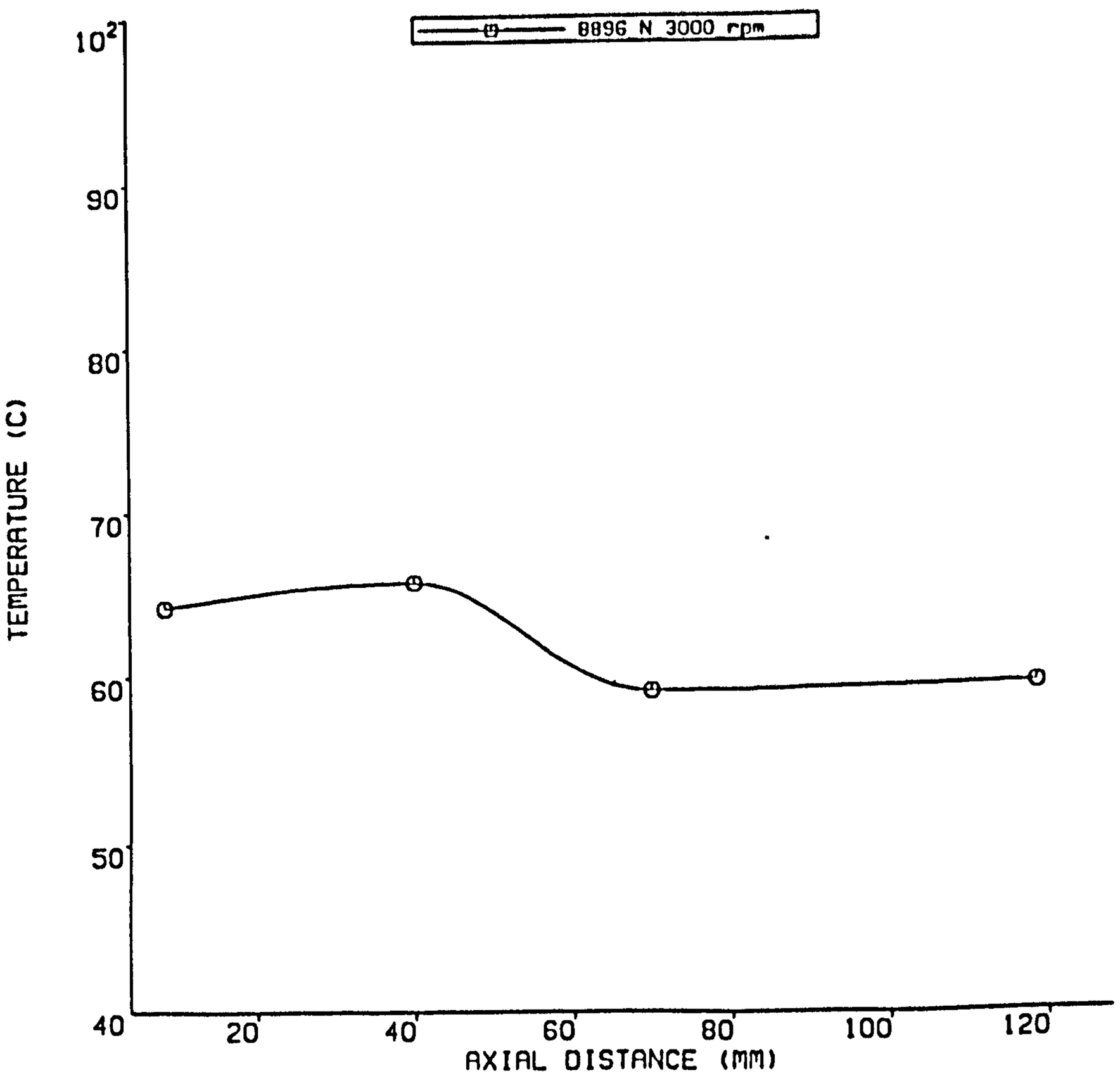

FIGURE 3.17 AXIAL TEMPERATURE VARIATION
OF SYMMETRICAL HELICAL GROOVE BEARING

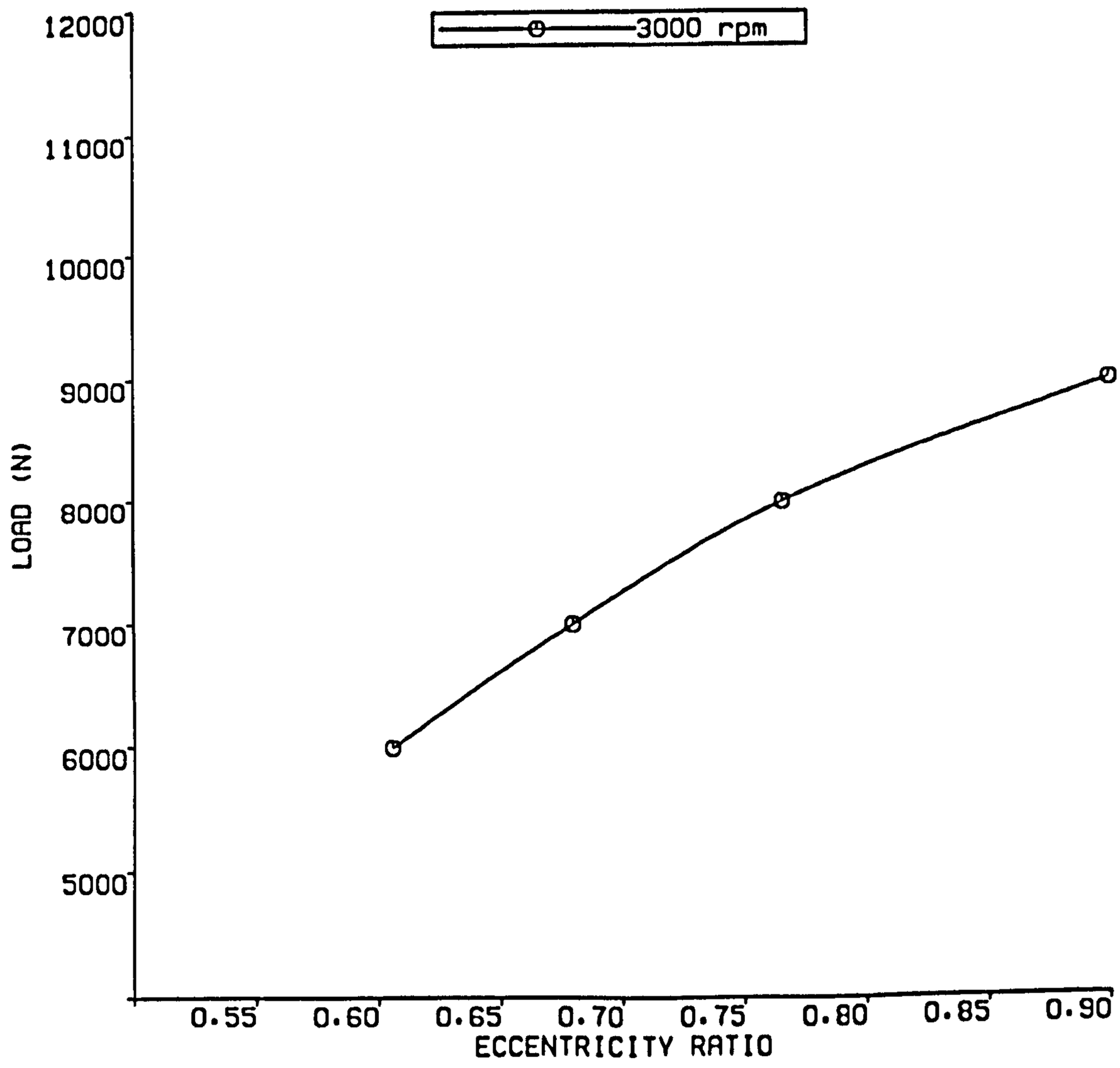

FIGURE 3.18 ECCENTRICITY VS LOAD

SYMMETRICAL HELICAL GROOVE JOURNAL BEARING

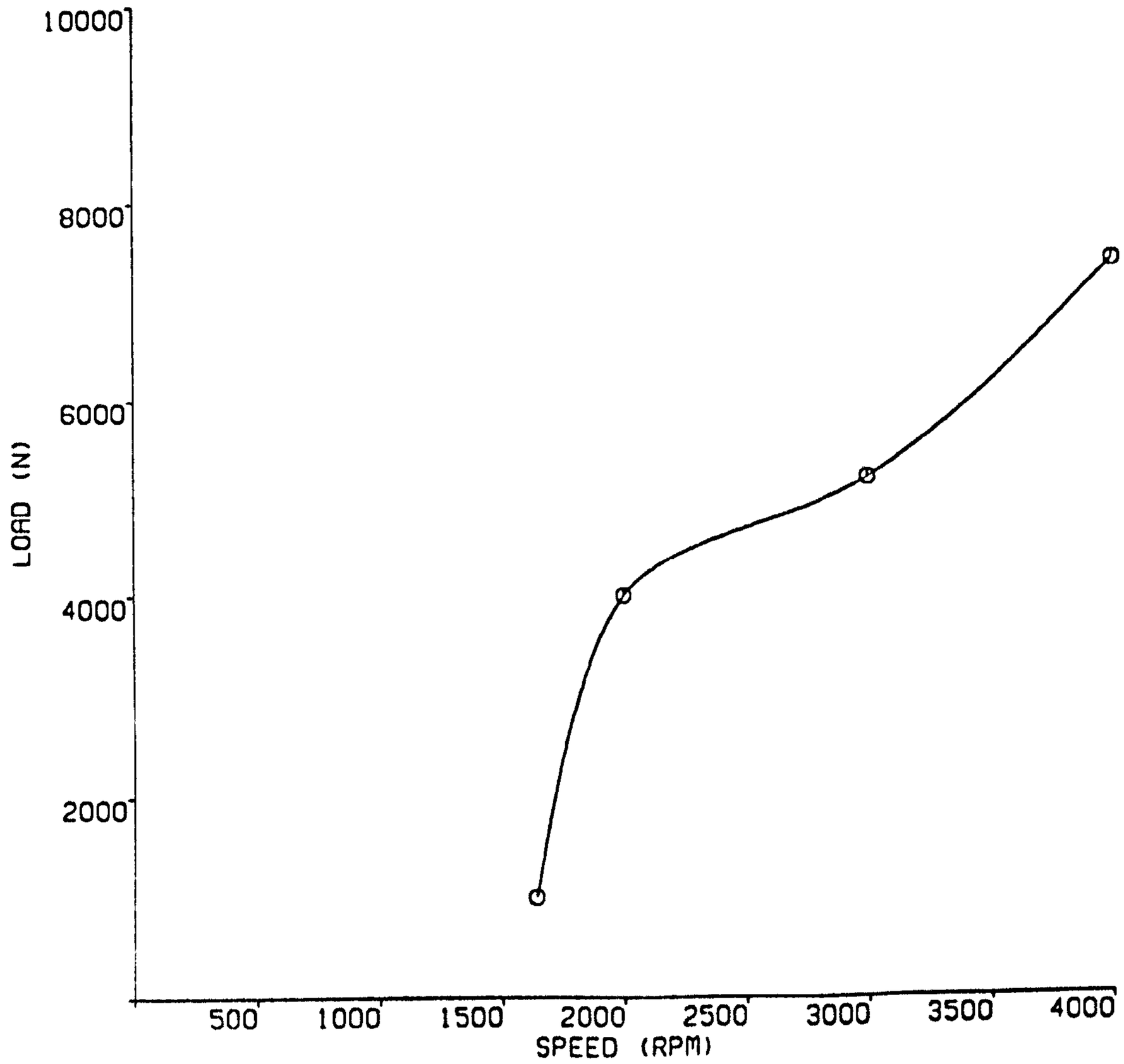

FIGURE 3.19 STABILITY PLOT
SYMMETRICAL HELICAL GROOVE JOURNAL BEARING

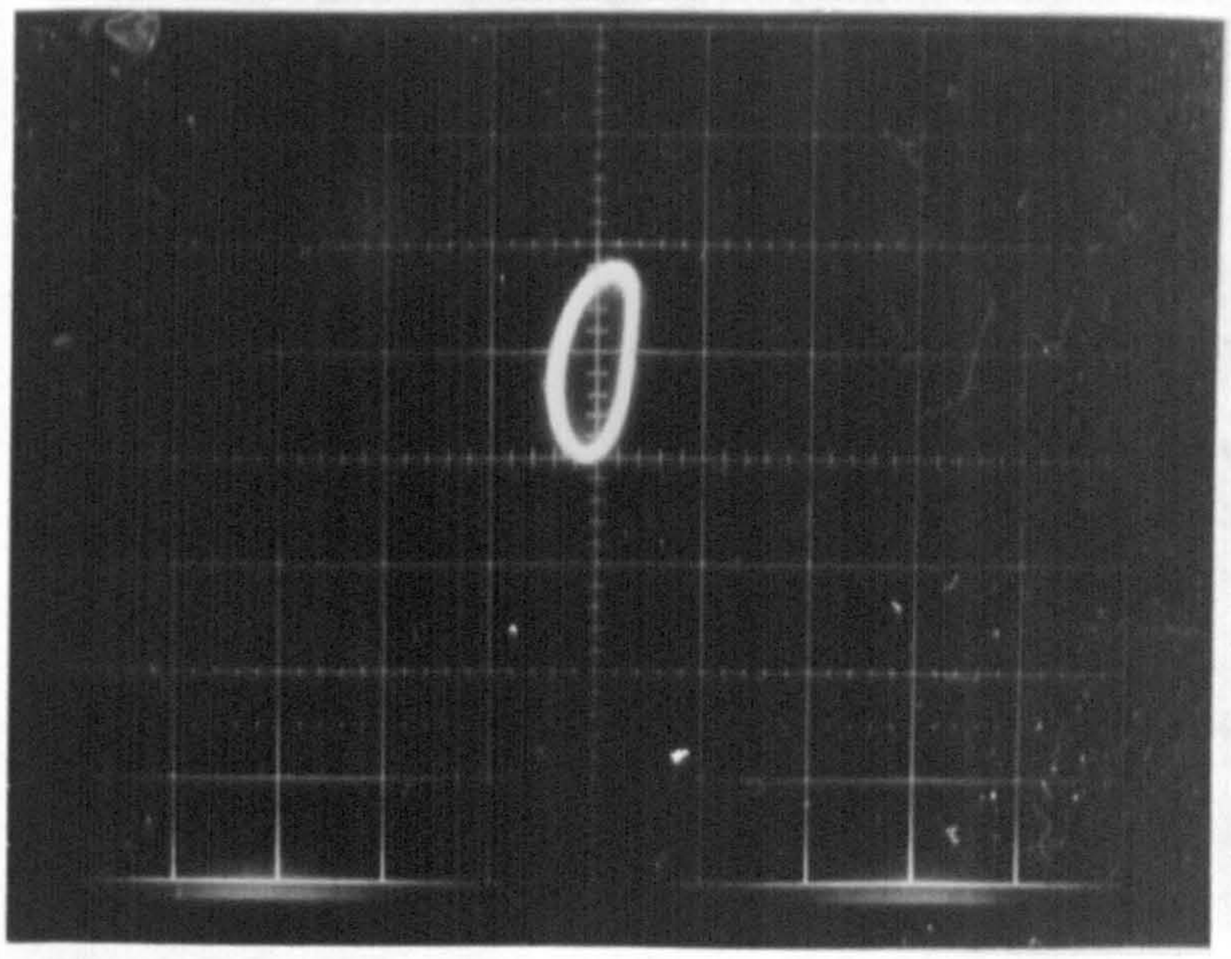

a) *Scale* 36.36 μm *per centimeter*

Load 4448 N
Speed 2000 rpm

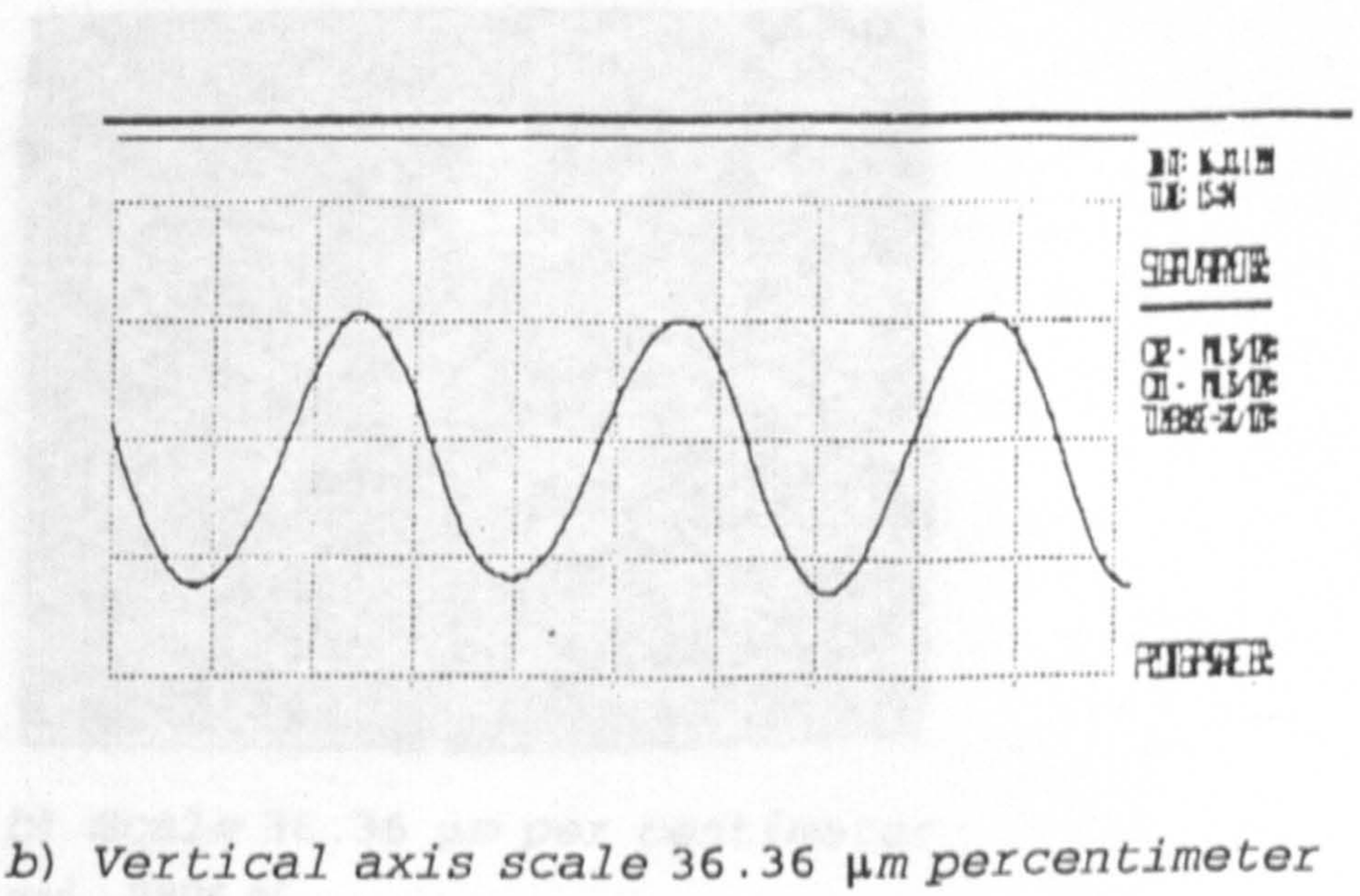

b) *Vertical axis scale* 36.36 μm *percentimeter*

Horizontial axis scale 20 ms per centimeter
Load 4448 N
Speed 2000 rpm

Figure 3.20 Orbit of symmetrical helical groove journal bearing below threshold of instability

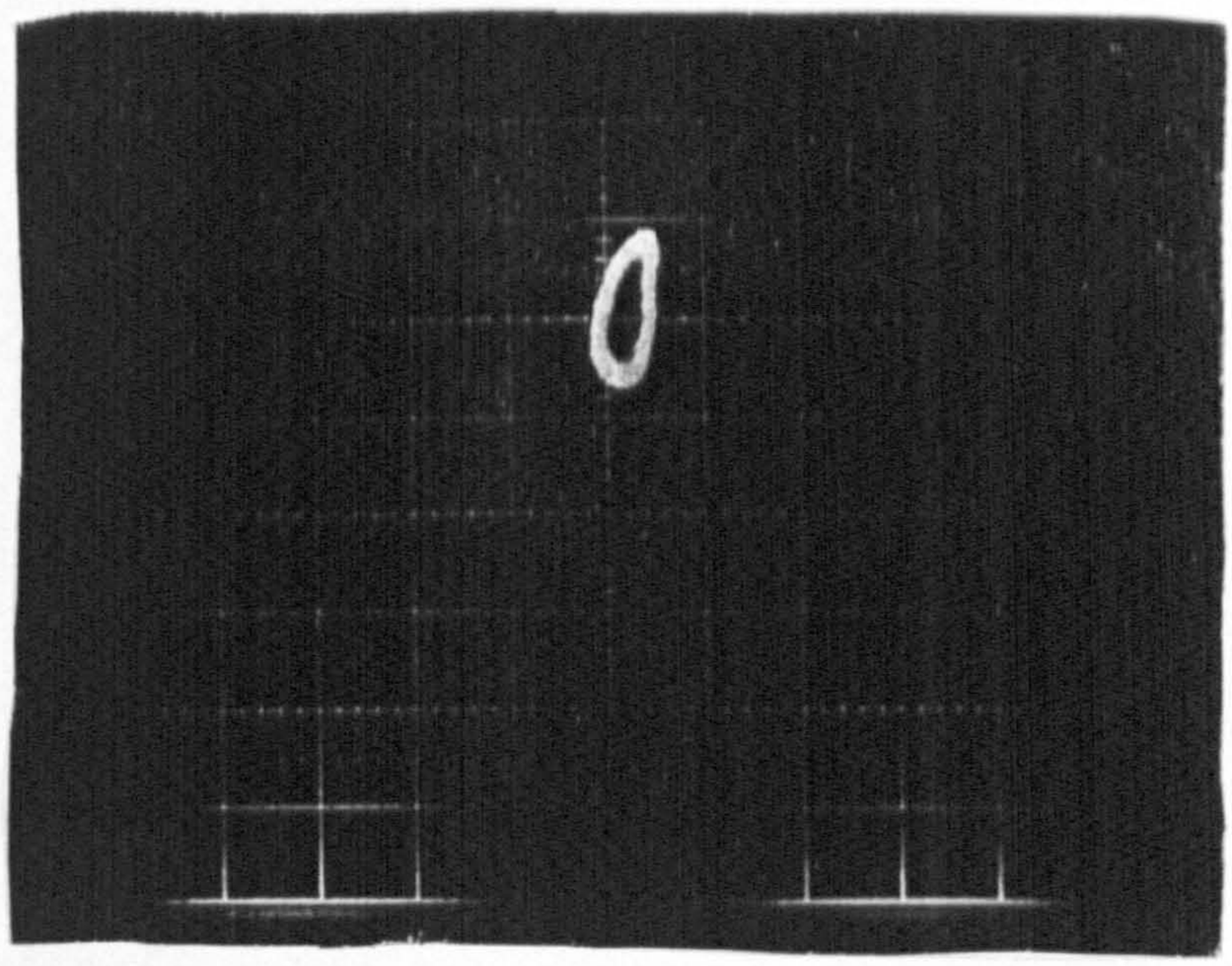

a) *Scale* 36.36 μm *per centimeter*

Load 8896 N
Speed 3000 rpm

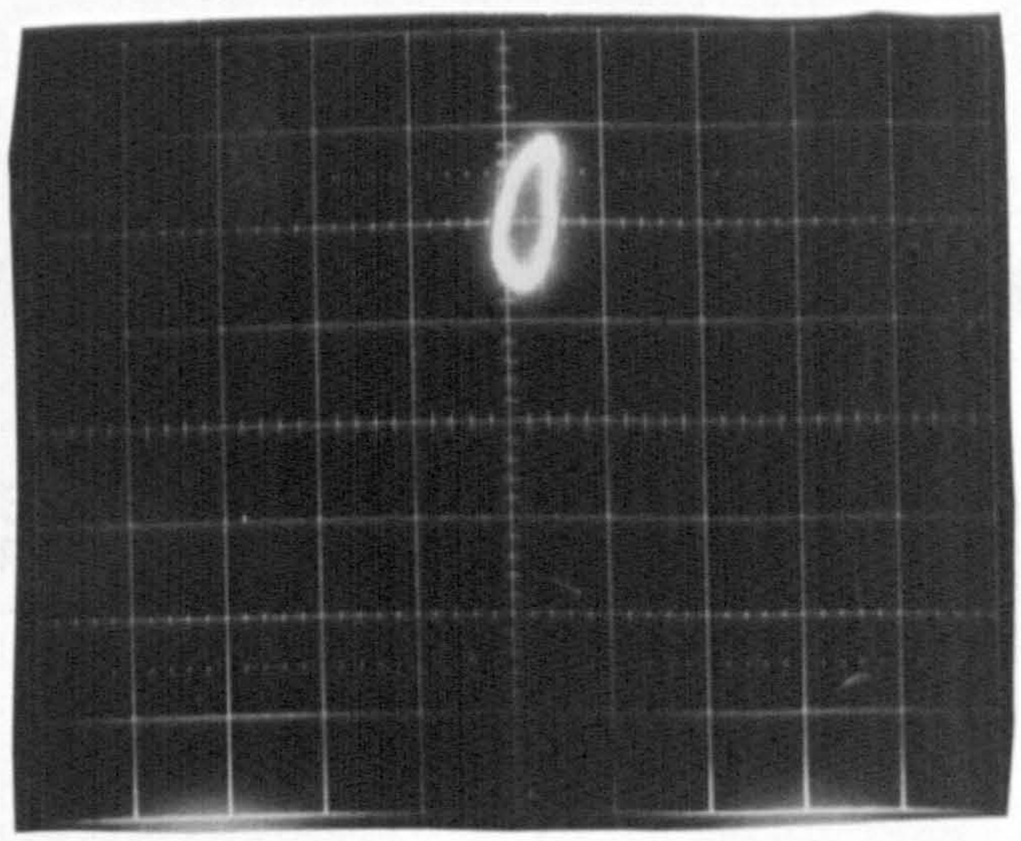

b) *Scale* 36.36 μm *per centimeter*

Load 8896 N
Speed 4000 rpm

Figure 3.21 Orbit of symmetrical helical groove bearing below threshold of instability

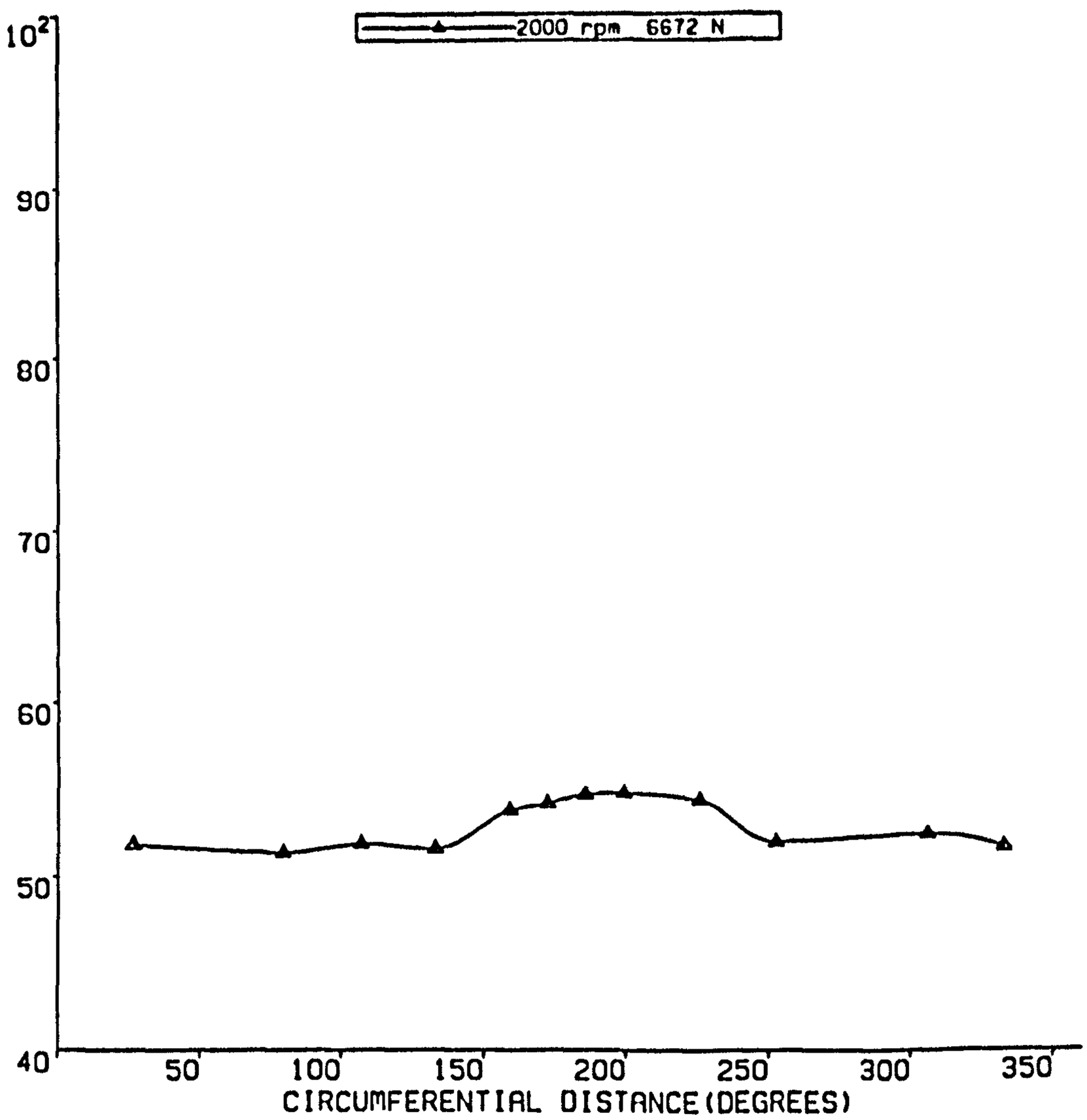

FIGURE 3.22 TEMPERATURE PROFILE AT 2000 RPM
ASYMMETRICAL HELICAL GROOVE JOURNAL BEARING

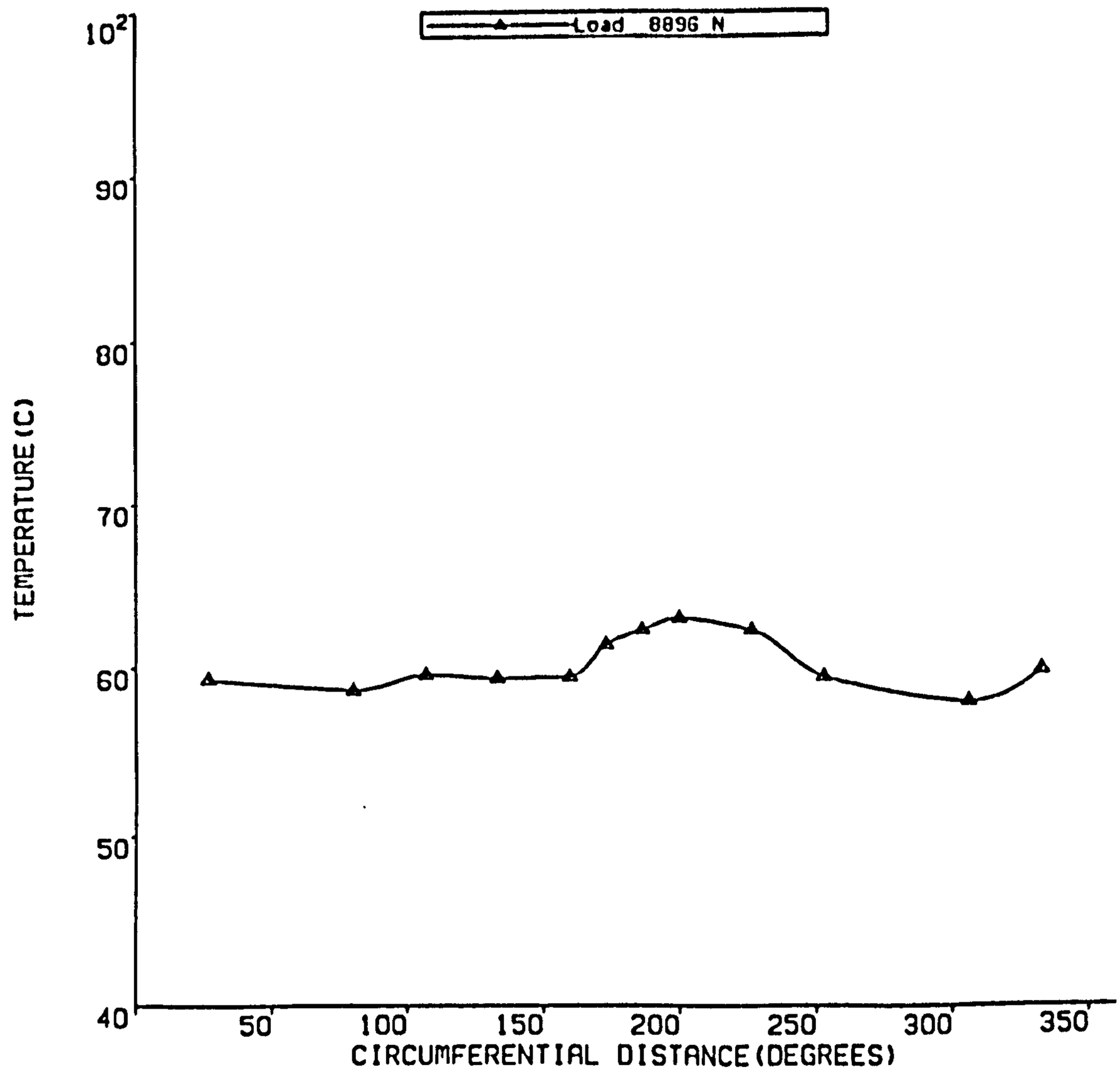

FIGURE 3.23 TEMPERATURE PROFILE AT 3000 RPM

ASYMMETRICAL HELICAL GROOVE JOURNAL BEARING

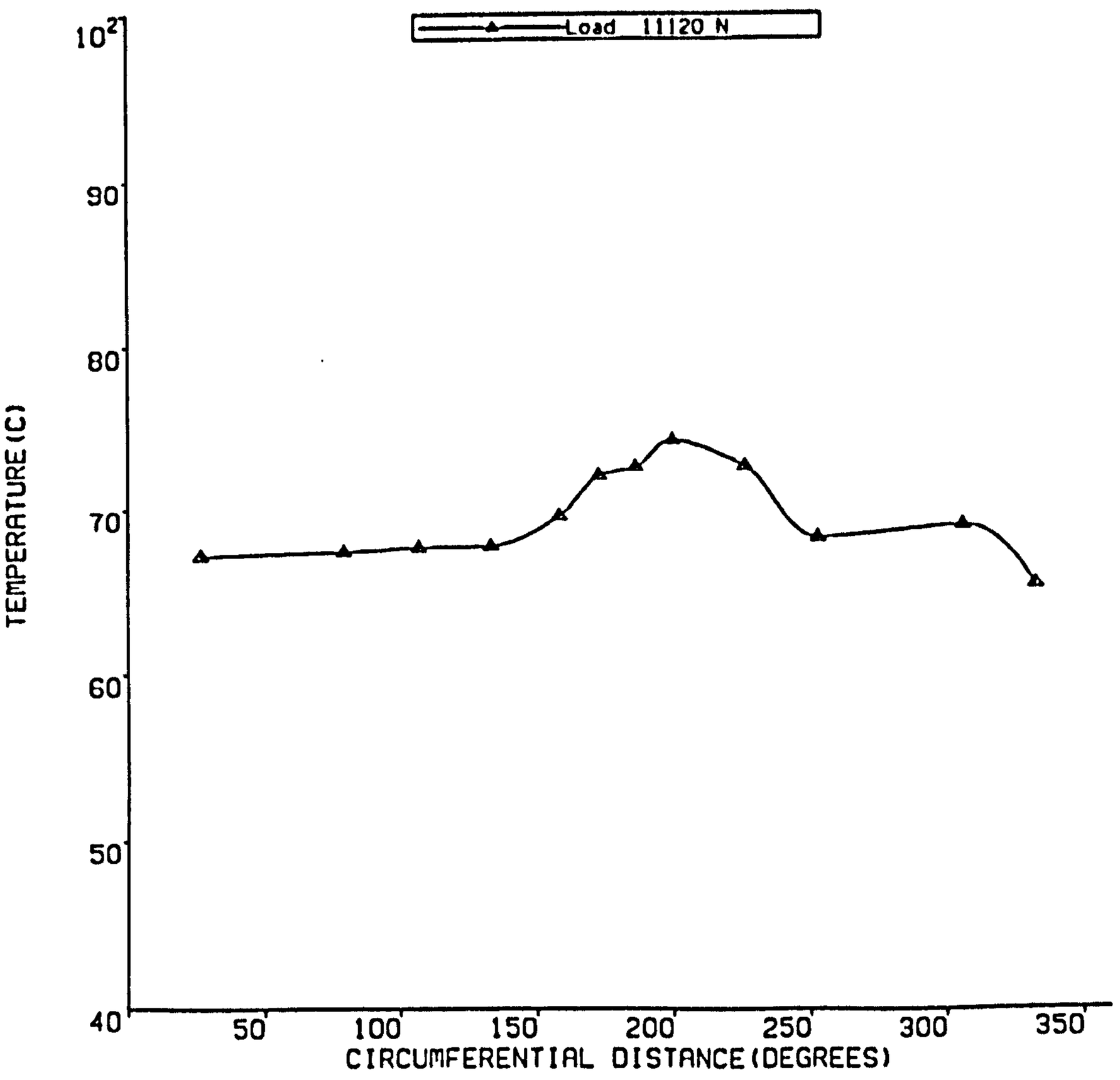

FIGURE 3.24 TEMPERATURE PROFILE AT 4000 RPM

ASYMMETRICAL HELICAL GROOVE JOURNAL BEARING

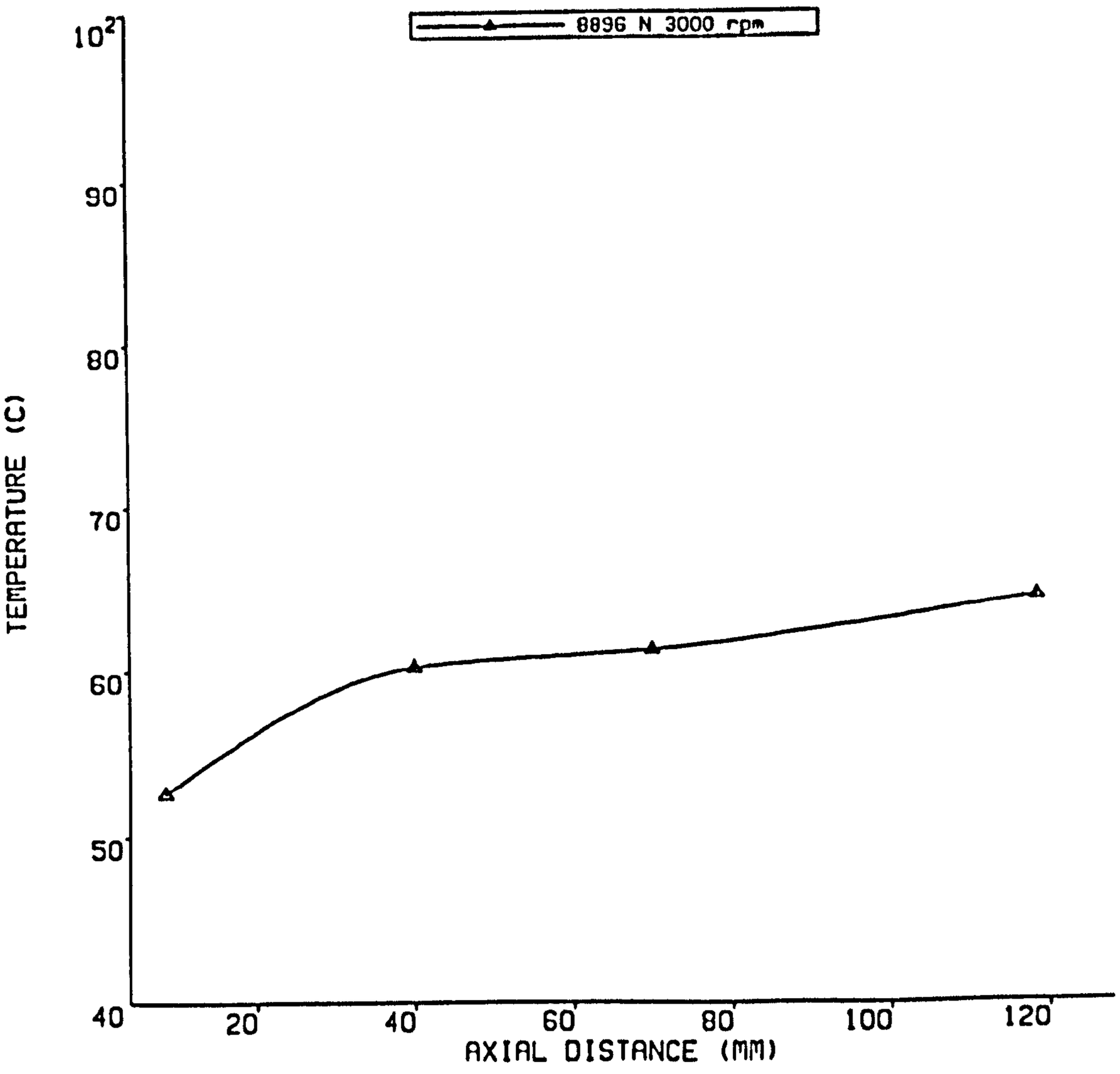

FIGURE 3.25 AXIAL TEMPERATURE VARIATION
ASYMMETRICAL HELICAL GROOVE JOURNAL BEARING

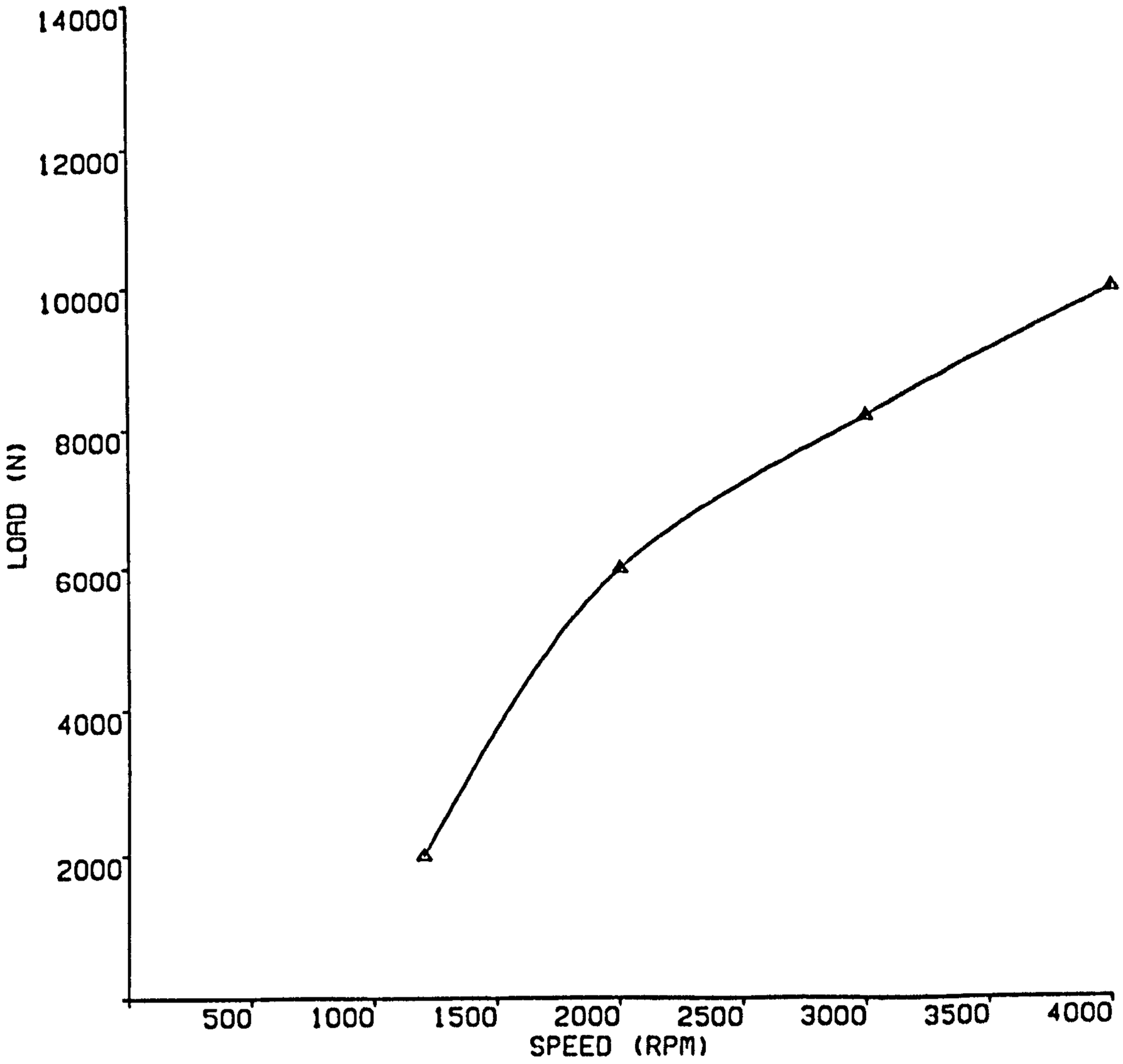

FIGURE 3.26 STABILITY PLOT
ASYMMETRICAL HELICAL GROOVE JOURNAL BEARING

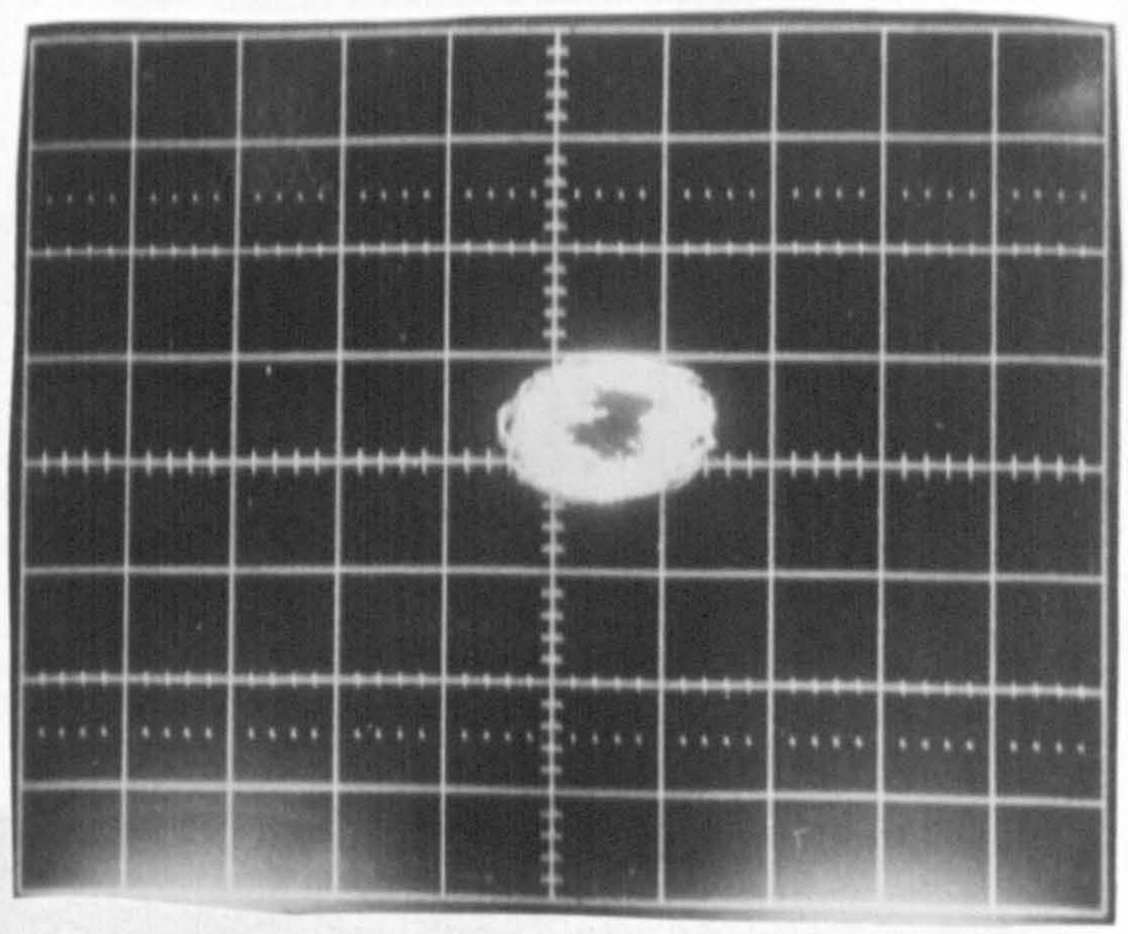

a) *Scale* 36.36 μm *per centimeter*

Load No load
Speed 1280 rpm

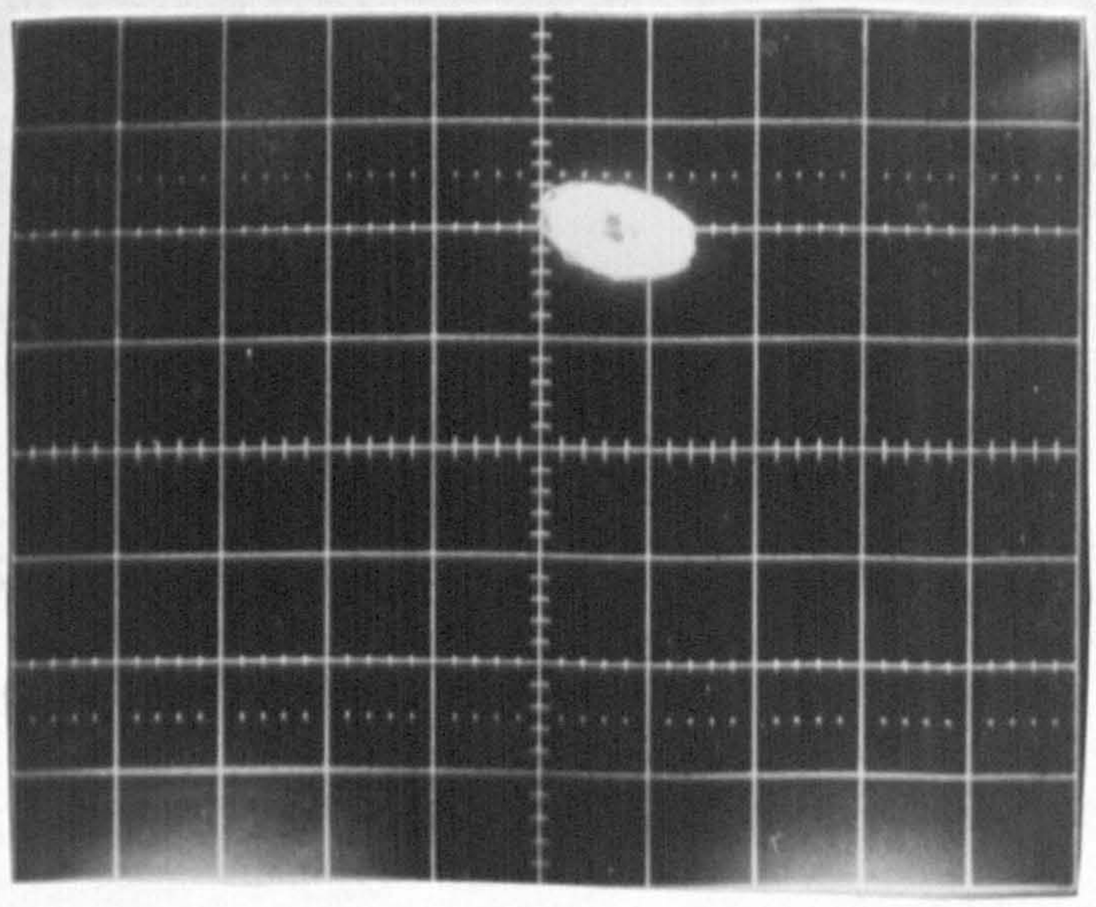

b) *Scale* 36.36 μm *per centimeter*

Load 6672 N
Speed 2000 rpm

Figure 3.27 Orbit of asymmetrical helical groove bearing below threshold of instability

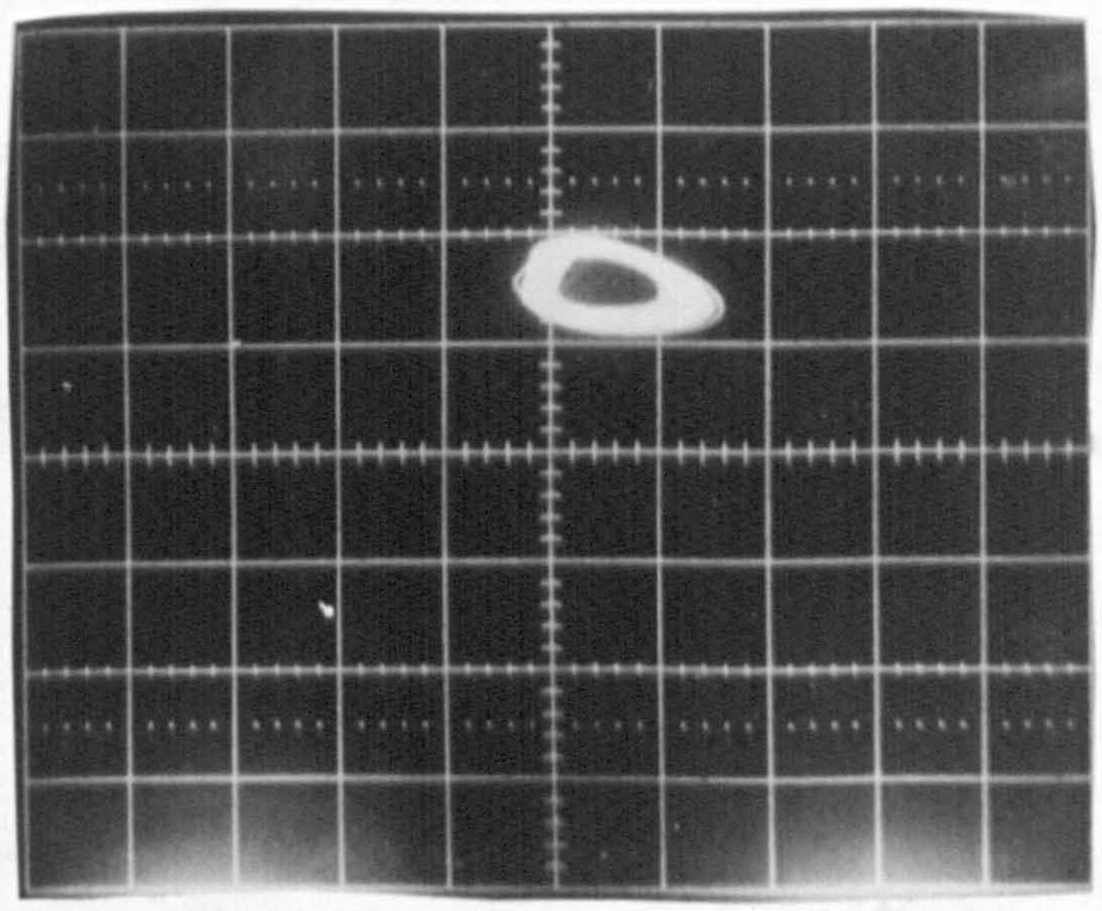

Scale 36.36 µm *per centimeter*

Load 6673 N
Speed 3000 rpm

Figure 3.28 Orbit of asymmetrical helical groove bearing below threshold of instability

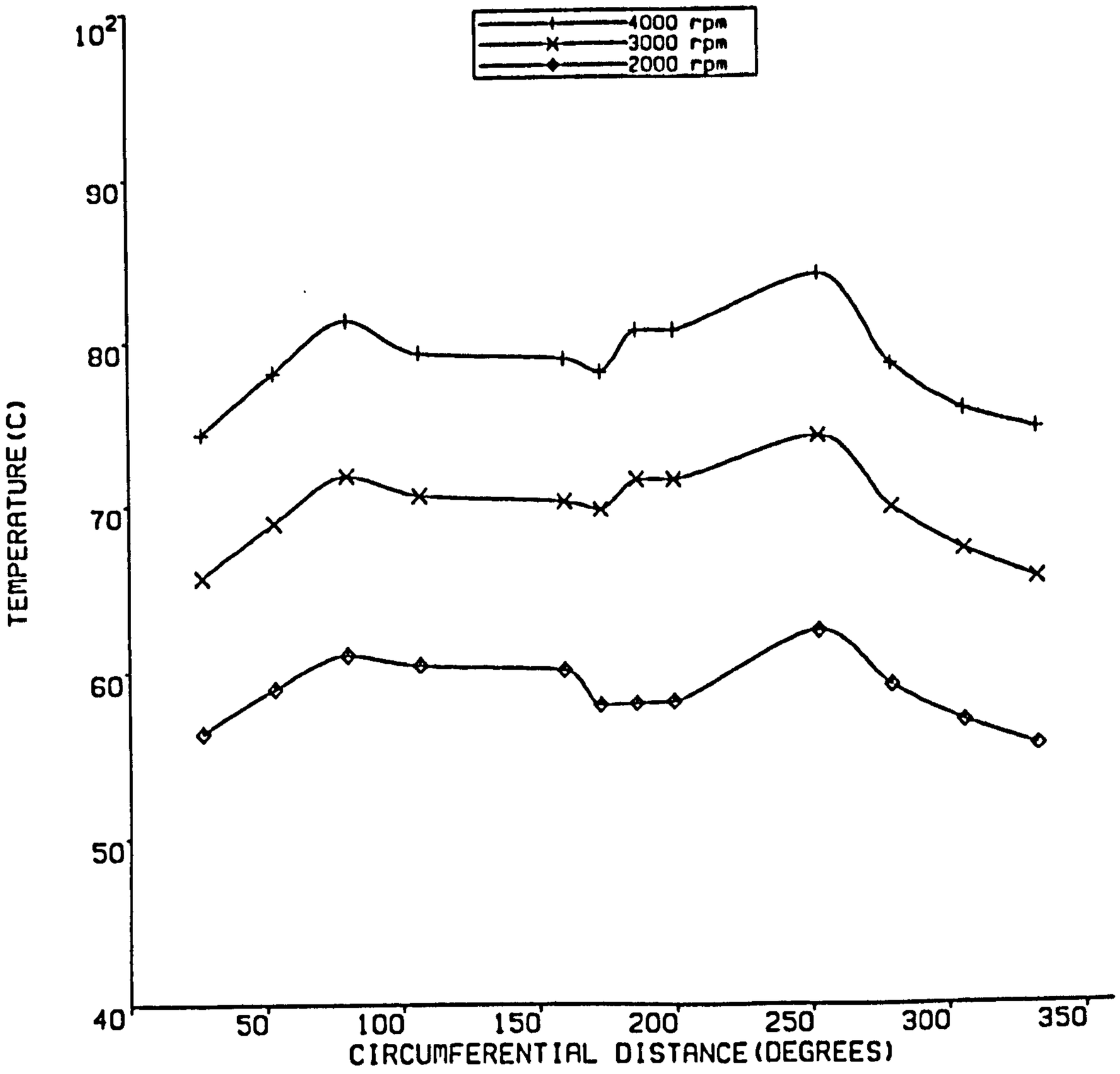

FIGURE 3.29 TEMPERATURE PROFILES AT NO LOAD

PARTIAL HELICAL GROOVE JOURNAL BEARING

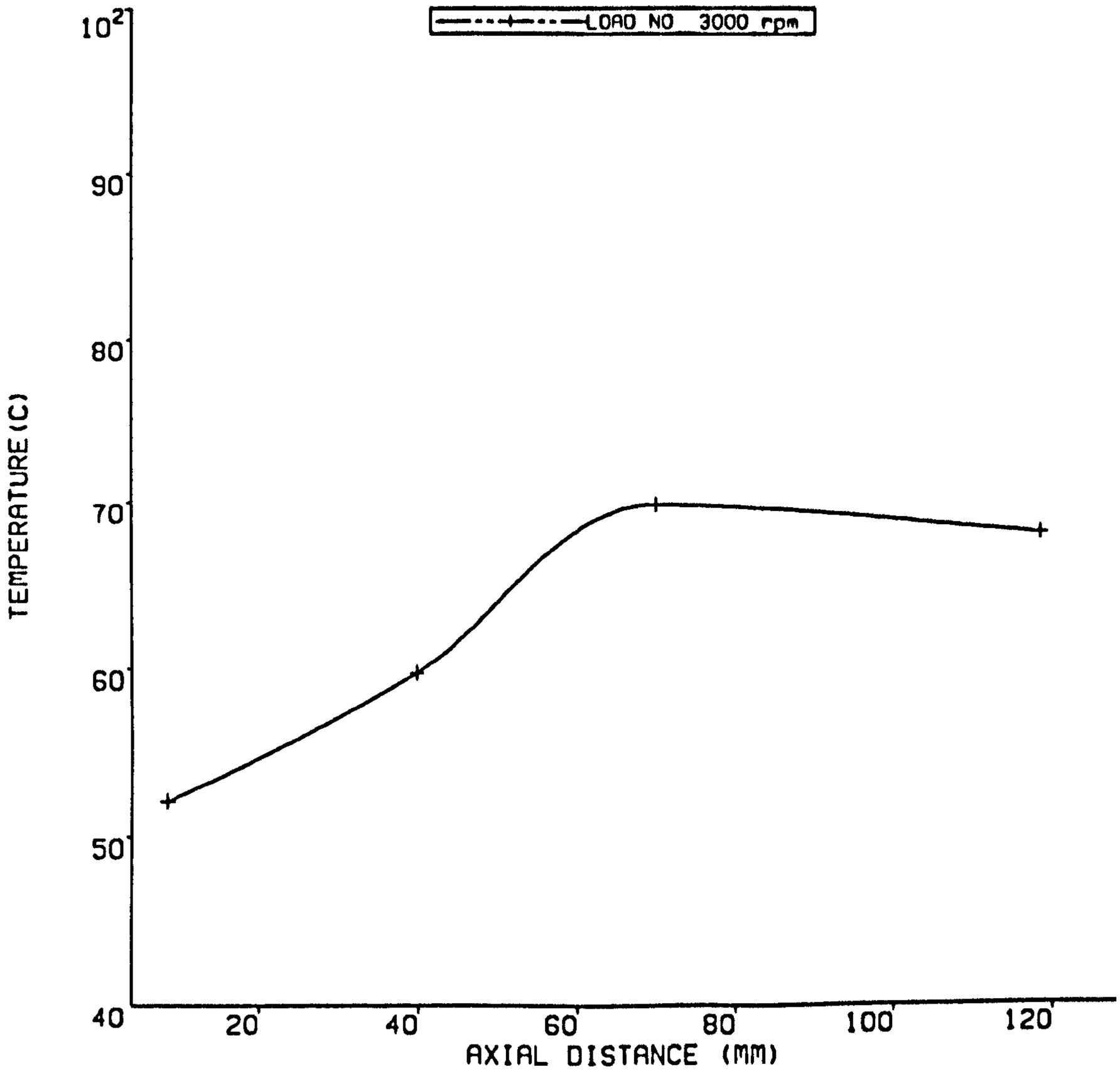

FIGURE 3.30 AXIAL TEMPERATURE VARIATION
PARTIAL HELICAL GROOVE JOURNAL BEARING

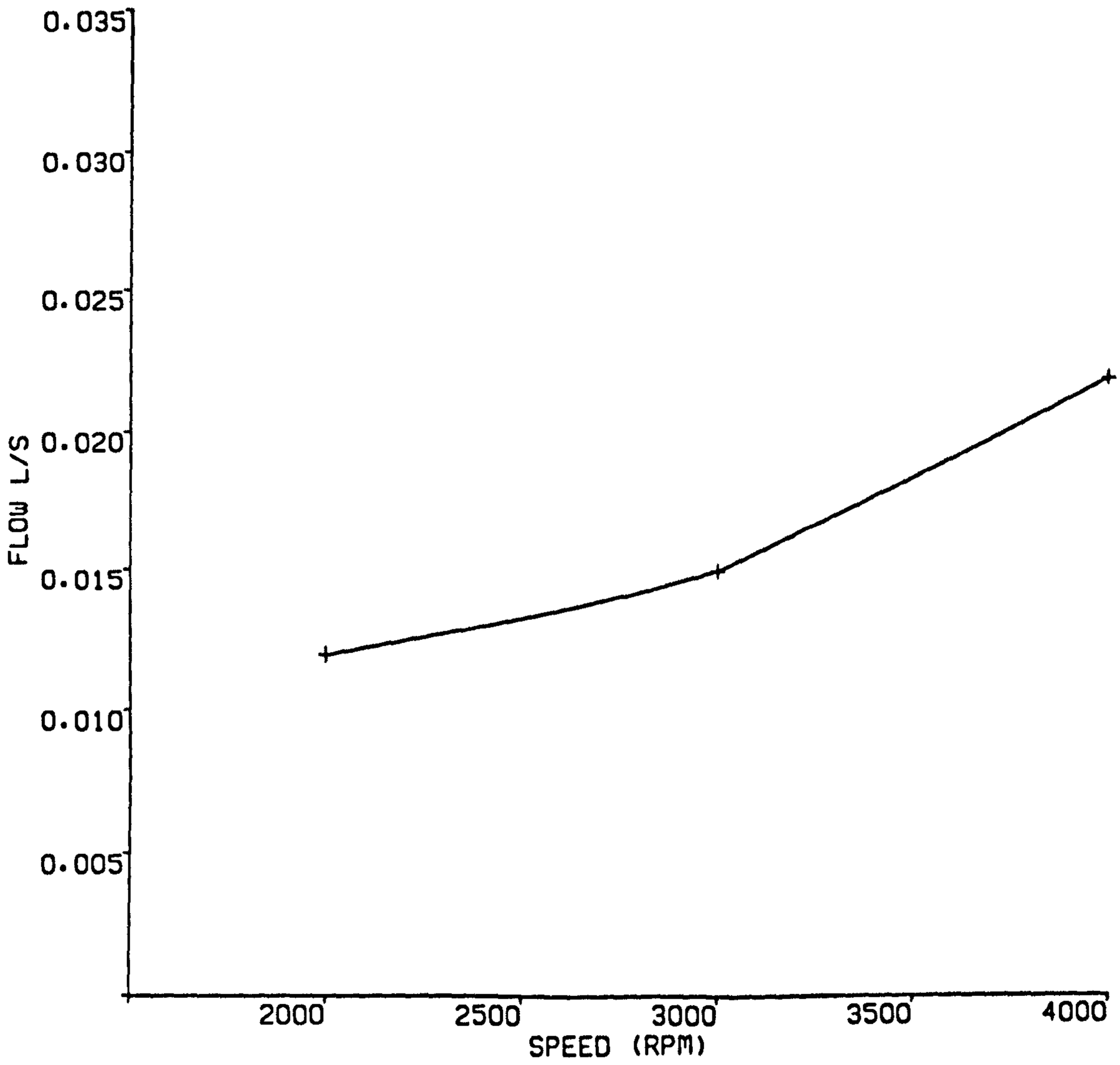

FIGURE 3.31 FLOW RATE VS. SPEED

PARTIAL HELICAL GROOVE JOURNAL BEARING

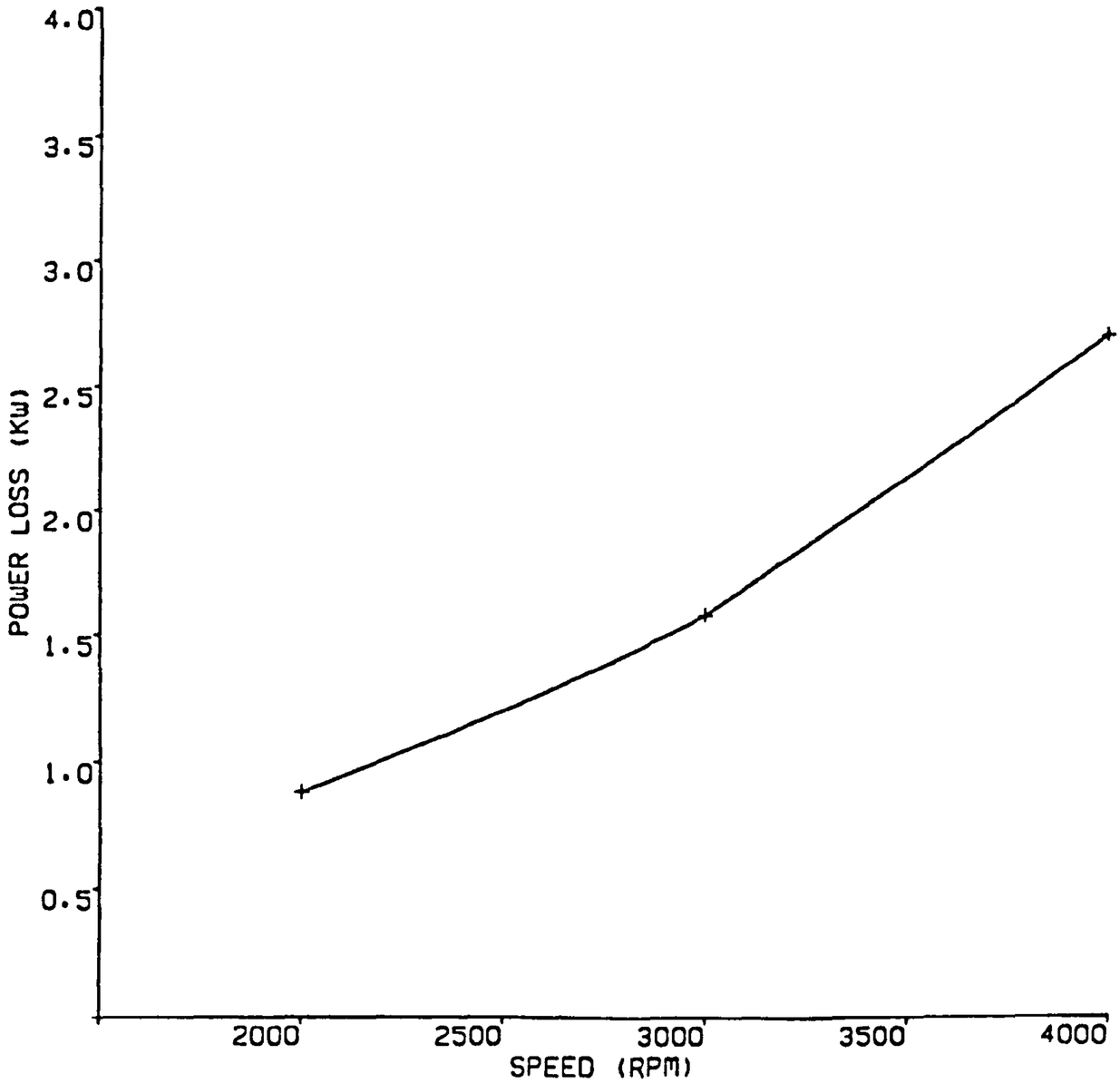

FIGURE 3.32 POWER LOSSESS VS. SPEED

PARTIAL HELICAL GROOVE JOURNAL BEARING

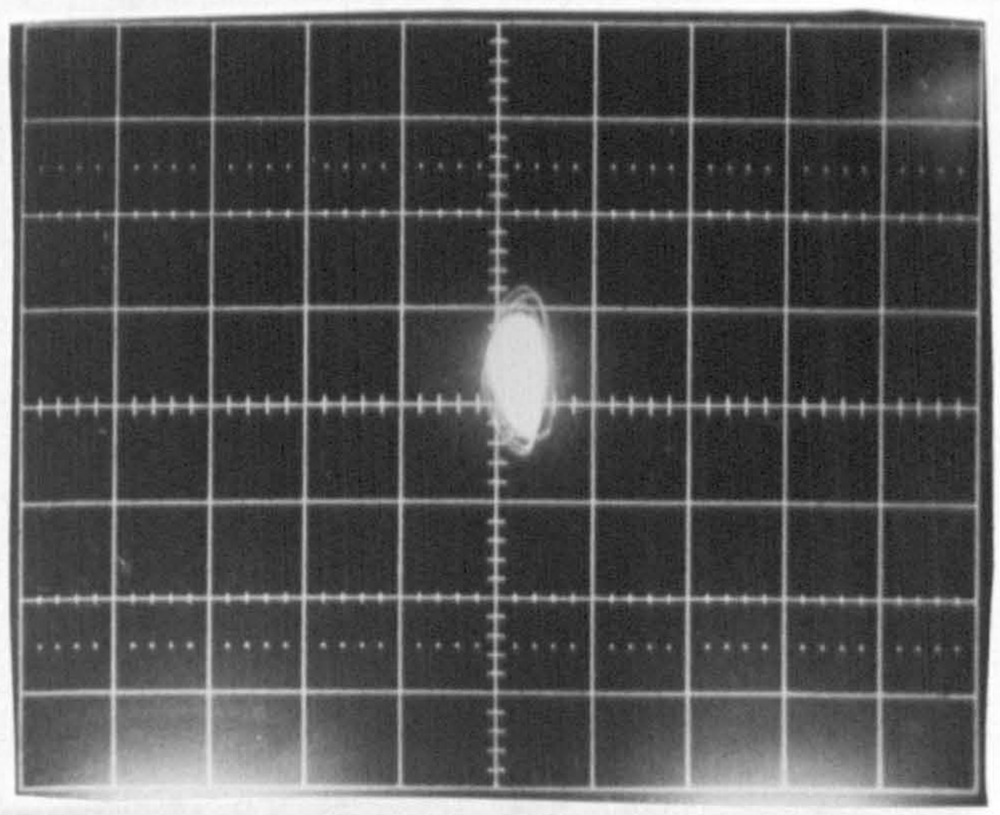

a) *Scale* 36.36 μm *per centimeter*

Load No load
Speed 1154 rpm

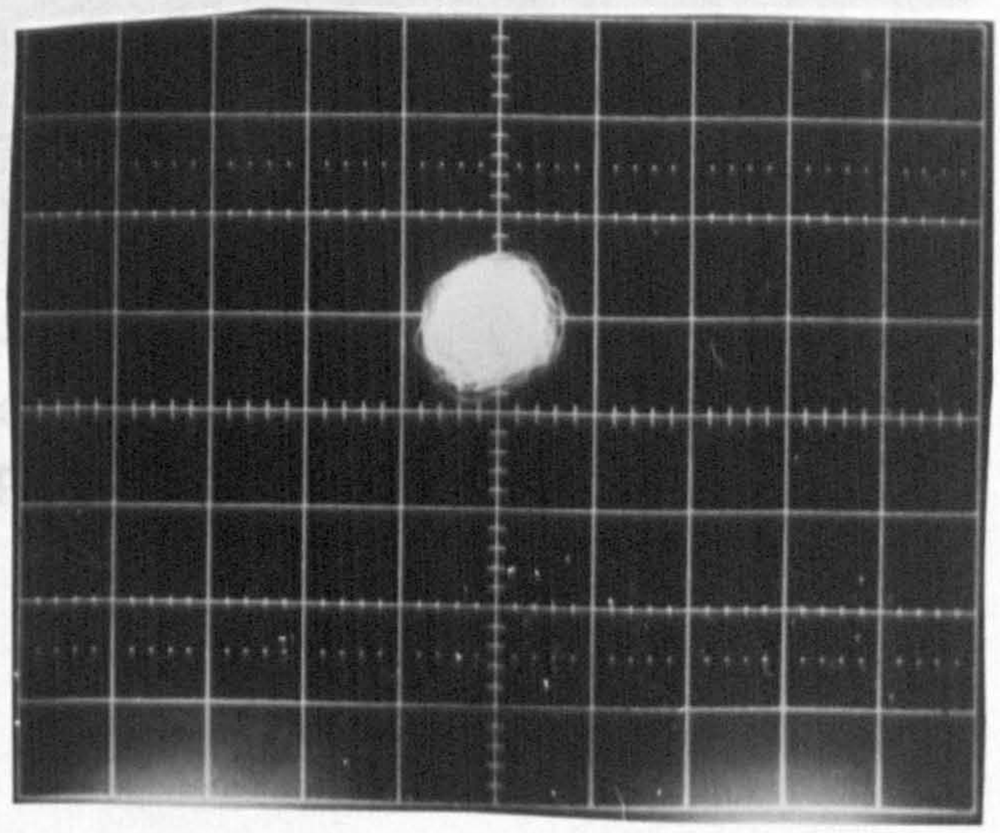

b) *Scale* 36.36 μm *per centimeter*

Load No load
Speed 3000 rpm

Figure 3.33 Orbit of partial helical groove bearing below threshold of instability

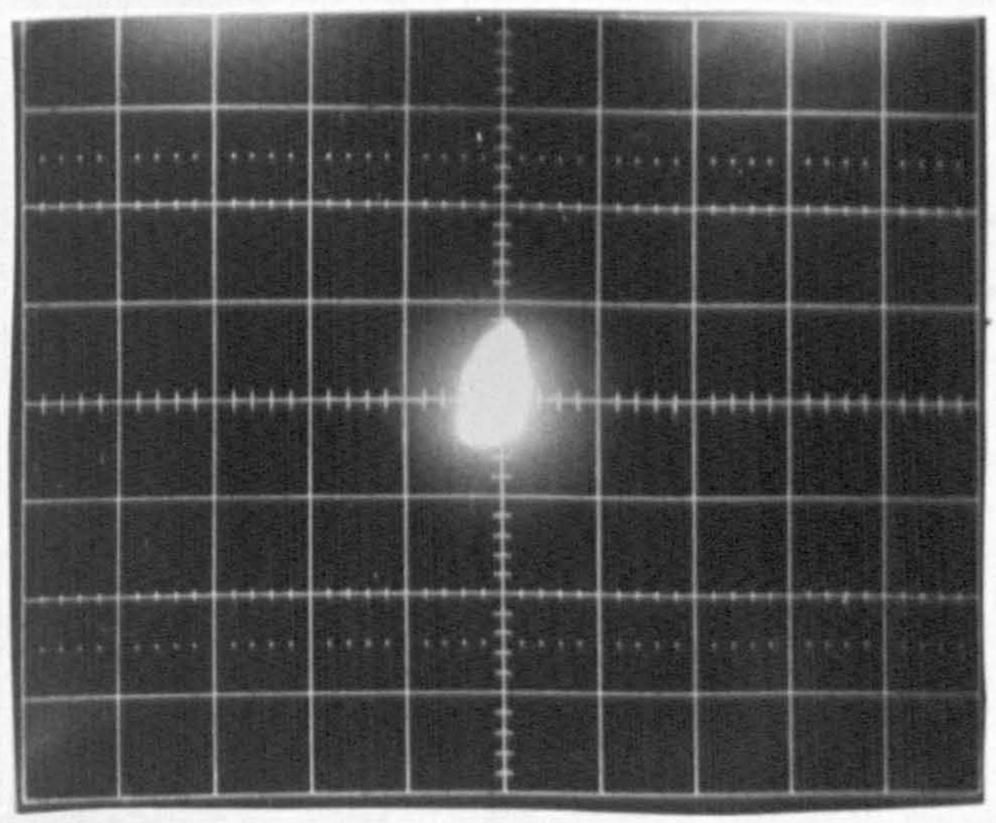

Scale 36.36 μm *per centimeter*

Load No load
Speed 3929 rpm

Figure 3.34 Orbit of partial helical groove bearing
below threshold of instability

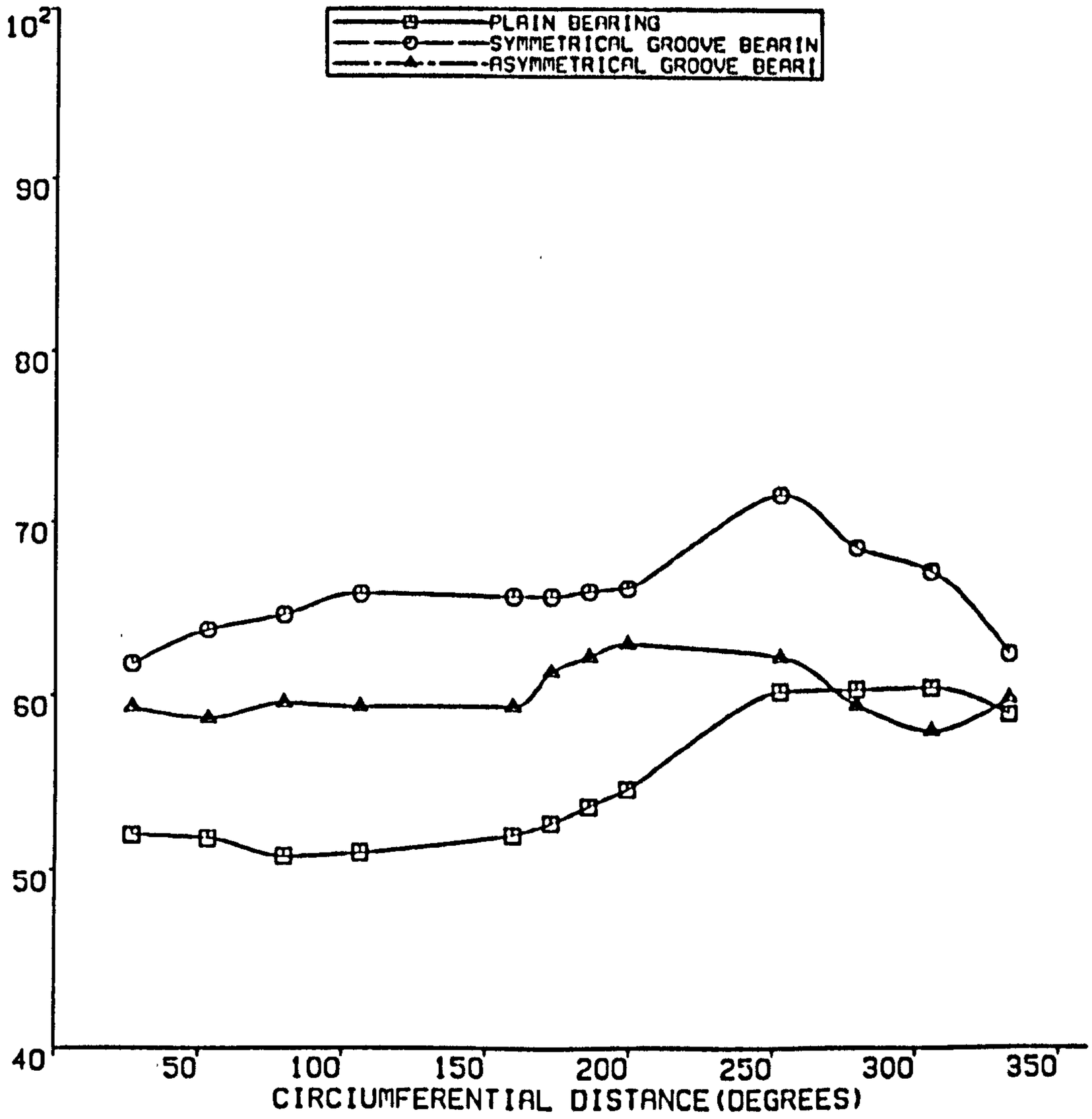

FIGURE 3.35 TEMPERATURE COMPARISION
AT LOAD 8896 N 3000 RPM

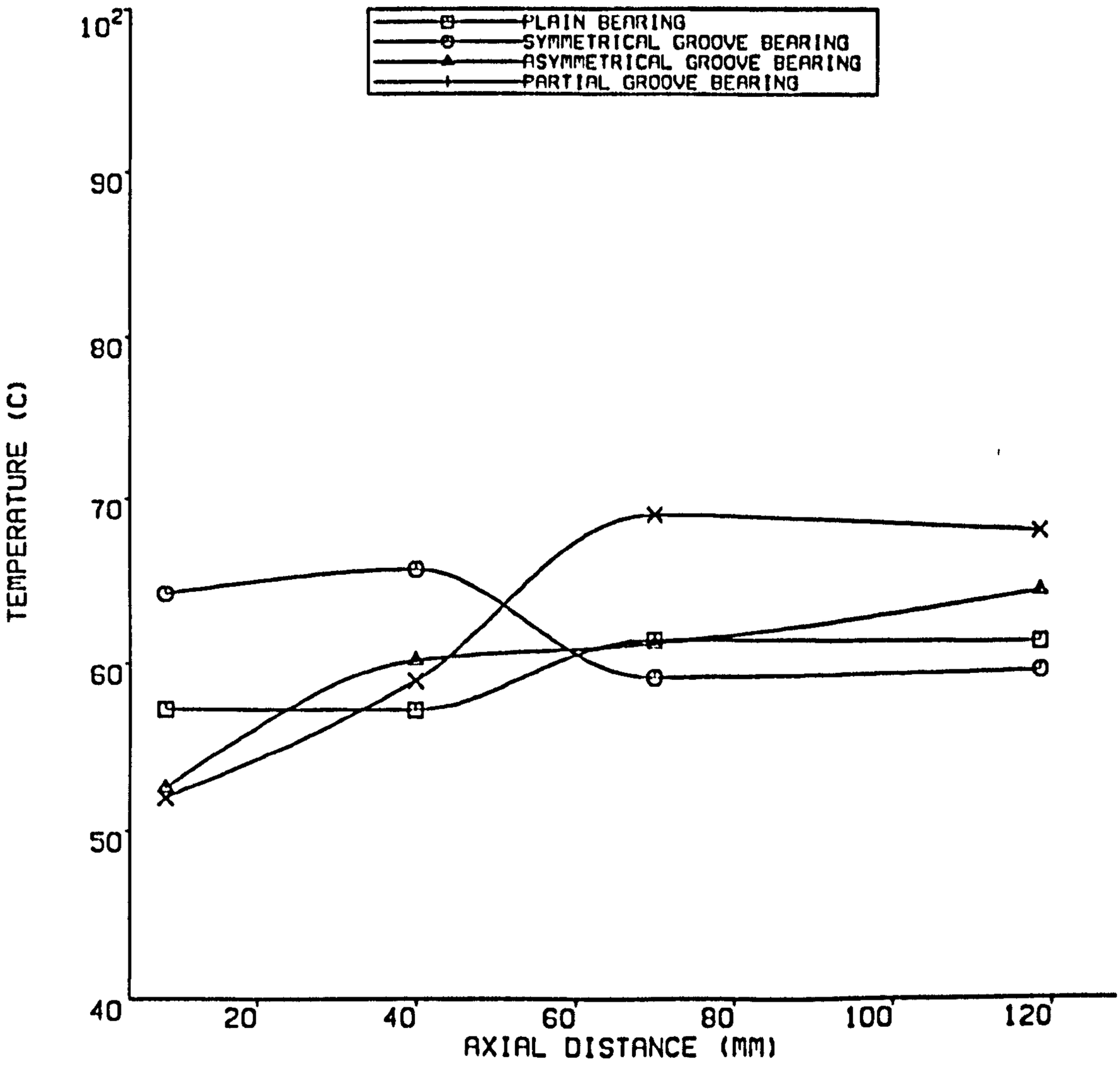

FIGURE 3.36 COMPARISON OF AXIAL VARIATION
OF TEMPERATURE
AT LOAD OF 8996 N 3000 rpm

PARTIAL BEARING PLOT IS WITHOUT LOAD

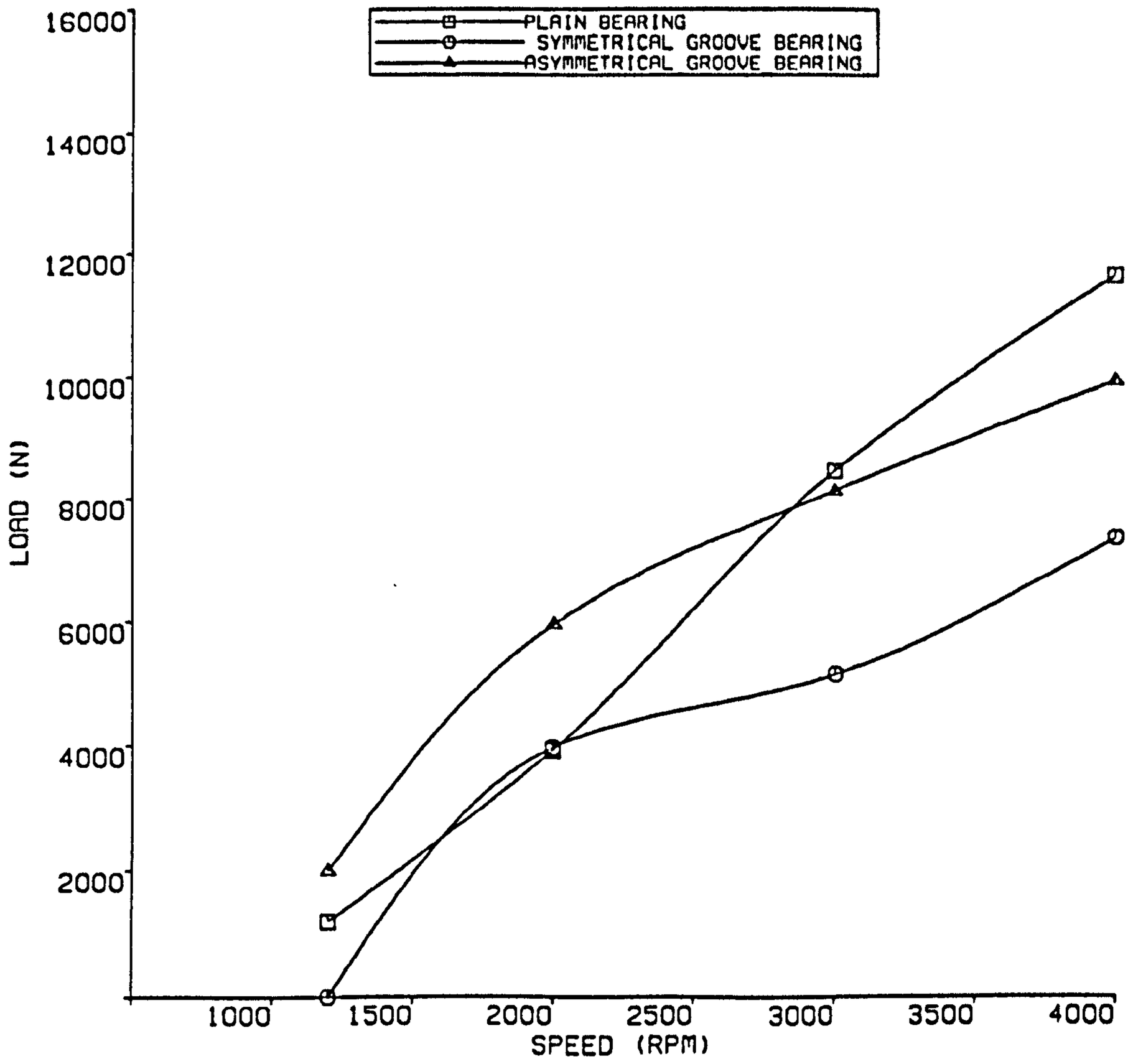

FIGURE 3.37 COMPARISON OF STABILITY EXPERIMENTAL RESULTS

CHAPTER 4

THEORETICAL MODEL

4.1 Introduction

As mentioned in chapter 1, a number of theoretical models for the helical groove journal bearing have been developed. Information about different types of helical groove bearing lubricated with air, water, grease, process fluid and oil is scattered in the literature. Some of the theoretical work found in the literature has not been validated.

In this work an approach similar to that of Bootsma [12] and Reinhoudt [16] has been adopted to produce a theoretical model of helical groove journal bearings. The model is validated with the results of other theoretical models presented in the literature. It is also validated against the experimental data presented in Chapter 3. In this chapter the results of the theoretical model are presented and discussed.

4.2 Governing Equations

4.2.1 Reynolds Equation

The pressure in the lubricating film between two bearing surfaces is governed by the Reynolds equation. The Reynolds equation in two dimensional form and in Cartesian coordinates, Figure 4.1, is given below [8,9,16].

$$\frac{\partial}{\partial X}\left(H^3\frac{\partial P}{\partial X}\right)+\frac{\partial}{\partial Z}\left(H^3\frac{\partial P}{\partial Z}\right)=6\mu U\frac{dH}{dX}+12\mu\frac{\partial H}{\partial t} \qquad (4.1)$$

Where , $\frac{\partial H}{\partial t}$ is the radial component of velocity of the journal centre.

The equation (4.1) is derived from the Navier Stokes equations and the flow continuity equation using the following assumptions:

1 The lubricant viscosity is constant through the film thickness.

2 Pressure is constant through the film thickness.

3 The curvature of the bearing surface is large in comparision to film thickness.

4 The lubricant is Newtonian.

5 There is no slip at the fluid solid interfaces.

6 Fluid inertia is neglected.

The flow rate per unit length in the circumferential and axial (figure 4.1) direction is given by the following expressions.

$$Q_x=-\frac{H^3}{12\mu}\frac{\partial P}{\partial X}+\frac{1}{2}U_xH$$

$$Q_z=-\frac{H^3}{12\mu}\frac{\partial P}{\partial Z}+\frac{1}{2}U_zH \qquad (4.2)$$

Continuity of flow demands that :

$$\frac{\partial Q_x}{\partial X} + \frac{\partial Q_z}{\partial Z} + \frac{\partial H}{\partial t} = 0 \qquad (4.3)$$

When Q_x and Q_z are presented in dimensionless form, equation (4.2) assumes the following form :

$$q_x = -h^3 \frac{\partial p}{\partial x} + \frac{1}{2} u_x h \qquad (4.4)$$

$$q_z = -h^3 \frac{\partial p}{\partial z} + \frac{1}{2} u_z h$$

i.e

$$\boldsymbol{q} = -h^3 \nabla p + \frac{1}{2} hu \qquad (4.5)$$

The dimensionless flow continuity equation can be written as :

$$\nabla . q + \frac{\partial h}{\partial T} = 0 \qquad (4.6)$$

i.e

$$\nabla . (h^3 \nabla p) - \frac{1}{2} (\nabla . (hu)) - \frac{\partial h}{\partial T} = 0 \qquad (4.7)$$

Equation (4.7) is the Reynolds equation in dimensionless form.

4.2.2 Generalized Reynolds Equation

4.2.2.1 The Geometry of the Helical Groove Journal Bearing

The detailed description of the helical groove journal bearing is given in Chapter 2. In order to provide a ready reference to the helical groove journal bearing an outline of its features is shown in Figure 4.2. The shallow grooves of rectangular shape are machined into the surface of the bush, and are inclined at angle α to the direction of rotation of the journal. These grooves are effective in only one direction of rotation. Due to the rotation of the shaft, pumping action is induced by the grooves and pressure is generated within the bearing. This pressure is governed by the generalised Reynolds equation, which is a modified form of the basic Reynolds equation (4.1). In order to take in to account of the helical groove configuration, an additional set of skew coordinates (R,S) is used as shown in Figure 4.1. The Reynolds equation (4.1) is then converted into (R,S) coordinates, (Appendix E). The dimensionless mass flow rate in the R and S direction is given by :

$$q_r = -(h_r+h_g)^3 \frac{\partial \overline{p}}{\partial r} + \frac{1}{2}(h_r+h_g)\, u_r \cos\alpha$$

$$q_s = -(h_r+h_g)^3 \frac{\partial \overline{p}}{\partial s} + \frac{1}{2}(h_r+h_g)\, u_s \sin\alpha \quad (4.8)$$

or

$$q_r = -h^3 \frac{\partial \overline{p}}{\partial r} + \frac{1}{2} h u_r \cos \alpha$$

$$q_s = -h^3 \frac{\partial \overline{p}}{\partial s} + \frac{1}{2} h u_s \sin \alpha \qquad (4.9)$$

where, $h = h_r + h_g$

where, $\overline{p}$ is a local pressure over a groove ridge pair

Continuity of flow requires that :

$$\frac{\partial q_r}{\partial r} + \frac{\partial q_s}{\partial s} + \frac{\partial h}{\partial T} = 0 \qquad (4.10)$$

The performance characteristics of helical groove journal bearings are usually determined with the help of the concept of a "smoothed pressure" distribution around the bearing which ignores the details of the local pressure profile arising from discontinuties in the geometry of the bearing surface.

The approximations and assumptions involved in this approach have been discussed in detail elsewhere [11,12,16]. Here, only the essential assumption required for the solution of equations (4.8) or (4.9) and (4.10) are presented.

$q_s =$ Constant

$q_r =$ Function (s)

$$\frac{\partial \overline{p}}{\partial s} = \text{Function (s)}$$

$$\frac{\partial \overline{p}}{\partial r} = \text{Constant} \qquad (4.11)$$

The mean pressure across a ridge and a groove at every point in the lubricating film is defined as

$$Mean\ pressure(p) = \frac{1}{b} \int_{s-\frac{b}{2}}^{s+\frac{b}{2}} \bar{p}\ ds \qquad (4.12)$$

Here b is the combined width of a groove and the ridge pair as illustrated in Figure 4.3. It is assumed that b is so small that the slope of the pressure remains linear over the groove and ridge pair and that the local pressure $\bar{p}$ can be replaced by what is known as a "smoothed pressure" p. The mean thickness of the film is defined in the same way :

$$I_J = \frac{1}{b} \int_{s-\frac{b}{2}}^{s+\frac{b}{2}} h\ ds \qquad (4.13)$$

On account of the grooves, both the pressure and film thickness vary mainly in the circumferential direction. In order to determine the smoothed pressure distribution in the lubricating film, equation (4.10) is integrated between (s-b/2) and (s+b/2) in the same way as equations (4.12) and (4.13) and it is written as

$$\frac{1}{b}\ [\frac{\partial}{\partial s} \int_{s-\frac{b}{2}}^{s+\frac{b}{2}} q_s ds + \frac{\partial}{\partial r} \int_{s-\frac{b}{2}}^{s+\frac{b}{2}} q_r ds + \int_{s-\frac{b}{2}}^{s+\frac{b}{2}} \frac{\partial h}{\partial t} ds] = 0 \qquad (4.14)$$

By integrating this equation and applying the assumptions and approximations of equations (4.12) and (4.13) to each of its terms, the following are obtained : The first term of equation (4.14) is

$$q_s = -\frac{1}{I_{-3}}\frac{\partial p}{\partial s} + \frac{I_{-2}}{I_{-3}}\frac{u_s}{2}\sin\alpha \qquad (4.15)$$

the second term is

$$q_r = -I_{+3}\frac{\partial p}{\partial r} + I_{+1}\frac{u_r}{2}\cos\alpha \qquad (4.16)$$

the last term is

$$\frac{\partial h}{\partial T}$$

Taking the above into account the generalised Reynolds equation in (R,S) coordinates and in dimensionless form can be written as

$$\frac{\partial}{\partial s}\left(-\frac{1}{I_{-3}}\frac{\partial p}{\partial s}+\frac{I_{-3}}{I_{-2}}\sin\alpha\right) + \frac{\partial}{\partial r}\left(-I_{+3}\frac{\partial p}{\partial r} + I_{+1}\cos\alpha\right) + \frac{\partial h}{\partial T} = 0 \qquad (4.17)$$

where I_{-3}, I_{+3}, I_{-2}, and I_1 are the integrals for a groove of rectangular shape as defined in reference [16] and are obtained from the integration of equation (4.13) and given in Appendix G. For computational purposes the equation (4.17) is converted into the Cartesian coordinates system see Appendix F. Continuity of flow demands that:

$$\frac{\partial q_x}{\partial x} + \frac{\partial q_z}{\partial z} + \frac{\partial h}{\partial T} = 0 \qquad (4.18)$$

Where

$$q_x = -A\frac{\partial p}{\partial x} - E\frac{\partial p}{\partial z} + \frac{1}{2}U_x G_1$$

$$q_z = -E\frac{\partial p}{\partial x} - F\frac{\partial p}{\partial z} + \frac{1}{2}U_z G_2 \qquad (4.19)$$

are A, E, F, G_1, and G_2 are dimensionless coefficients of the differential equation and are a function of the groove shape. The specific forms of these coefficients are given below .

$$A = \cos^2\alpha I_{+3} + \sin^2\alpha \frac{1}{I_{-3}}$$

$$F = \cos\alpha\sin\alpha\left(I_{+3} - \frac{1}{I_{-3}}\right)$$

$$E = \sin^2\alpha I_{+3} + \cos^2\alpha \frac{1}{I_{-3}}$$

$$G_1 = \cos^2\alpha I_{+1} + \sin^2\alpha \frac{I_{-2}}{I_{-3}}$$

$$G_2 = \sin\alpha\cos\alpha\left(I_{+1} - \frac{I_{-2}}{I_{-3}}\right) \qquad (4.20)$$

The matrix form of equations (4.19) is

$$q = \begin{bmatrix} q_x \\ q_z \end{bmatrix}$$

where

$$u = \begin{bmatrix} u_x \\ u_z \end{bmatrix}$$

$$C = [C] = \begin{bmatrix} A & E \\ E & F \end{bmatrix} \qquad (4.21)$$

$$B = [B] = \begin{bmatrix} G_1 & 0 \\ 0 & G_2 \end{bmatrix}$$

$$q = -C\nabla p + \frac{1}{2} BU \qquad (4.22)$$

From the continuity of flow

$$\nabla . q + \frac{\partial h}{\partial T} = 0$$

or

$$\nabla . (C\nabla p) - \frac{1}{2} \nabla . (BU) - \frac{\partial h}{\partial T} = 0 \qquad (4.23)$$

Equation 4.23 is the generalised Reynolds equation for a helical journal bearing.

The boundary conditions for a helical groove journal bearing are :-

(i) The pressure at the ends of the bearing is taken to be zero.

(ii) For cavitation, Reynolds boundary conditions are used as suggested by Vohr and Chow [32].

4.3 Approximate Technique used to Solve the Generalised Reynolds Equation.

The most commonly used approximate numerical method to solve the Reynolds equation for a journal bearing is the finite difference method. However,

the finite difference method becomes difficult to use in the analysis of a journal bearing in which sudden changes in the film thickness occur, as is the case of a helical groove bearing. Abrupt changes in film thickness are however, easily handled by the finite element method. It was therefore decided to apply the finite method to solve the generalised Reynolds equation (4.23), and hence calculate the steady state and dynamic properties of the various configurations of helical groove bearing.

The finite element method cannot be implemented directly to solve the generalised Reynolds equation in the form given by equation (4.23). However, by using variational calculus an equivalent functional equation can be generated which can then be used in the finite element method. The functional equation derived in this way [16] has the form :

$$J(P) = -\iint_A \left(C\nabla p.\nabla p - \frac{1}{2}(BU).\nabla p + \frac{\partial h}{\partial T}P \right) dA$$

$$-\int_R \left(-C\nabla p + \frac{1}{2}(BU).n \right) dR \qquad (4.24)$$

The bearing area is A, over which the integral is calculated with prescribed boundary conditions on its boundary R. Here **n** is the unit outward normal vector on the boundary R. If the pressure boundary conditions are specified at the ends of the bearing then the second part of the above integral equation vanishes.

An assumption of the analysis, based on the smoothed pressure concept is that the distance between the grooves are small and the pressure in the lubricating film remains linear over a groove and ridge pair. This assumpion can be restated i.e, the integral area of the lubricating film can be subdivided into small regions in

which the pressure variation remains linear and the boundaries of the subregions need not necessarily lie on a groove boundary [15].

In the finite element method, the integral area is subdivided into small sub regions. These subregions can be of different shape, for instance quadrilateral or triangular elements. A triangular element is shown in Figure 4.4.

The theory of the finite element method [42] assumes that the pressure in every element can be described in terms of the pressure at the nodes of the element, Figure 4.4. Assuming the pressure to vary linearly within the element the following equation can be written for a tringular element :

$$p(X,Z) = \alpha_1 + \alpha_2 X + \alpha_3 Z \qquad (4.25)$$

$$P_I = \alpha_1 + \alpha_2 X_I + \alpha_3 Z_I$$

$$P_J = \alpha_1 + \alpha_2 X_J + \alpha_3 Z_J$$

$$P_K = \alpha_1 + \alpha_2 X_K + \alpha_3 Z_K \qquad (4.26)$$

The above equations can be solved for $\alpha_1, \alpha_2, \alpha_3$ and these values can be subsituted in equation (4.25).

Taking into account the coordinates of the nodes equation (4.25) can be written

$$p(X,Z) = \frac{(a_I+b_I X+c_I Z)\,p_I}{2A_e} + \frac{(a_J+b_J X+c_J Z)\,p_J}{2A_e} + \frac{(a_k+b_k X+c_k Z)\,p_k}{2A_e} \qquad (4.27)$$

In term of the interpolation function [42] equation (4.27) can have the form:

$$p(X, Z) = N_I\, p_I + N_J\, p_J + N_K\, p_K \qquad (4.28)$$

$$[p] = [N_I\ N_J\ N_K] \begin{bmatrix} p_I \\ p_J \\ p_K \end{bmatrix}$$

$$[p] = [N]\ \{P\} \qquad (4.29$$

In equation (4.27) a_I , b_I and c_I denotes the abbreviations for the coordinates values like

$$a_I = (X_J\, Z_K - X_K\, Z_J)$$

$$b_I = (Z_J - Z_K)$$

$$c_I = (X_K - X_J)$$

The other coefficients are obtained from the cyclic permutation of the subscripts.

From equation (4.27) it is possible to calculate the pressure differential ∇p of equation (4.24) and introduce it in equation (4.24). Thus,

$$\frac{\partial p}{\partial x} = \frac{1}{2Ae}\ [b_I\ b_J\ b_K] \begin{bmatrix} p_I \\ p_J \\ p_K \end{bmatrix}$$

$$\frac{\partial p}{\partial z} = \frac{1}{2Ae}\ [c_I\ c_J\ c_K] \begin{bmatrix} p_I \\ p_J \\ p_K \end{bmatrix} \qquad (4.30)$$

This can be written as

$$J(p) = \iint_{Ae} \left(\frac{1}{2} \{p\}^T [K]^T [c] [K] \{p\} - \frac{1}{2} [U]^T [B] [K] \{p\}^T + \frac{\partial h}{\partial t} [N^T] \{p\}^T \right) dA$$

$$J(P) = \{P\}^T ([k] \{p\} - \{k_u\} + \{k_s\}) \qquad (4.31)$$

where

$$[k_p] = \iint_{Ae} [k]^T [c] [k] \, dA$$

$$\{k_u\}^T = \iint_{Ae} [u]^T [B] [k] \, dA$$

$$\{k_s\}^T = \iint_{Ae} \frac{\partial h}{\partial t} [N]^T dA$$

In the finite element method equation (4.31) has to be minimized with respect to each nodal pressure p_I, p_J, p_K. After the minimization of the functional the equation for an element can be produced in the following form:

$$[k_p] \{p\} - \{k_u\} + \{k_s\} = 0 \qquad (4.32)$$

The system of linear equations (4.32) consists of the same number of equations as there are nodes of the finite elements into which the bearing surface has been divided. These are solved iteratively or directly in order to find the pressure at each node.

4.4 Bearing Characteristics

4.4.1 Steady State Characteristics

It follows from the generalised Reynolds equation (4.23), that the pressure p in the lubricating film depends upon, viscosity, speed, film thickness and its time derivative and the boundary conditions. The expression for the film thickness in the fixed Cartesian system of coordinates can be written as [52]:

$$H = C - EX\cos\theta - EY\sin\theta \tag{4.33}$$

and in dimensionless form as:

$$h = 1 - ex\cos\theta - ey\sin\theta \tag{4.34}$$

If the groove angle α and the groove depth for the helical groove bearing are equated to zero, then equation (4.34) describes the film thickness of a plain journal bearing. For the helical groove journal bearing this film thickness is taken as that at the ridge and is used to calculate the integrals I_{-3}, I_{+3} I_{-2}, and I_{+1}, Appendix E. The time derivative of the film thickness is the radial velocity of the journal centre. The expression for the radial velocity of the journal used in the computer programme is given as [52]:

$$V_o = -\dot{e}x\cos\theta - \dot{e}y\sin\theta \tag{4.35}$$

Where $\dot{e}x$ and $\dot{e}y$ are the velocities of the journal centre in the respective directions.

4.4.2 Bearing Load Calculation

The pressure distribution in the lubricating film was determined by the finite element method. The components of oil film forces along the x and y axis are given as :

$$f_x = \int_0^L \int_0^{2\pi} p \cos\theta \, R d\theta dz$$
$$f_y = \int_0^L \int_0^{2\pi} p \sin\theta \, R d\theta dz \qquad (4.36)$$

The dimensionless bearing load is calculated from the forces components i.e

$$f = \sqrt{(f_x)^2 + (f_y)^2} \qquad (4.37)$$

and the attitude angle is calculated as :

$$\phi = \tan^{-1}(f_y / f_x) \qquad (4.38)$$

4.4.3 Stiffness and Damping Characteristics

In the case of a rotor running in fluid film journal bearings, the components of the bearing reaction forces f_x and f_y are functions of the rotor equilibrium position. If it is assumed that the rotor is displaced from its equilibrium position without being misaligned, then the changes in fluid film forces due to small changes in displacement and velocity can be represented by equivalent stiffness and damping coefficients [44,45,46]. The expressions relating the forces, displacements and velocities in of term of linearized coefficient are :

$$\Delta F_x = -A_{xx}X - A_{xy}Y - B_{xx}\dot{X} - B_{xy}\dot{Y}$$
$$\Delta F_y = -A_{xx}X - A_{yy}Y - B_{yx}\dot{X} - B_{yy}\dot{Y} \qquad (4.39)$$

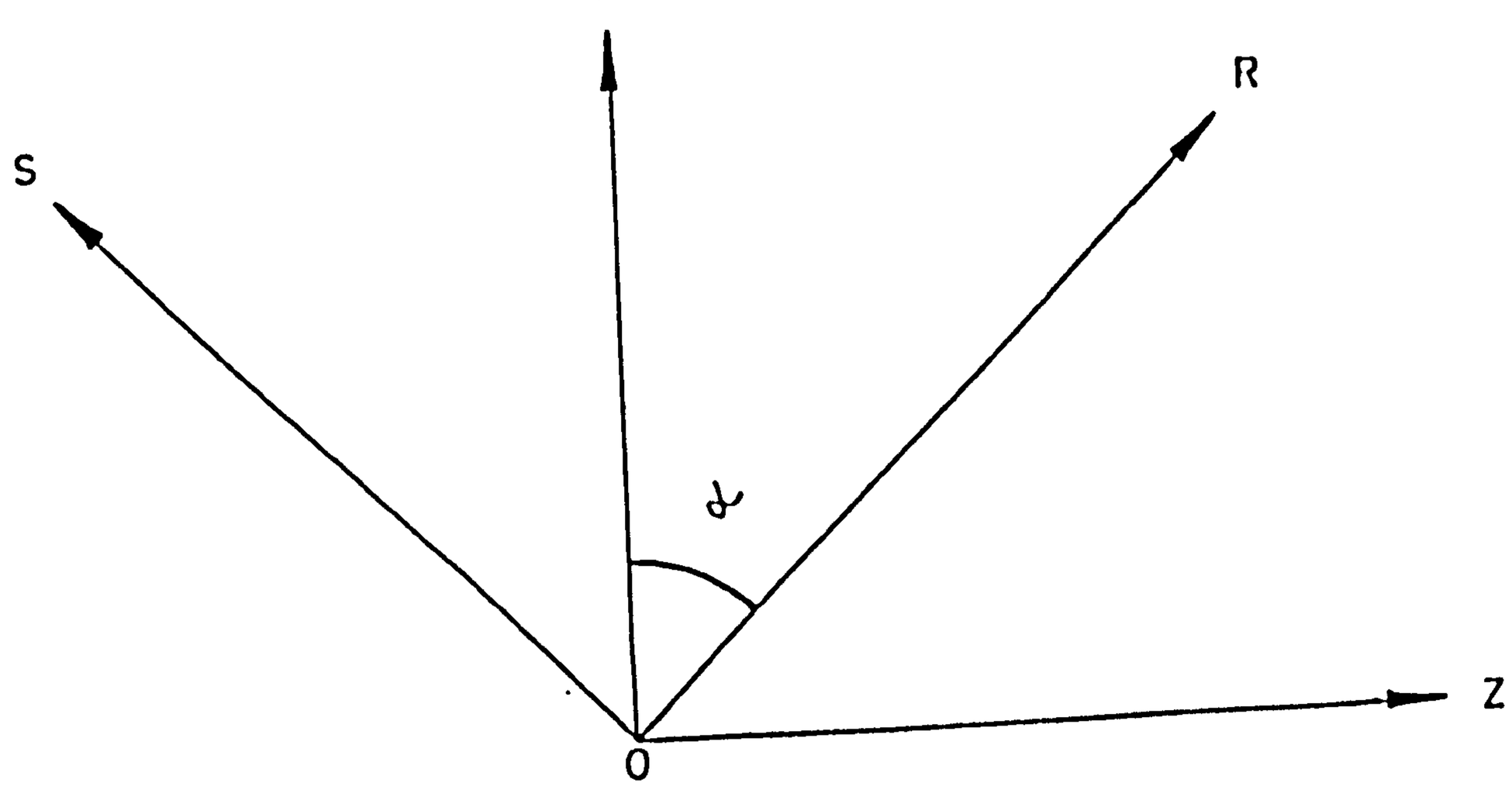

Figure 4.1
R Coordinates in the direction of the groove
X Circumferential coordinates
Z Axial coordinates
S Coordinates perpendicular to the direction of groove

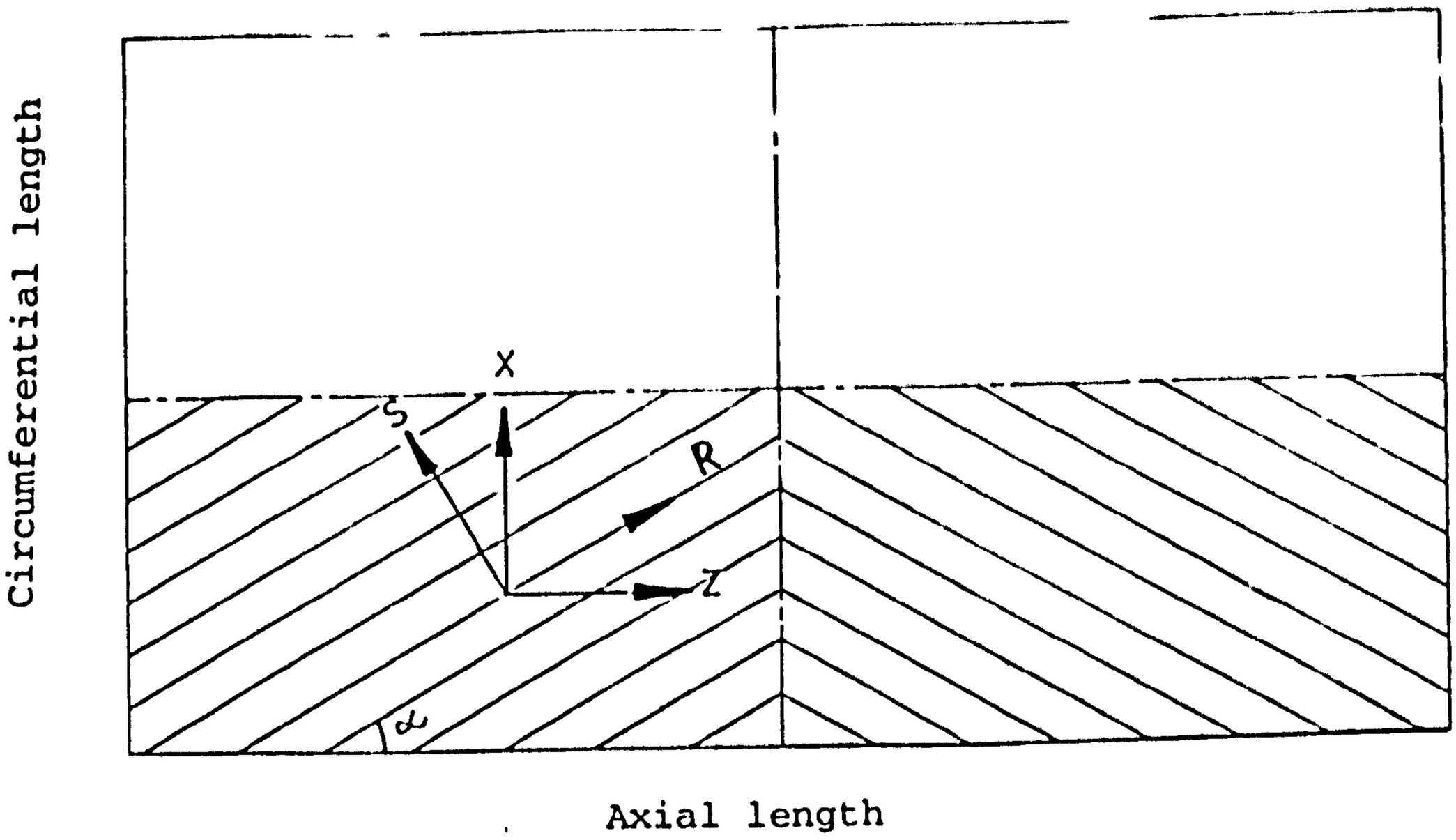

Figure 4.2 Schematic diagram of helical groove journal bearing

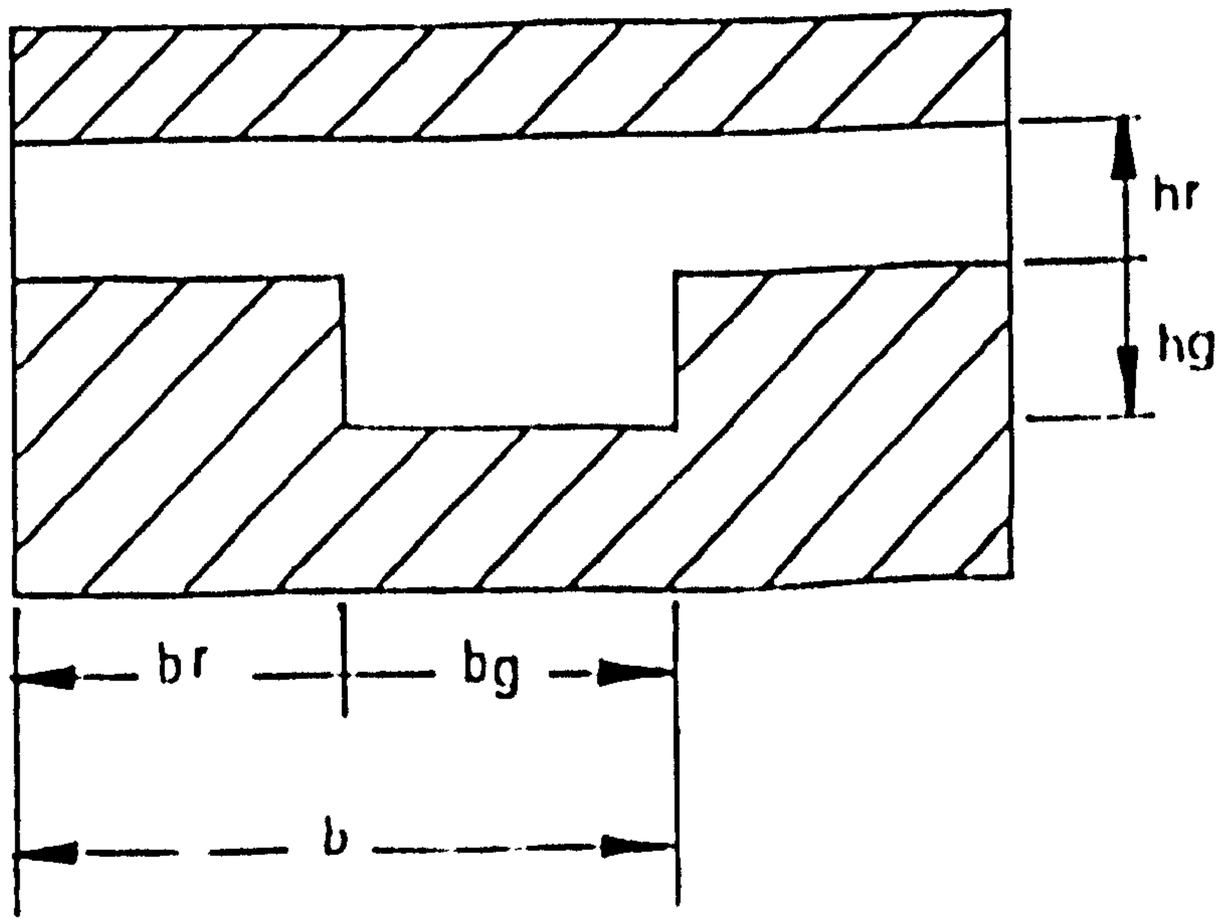

Figure 4.3 Geometry of a groove ridge pair

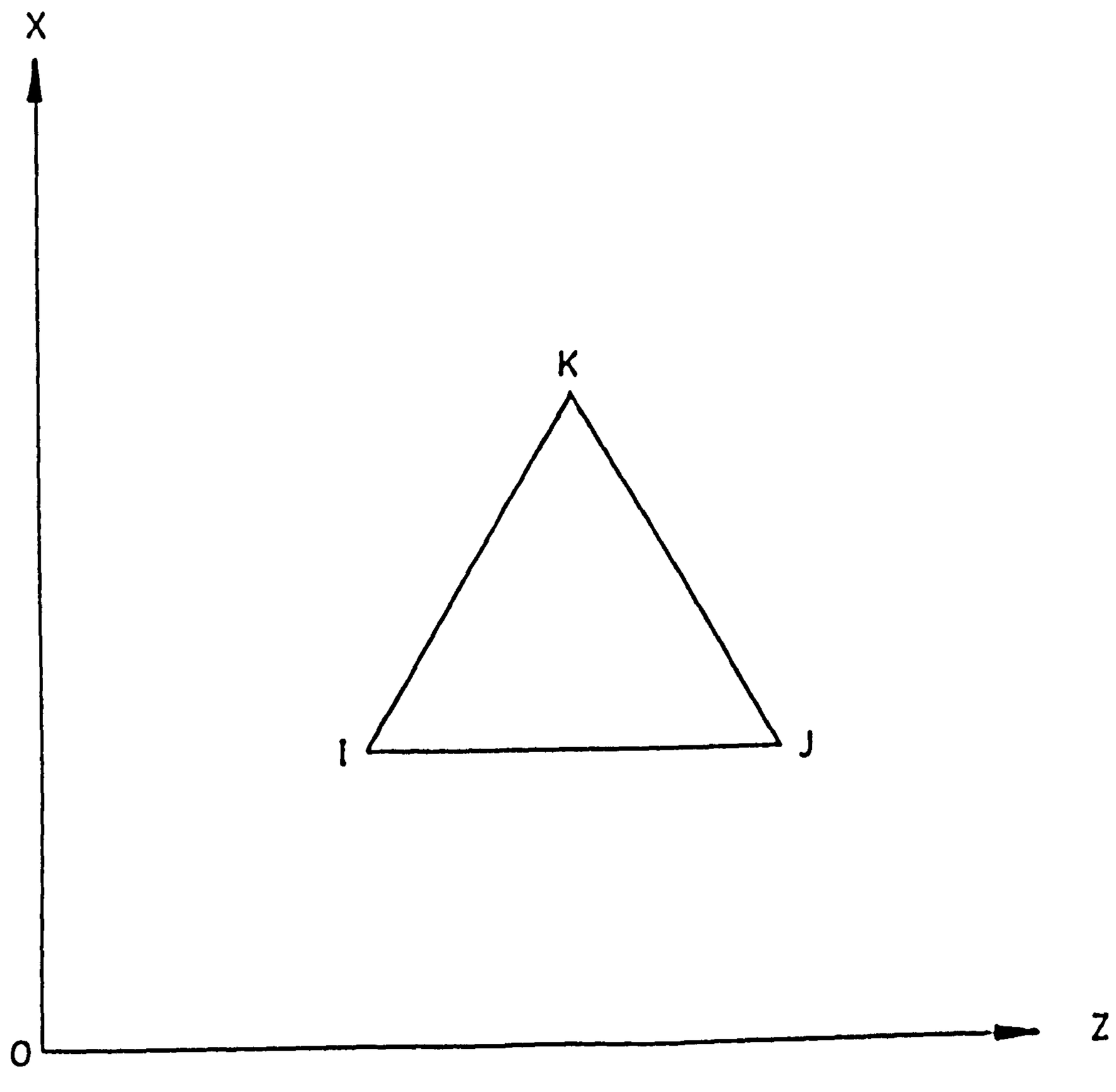

Figure 4.4 Linear triangular element ,I,J,K are the local labelling of the nodes

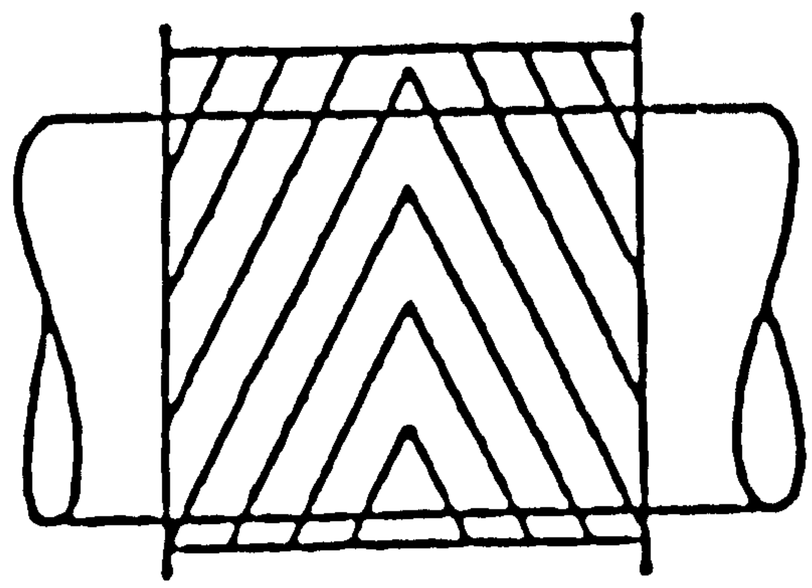

a)

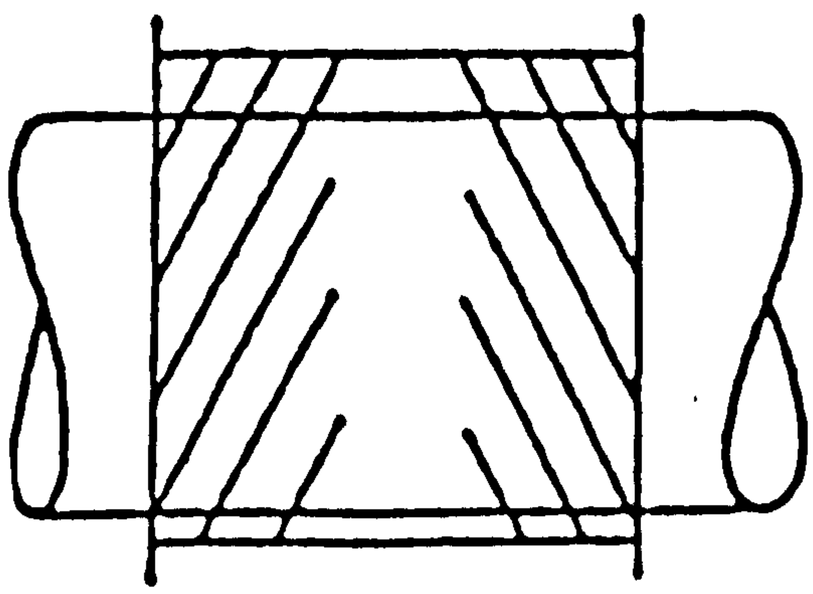

b)

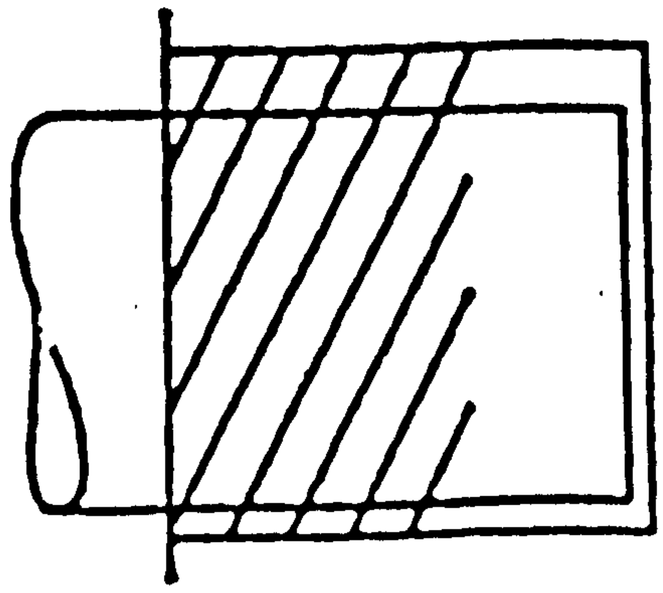

c)

Figure 4.5 (a) Symmetrical helical groove journal bearing (b) Symmetrical bearing with plain middle portion (c) Partial helical groove journal bearing (d See figure 2.12, asymmetrical helical groove bearing.

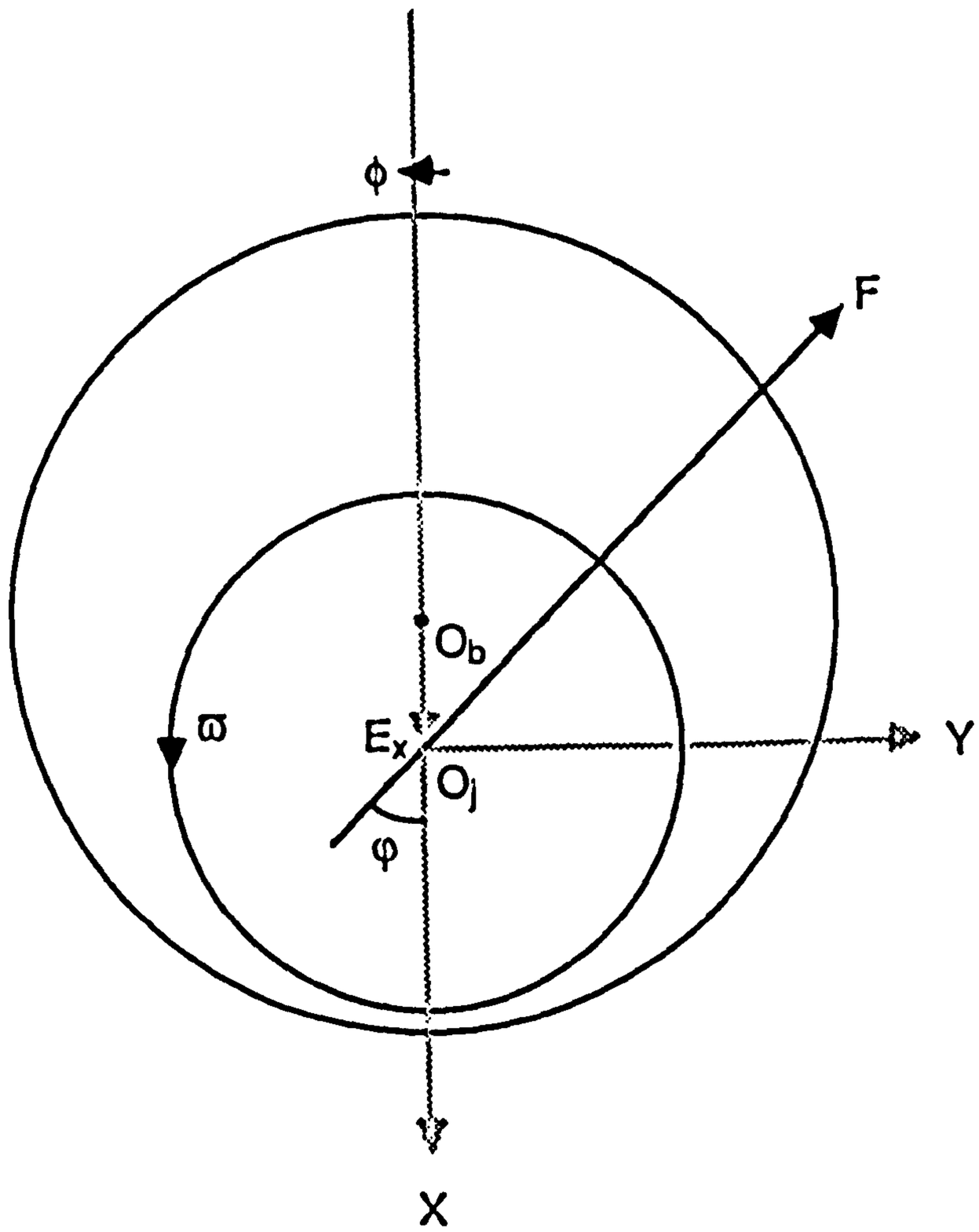

Figure 4.6 Illustration of the displacenment Ex of the journal centre from the centre of the bearing.

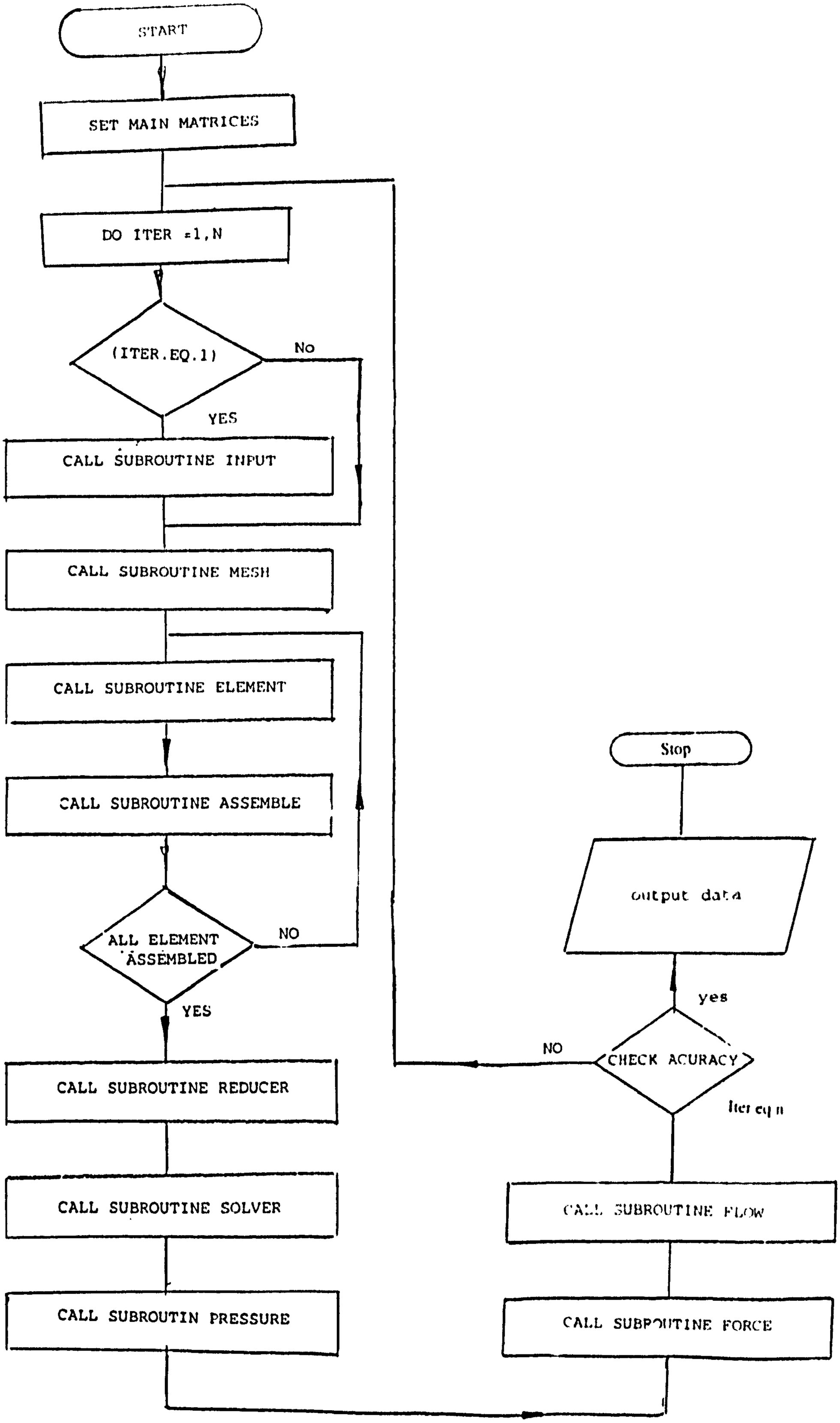

Figure 4.7a Steady state program flow chart (i)

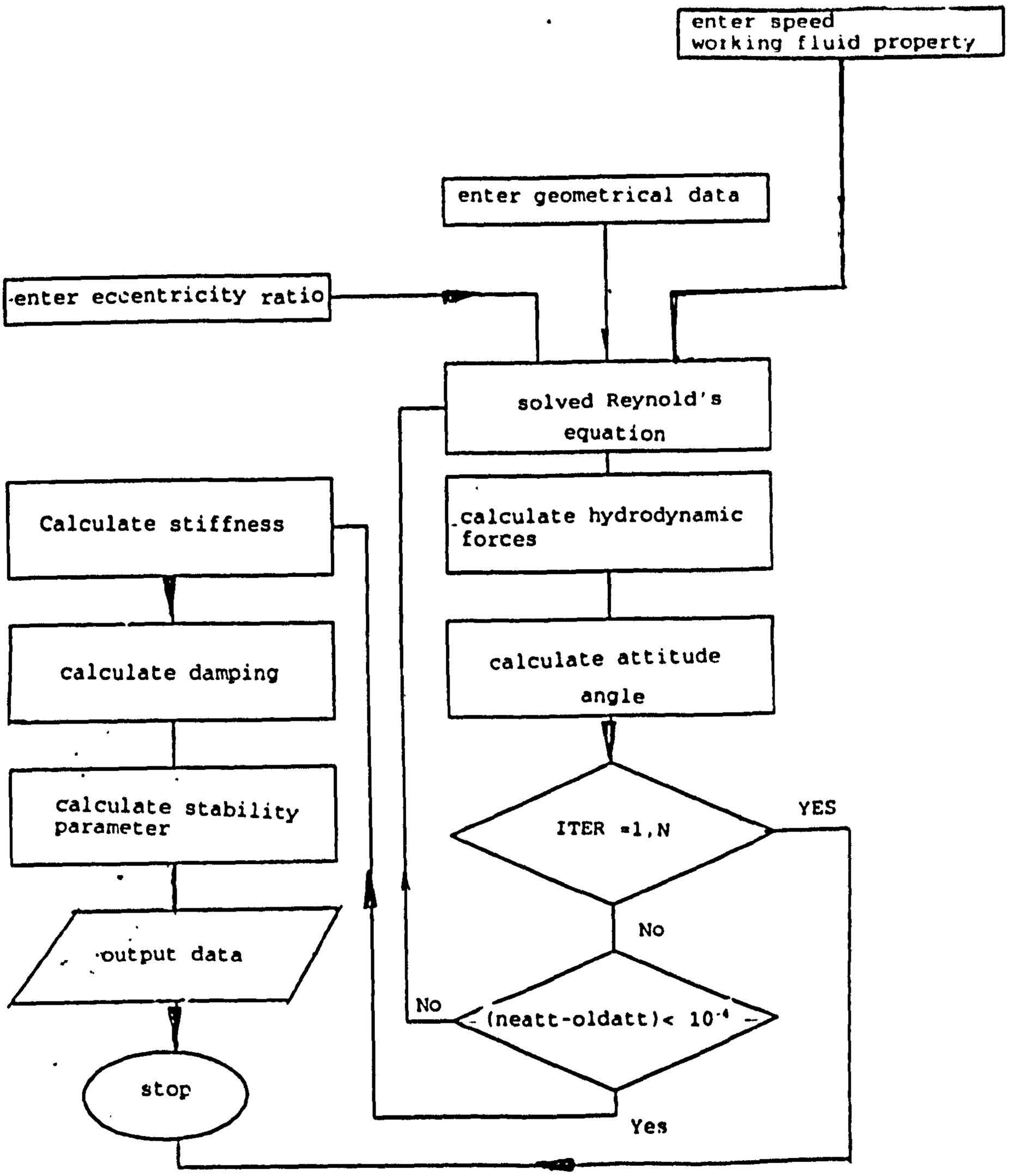

Figure 4.7a Dynamic Program flow chart (ii)

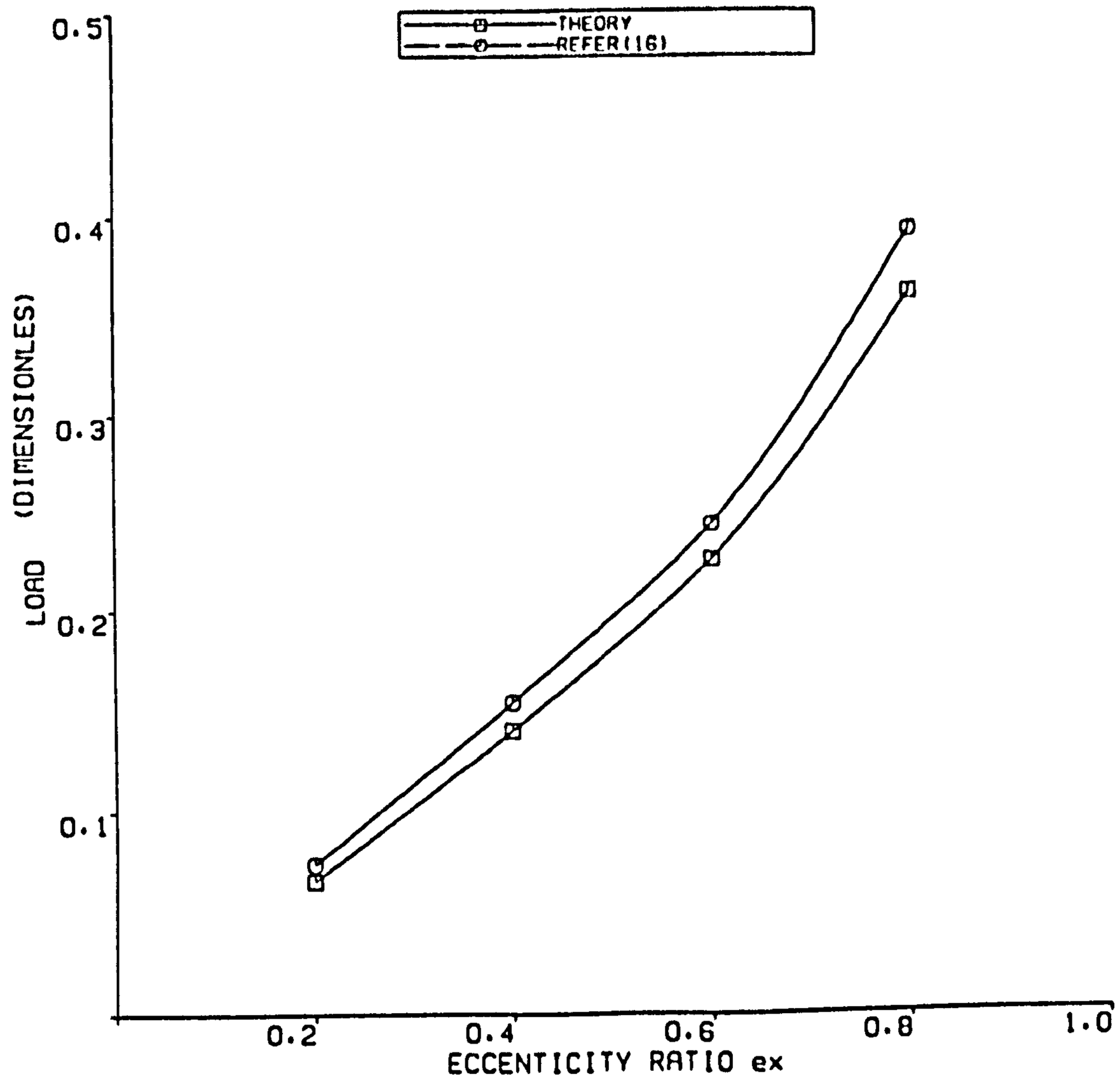

FIGURE 4.7 COMPARISON OF LOAD CAPACITY
WITH REINHOUDT(16)
HELICAL GROOVE JOURNAL BEARING L/D=1

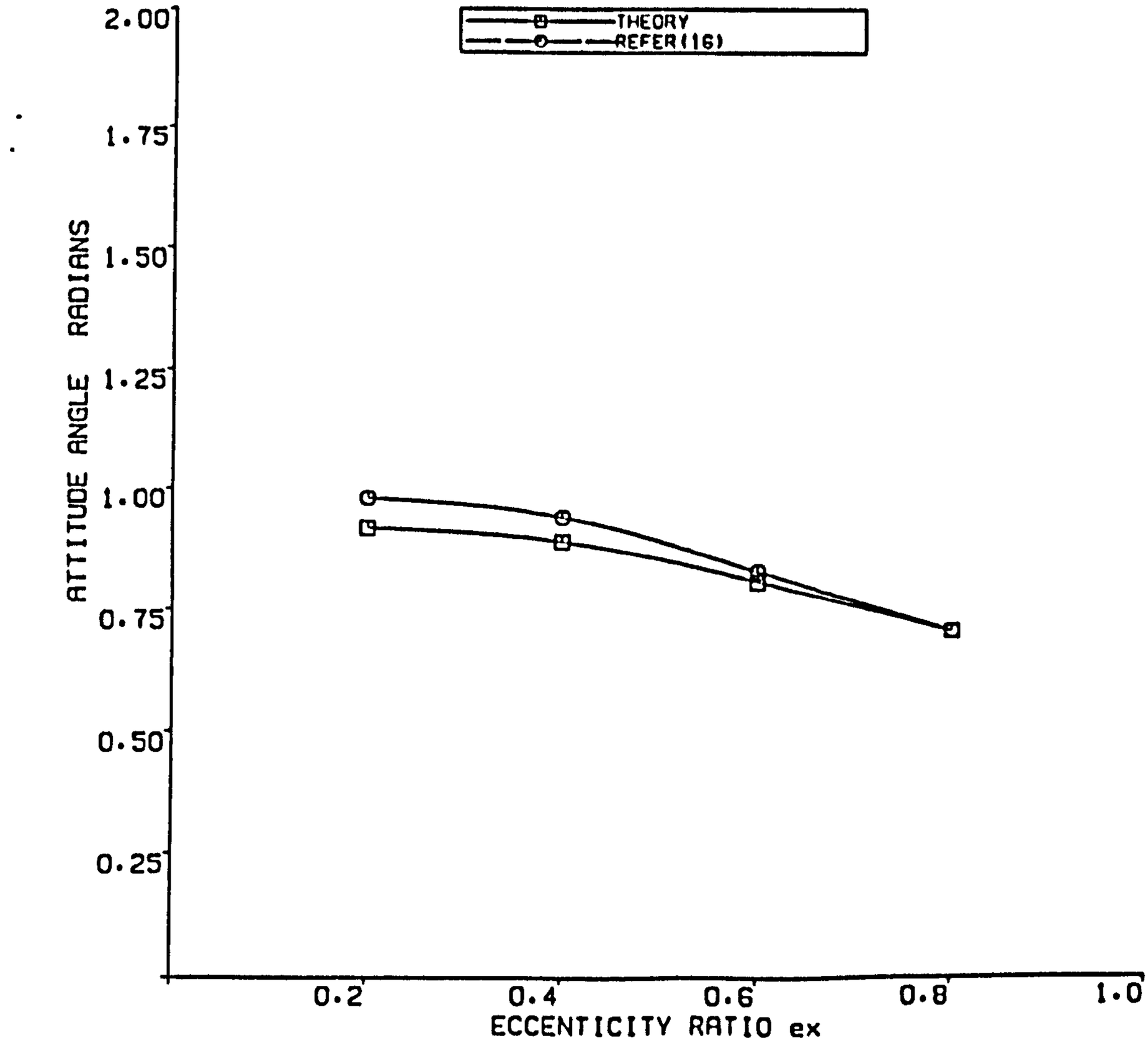

FIGURE 4.8 COMPARISON OF ATTITUDE ANGLE
WITH REINHOUDT(16)
HELICAL GROOVE JOURNAL BEARING L/D=1

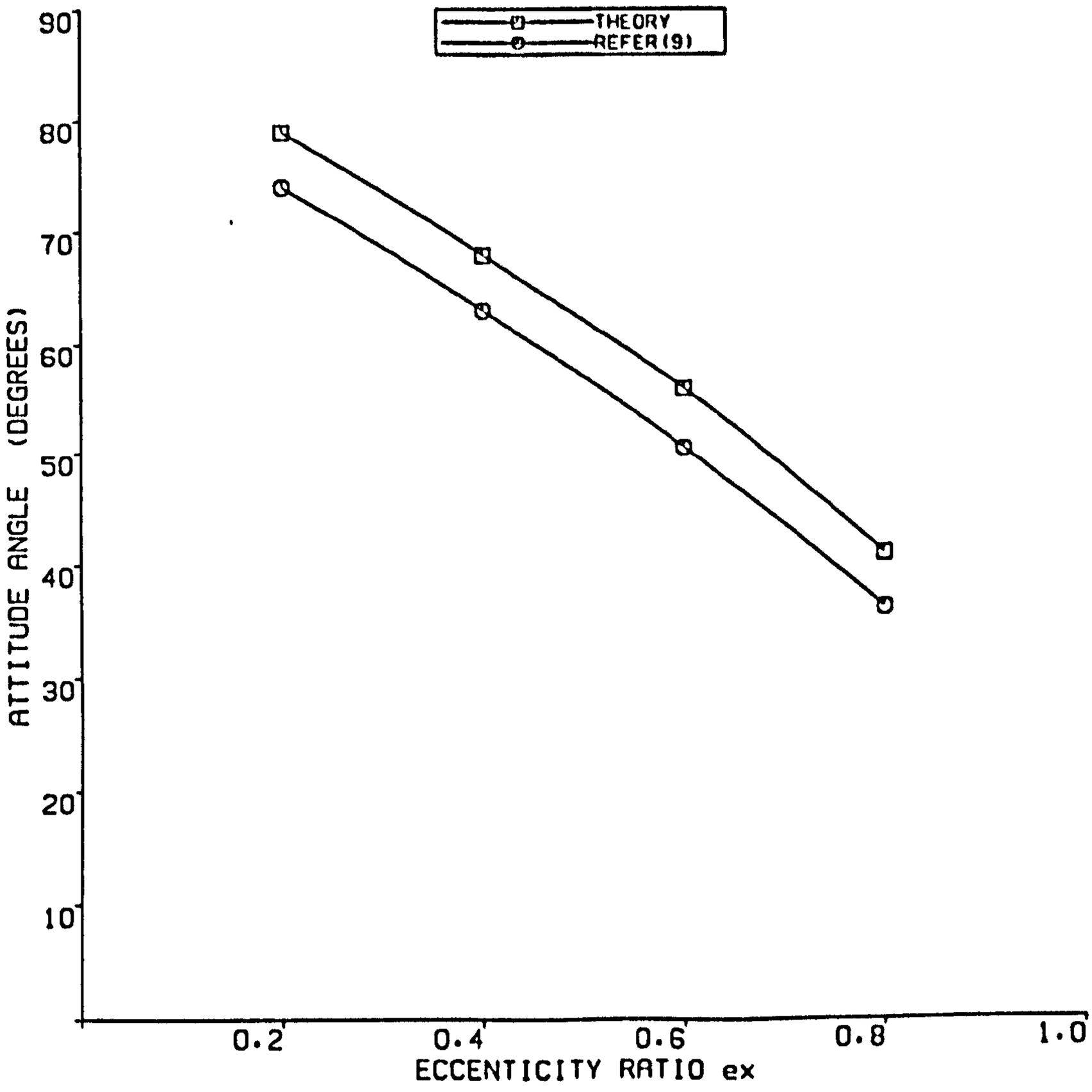

FIGURE 4.8a COMPARISON OF ATTITUDE ANGLE
PLAIN JOURNAL BEARING L/D=1
WITH CAMERON (9)

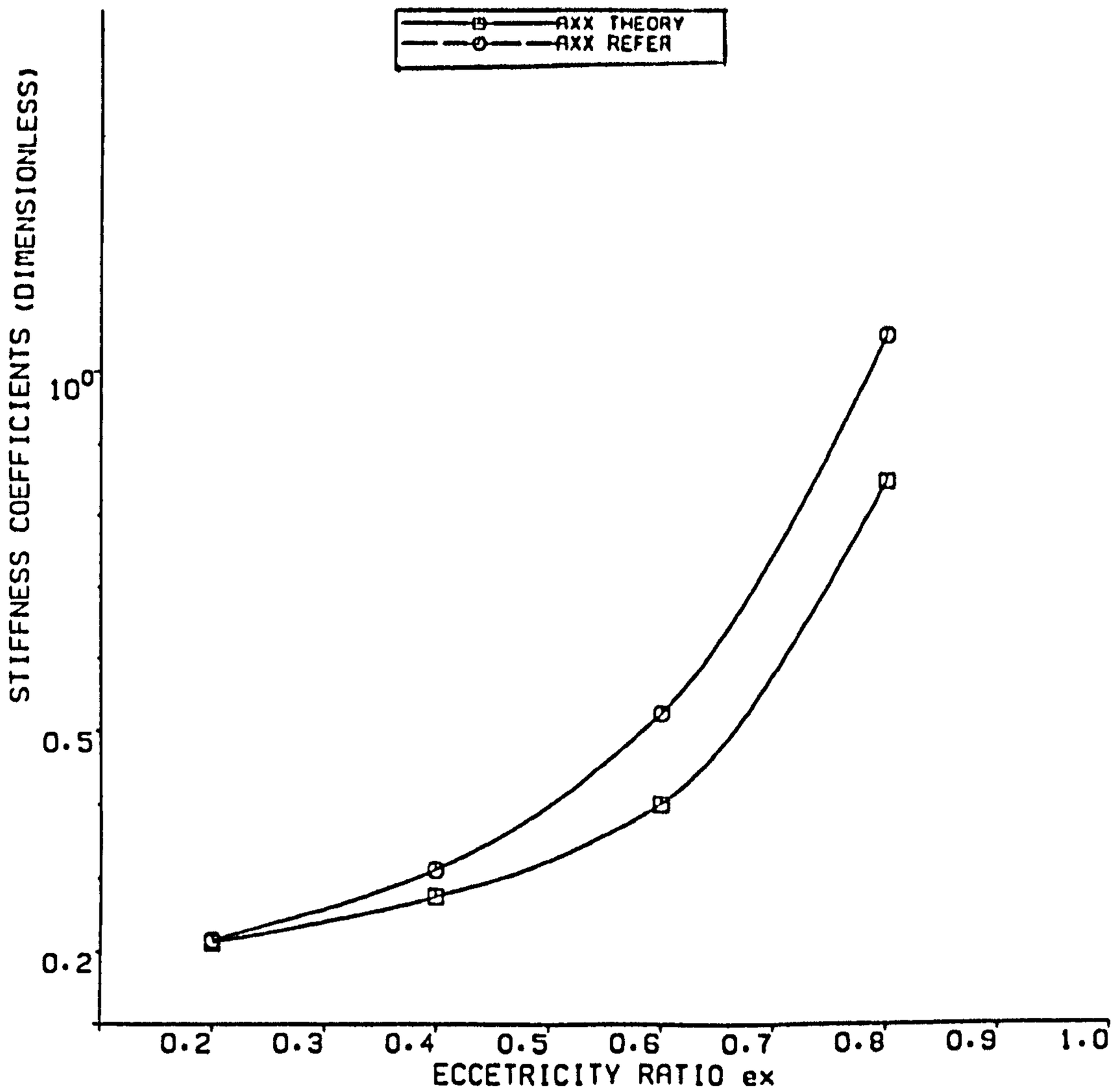

FIGURE 4.9a COMPARISON OF STIFFNESS COEFFICIENTS WITH REINHOUD(16) HELICAL GROOVED JOURNAL BEARING L/D=1

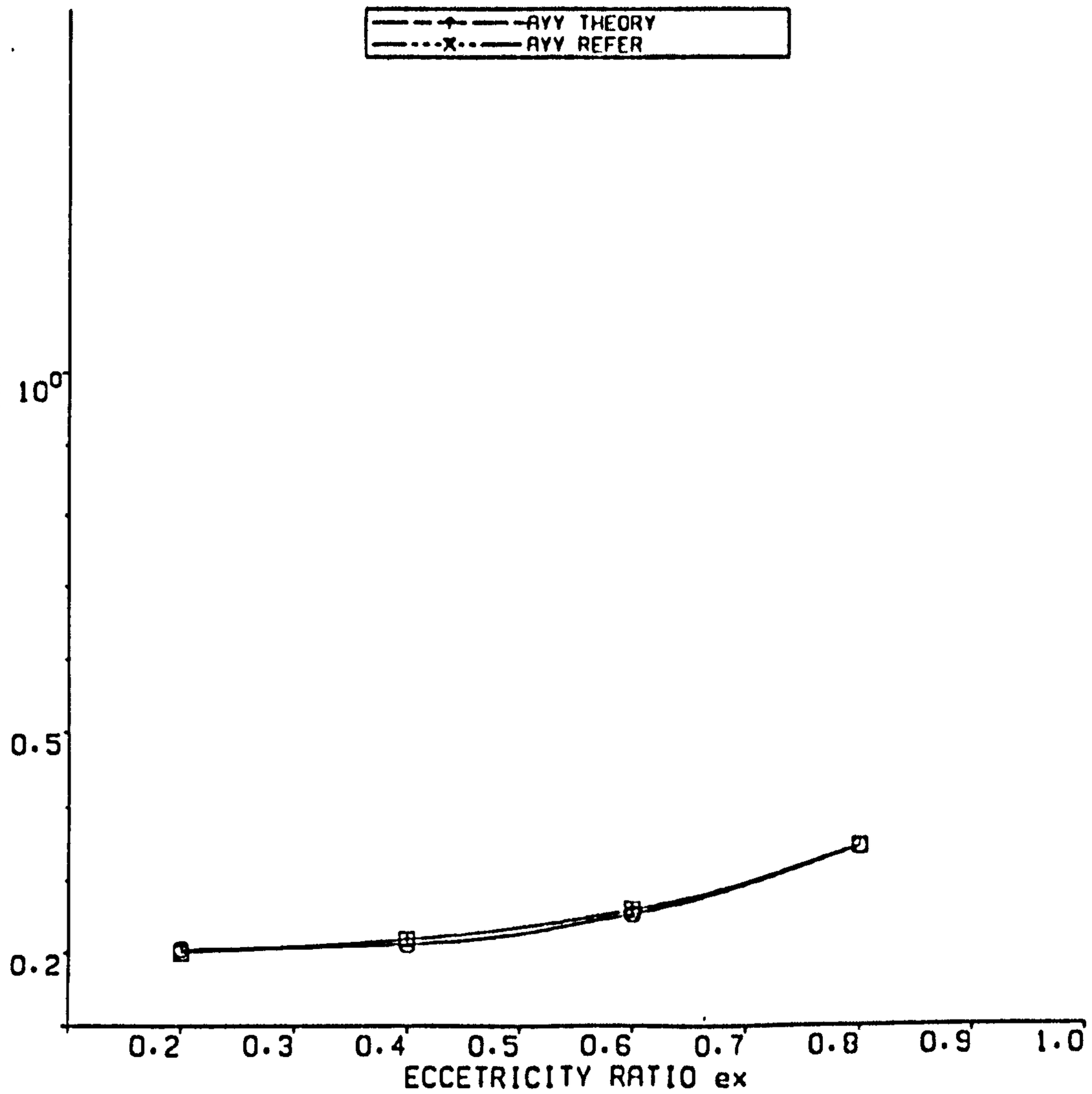

FIGURE 4.9b COMPARION OF STIFFNESS
COEFFICIENTS WITH REINHOUDT(16)
HELICAL GROOVED JOURNAL BEARING L/D=1

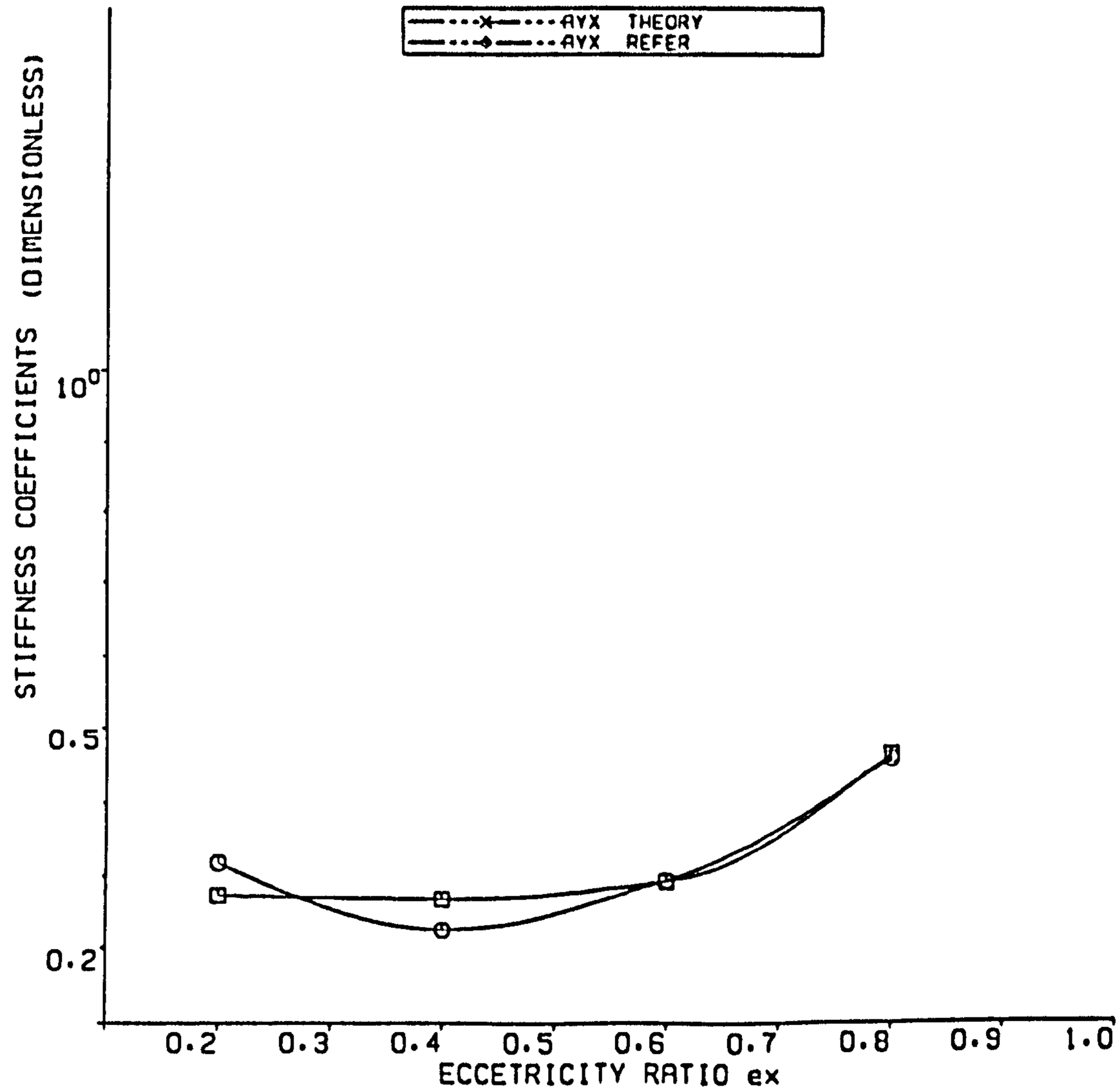

FIGURE 4.9C COMPARION OF STIFFNESS COEFFICIENTS WITH REINHOUDT(16) HELICAL GROOVED JOURNAL BEARING L/D=1

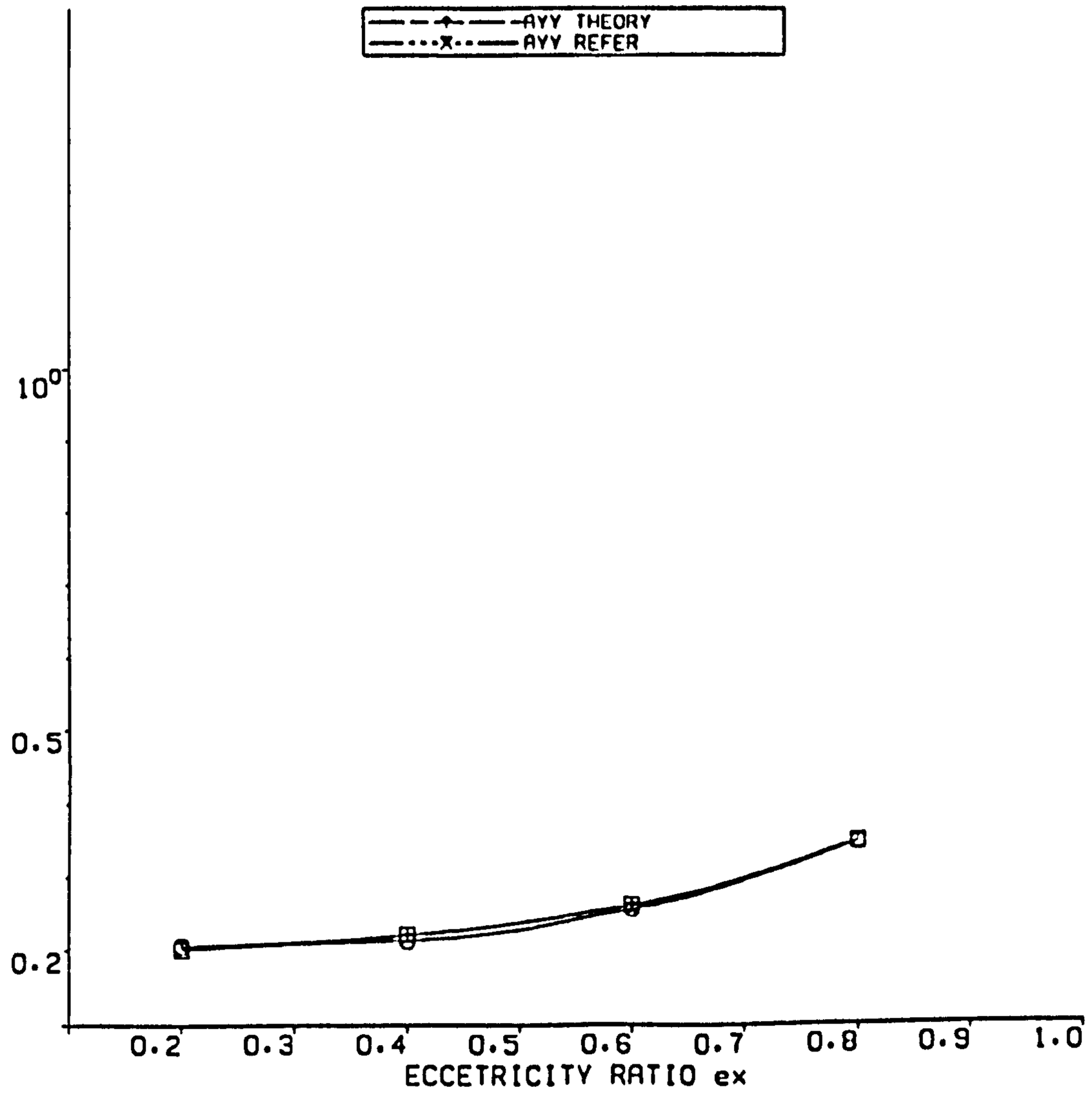

FIGURE 4.9d COMPARION OF STIFFNESS
COEFFICIENTS WITH REINHOUDT(16)
HELICAL GROOVED JOURNAL BEARING L/D=1

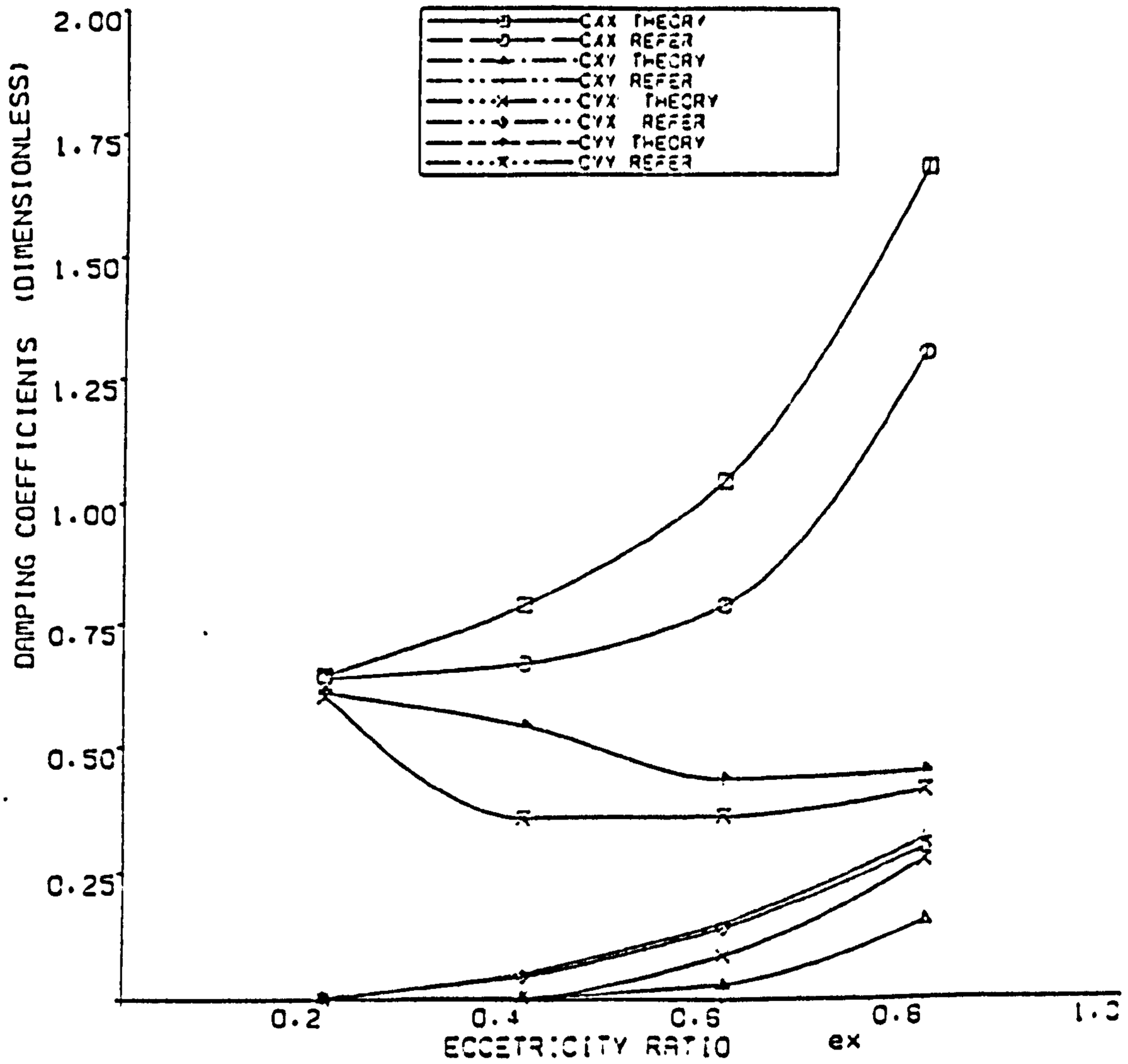

FIGURE 4.10 COMPARISON OF DAMPING COEFFICIENTS WITH REINHOUDT (16) HELICAL GROOVE JOURNAL BEARING L/D=1

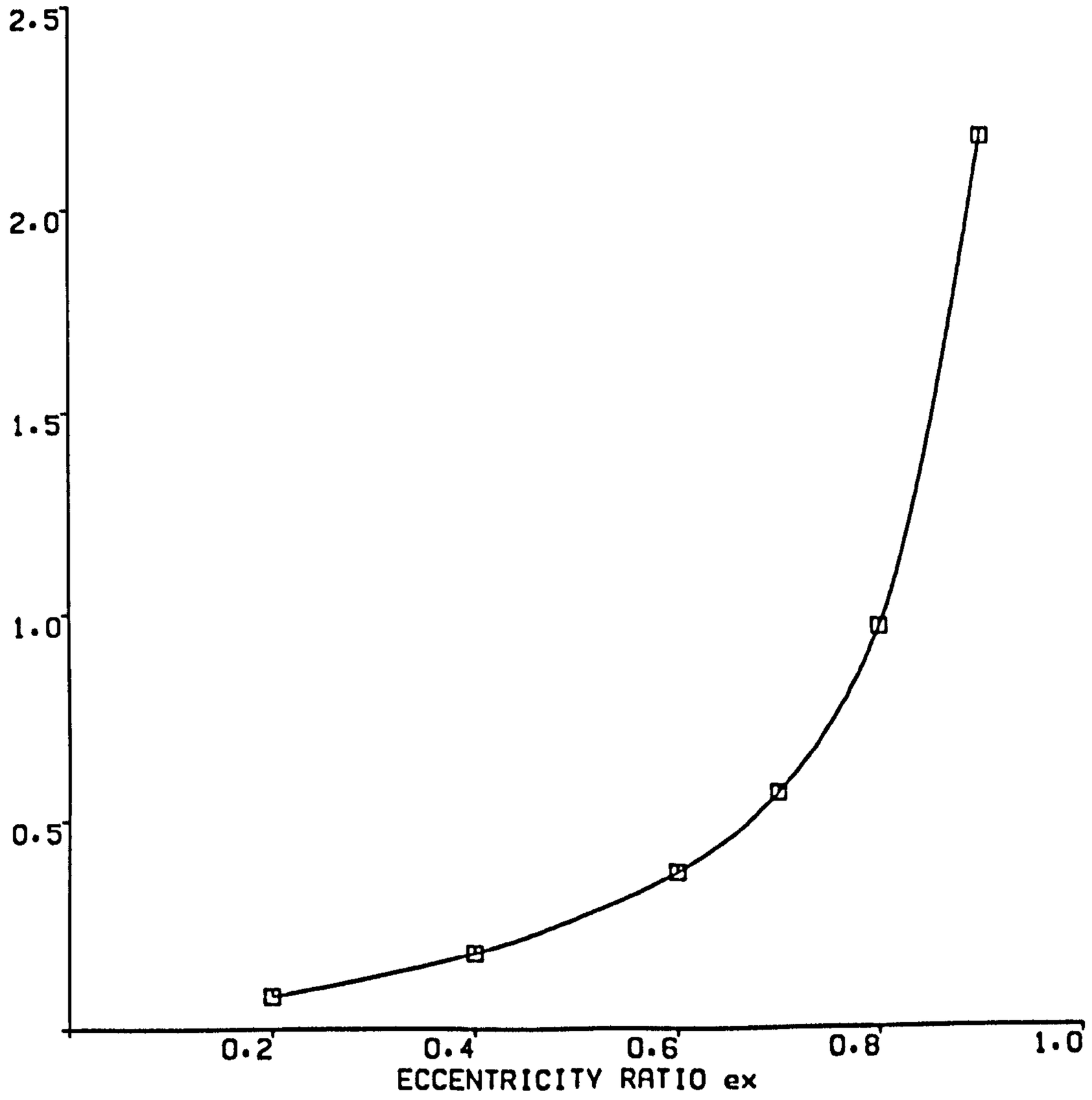

FIGURE 4.11 LOAD VS ECCENTRICITY
PLAIN JOURNAL BEARING L/D=1

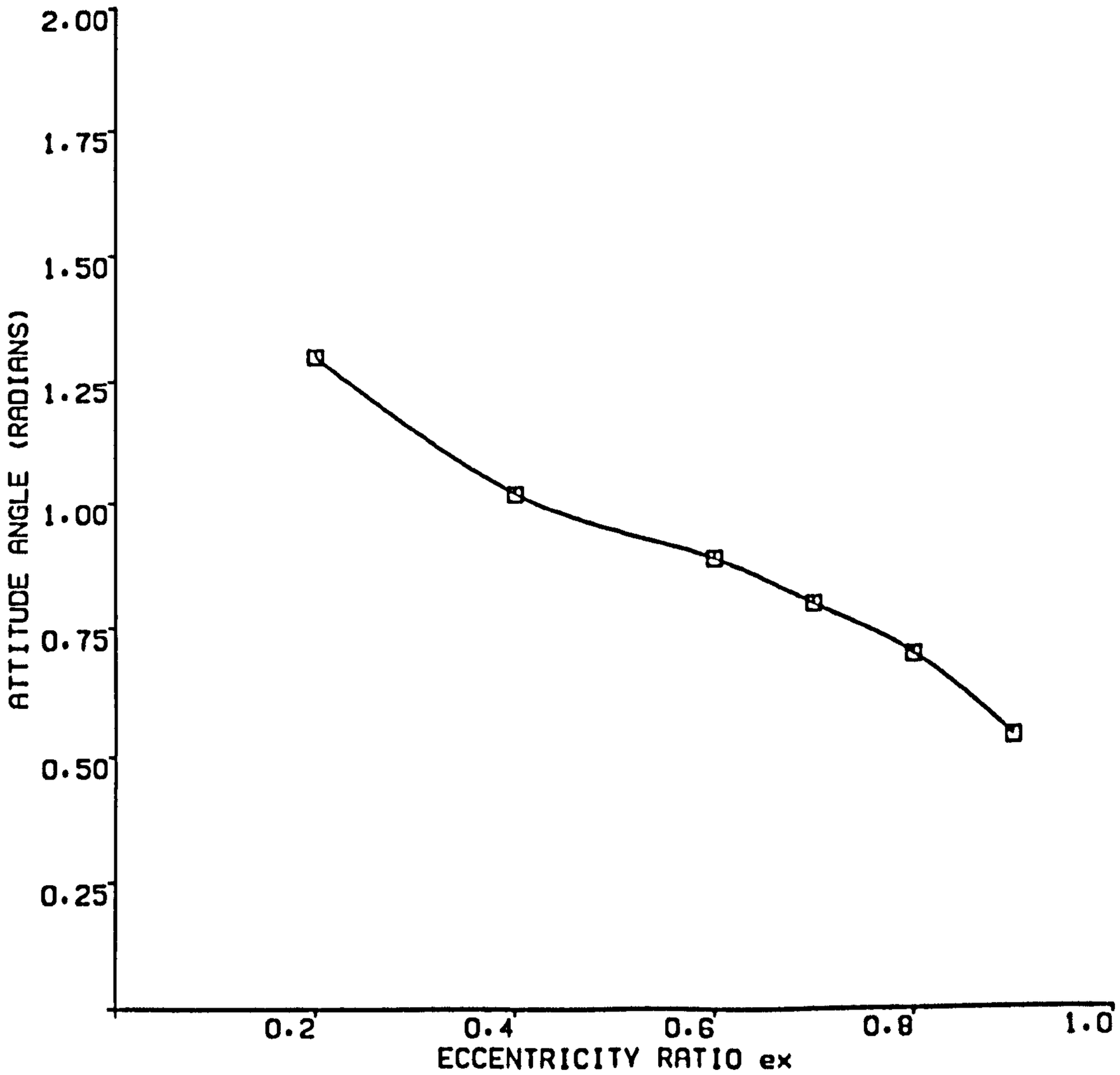

FIGURE 4.12 ATTITUDE ANGLE VS ECCENTRICITY
PLAIN JOURNAL BEARING

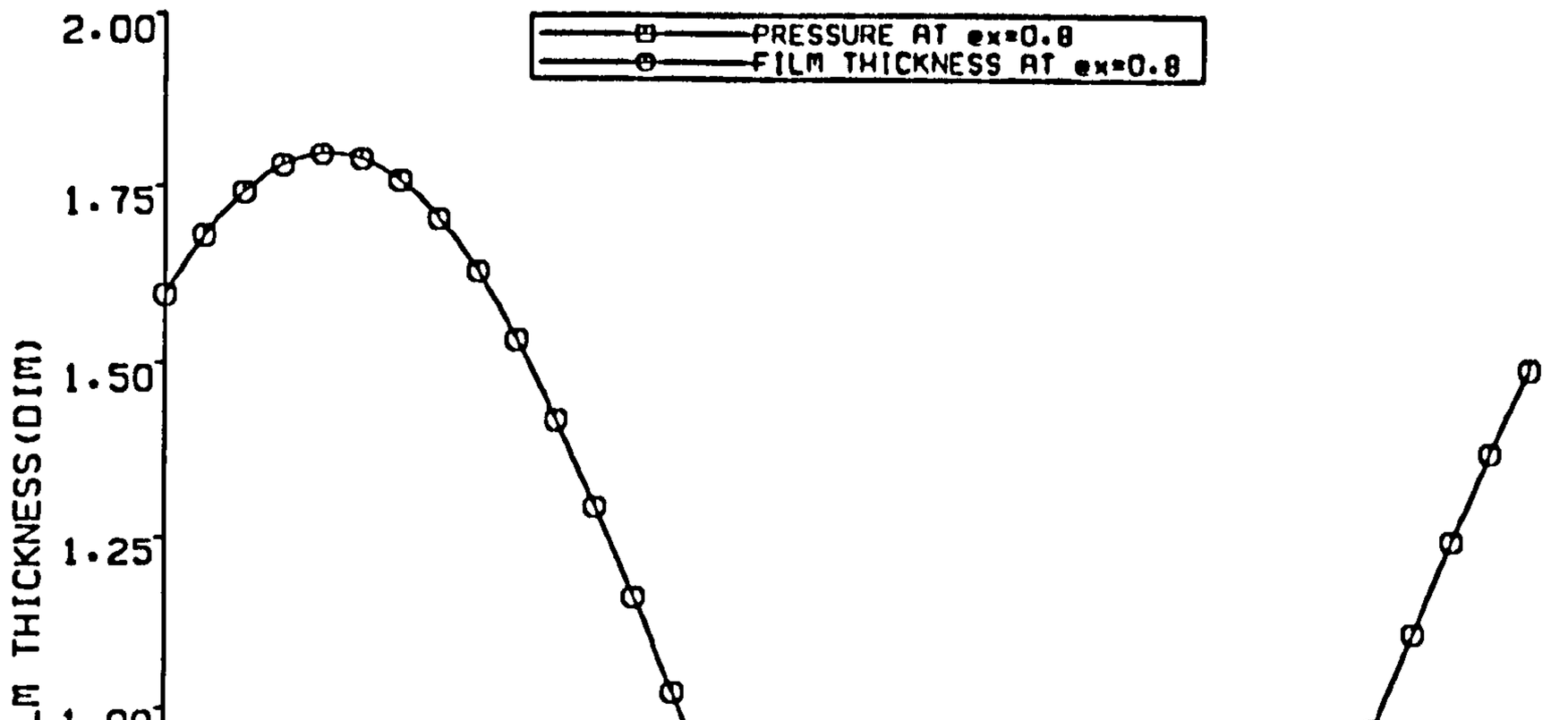

FIGURE 4.13 PRESSURE AND FILM THICKNESS PROFILES

PLAIN JOURNAL BEARING

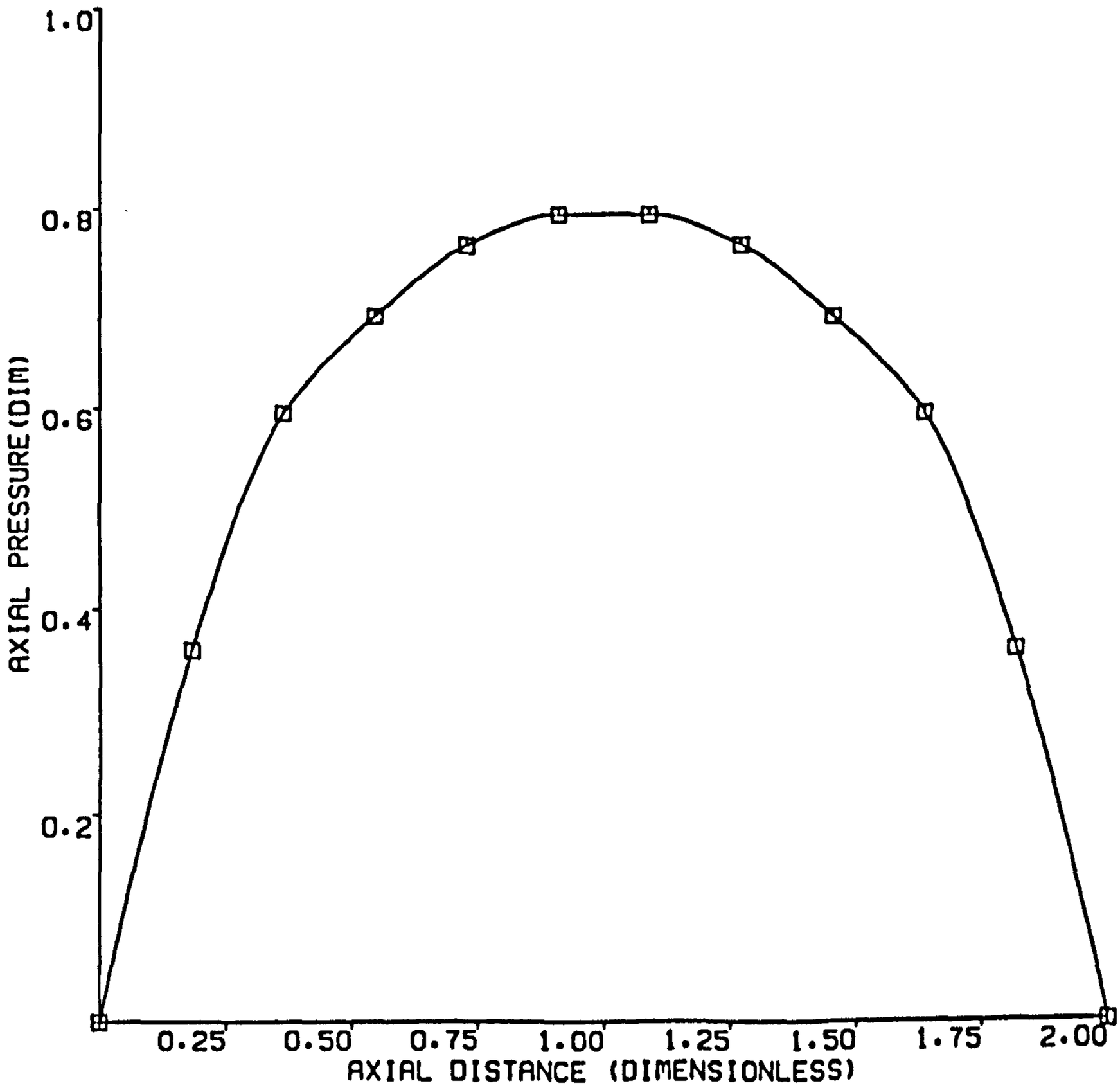

FIGURE 4.14 AXIAL PRESSURE VARIATION
AT ECCENTRICITY RATIO ex=0.8

PLAIN JOURNAL BEARING

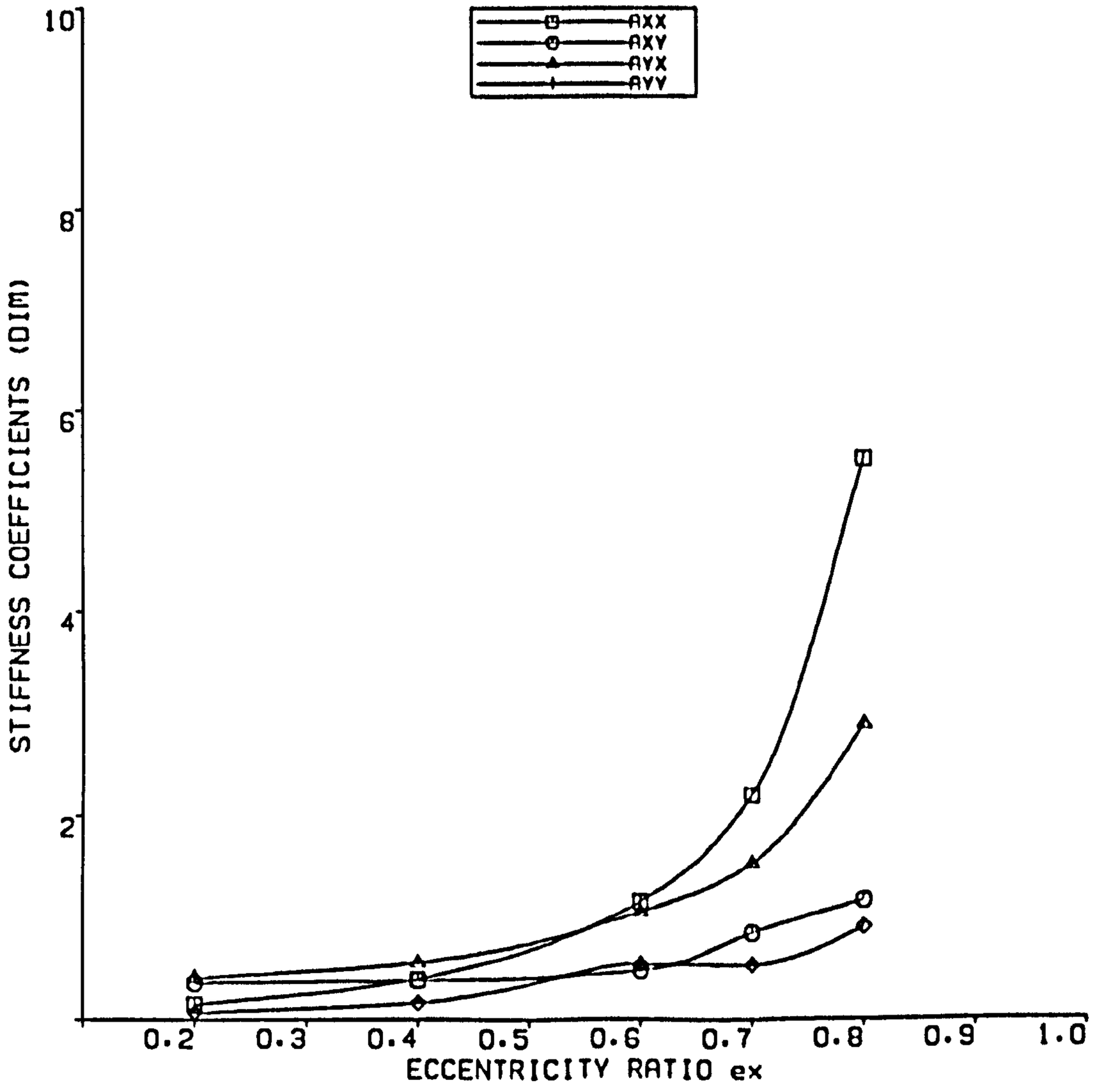

FIGURE 4.15 STIFFNESS COEFFICIENTS
PLAIN JOURNAL BEARING L/D=1

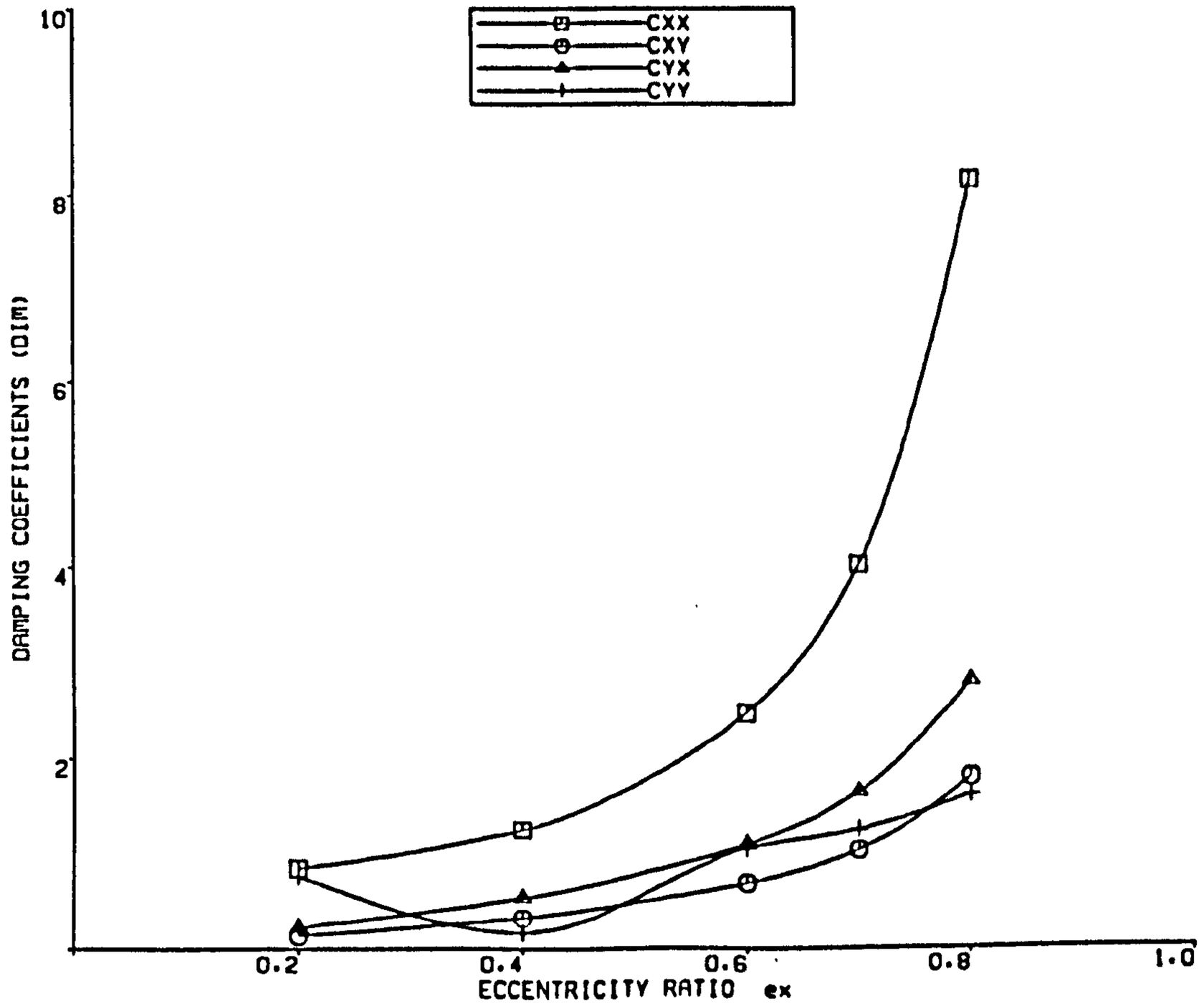

FIGURE 4.16 DAMPING COEFFICIENTS
PLAIN JOURNAL BEARING L/D=1

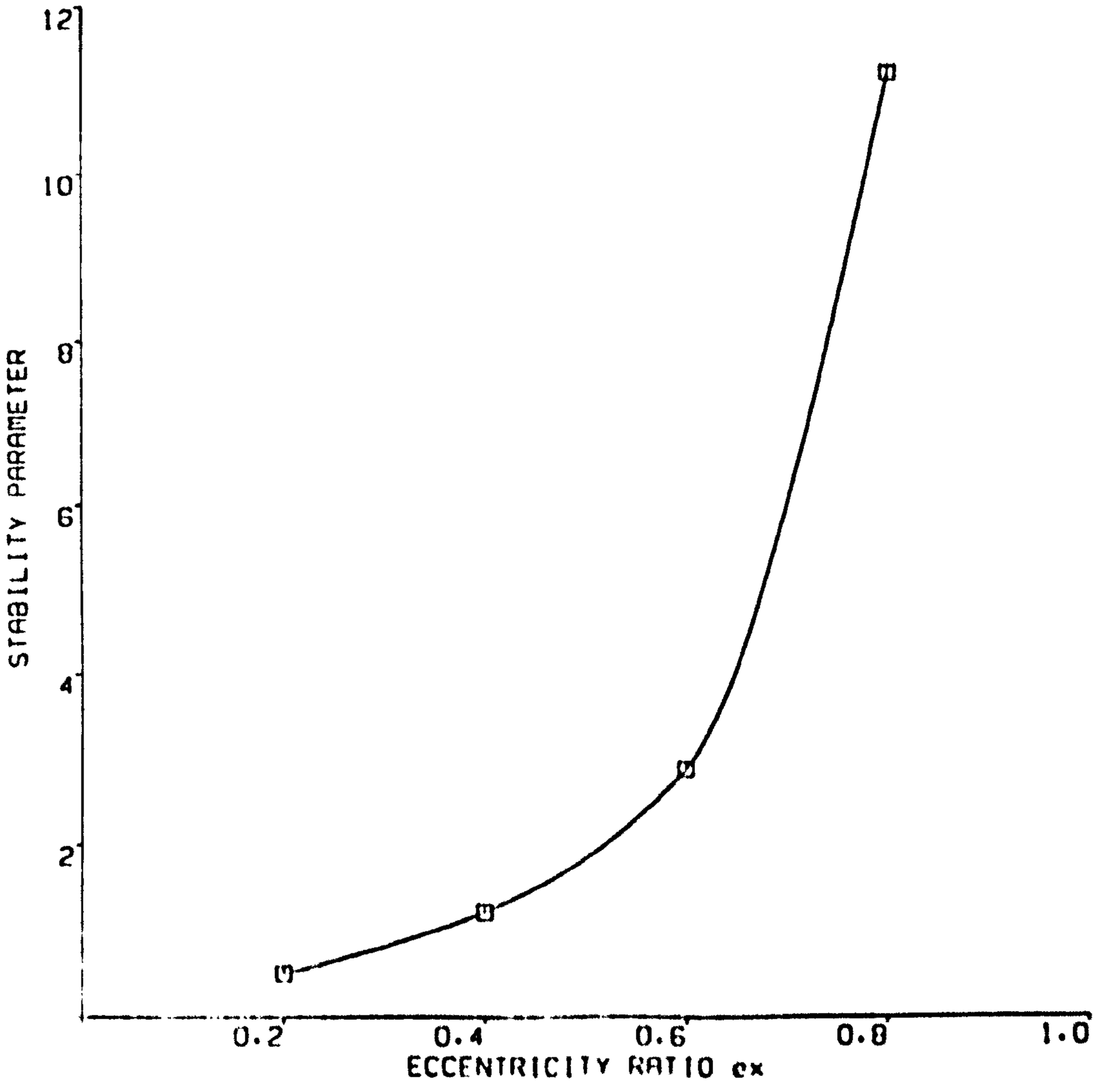

FIGURE 4.17 STABILITY PARAMETER .

PLAIN JOURNAL BEARING

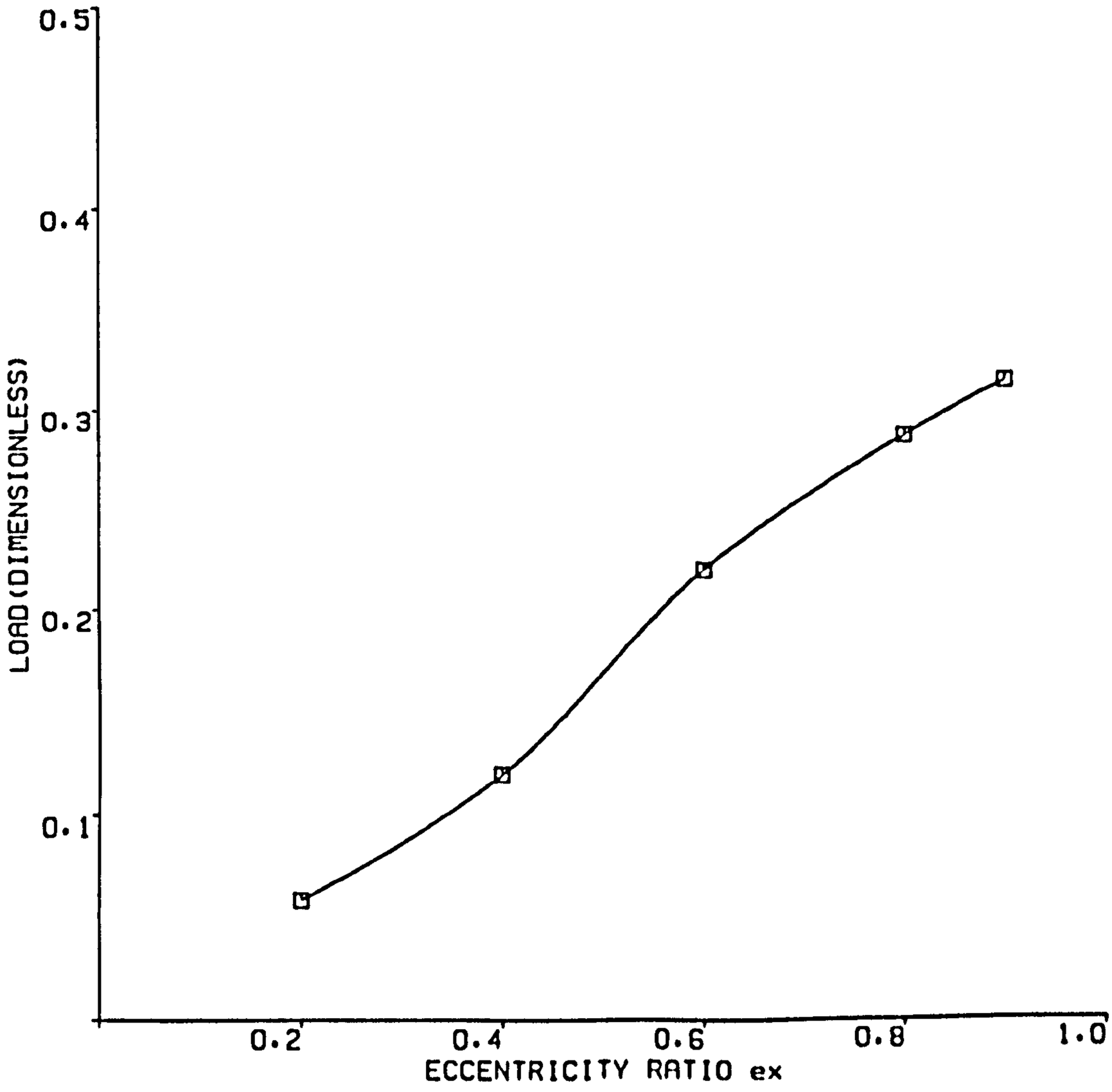

FIGURE 4.18 LOAD VS. ECCENTRICITY RATIO

SYMMETRICAL HELICAL GROOVE JOURNAL BEARING

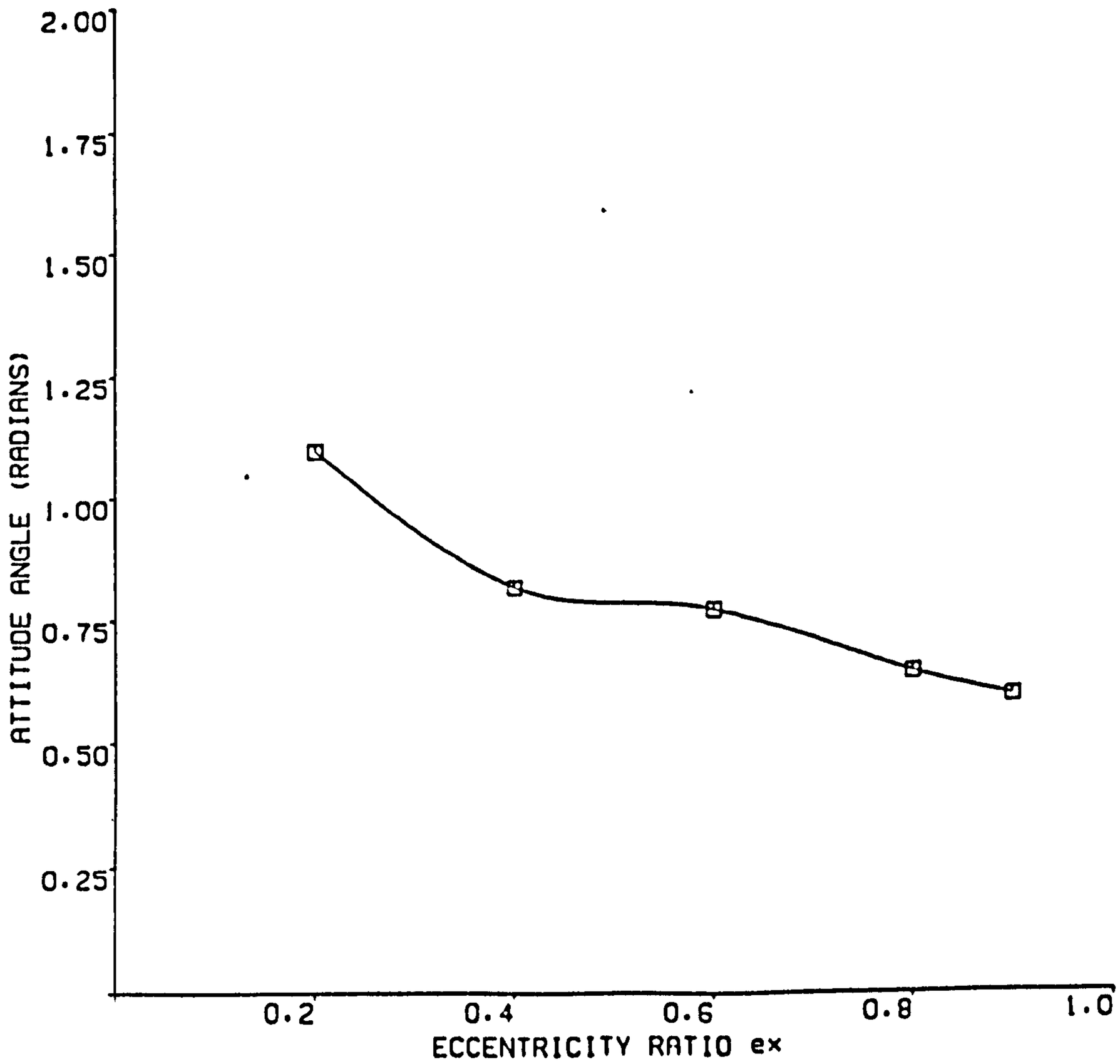

FIGURE 4.19 ATTITUDE ANGLE VS.ECCENTRICITY

SYMMETRICAL HELICAL GROOVE JOURNAL BEARING

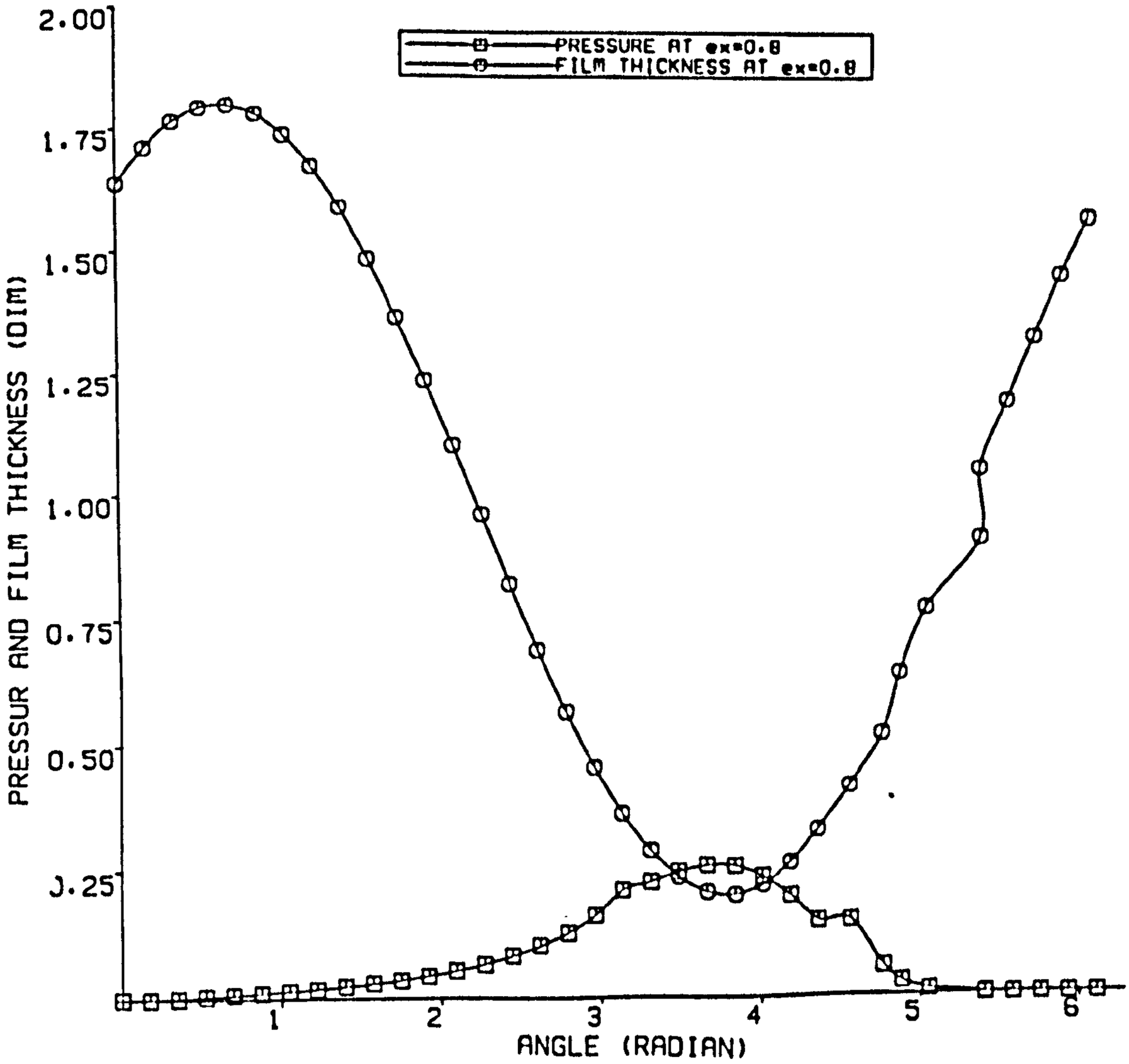

FIGURE 4.20 PRESSURE AND FILM THICKNESS PROFILES

SYMMETRICAL HELICAL GROOVE JOURNAL BEARING

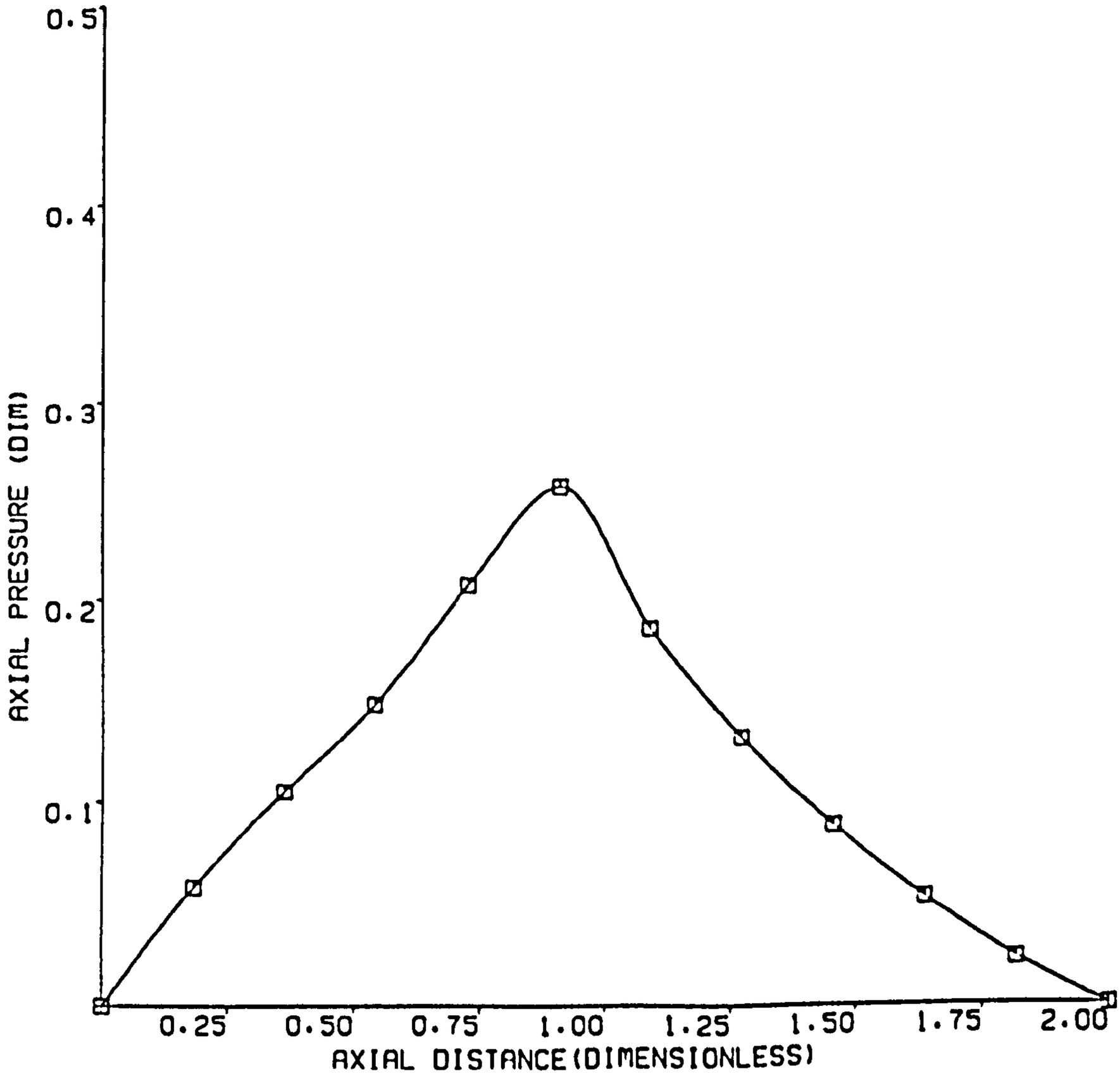

FIGURE 4.21 AXIAL PRESSURE VARIATION

SYMMETRICAL HELICAL GROOVE JOURNAL BEARING

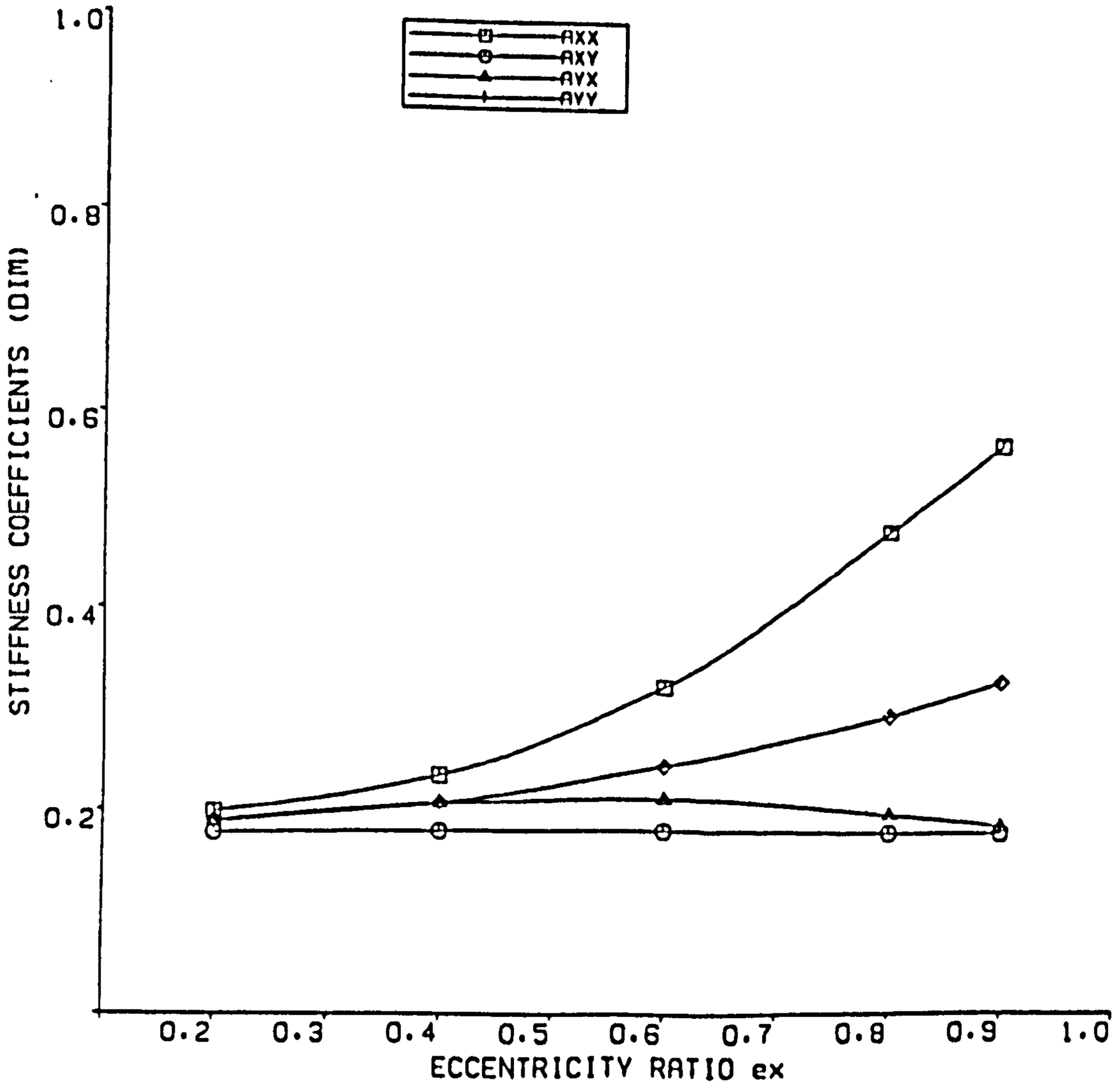

FIGURE 4.22 STIFFNESS COEFFICIENTS
SYMMETRICAL HELICAL GROOVE JOURNAL BEARING L/D=1

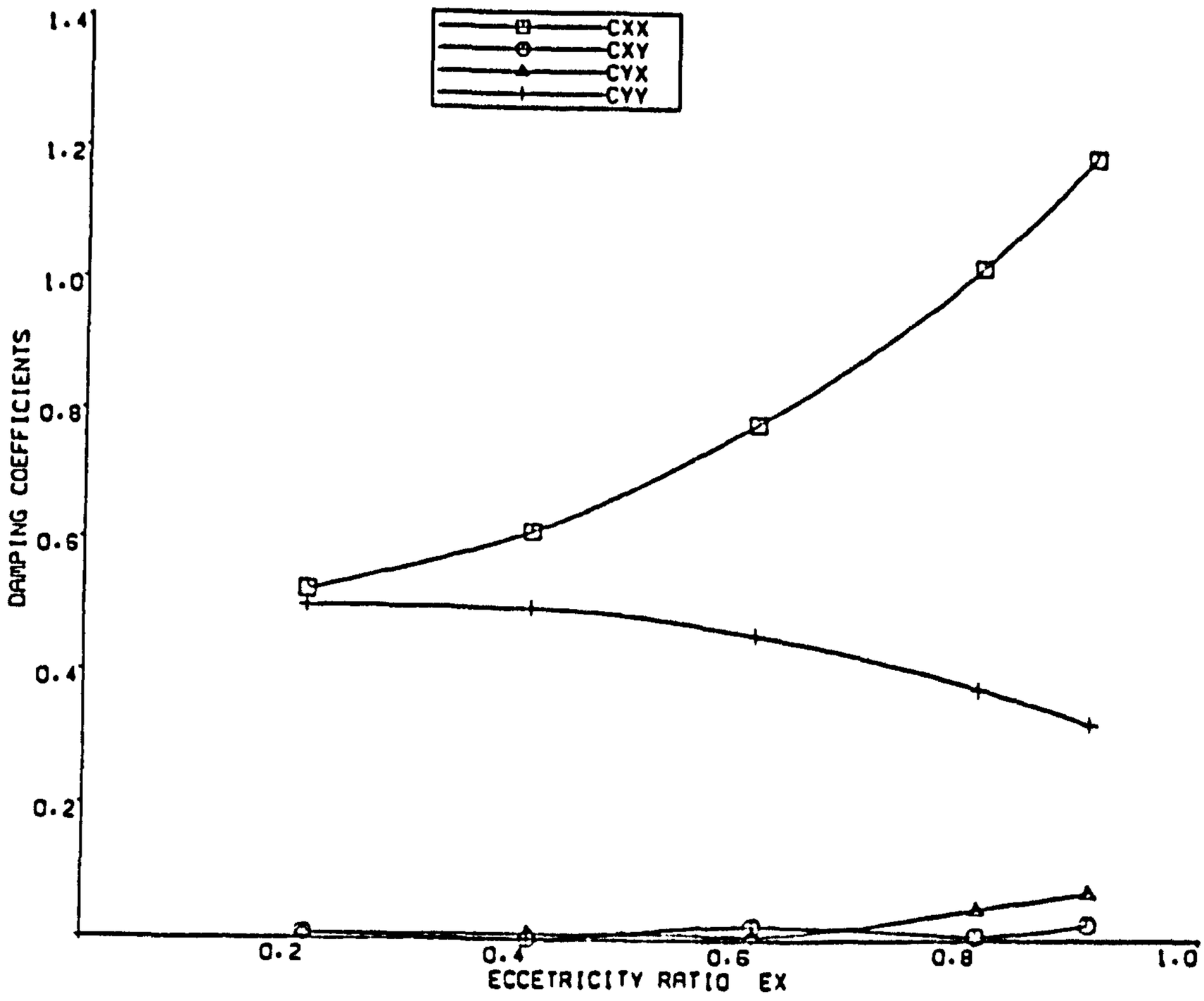

FIGURE 4.23 DAMPING COEFFICIENTS
SYMMETRICAL HELICAL GROOVE JOURNAL BEARING L/D=1

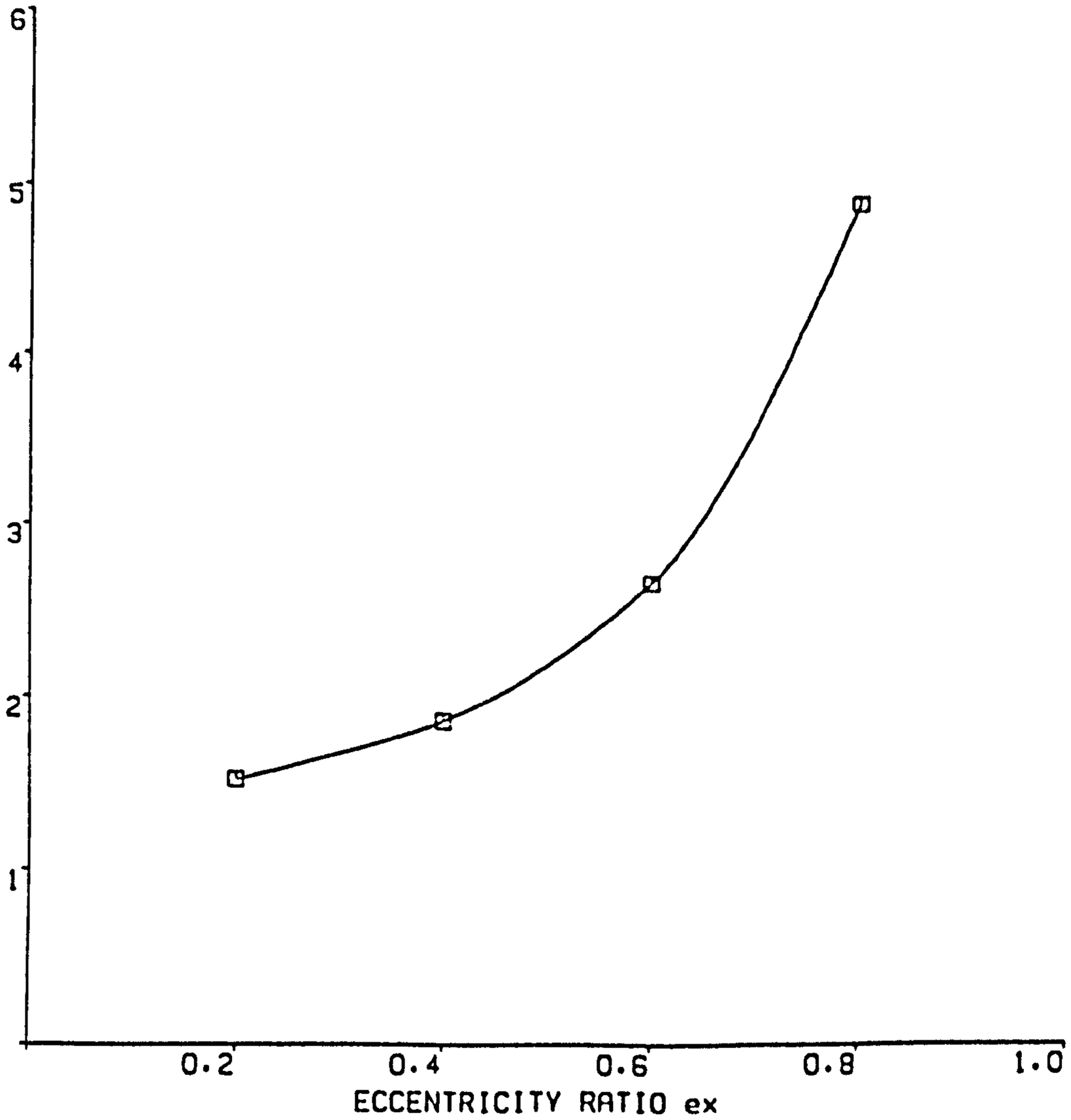

FIGURE 4.24 STABILITY PARAMETER
SYMMETRICAL HELICAL GROOVE BEARING

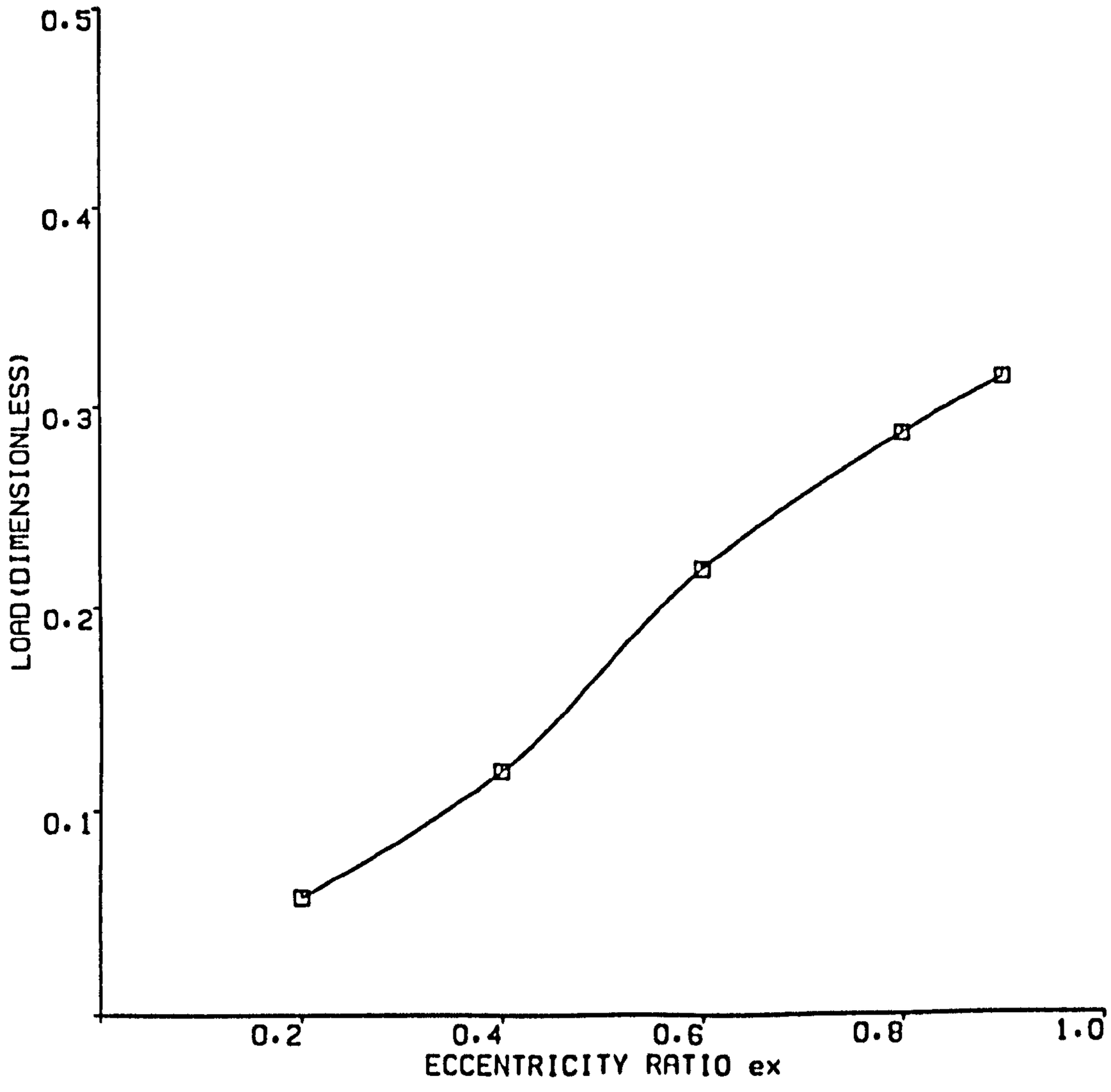

FIGURE 4.25 LOAD VS. ECCENTRICITY RATIO

ASYMMETRICAL HELICAL GROOVE JOURNAL BEARING

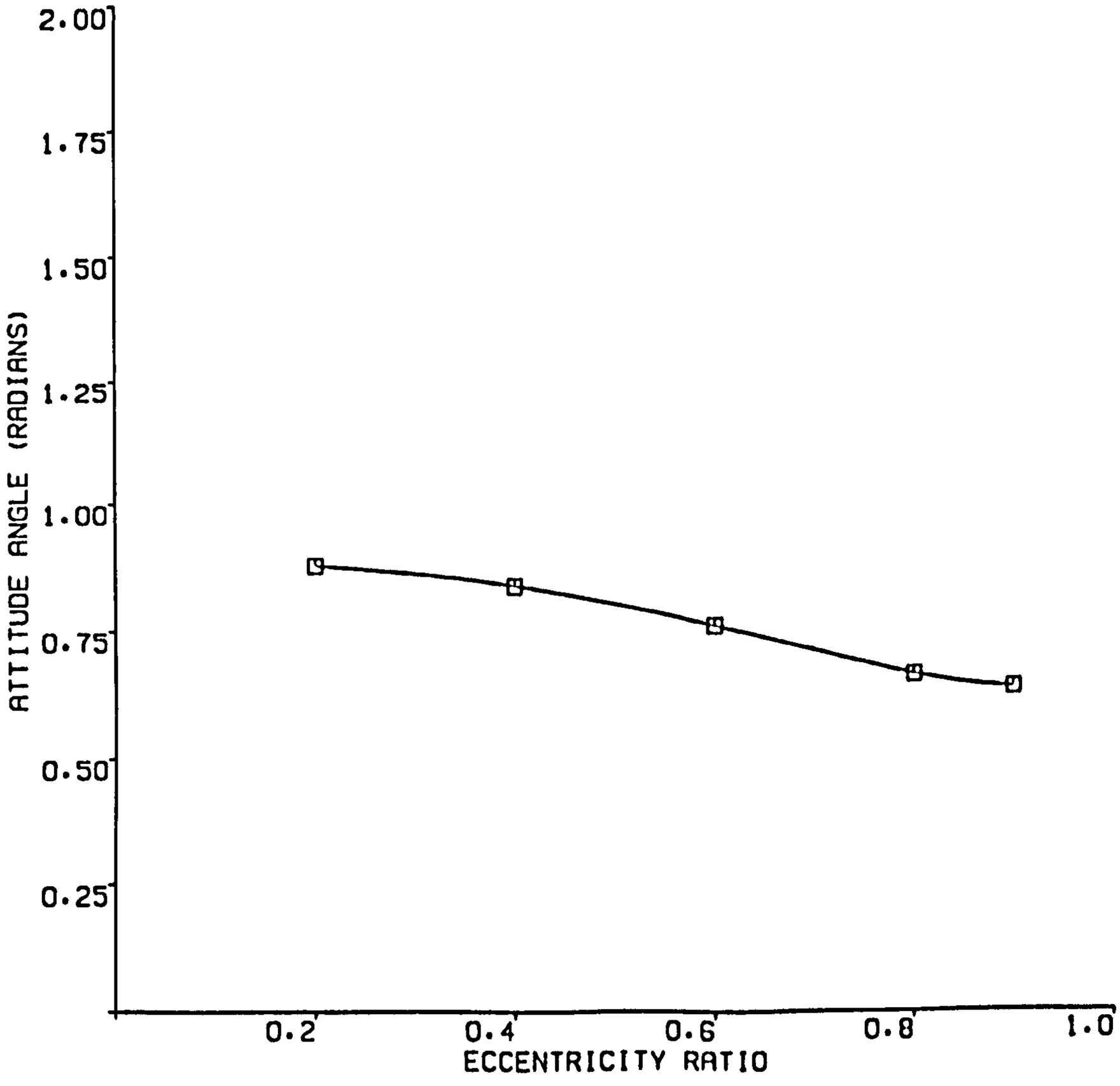

FIGURE 4.26 ATTITUDE ANGLE VS.ECCENTRICITY

ASYMMETRICAL HELICAL GROOVE JOURNAL BEARING

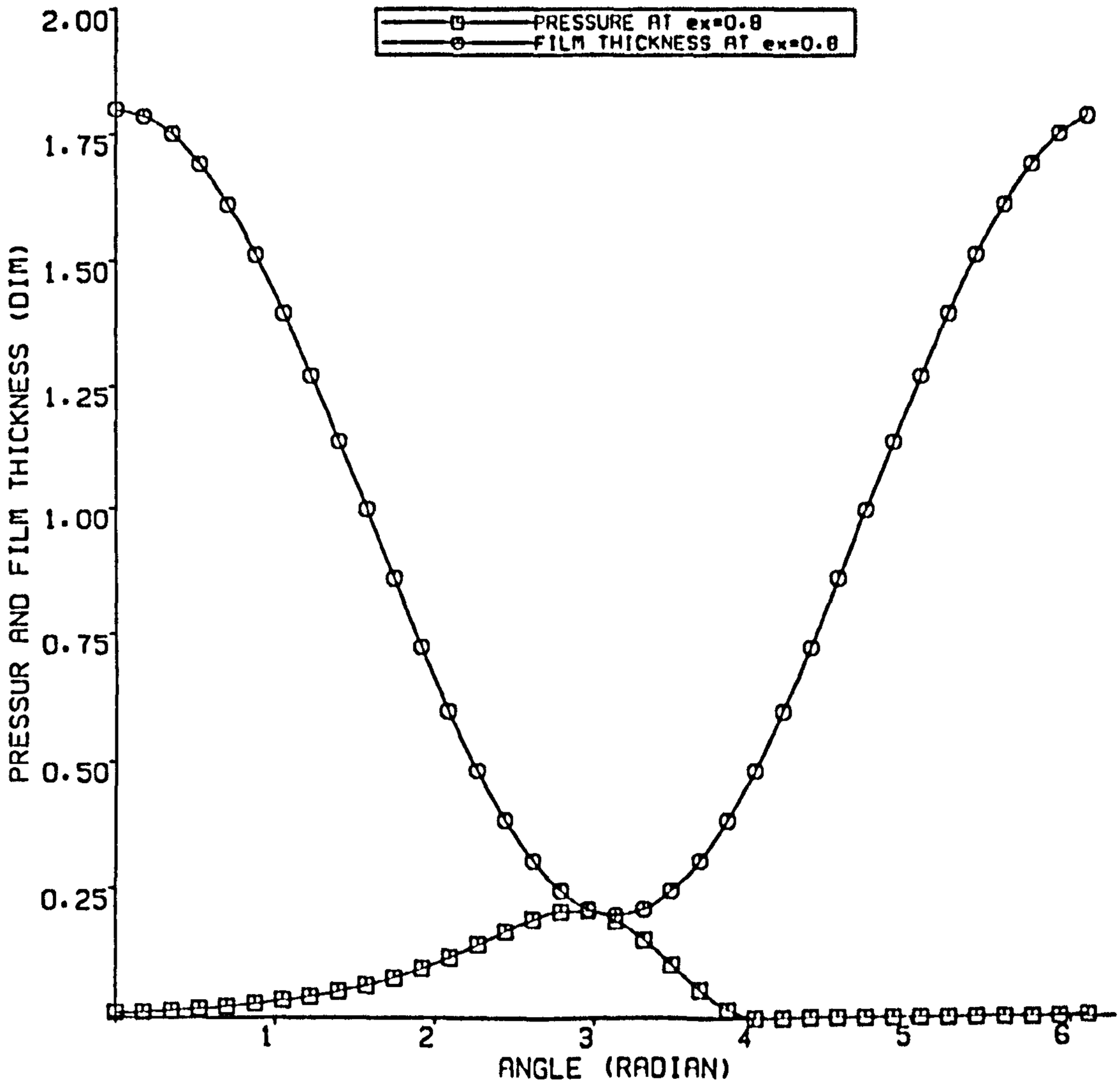

FIGURE 4.27 PRESSURE AND FILM THICKNESS PROFILES

ASYMMETRICAL HELICAL GROOVE JOURNAL BEARING

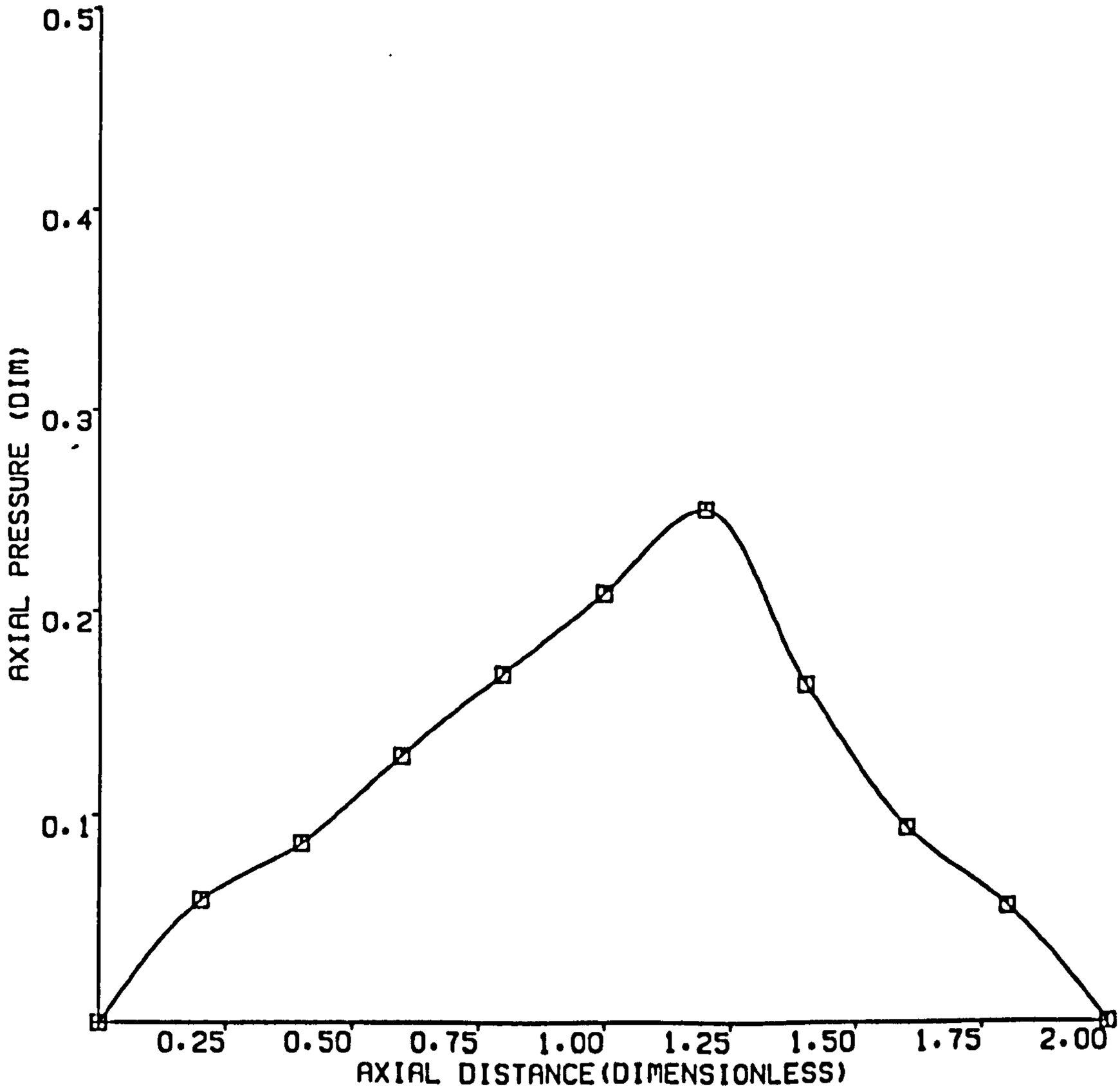

FIGURE 4.28 AXIAL PRESSURE VARIATION
AT ECCENTRICITY RATIO OF ex= 0.8

ASYMMETRICAL HELICAL GROOVE JOURNAL BEARING

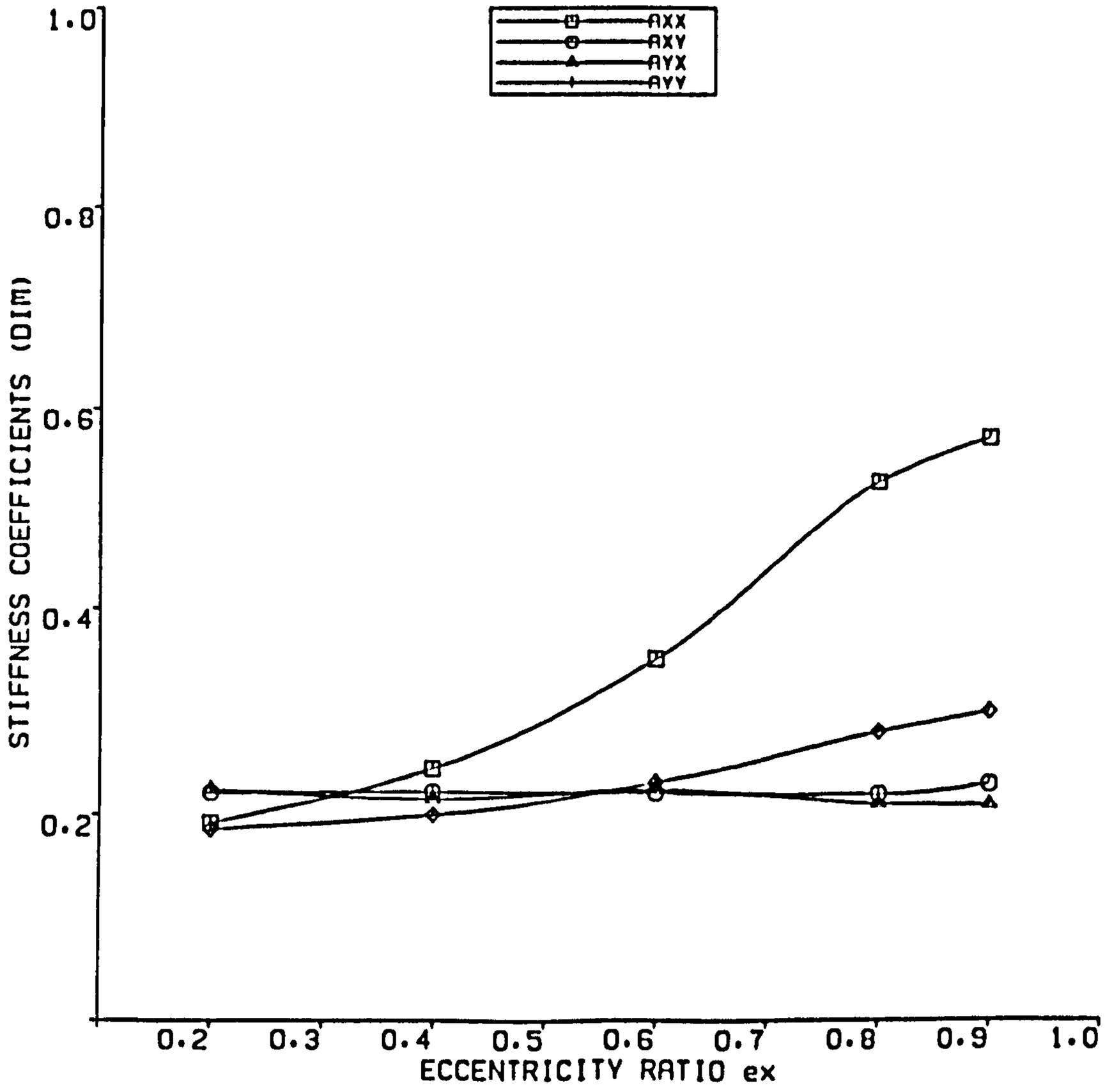

FIGURE 4.29 STIFFNESS COEFFICIENTS
ASYMMETRICAL HELICAL GROOVE JOURNAL BEARING L/D=1

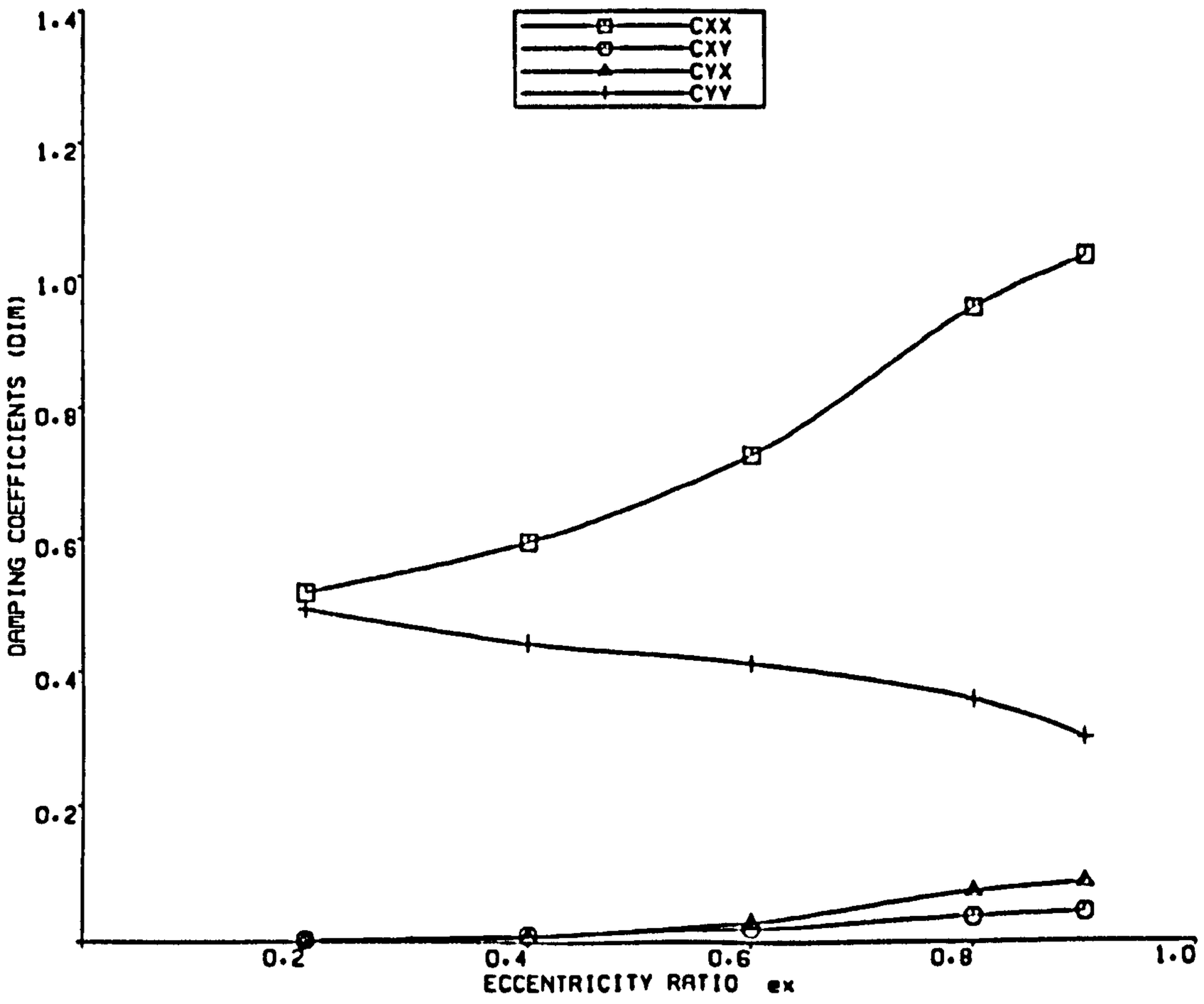

FIGURE 4.30 DAMPING COEFFICIENTS
ASYMMETRICAL HELICAL GROOVE JOURNAL BEARING L/D=1

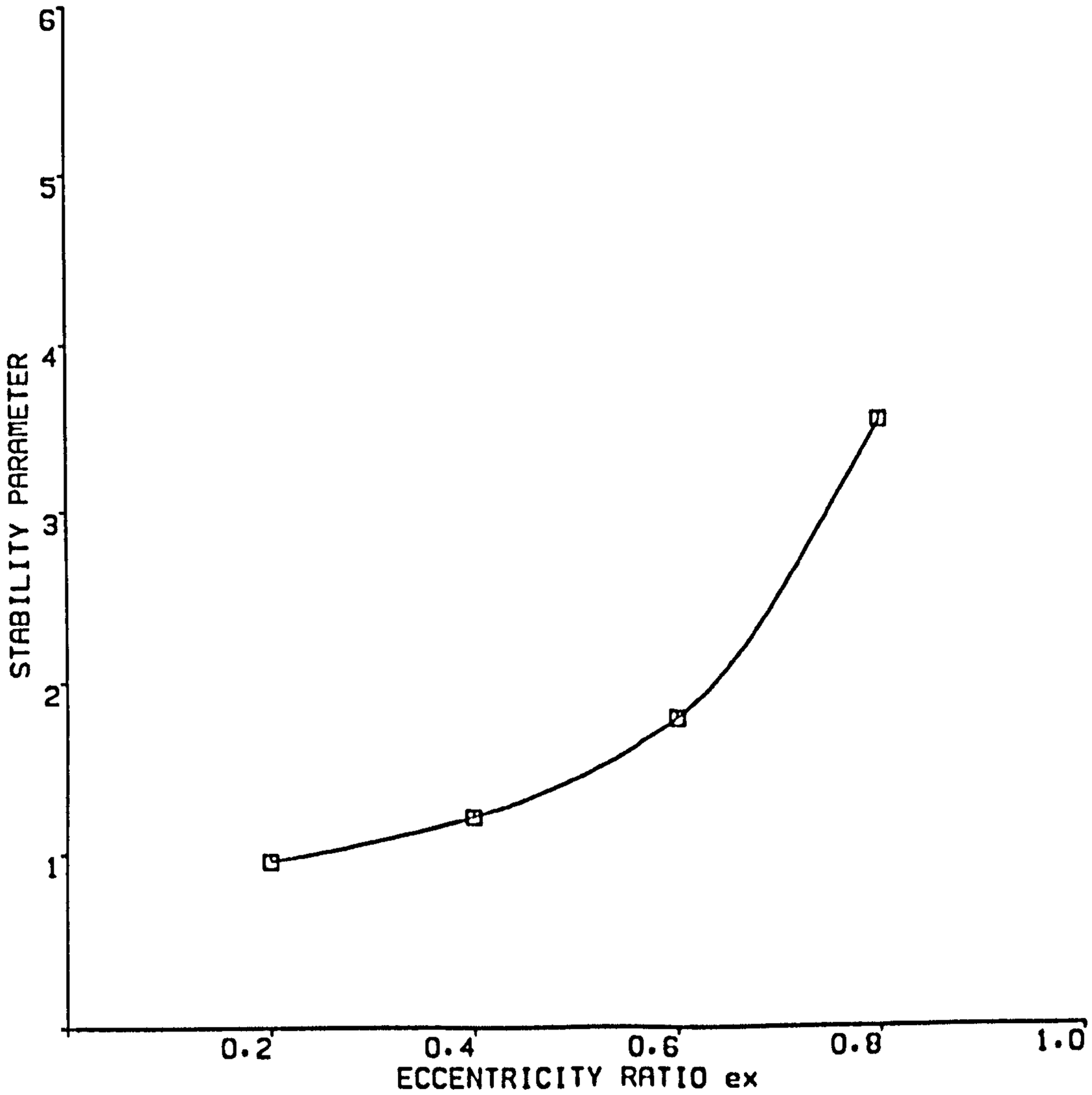

FIGURE 4.31 STABILITY PARAMETER
ASYMMETRICAL HELICAL GROOVE BEARING

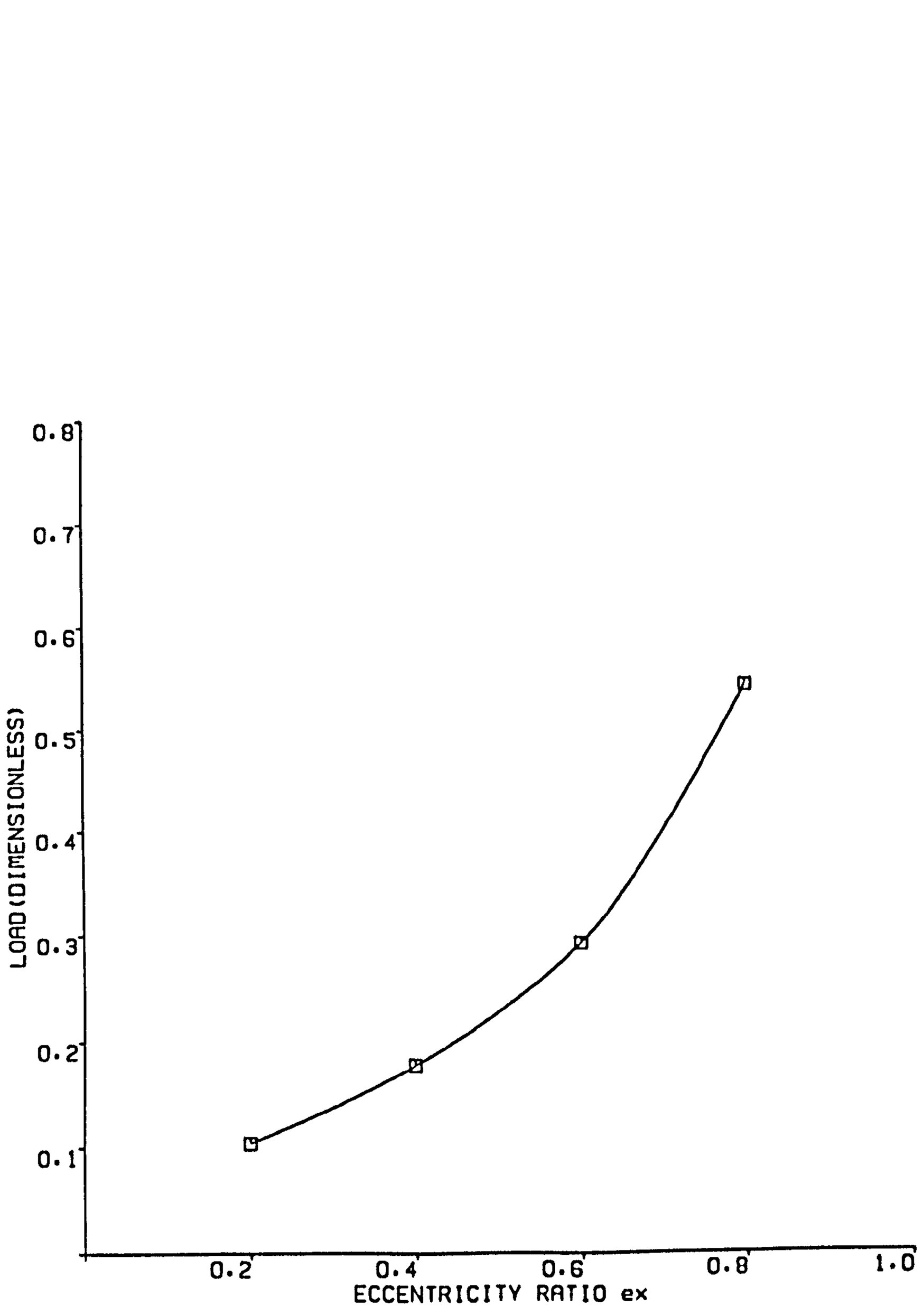

FIGURE 4.32 LOAD VS. ECCENTRICITY

PARTIAL HELICAL GROOVE JOURNAL BEARING

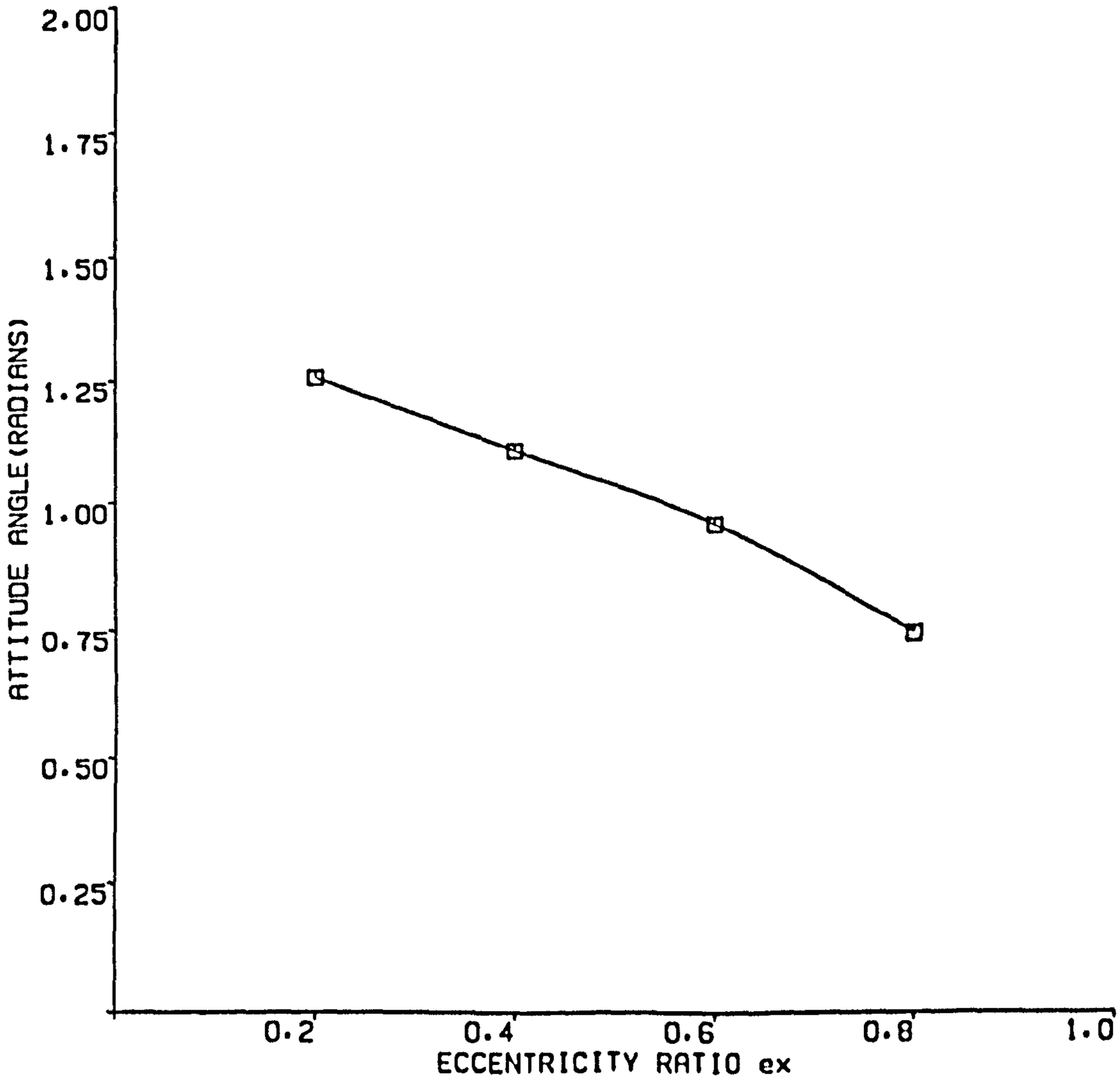

FIGURE 4.33 ATTITUDE ANGLE VS ECCENTRICITY

PARTIAL HELICAL GROOVE JOURNAL BEARING

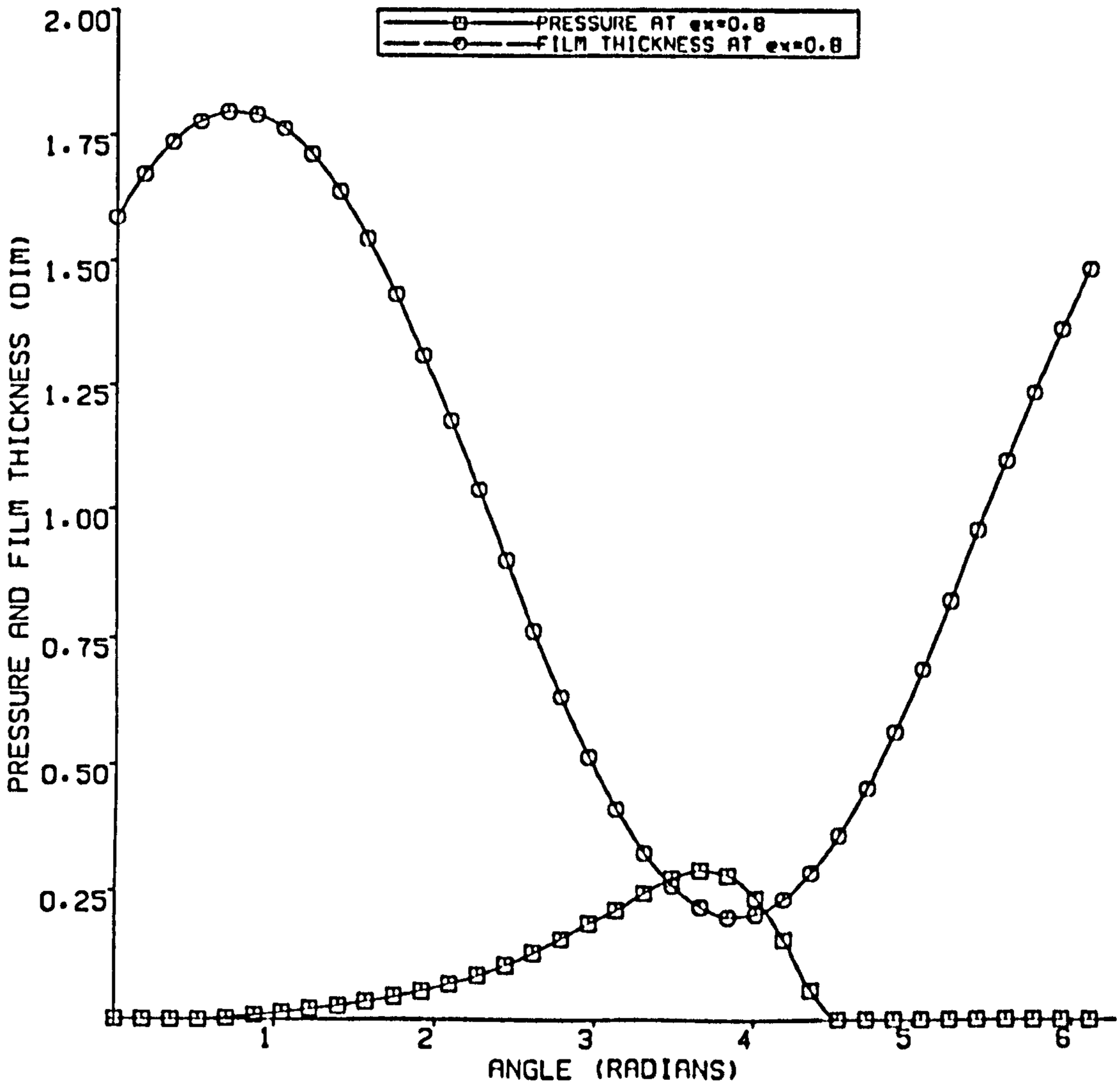

FIGURE 4.34 PRESSURE AND FILM THICKNESS PROFILES

PARTIAL HELICAL GROOVE JOURNAL BEARING

and in dimensionless form they become:

$$\begin{aligned} \Delta f_x &= -K_{xx}X - K_{xy}Y - C_{xx}\dot{X} - C_{xy}\dot{Y} \\ \Delta f_y &= -K_{xy}X - K_{yy}Y - C_{yx}\dot{X} - C_{yy}\dot{Y} \end{aligned} \qquad (4.40)$$

The calculation of the dynamic coefficients require some further explanation. The stiffness coefficients A_{xx} and A_{yx} , for example, determined by the displacement of the journal through a small distance x from the equilibrium position x = 0. This results in increments of ΔF_x and ΔF_y in F_x and F_y respectively, so that

$$A_{xx} = -\frac{\Delta F_x}{X}$$

$$A_{yx} = -\frac{\Delta F_y}{X}$$

Similarly, A_{yy} and A_{xy} are determined with a small change in displacement y, B_{xx} and B_{yx} are determined with the small change in velocity $\dot{x}$, B_{xy} and B_{yy} are determined with a small change in velocity $\dot{y}$. The perturbation of position and velocity should be small enough such that the incremental change in forces is approximately linear.

4.4.4 Stability Analysis

Bearing stability is usually investigated by considering a very rigid rotor. In the present analysis it is assumed that the bearing housing of mass M undergoes free vibration. All the other forces such as unbalance forces are considered zero. The equations of motion describing the free vibrations are given below [44,45,46].

$$M\ddot{X} + A_{xx}X + A_{xy}Y + B_{xx}\dot{X} + B_{xy}\dot{Y} = 0$$
$$M\ddot{Y} + A_{yx}X + A_{yy}Y + B_{xy}\dot{X} + B_{yy}\dot{Y} = 0 \qquad (4.41)$$

If a small perturbation is assumed then an analysis of the perturbation growth or decay with time about the equilibrium position is required.

Consider the oil film forces acting as though they were produced by linear springs and dampers. The displacement of the journal within the oil film can then be represented by:

$$X = \bar{X}e^{\lambda t}$$
$$Y = \bar{Y}e^{\lambda t} \qquad (4.42)$$

Where λ is a complex number i.e. $\lambda = P + j\,\Omega$, where $j = \sqrt{-1}$ and Ω is the frequency of vibration. If λ is positive, the journal motion is unstable and grows with time. If λ is negative, the journal motion is stable and decays with time. If the system is operating at the stability threshold then $P = 0$. Hence, at the onset of instability for small disturbances, the displacement response is :

$$X = \bar{X}e^{j\Omega t}$$
$$Y = \bar{Y}e^{j\Omega t} \qquad (4.43)$$

The stability analysis which is detailed in Appendix H, produces a stability parameter, i.e

$$S_p = \frac{\omega^2 MC}{W_b} \qquad (4.44)$$

where,

M = Mass of the bearing housing [kg]

ω = Angular speed of the Journal [rad/sec]

C = Radial clearance [m].

w_b =Bearing load at the threshold of instability [N]

For a given bearing the linearized analysis produces a threshold value of S_p below which the journal is unstable [3]. In the present analysis the bearing load at the threshold of instability for each speed and equilibrium position is calculated by using equation (4.44).

4.5 Computer Program

A computer program which used the finite element method was developed for the calculation of the steady state and dynamic characteristics of journal bearings both with and without rectangular grooves. With this program, it was possible to calculate the performance of both a plain journal bearing, and helical groove journal bearings of various configurations, Figures 4.5a to 4.5d.

A comparison of theoretical results with published work was made. In this regard, the assumptions and approximations involved in the derivation of the generalised Reynolds equation (4.23) are similar to those of Reinhoudt [16]. The steady state and dynamic properties are calculated in [16] for a helical groove bearing bearing, Figure 4.5b and other types of journal bearings, using a component of eccentricity EX as illustrated in Figure 4.6. In the present program, as data the eccentricity EX is input. The mesh size was chosen on the basis of the smoothed pressure concept i.e , a finite number of grooves were not taken into account. A similar approach was adopted by other authors, Bootsma [12,13], Vohr and Chow [32] and Smally [15].

On a Sun work station,it was possible to use a 36 x 12 nodes mesh to cover

the full bearing surface. For bearings such as the plain journal bearing, the pressure profile is symmetric about mid axial plane and so only half the bearing needed to be considered and so a mesh size of 45 x 4 nodes was used.

Outlined in the flow charts in Figure 4.7a, first is the flow chart of the computer program to compute steady state properties, whilst the second is the flow chart of the program to compute the response coefficients and stability parameter of the bearing is shown. The program starts by reading in the bearing geometry, clearance, lubricant viscosity, boundary conditions and speed. The static eccentricity EX is input to the computer program. The mesh size i.e the number of elements along the circumference and along the axial length of the bearing is also established at this stage. The data are read through the subroutine 'INPUT.

In the first part of the program the subroutin " MESHGEN " generates the coordinates of the nodal points, and also form the triangular elements. The nodes with specified boundary conditions are then segregated. Because the static eccentricity is input, the film thickness corresponding to this eccentricity is calculated for each node.

In the next step is that the contribution of each element to the main matrix is determined by the subroutine "ASSEMBLE". The set of simultaneous equations for the nodal pressure are obtained after the application of the boundary conditions in subroutine "REDUCER". The equations are then solved by subroutine "SOLVER" using Gaussian elimination and the nodal pressures are obtained. The nodal pressures are then used to calculate the bearing reaction forces. To ensure the accuracy of the solutions the following convergence limits were imposed in the iterative calculation of pressures and attitude angle.

$$Accuracy = Abs \frac{[New\ pressure - Old\ pressure]}{New\ pressure} < 10^{-4}$$

$$Accuracy = Abs\ [New\ attitude - Old\ attitude] < 10^{-4}$$

In the program negative pressures were set to zero before the pressure field was integrated for the calculation of load, attitude angle and for the plotting of the pressure profile. Following convergence of the pressure field, the equilibrium position of the journal centre was obtained by iteration of the attitude angle until required accuracy was achieved. In order to find the stiffness coefficients, the journal centre was perturbed in the x and y direction by a small amount, typically .0001. Similarly, by perturbing the journal centre velocity, and repeating the calculations, the damping coefficients were determined. Using the response coefficients, the stability parameter and the bearing load at the threshold of instability were then calculated.

4.6 Program Validation

In order to determine the accuracy of a theoretical model, it is common practice to compare results with other results or with experimental results. The results of the present model have been compared with those of Reinhoudt [16], Nobuyoshi, et al. [37] and Cameron [9].

4.6.1 Comparison with Reinhoudt

The theoretical model of the helical groove journal bearing adopted in this work was first used to model the bearing illustrated in Figure 4.5b. The bearing aspect ratio was 1 and data were input to the computer program in dimensionless

form. The groove data in the dimensionless form are given in Table 4.1.

Table 4.1 Groove data of Reinhoudt Bearing

Groove Depth h_g	Groove Angle	bg/br
1.1	0.52 radians	1.0

It was assumed that:

(i) The pressure at the ends of the bearing was zero.

(ii) At cavitation the Reynolds boundary conditions were used.

The results compared with those in reference [16], are shown in Figures 4.7 to 4.10. These curves show that the difference in dimensionless load is about 8 to 9%, the difference in stiffness coefficients is approximately 12%, and the difference in damping coefficients is slightly higher than 12%

4.6.2 Comparison with Nobuyoshi

The present model was also compared with the recently published work of Nobuyoshi et al [37] on the static characteristics of an irreversible herringbone groove journal bearing. Their analysis was based on a narrow groove theory. The differential equation for nodal pressure was solved by the finite difference method.

The bearing aspect ratio was 1 and the groove data in dimensionless form are given in Table 4.2.

Table 4.2 Groove Data of Nobuyshi Bearing

Groove Depth h_g	Groove Angle	bg/br
1.1	0.52 radians	1.0

The following boundary conditions were adopted :

(i) Pressure at the edge of the bearing was taken to be zero.

(ii) The Gumbel boundary conditions were used i.e. all the negative pressures are set to zero before integrating to obtain the load.

The results, in the form of dimensionless load capacity are compared in Table 4.3.

Table 4.3 Comparison of Load Capacity

	Eccentricity	Dimensionless bearing load
Present work	0.25	0.06
Reference [37]	0.25	0.06
Present work	0.5	0.13
Reference [37]	0.5	0.12
Present work	0.75	0.24
Reference [37]	0.75	0.23

The agreement is satisfactory. The present work predicts a bearing load which is about 7% greater than the load calculated by Nobuyoshi.

4.6.3 Comparison with Cameron [9]

The computed results of attitude angle for a plain journal bearing with L/D =1 are compared in Figure 4.8a. The model results are about 11.5 to 12 % higher than those of Cameron [9].

4.6.4 Reasons for Discrepancies

There could be a number of reasons for the differences between the results of the present model and those of Reinhoudt. The most obvious differences are probably related to different computational techniques used.

(1) In the finite element method the solution accuracy depends upon the type of element and the number of elements used to subdivide the bearing surface. The accuracy can be improved by making the element mesh finer. However, the choice of element mesh size has to be considered with respect to the calculation. The mesh size used in the present work is described in section 4.5. Nothing is known about the mesh size used in the work of Reinhoudt [16].

(2) The results of Reinhoudt for the helical groove journal bearing Figure 4.5b, were not previously compared with any experimental or theoretical results.

(3) The finite element method generates the algebraic equations. The overall accuracy of the finite element method depends on the method of solution of these equations. It is known, for example, that the direct method of solution produces truncation errors [51].

4.7 Theoretical Results

Numerical results for four types of bearing are now presented and discussed. The numerical model predictions are about 11 to 12 % less in comparison to those in published work [16] , as described in section 4.6. The bearing load is obtained by integrating the hydrodynamic pressure. Linearized

dynamic coefficients are obtained from small numerical perturbations of the journal equilibrium position. The dynamic coefficients so obtained are used to determine the stability of the bearing about the equilibrium position. The theoretical results such as bearing load, attitude angle, response coefficients and stability parameter are plotted vs eccentricity ex, defined in Section 4.5.

4.7.1 Plain Journal Bearing

The dimensionless bearing load and attitude angle as functions of eccentricity ratio are shown in Figures 4.11 and 4.12 respectively. The dimensionless circumferential pressure and film thickness profiles are given in Figure 4.13, whilst the axial pressure profile of the bearing is shown in Figure 4.14. The dimensionless stiffness and damping coefficients as functions of eccentricity are plotted in Figures 4.15 and 4.16 respectively. In Figure 4.17 is shown the stability parameter as a function of eccentricity ratio.

4.7.2 Symmetrical Helical Groove Journal Bearing

The steady state characteristics such as dimensionless bearing load and attitude angle are shown in Figures 4.18 and 4.19 as a function of eccentricity ratio. The circumferential pressure and film thickness profiles are plotted in Figure 4.20, whilst the axial pressure profile of the bearing is given in Figure 4.21. The dimensionless stiffness and damping coefficients as functions of journal equilibrium position are shown in Figures 4.22 and 4.23. The graph in Figure 4.24 shows the stability parameter as a function of eccentricity ratio.

4.7.3 Asymmetrical Helical Groove Journal Bearing

The curves in Figures 4.25 and 4.26 show the dimensionless bearing load and attitude angle respectively. The circumferential pressure and film thickness profiles are plotted in Figure 4.27. The axial pressure profile is shown in Figure 4.28. Figures 4.29 and 4.30 show the linearized coefficients as a function of journal eccentricity ratio. The dimensionless stability parameter vs eccentricity ratio is shown in Figure 4.31.

4.7.4 Partial Helical Groove Journal Bearing

The load capacity and attitude angle graphs are shown in Figures 4.32 and 4.33 respectively. The circumferential pressure and film thickness profiles are given in Figure 4.34. The axial variation of the pressure is shown in Figure 4.35. The curves plotted in Figures 4.36 and 4.37 show the dimensionless stiffness and damping coefficients as functions of eccentricity ratio . The stability parameter of the bearing vs eccentricity is shown in Figure 4.38.

4.7.5 Overall Comparison of the Bearing Performance

4.7.5.1 Bearing Load

It can be seen from Figure 4.39 that in the eccentricity range from 0.6 to 0.8 the load capacity of the plain bearing is appreciably greater than that of the helical groove bearings. However, in the same eccentricity range the load capacity of the partial helical groove bearing is higher than that of the symmetrical and asymmetrical helical groove bearings. The reason for this is because the partial helical groove bearing contains an ungrooved part, which

contributes considerably to the load capacity. The load capacity of both symmetrical and asymmetrical helical groove bearings is almost the same.

4.7.5.2 Attitude Angle

A comparison of attitude angle ϕ between the four types of bearings investigated is made in Figure 4.40. It can be seen that at low eccentricities the symmetrical and asymmetrical bearings are run with a much lower attitude angle as compared with the plain bearing and partial bearing. However, at greater eccentricities, all four bearings run with smaller attitude angle. This is because, in the plain bearing and also in the partial bearing, the large value of attitude angle is due to the fact that the plain bearing derives most of the load capacity from the wedge effect. As the eccentricity increases, the attitude angle becomes smaller because of cavitation and stability is improved. In the case of a grooved bearing, beside the wedge effect, the action of a groove itself is very important. The groove produces a pressure field in addition to that of wedge effect. It is generally known that in the case of the plain journal bearing the wedge effect remains small or vanishes due to whirling motion of the journal at half of the journal speed [16]. However, if the journal in the grooved bearing whirls, pressure will still be generated by the groove effect.

4.7.5.3 Comparison of Stability

The critical mass is determined from the numerical solution of the linearized equations of motion, Appendix H, and is given by equation (4.44). The critical mass as defined by Lund [44] is considered as a measure of

sensitivity of a particular bearing to instability. It gives a quantitative indication of the bearing load at the threshold of instability, below which the bearing is unstable.

In Figure 4.41 the dimensionless critical mass is plotted against eccentricity ratio. It should be noted, that at low eccentricities the plain bearing is the least stable bearing and is followed by the partial bearing. The most stable bearing at low eccentricities is the symmetrical bearing and the stability of the asymmetrical bearing is somewhere between that of the plain and symmetrical bearings. At an eccentricity higher than 0.6, the plain journal bearing is the more stable. In general the vibration amplitude of a rotor is governed by the amount of damping and its critical speed by the stiffness of the bearing oil film . If the machine has to run at low eccentricity then the helical groove journal bearing is a preferred choice. In the case of higher eccentricity operation, a plain journal bearing is preferred because of its load capacity and stability.

4.7.6 Discussion of Theoretical Results

The calculation of pressure in the lubricating film of the helical groove journal bearing was based on the concept of a smoothed pressure. The circumferential pressure and film thickness profiles for the plain journal bearing are shown in Figures 4.13 whilst Figures, 4.20, 4.27 and 4.34 show the same for the helical groove bearings.

The extent of cavitation in the case of the helical groove bearings is much less, as compared to that of the plain journal bearing. The maximum

dimensionless negative pressure at an eccentricity ratio of 0.8 is - 0.0235 in the case of the helical grooved bearing and it is -0.7688 in the case of the plain journal bearing. These values correspond to the bearing boundaries being assumed to be at the atmospheric pressure, i.e gauge pressure. It can be seen, in the case of a bearing with an axial through flow of lubricant, such as asymmetrical helical groove journal bearing Figure 4.27 that the cavitation boundaries are about the same as that in the plain journal bearing, Figure 4.13. The cavitation boundaries of the partial and symmetrical helical groove bearing Figures 4.20 and 4.34 are however different. This is due to the sealing effect of the grooves causing the lubricant to be retained in the bearing, and as a result the pressure inside the bearing is increased . It can be said that for the self-sealing helical groove bearing cavitation may not occur at all. The axial pressure profiles of the plain bearing and the symmetrical bearing Figures 4.14, 4.21 are almost symmetrical at about the mid axial plane. The axial pressure profile of the asymmetrical bearing is plotted in Figure 4.28. The axial pressure profile about the mid axial plane in partial bearing, Figure 4.35 is not symmetric and is in addition much higher over the plain portion of the bearing. Due to this, the bearing tends to become misaligned (as this was observed during experiment) and the stiffness varies along the axial length of the bearing and so affects the stability of the bearing.

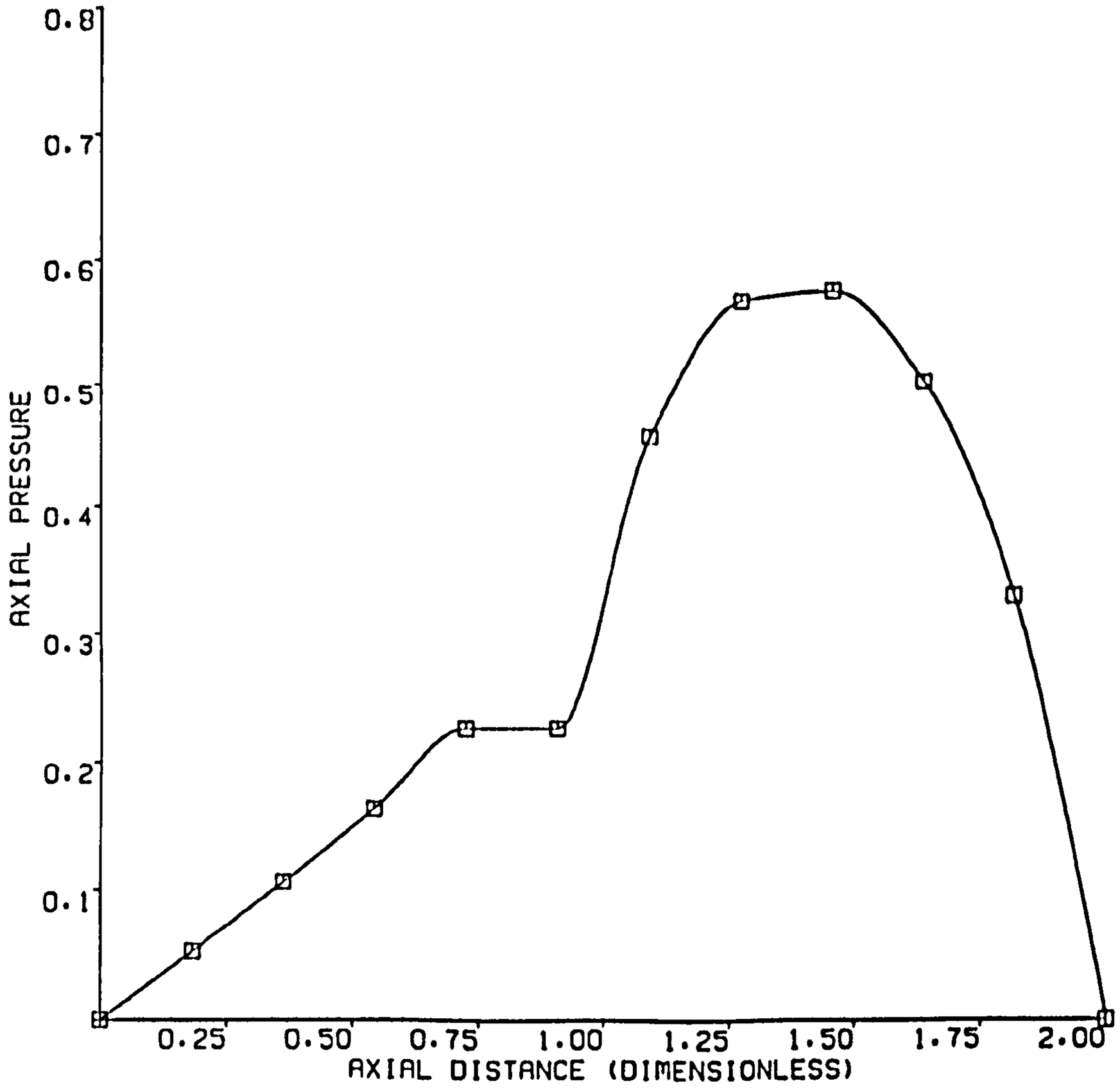

FIGURE 4.35 AXIAL PRESSURE (DIM) VARIATION
AT ECCENTRICITY RATIO OF ex=0.8

PARTIAL HELICAL GROOVE JOURNAL BEARING

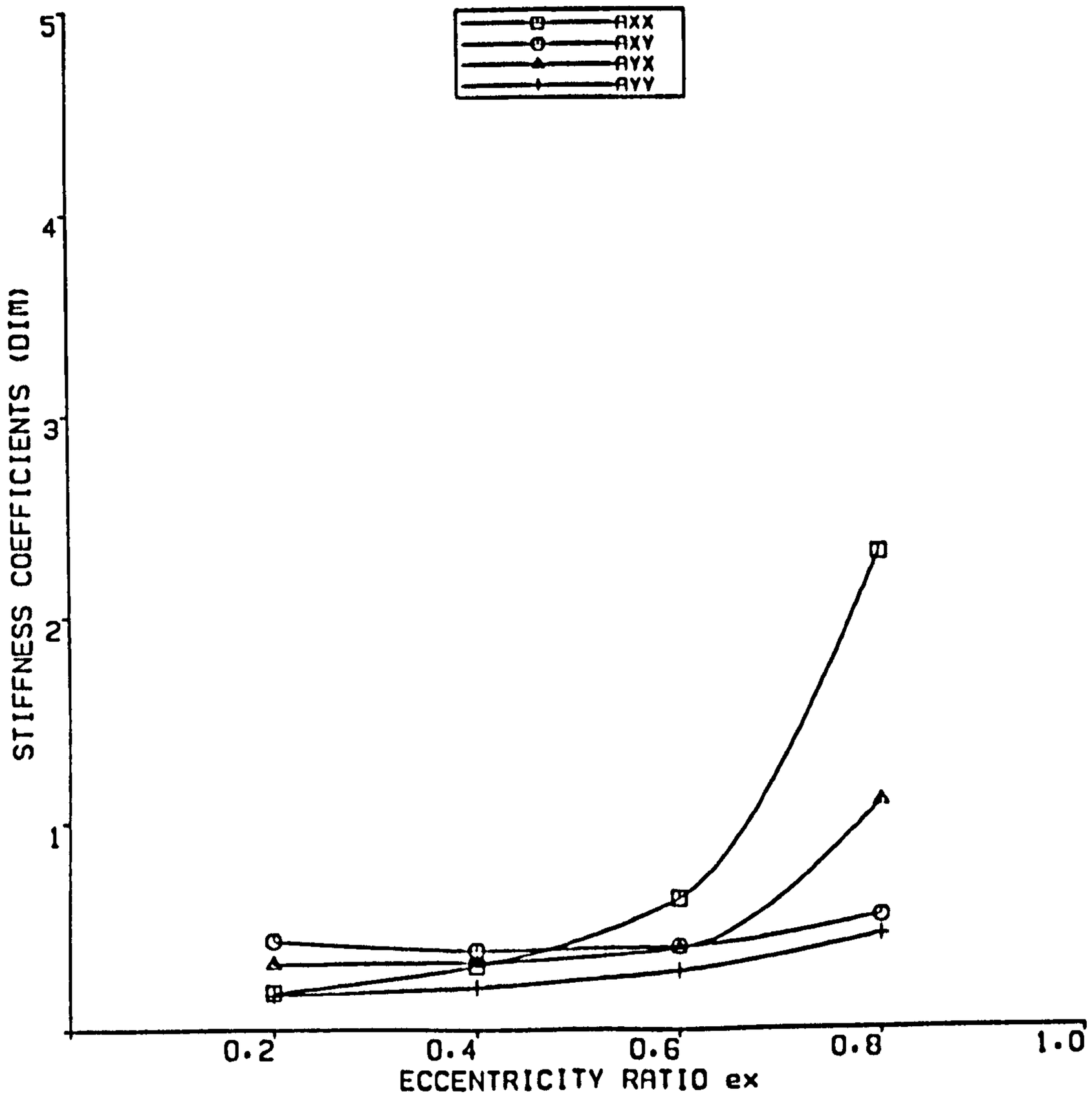

FIGURE 4.36 STIFFNESS COEFFICIENTS
PARTIAL HELICAL GROOVE JOURNAL BEARING L/D= 1

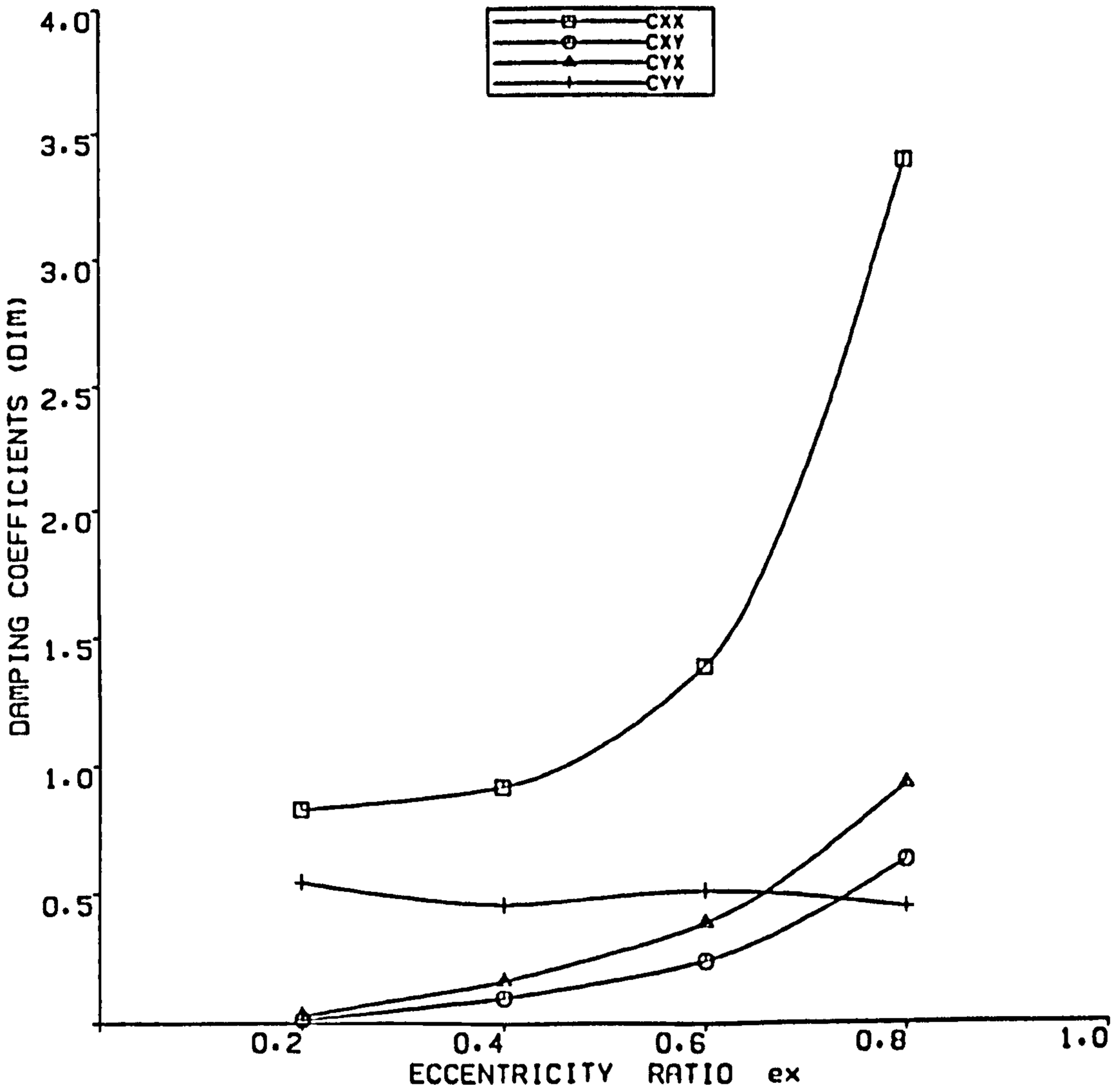

FIGURE 4.37 DAMPING COEFFICIENTS
PARTIAL HELICAL GROOVE JOURNAL BEARING L/D= 1

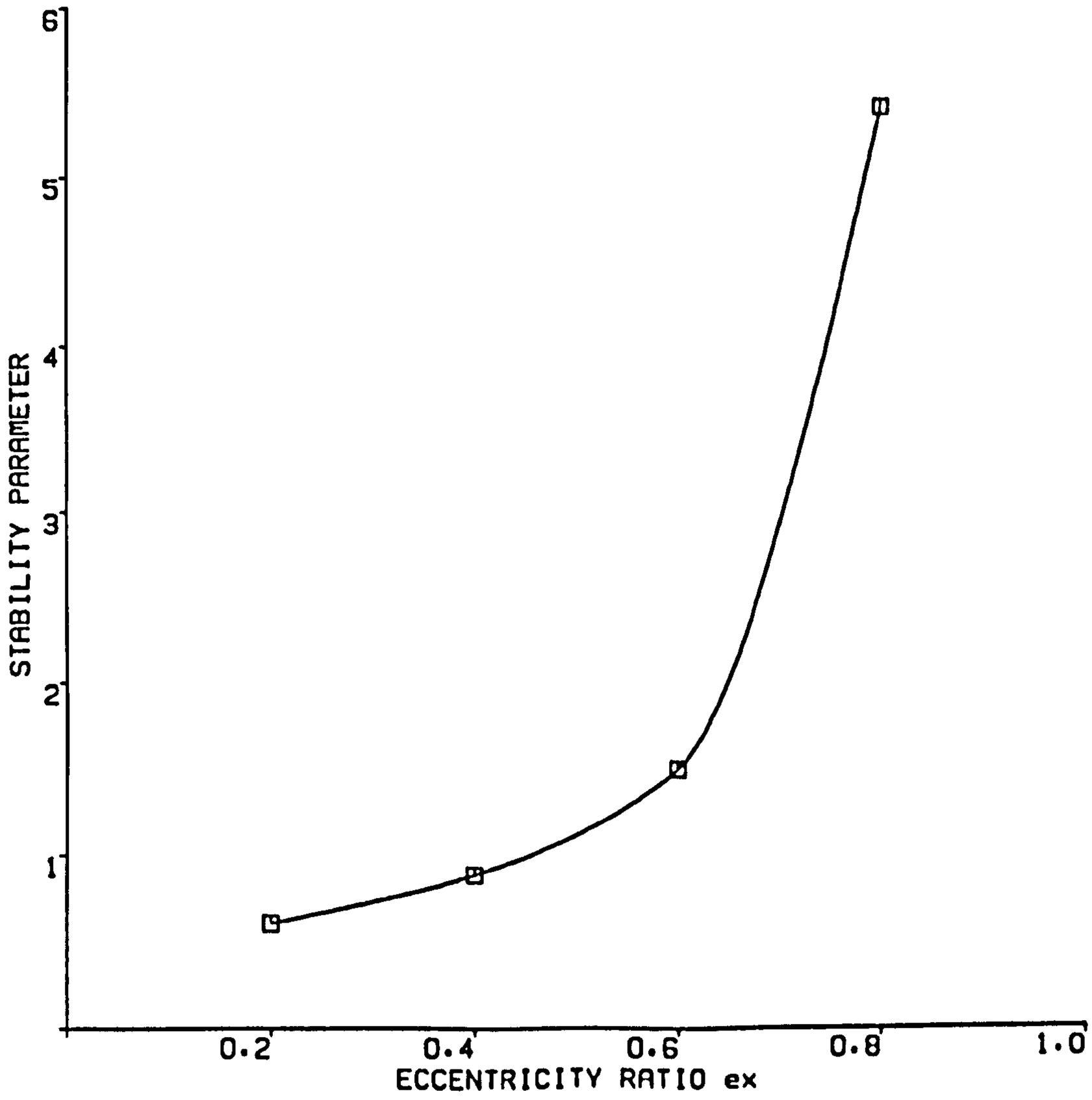

FIGURE 4.38 STABILITY PARAMETER VS ECCENTRICITY RATIO

PARTIAL HELICAL GROOVE JOURNAL BEARING

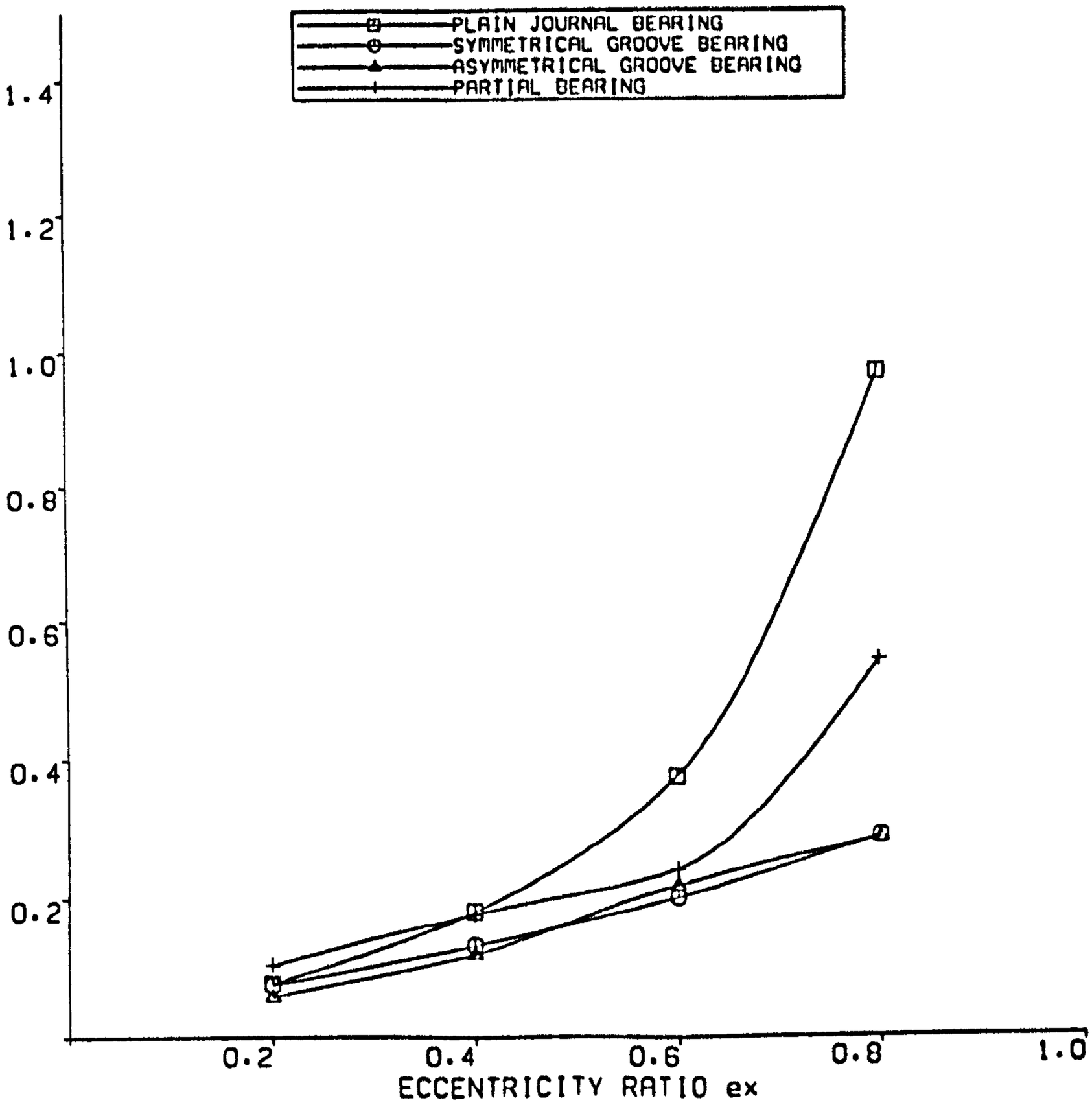

FIGURE 4.39 COMPARISON OF LOAD
OF FOUR TYPES OF BEARING

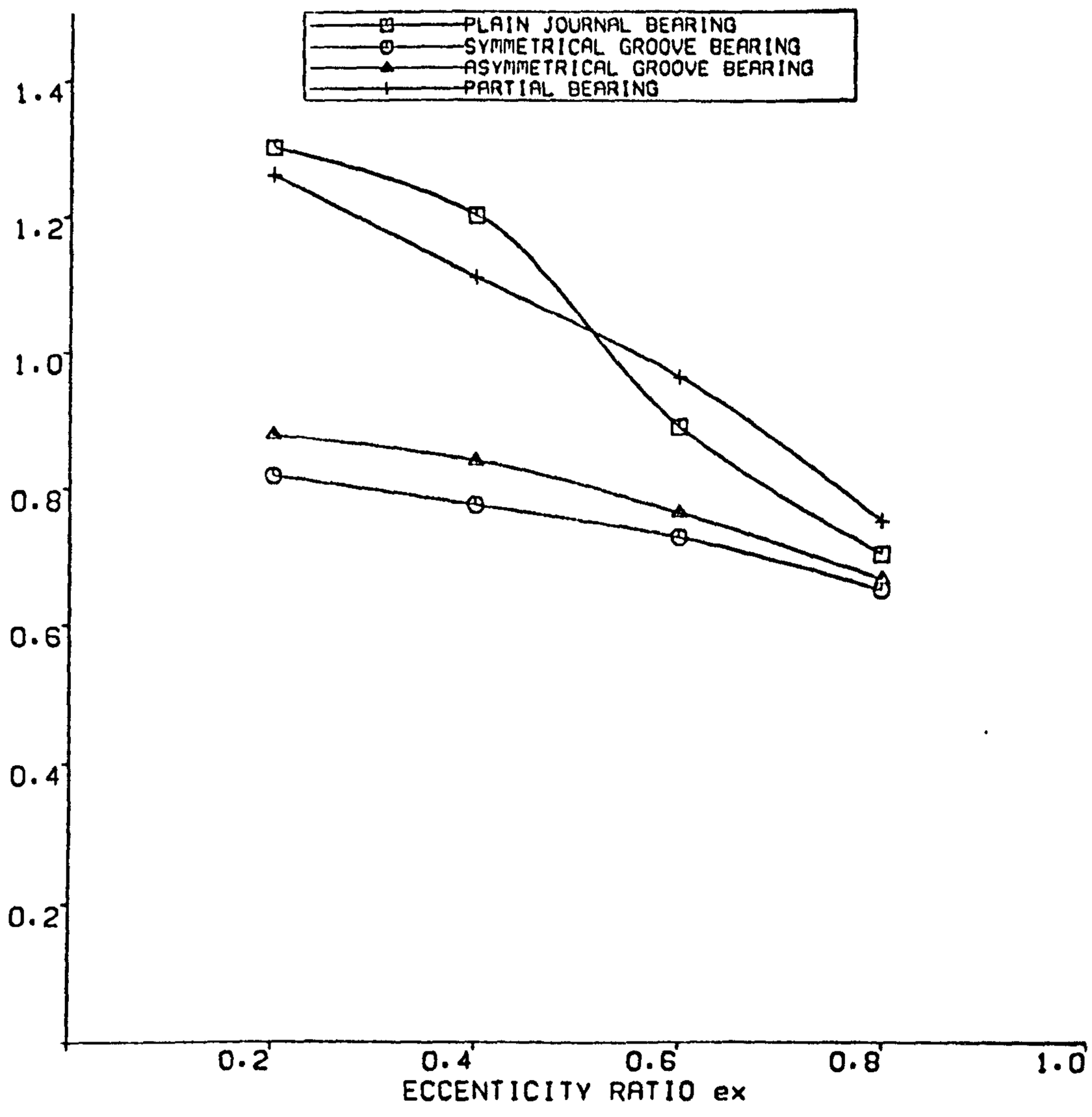

FIGURE 4.40 COMPARISON OF ATTITUDE ANGLE

OF FOUR TYPES OF BEARING

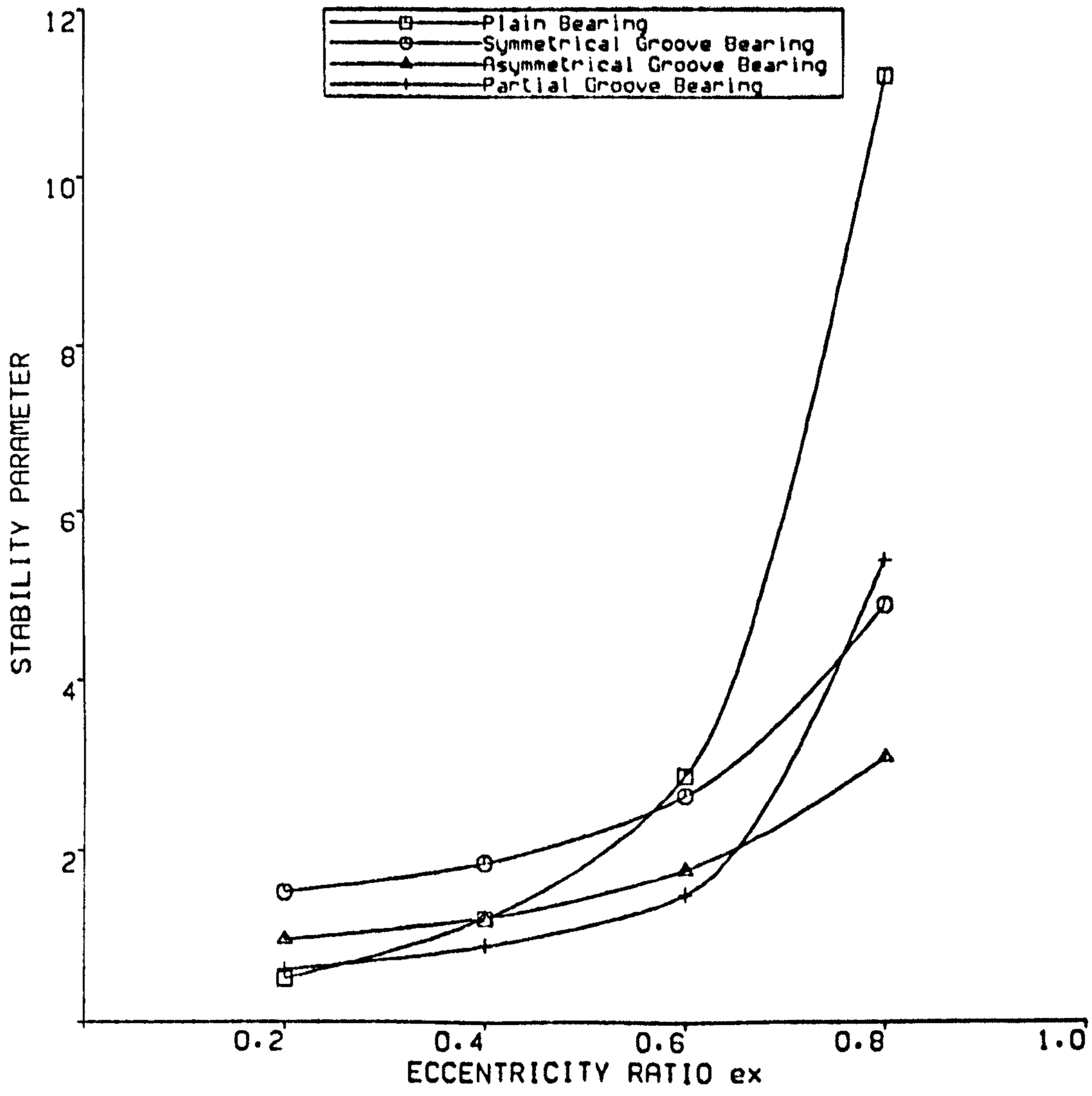

FIGURE 4.41 COMPARISON OF STABILITY
OF FOUR TYPES OF BEARING

CHAPTER 5

COMPARISON OF THEORETICAL AND EXPERIMENTAL RESULTS

5.1 Introduction

In this chapter theoretical results such as the load on the bearing at the threshold of its instability and the static bearing load, determined for the plain bearing and a symmetrical and an asymmetrical groove bearings, are compared with experimental results. The theoretical results for the partial bearing are not compared with experimental data because this bearing was only tested at the concentric position for reasons described in Chapter 3.

In general, there is fairly good agreement between the bearing loads determined theoretically and those obtained experimentally. However, the theoretical loads tended to be slightly higher than those found experimentally.

The main difference between the model results and experiment results is in the area of bearing contribution to rotor stability. The present model overestimates the stability. It is known that the stability of a rotor bearing system is influenced by the stiffness and damping properties of the bearing. If these properties are determined theoretically then they are governed by :

1) The accuracy of the numerical solution of the Reynolds equation and its boundary conditions.

2) The running conditions of the bearing represented by the Sommerfeld number [53]

$$S = \frac{N\mu}{60P} \left(\frac{R}{C}\right)^2 \qquad (5.1)$$

where, N = speed (rpm)

C/R = Clearance ratio

μ = Viscosity of the lubricant

P = Bearing pressure N/m^2

The significance of running conditions will be discussed when comparing the theoretical and experimental results for each type of bearing tested.

5.2 Quantitative Comparison

In order to compare theoretical and experimental results quantitatively a correlation coefficient was used [54]. The correlation coefficient which measures the degree of correlation is given as:

$$r = \frac{\sum_{i=1}^{n} (x_i-\bar{x})\,(y_i-\bar{y})}{\sqrt{\left[\sum_{i=1}^{n} (x_i-\bar{x})^2\right]\left[\sum_{i=1}^{n} (y_i-\bar{y})^2\right]}} \qquad (5.2)$$

or,

$$r = \frac{\Sigma d_x d_y}{\sqrt{(\Sigma d_x^2)\ (\Sigma d_y^2)}}$$

where,

x_i - Denotes each theoretical value.

$\bar{x}$ - Denotes the mean value of the theoretical values.

$d_x=(x_i-\bar{x})$, deviation of each theoretical value from the mean.

y_i - Denotes each experimental value.

$\bar{y}$ - Denotes the mean value of all experimental values.

$d_y=(y_i - \bar{y})$, deviation of each experimental value from the mean.

$\Sigma d_x d_y$ Sum of the product of the deviations from the mean.

Σd_x Sum of the deviation of the theoretical data from the mean.

Σd_y Sum of the deviation of the experimental data from the mean.

The values of the sum of the product and the values of the sum of the mean are substituted in the correlation formula. The value of r is calculated and if it is equal to 1 then there is perfect correlation. If the value of r is equal to zero then there is no correlation.

5.3 Plain Bearing

5.3.1 Bearing Load

Theoretical and experimental values of load at various eccentricities are plotted in Figure 5.1. It can be seen that the two curves are close to each other, have similar shape and show the same trend. The correlation between them is 0.8 It can therefore be said that there is good quantitative agreement between the theoretical and experimental bearing load. However, at low and high eccentricity ratios, the theoretical results deviate from the experimental results. The results calculated by the theoretical model were based on a constant viscosity assumption. At a speed of 3000 rpm, the change of load from 8896 N to 11120 N resulted in

a temperature increase of about 4^0C in the minimum film region, Figure 5.1. At an eccentricity ratio of 0.8 the corresponding experimental load on the bearing was about 22000 N and therefore the temperature increase in the minimum film region would have to be higher. It is known, that a model that does not take in to account variable viscosity produces higher theoretical loads [57].

5.3.2 Stability

For a given journal speed, static load, and equilibrium eccentricity the bearing load at the threshold of instability was determined experimentally. The theoretical value of the critical load was calculated for the same speed and eccentricity ratio used during experiments. The following input data were used:

Journal speed = 2000 rpm

Bearing housing weight = 110 kgf

Stability parameter at eccentricity ratio of 0.65 from Figure 4.17 = 3.65

Radial bearing clearance = 0.125 mm

According to equation (4.44) the stability parameter is :

$$S_p = \frac{M\ C\ \omega^2}{W_b}$$

$$W_b = \frac{M\ C\omega^2}{S_p}$$

i.e w_b = 1612.6 [N]

The above example shows that at a speed of 2000 rpm and eccentricity ratio of 0.65 the journal will become unstable below a load on the bearing of 1612.6 N. The calculated and measured values of critical bearing load at the threshold of

instability are plotted in Figure 5.2. The comparison shows that at each speed the theoretical bearing load required to keep the journal stable is lower than the experimentally determined load. The correlation between theory and experiment is about 0.31 which points to rather poor quantitative agreement. However, it has to be pointed out that qualitative agreement between theory and experiment is quite good as indicated by the shape and trend of the curves in Figure 5.2. A number of reasons can be identified to account for the discrepancy between theory and experiment. In the theoretical model the viscosity of the lubricant was assumed constant. During the experiments when the oil inlet temperature was about 40 °C a rise in temperature of 30 ° C in temperature of the lubricant was quite possible due to the high shearing rates within the lubricating film. Besides, under certain conditions the film thickness profile, which is affected by the geometry of the bearing bore, loading and thermal effects is different in practice to the one used in the Reynolds equation [53]. A model which does not take into account the viscosity variation around the bearing calculations higher pressures within the oil film than there are in reality. Due to viscosity variation the equilibrium position of the shaft can also be different. These factors undoubtedly affect the stiffness and damping coefficients of the bearing and hence the critical bearing load..

Using short bearing theory and utilizing an exponentional relationship between temperature and viscosity Nikolajsen [55] showed that the instability threshold boundary can be increased. In this way, for example, the present model could be tuned to give better quantitative agreement with experiment.

5.4 Symmetrical Helical Groove Bearing

5.4.1 Bearing Load

Theoretical and measured loads at a speed of 3000 rpm and at different eccentricity ratios are compared in Figure 5.3. The theoretical model predicts slightly higher loads as compared to the measured loads. The correlation coefficient is 0.78 which points to reasonable quantitative agreement between theory and experiment and as in the case of the plain bearing, the qualitative agreement is also good. As before, the reason for the discrepancy is most probably the constant lubricant viscosity assumption in the model.

5.4.2 Stability

The experimental and theoretical loads at the threshold of instability are compared in Figure 5.4. It can be seen that there is a substantial difference between them. The correlation coefficient in this case is about 0.12. Although it points to poor quantitative agreement, nevertheless, the qualitative agreement is acceptable. The shape and trend of both the curves is the same and it seems that the model requires some modification to bring its predictions into line with experiment. The most obvious remedy is to relax the constant viscosity assumption. In addition in a helical groove bearing the performance characteristics depend upon the groove parameters such as, groove angle, ratio of groove width to ridge width, ratio of groove clearance to ridge clearance, etc. These parameters have been optimized by various authors [12, 15, 56] in order to secure optimum bearing performance. The optimum groove dimensions used in the model are given in Chapter 2 Section 2.2. In the model it is assumed that these dimensions are constant. However, in practice the bearing does have variations, for example, in

groove depth, which has an important affect on the load and stability of the bearing. Moreover, the stability of the bearing is known to be effected by the ratio of groove depth to ridge clearance [19,56]. These variations in the geometry of experimental bearing are bound to contribute to the discrepancy between theoretical and experimental results.

5. 5 Asymmetrical Helical Groove Bearing

The nominal dimensions of the bearing and the groove parameters of this type of bearing were the same as that of the symmetrical bearing. The arrangement of the groove length along the axial length of the bearing was however different and is detailed in Figure 2.12.

5.5.1. Bearing Load

As mentioned in Chapter 3, Section 3.3.6, the asymmetrical bearing was stable up to a speed of 1280 rpm without any load on the bearing. Above this speed the bearing was unstable below an eccentricity ratio of 0.7. Thus it was only possible to measure the load on the bearing above the eccentricity ratio of 0.7 and so the experimental data is limited to one measurement for each speed. The data is presented in Table 5.1. With one experimental data point for each speed it is difficult to draw firm conclusions. However, the trend of the relationship of the load with speed is the same in both the theoretical and experimented results. The higher theoretical loads seem to be due, as before, to the constant viscosity assumption.

Table 5.1

Eccentricity ratio	Speed rpm	Theoretical load	Experimental load
0.72	2000	4928 N	6672 N
0.85	3000	9483 N	8896 N
0.9	4000	11530 N	11200 N

5.5.2 Stability

Calculated and measured loads at the threshold of bearing instability are compared in Figure 5.5. The correlation coefficient between the results of model and experiment is about 0.1. The quantitative agreement between the theoretically calculated stability, represented by the critical load, and the experimentally determined value of load at the threshold of the bearing instability is poor. However, both curves shown in Figure 5.5 have the same trend and almost the same shape. The gap between the two curves could probably be reduced by relaxing the constant viscosity assumption. The performance of the helical groove bearing like the performance of other bearings depends upon the precision with which it was manufactured. Both the load capacity and stability of the helical bearing are adversely affected by any departure from the optimum groove geometry [19,56]. This provided further reason for the observed discrepancies between the results of the model and those of experiment.

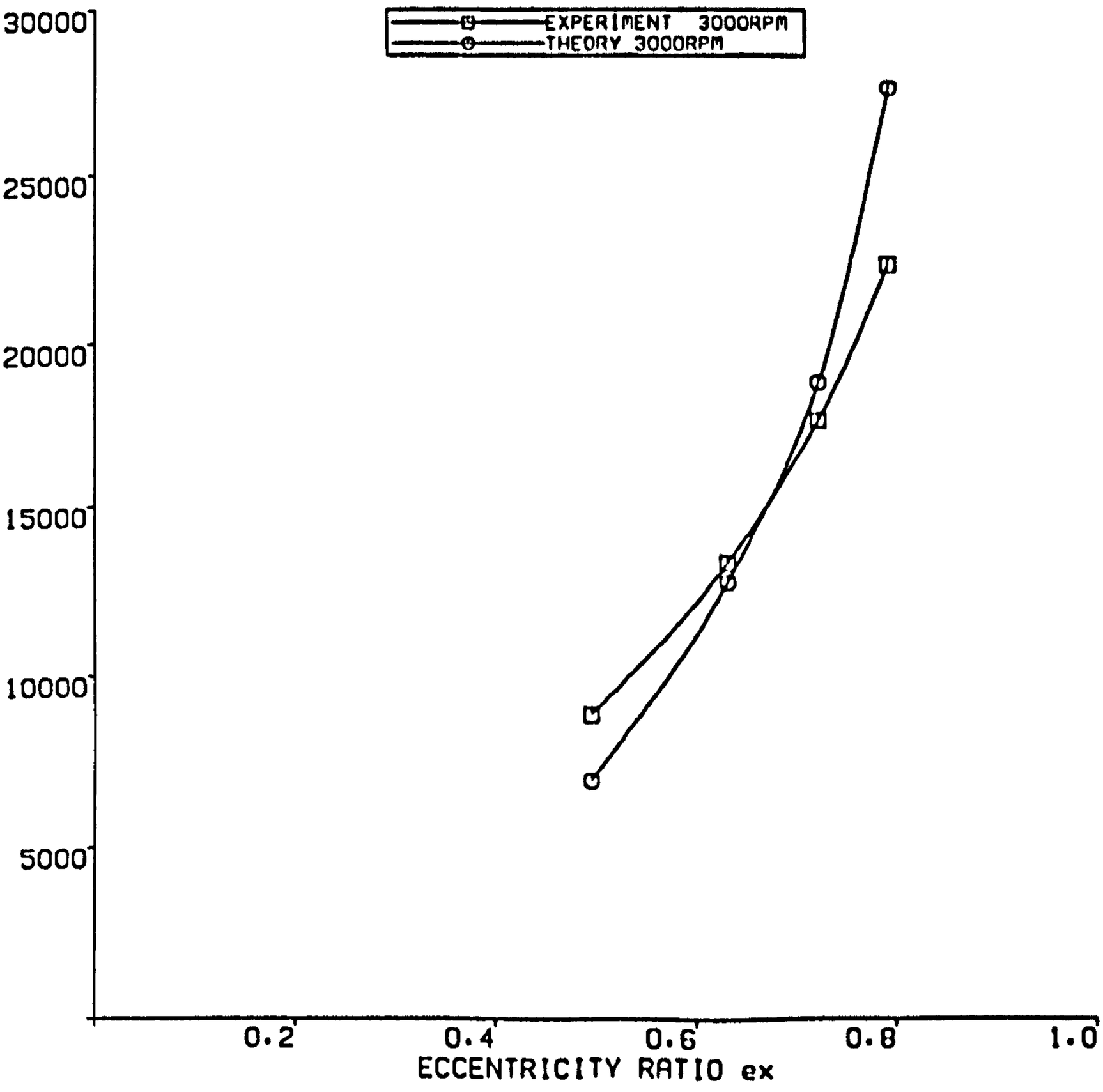

FIGURE 5.1, LOAD CAPACITY

PLAIN JOURNAL BEARING

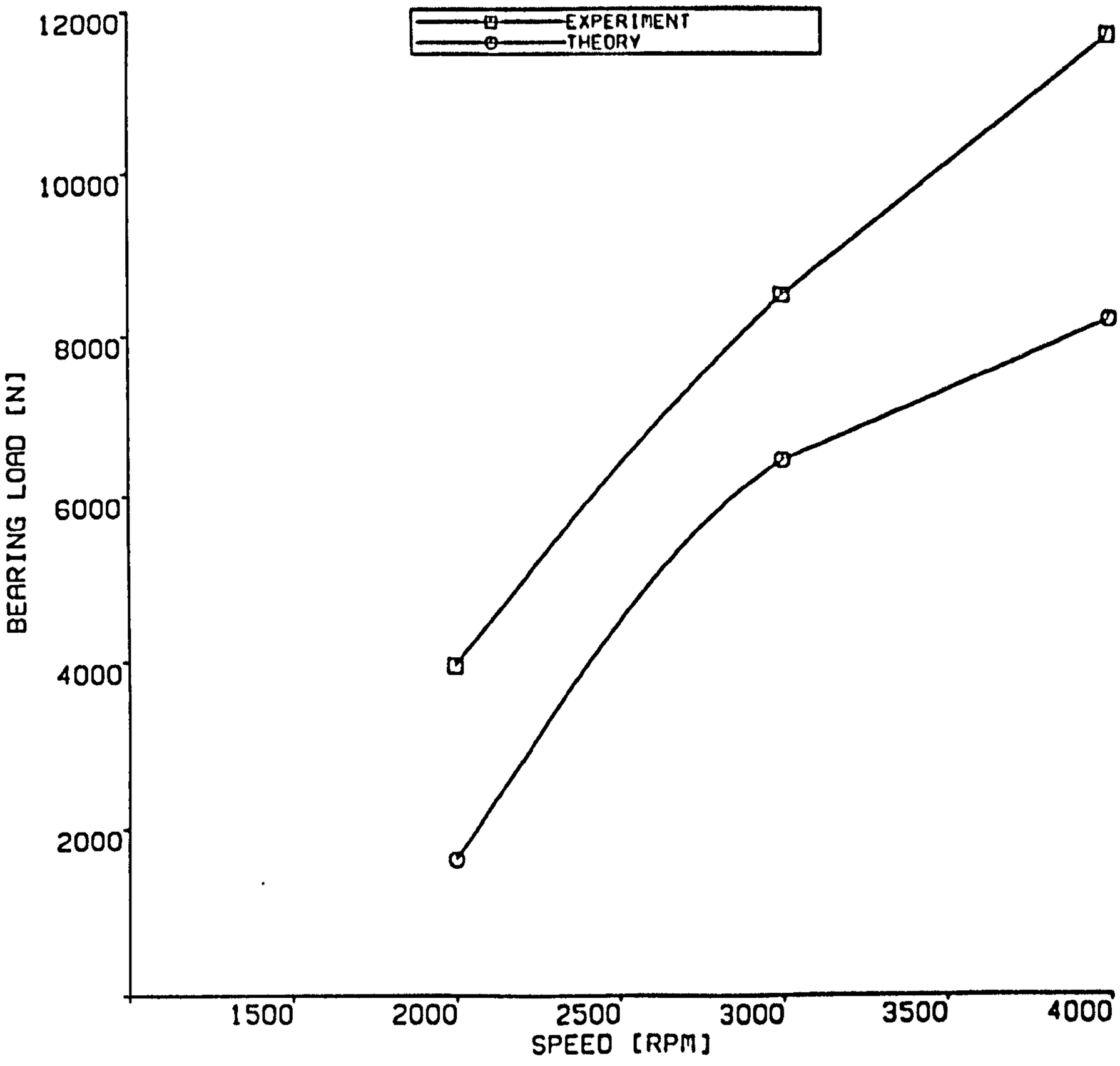

FIGURE 5.2 ,COMPARISON OF
BEARING LOAD AT THRESHOLD OF INSTABILITY

PLAIN JOURNAL BEARING

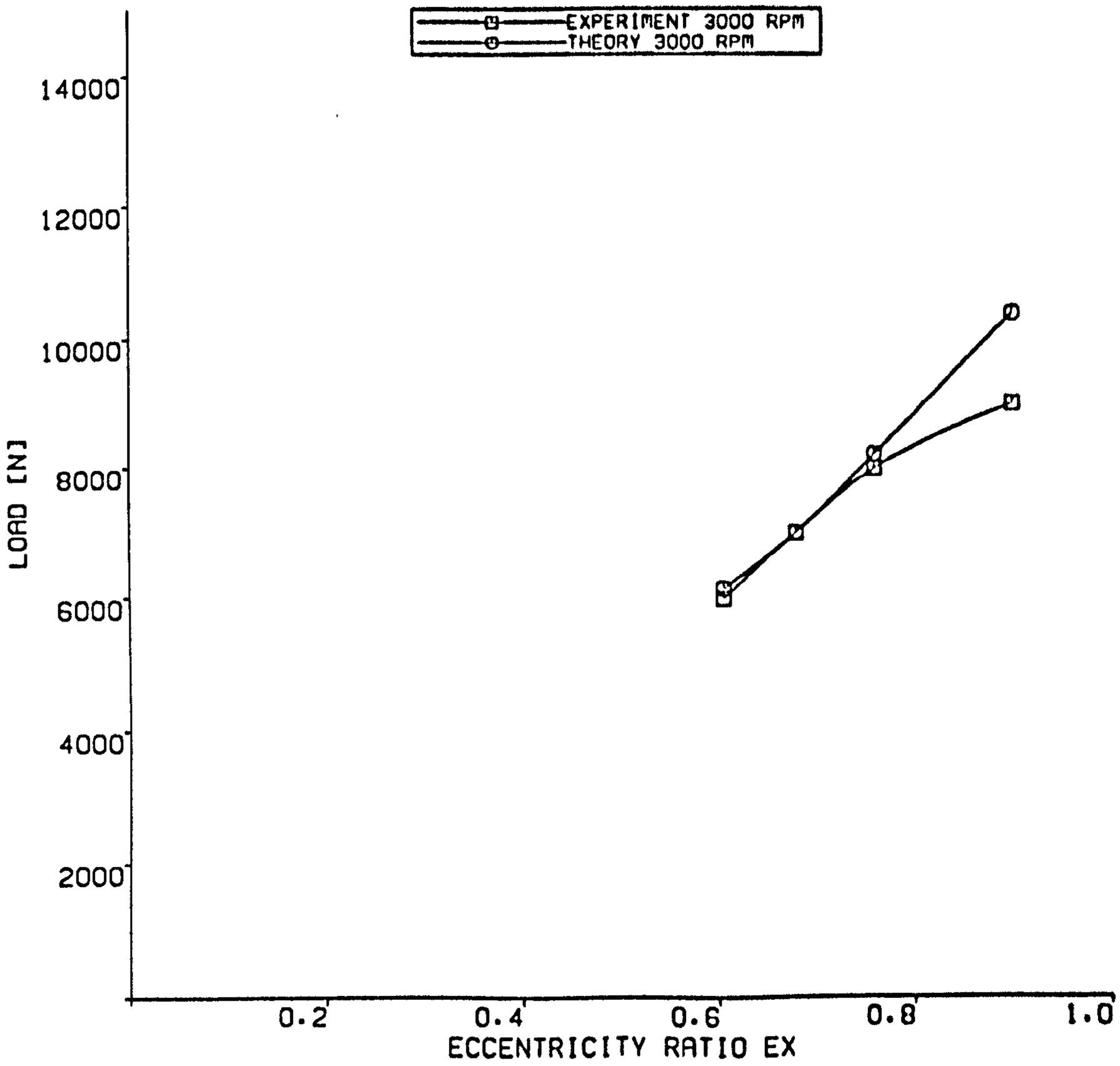

FIGURE 5.3 COMPARISON OF LOAD CAPACITY

SYMMETRICAL HELICAL GROOVE JOURNAL BEARING

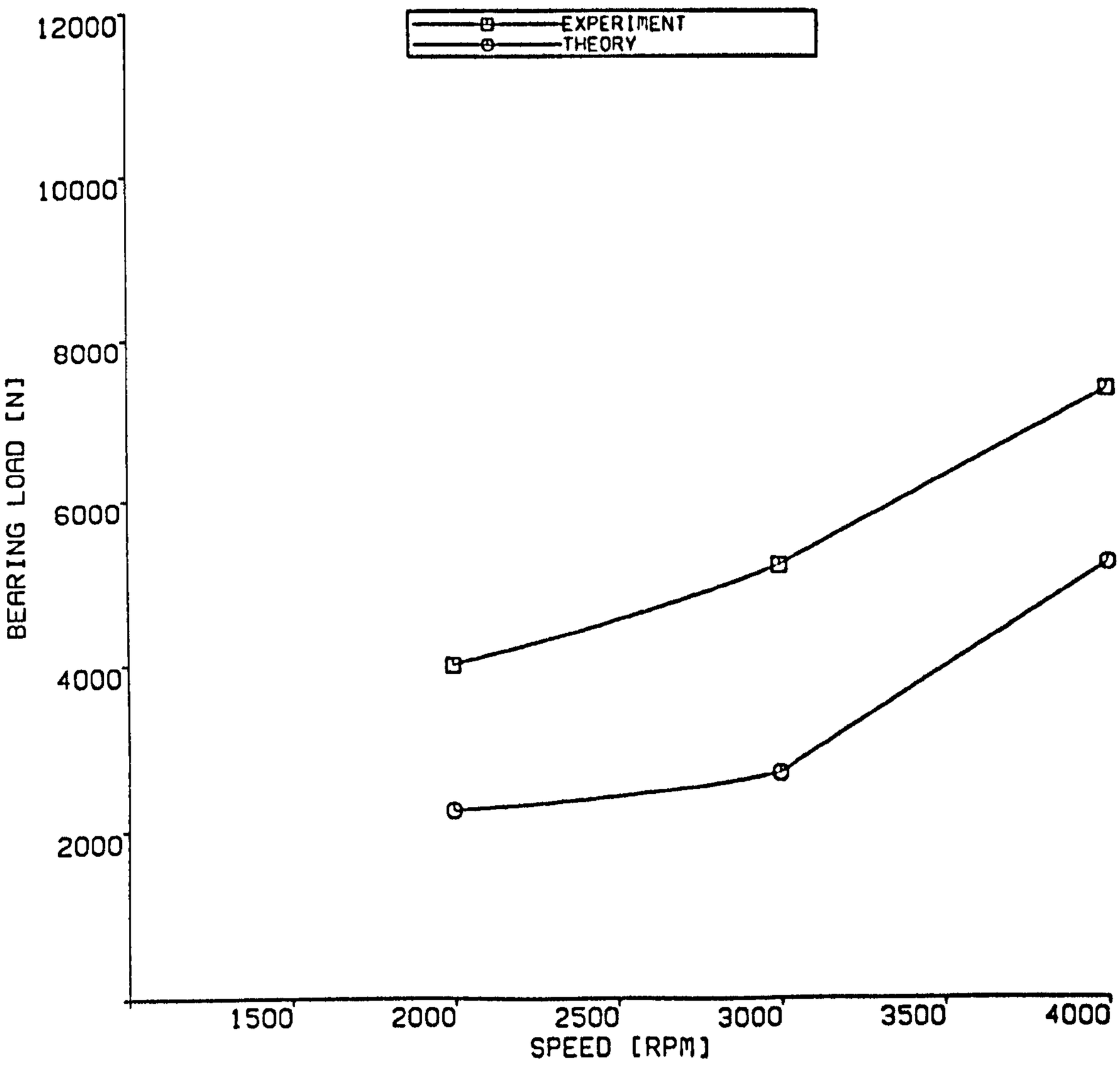

FIGURE 5.4 ,COMPARISON OF
BEARING LOAD AT THRESHOLD OF INSTABILITY

SYMMETRICAL HELICAL GROOVE JOURNAL BEARING

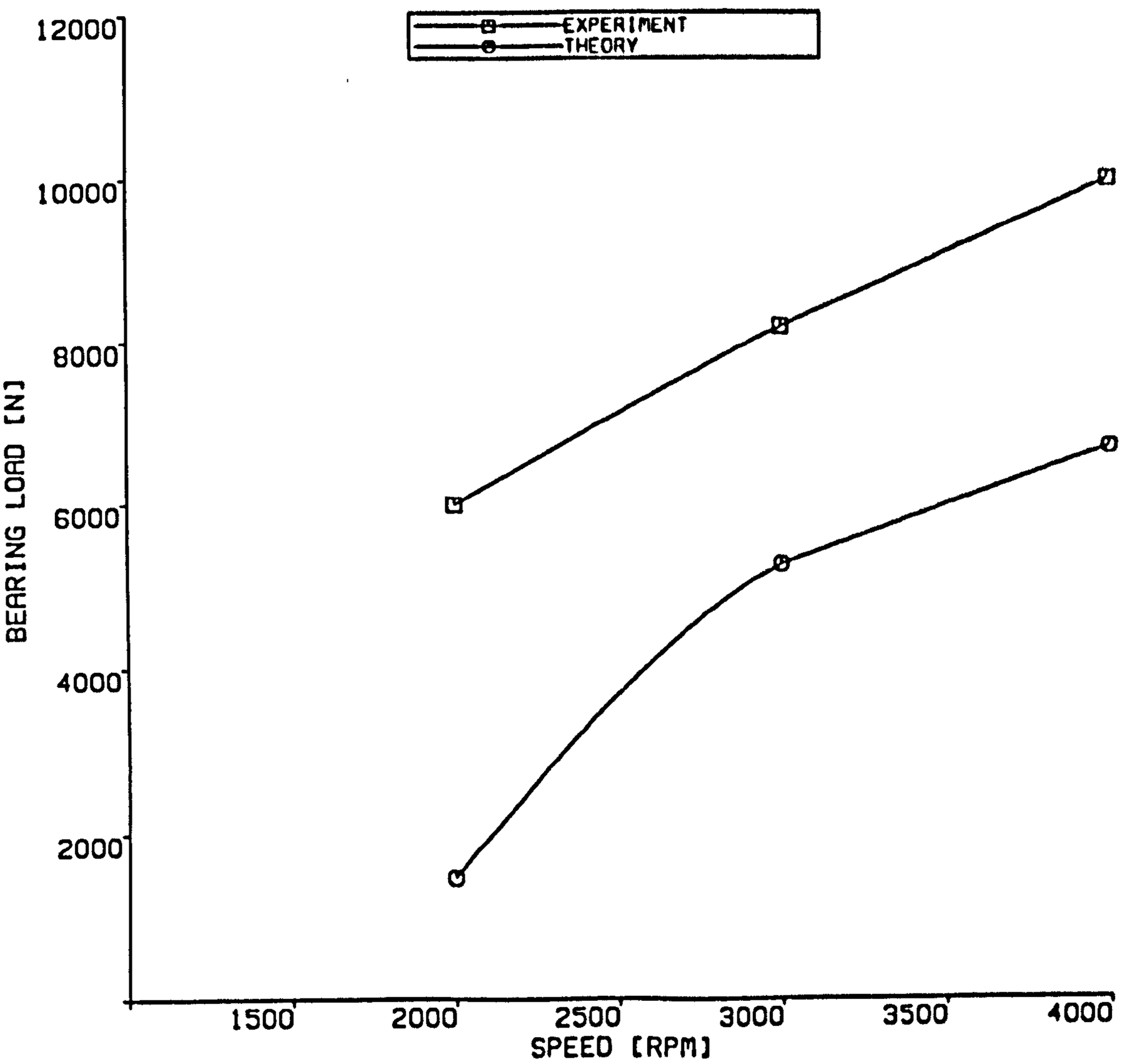

FIGURE 5.5 COMPARISON OF
BEARING LOAD AT THRESHOLD OF INSTABILITY

ASYMMETRICAL HELICAL GROOVE JOURNAL BEARING

CHAPTER 6

CONCLUSIONS

The experimental and theoretical studies have been conducted in order to determine the steady state and dynamic performance of a plain journal bearing and three types of helical groove journal bearing namely, a symmetrical, asymmetrical and partial groove bearing. On the basis of the results the following conclusions can be formulated:

(1) The load carrying capacity of the helical groove bearing is about half of the plain journal bearing as determined theoretically and experimentially.

(2) Under the same conditions of load and speed it was observed during experiment that the symmetrical helical groove bearing ran about 13.5 °C hotter than the other three bearings.

(3) The estimated power losses of the symmetrical bearing is 0.965 to 1.1 kW greater than those of the other three bearings studied experimentially.

(4) The symmetrical and asymmetrical bearings allows stable running at the speeds of 1645 rpm and at 1280 rpm respectively without any applied load. However, above these speeds the load must be applied to maintain stability. At higher eccentricity ratios, the plain bearing is more stable than the grooved bearing. It was observed in case of symmetrical helical groove bearing that below the threshold of instability the size of the whirl orbit remains restricted, where as in the case of the plain journal bearing the whirl amplitude grows rapidly. This can be regarded as an advantage of the

grooved bearing in the case of high amplitude vibration.

(5) The partial helical groove bearing is not a practical bearing because the bearing becomes misaligned when loaded above 2224 N.

(6) Depending upon the boundary conditions, the extent of cavitation in the helical groove bearing is much less than that in the plain journal bearing.

(7) The stability of the helical groove bearing generally does not increases so rapidly as that of plain bearing with increase in eccentricity ratio, particular a higher eccentricity ratio.

The overall conclusion of the investigation is that if a bearing of a turbo-machine has to run at low eccentricity ratios then a helical groove bearing could improve its margin of stability. In case of higher eccentricities, however, the plain journal bearing is the better choice because of its greater stability and higher load capacity.

Two additional lines of study can be suggested, they are :

(1) For high speed and light load it is important that the bearing should run stable and cool. For this purpose the asymmetrical bearing should be further optimized.

(2) A journal bearing with a circumferential groove in the middle and only few helical grooves ought to be investigated. In such a bearing the direction of the helical groove should interact with rotation of the journal in order to pump the lubricant toward the end of the bearing. This type of bearing could be more stable and have increased load capacity. Besides,the better removal of the heat due to the outward pumping action of the grooves, would probably ensure cooler running of the bearing.

REFERENCES

[1] Newkirk,N.Y, Varieties of the Shaft Disturbances due to Fluid Film in Journal bearings, Trans. ASME, Journal of Lubrication Technology, pp.985-988, July 1956.

[2] Sternlicht, B. and Rieger, N.F., Rotor Stability, Proc. Institute of Mech Engrs, Vol. 182, Pt. 3a, pp. 82-89, 1967-1968.

[3] Akkok, M. and Ettles.C.M.M., The Onset of Whirl Instability in Journal Bearings of Various Bore Shape and Groove Size, Journal of Lubrication Technology, Vol. 105, pp. 342-352, July 1983.

[4] Gozdawa, R.J., Design Problems in Turbo Machinery Bearing Selection, Charted Mechanical Engineers, pp.45-48. Sept 1986.

[5] Whipple, R.T.P., Herringbone Pattern Thrust Bearing, AERE T/M 29, 1949.

[6] Muijderman, E.A., New Possibilities for the Solution of Journal Bearing Problems by Mean of Spiral Groove Principle, Proc. Inst. of Mech. Eng., 1965-1966.

[7] Muijerderman, E.A., Spiral Groove Bearings. Cleaver-Hume Press, 1966

[8] Pinkus, O. and Sternlicht, B., Theory of Hydrodynamic Lubrication. McGraw Hill, 1961.

[9] Cameron, A., The Principles of Lubrication, Longman Green and Co Ltd, 1966.

[10] Vohr, J.H. and Chow C.Y., Characteristics of Herringbone Grooved Gas Lubricated Journal Bearings. Trans. ASME, Vol. 87, No. 3, pp. 568-578, Sept 1965.

[11] Hirs, G.S., The Load Capacity and Stability Characteristic of Hydrodynamic Grooved Journal Bearings, ASLE Trans, Vol. 8, pp. 296-305. 1965.

[12] Bootsma, J., The Gas Liquid Interface and Load Capacity of Helical Groove Journal Bearings, Trans. ASME, Journal of Lubrication Technology, pp. 94-100, Jan. 1973.

[13] Bootsma, J., The Gas to Liquid Interface of Spiral Grooved Journal Bearings and its Effects on Stability, Journal of Lubrication Technology, pp. 337-345, July, 1974.

[14] Castelli, V. and Vohr, J H., Performance Characteristics of a Herringbone Grooved Journal Bearing Operating at High Eccentricity Ratio with Misalignment, University of Southampton, Department of Mechanical Engineering, Gas Bearing Symposium, April, 1967.

[15] Smally, A.J., The Narrow Groove Theory of Spiral Groove Gas Bearings Development and Application of a Generalized Formula for Numerical Solution, Trans. ASME, Journal of Lubrication Tech. Vol. 94, pp. 86-92, 1972.

[16] Reinhoudt, J.P., On the Stability of Rotor and Bearing System and on the Calculation of Sliding Bearings, Phillips Res. Report Supp., vol. 1, 1972

[17] Yavelov, I.S., Finite Element Method Analysis of Hydrodynamic Bearings with Spiral Grooves, Trenie Izones, Vol. 5, 6, pp. 878-884, 1985.

[18] Yavelov, I.S., On the Influence of Spiral Groove Depth on the Experimental Characteristic of Radial Hydrodynamic Bearings, Trenie Iznos Vol. 4, No. 1, pp. 134-146, 1983.

[19] Schuller, F.T. and Fleming, D.P. Experiments on the Stability of Water Lubricated Herringbone Groove Journal Bearings Effects of Configuration and Groove to Ridge Clearance Ratio, Lewis Research Centre, Cleveland, Ohio, Feb. 12, 1970.

[20] Fleming, D.P. and Hamrock, B.J., Optimization of Self-Acting Herring Bone Journal Bearing for Maximum Stability. 6th International Gas Bearing Symposium, University of Southamption England, March 27-29, pp. 1974

[21] Hirs, G.G., A New Method for Etching the Surfaces of Bearings and Other Machine Elements, Trans. ASME, Journal of Lubrication Technology, Vol. 102, pp. 395-401, July 1980,

[22] Muijderman, E.A, et al., Grease Lubricated Spiral Groove Bearings, Phillips Tech. Rev. 39, No. 6/7, pp. 187-199, 1980.

[23] Cunning, R.E. and Fleming, D.P., Experimental Stability Studies of the Herringbone Grooved Gas Lubricated Journal Bearing, Trans. ASME, Journal of Lubrications Technology, Jan. 1965.

[24] Malanski, S.B., Experiments on a Ultrastable Gas Journal Bearing, Trans ASME, Journal of Lubrication Technology, Oct. pp. 52-58, 1967.

[25] Molyneaux, A. K., et al., The Use of Spiral Groove Gas Bearings in a 350000 rpm Cryogenic Expander. STLE Tribology Transaction, Vol.32, 1989.

[26] Yang, K.J. and Munday, A.J., *A Groove Self Acting Gas Bearing for Use* in a Cryogenic Expansion Turbine, Conference Cryogenic Processes and Equipment, Los Angles, USA. 1982.

[27] Bos, J. G. G., Grease Lubricated Bearing, Phillips Tech. Rev. 35, 137, 1975, pp 137-141.

[28] Muijderman, E.A., Grease Lubricated Spiral Groove Bearings, Tribology International, pp. 131-137. June, 1979.

[29] Dewar, D.M., An Analysis of Groove and Oil Lubricated Spiral Grooved Bearings, Trans. ASME, Journal of Lubrication Technology, pp. 275-283, April, 1974.

[30] Fedrick, T, et al., Operation of Hydrodynamic Journal Bearings in Sodium at a Temperature of 800 °F. National Aeronatuic and Space Administration, Lewis Research Centre Cleveland Ohio, August 10, 1967

[31] Fedrick, T, et al., Theoretical Consideration and Clearance Effects. National Aeronautic and Space Administration, Lewis Research Centre, Cleveland,, August, 1967.

[32] Chow, C.Y. and Vohr, J.H., Helical Groove Journal Bearing Operated in Turbulence Regime, Trans. ASME, Journal of Lubrication Technology, pp. 346-357, April 1970.

[33] Bootsma, J., The Effects of Viscosity Variation with Temperature on the Performance of Spiral Groove Thrust Bearings. ASLE Transactions, No.12, 1964.

[34] Chow, C.Y., Dynamic Characteristic and Stability of Helical Groove Floating Ring Journal Bearing Operated in the Turbulent Regime. ASLE Trans. Vol. 2, pp 154- 163, 1983.

[35] Yavelov, I.S., Characteristics of Radial Hydrodynamic Bearing with Spiral Grooves, Mashinovednie, Part No. 3, 1981.

[36] Yavelov, I.S., Characteristics of Loaded Hydrodynamic Journal Bearing Spiral Grooves, Soviet Journal of Fiction and Wear, Vol. 8, Part No. 3, 1987.

[37] Nobuyoshi, K., Yasumi Ozawa Shuji Kamaya and Mutaka Miyake., Static Characteristics of the Regular and Reversible Rotation type Herringbone Grooved Journal bearing, Trans. ASME, Journal of Tribology, Vol. 11, pp. 484-490, July 1989.

[38] Hirs, G.S., Externally Pressurized Bearing with Inherent Friction Compensation, Trans. ASME, Journal of Lubrication Technology, pp. 285-V 289, June, 1965.

[39] Vohr, J.H., and Chow, C.Y., Theoretical Analysis of Spiral Grooved Screw Seal for Turbulent Operation, Trans. ASME, Journal of Lubrication Technology, pp. 676-684. Oct. 1969.

[40] Heitel, K., Concentric and Eccentric Running Screw Seals with Laminar Flow Theory and Experiment, 8th International Conference on Fluid Sealing, pp. 11-13th September, 1978.

[41] Harangozo, A.V., An Investigation in to the Effects of Lubrication Methods on the Performance of the Tilting Pad Journal Bearing, Ph.D. Thesis, Dept. of Mech. Eng., Brunel University, March 1990.

[42] Reddi, M.M., Finite Element Solution of the Incompressible Lubrication Problem. Journal of Lubrication Technology, Trans. ASME, pp. 524-533, July, 1969.

[43] Lund, J.W., Rotor Bearing Dynamics Design Technology, Part III, Design Handbook for Fluid Film Type Bearings, Report No. AFAPL TR65-45, Air Force Aero Propulsion laboratory, 1965.

[44] Lund, J.W., Review of the Concept of Dynamic Coefficient for Fluid Film Journal Bearings, Trans. ASME, Journal of Tribology, Vol. 109, pp. June, 1987.

[45] Narret, L.E., Allaire, P.E., and Gunter, E. J., Stability and Dynamic Response of Pressurised Journal Bearings with Nuclear Water Pump Application, Annals of Nuclear Energy, Vol.[47] Akkok, M. and Ettles, C.M.M., The Effects of Load and Feed Pressure on Whirl in a Grooved Journal Bearing, ASLE Trans. Vol. 2, pp. 175-184, Oct. 1978.

[46] Lund, J.W. asnd Saibel, E., Oil Whip whirl 0rbits of a Rotor in Sleeve Bearing, Trans.ASME, Journal of Engineering for Industry, pp 813- 823 ,Nonember.1969.

[47] Akkok, M. and Ettles, C.M.M., The Effect of feed pressure on the whirl in a Grooved Journal Bearing, ASLE Trans., Vol 2, pp. 175 -184, Oct .1978.

48] Orcutt, F.K. and Arwas. E.B., The Steady State and Dynamic Characteristics of a Full Circular Bearing and Partial Arc Bearing in the Laminar and Turbulent Flow Regime, Trans. ASME, Journal of Lubrication Technology, pp. 143-152, April, 1967.

[49] Alliare, J. C., Nicholos, J.C. and Gunter, E., Systems of Finite Elements

for the Finite Bearing. Trans. ASME. Journal of Lubrication Technology, pp. 187-197, April, 1977.

[50] Singhal, G.C.. Computation Method for Hydrodynamic Problems (Reynolds Equation). Computer Aided Design, Vol. 13, No. 13, pp. 151-154, May, 1981.

[51] Booker, J.F., Hubner, K.H., Application of Finite Element Methods to Lubrication, An Engineer's Approach, Trans. ASME, Journal of Lubrication Technology, pp. 313-323, Oct. 1972.

[52] Goenka, K., Dynamically Loaded Journal Bearings, Finite Element Method Analysis, General Motor Research Laboratory, pp. 429-439. March 18, 1983.

[53] Morton, P.G., The Effect of Thermal Distortion on the Characterstics of Large Dynamic Bearings, Proc. Inst. of Mech. Engrs. Vol. 202, C3, 28, pp. 219-225, January 1988.

[54] Clarke, G.M. and Cook, D., A Basic Course in Statistics, Second Edition, Published by Edward Arnold Ltd. 1983.

[55] Nikolasjsen, J.L., The Effect of Variable Viscosity on the Stability of Plain Journal Bearing and Floating Ring Journal Bearing, Trans. ASME, Journal

of Lubrication Technology, Vol. 95, pp. 447-456, Oct. 1973.

[56] Schuller, F.T. Experiments on the Stability of Various Water Lubricated Fixed Geometry Hydrodynamic Journal Bearings at Zero Load, Trans. ASME, Journal of Lubrication Technology, pp. 434-446, Oct. 1973.

[57] Karlo, T. E., An Experimental Investigation of a Cylindrical Journal Bearing under Constant and Sinusoidal Loading, Proc. Inst. Mech. Engrs, Vol. 3N, pp. 100, 1963-1964.

APPENDIX A

TO CALCULATE NUMBER OF HELICAL GROOVES

In this appendix following parameters of the groove are to be calculated

i) Lead angle

II) Circular pitch

iii) Number of the groove to be provided in the surface of the bearing

i) The lead angle ψ is the angle of inclination of the groove with the job axis as shown in the figure below:

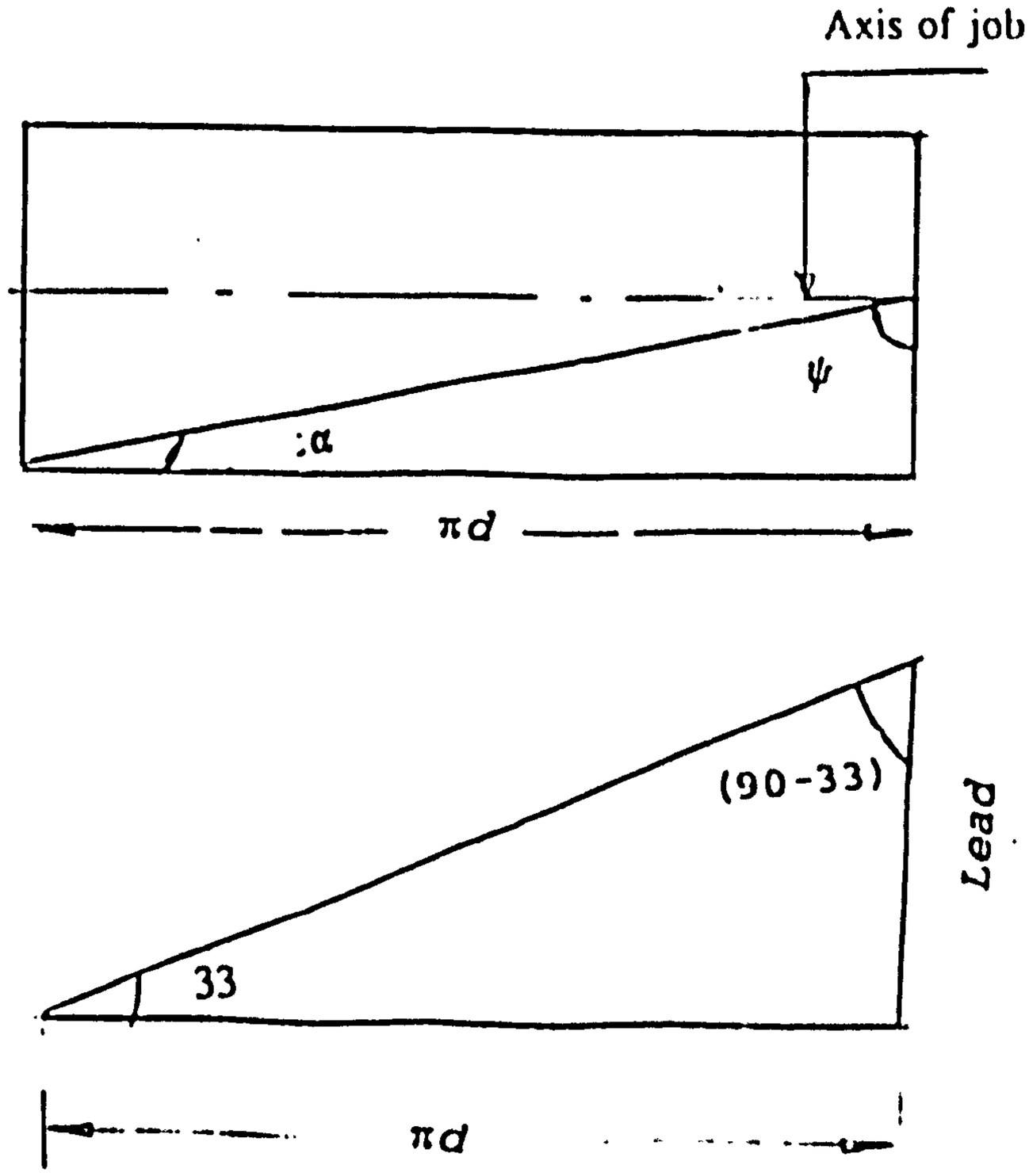

$$\cot\Psi = \frac{Lead}{\pi d}$$

$$Lead = \pi d \cot\psi = \pi d \cot(90-33)$$

Lead= $\pi d \tan\alpha = 3.14*127*0.649$

Lead = 259.10

p_c = Circular pitch

p_n = Normal pitch =2.0

x = Circular position of individual cut

x = 2.0* cosec 33 =3.676

P_c = 2.0* x =7.352

(iii) Therefore the number of grooves are given as :

N = (3.14* 127.0)/ 7.352 = 54

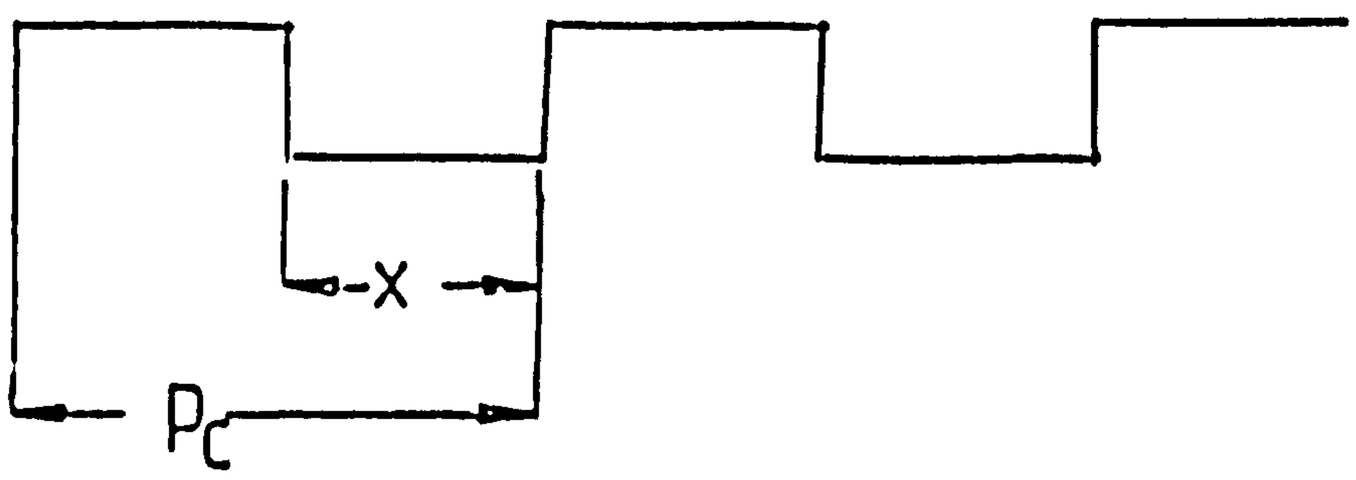

FIGURE A.1

APPENDIX B

THERMOCOUPLE CALIBRATION

The thermocouples are calibrated at two temperatures i.e at the boiling point of water and freezing point. There is no provision in the data acquistion system to correct the false temperature measured by the thermocouple. Therefore, in the data acquisition computer program it was arranged to correct the measured temperatures before they are displayed on the screen. The formula used to calculate correct temperature is given as:

$$T_t = \frac{T_a (T_f - T_0)}{(T_{100} - T_0)}$$

Where,

T_t Is a corrected temperature.

T_f Is a false temperature measured by the thermocouple.

T_{100} Boiling point temperature of the water measured by the thermocouple.

T_0 Zero point temperature °C measured by the thermocuple.

T_a Boiling point temperature of the water which is 100 at atmospheric pressure of 760 mm Hg.

APPENDIX C

FLOWMETER CALIBRATION

The flowmeter was calibrated using a variation of the "bucket and stopwatch" technique. The return pump of the lubricating system has greater pumping performance than the supply pump and so emptying of the sump by the return pump had to be controlled by float switch Figure A.2.

The volume of the oil between the two switch levels was determined by carefully adding measured amounts of oil in to the sump. The flowrate of oil in to the sump could then be obtained by measuring the time between the return pump switching off and on then dividing in time to the volume. The flowmeter was thus calibrated over the flow range, for experimental oil at 40^0C and the calibration curve is given in Figure A.3

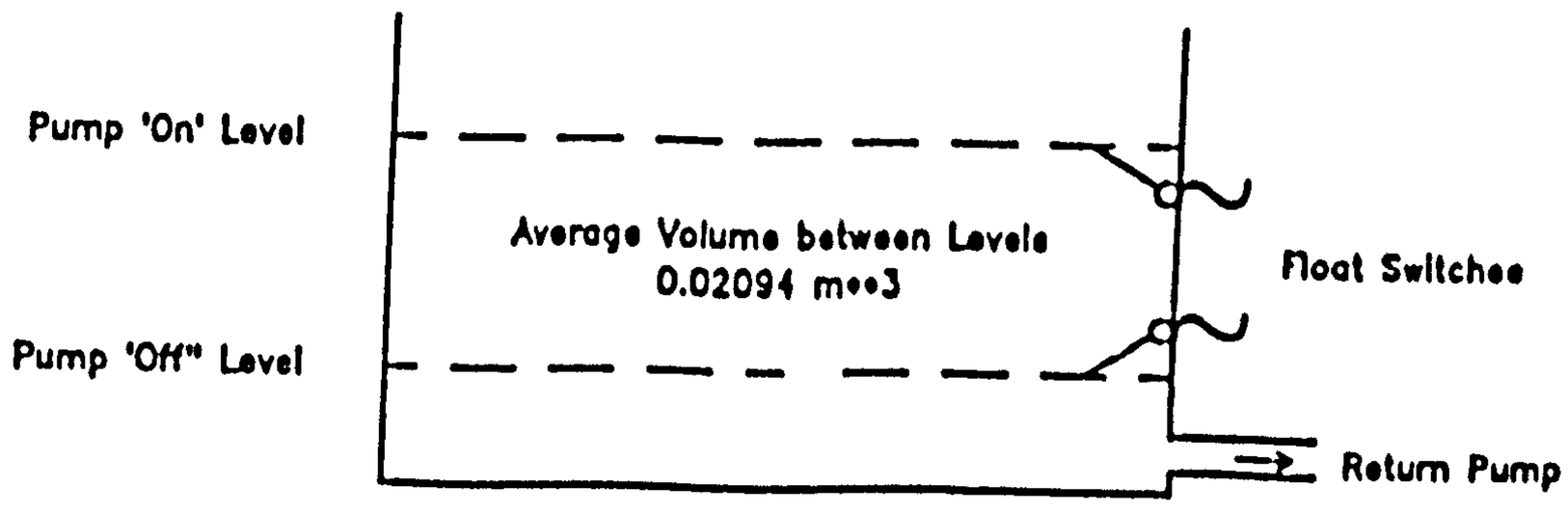

Figure A.2 Schematic Diagram of Lubrication System Sump

APPENDIX D

POWER LOSS ESTIMATION

Power absorbed by the bearing due to the shearing of the oil film in the bearing, produces temperature rise in the oil, bearing components and shaft. Due to the temperature rise, heat then flows from the bearing system by the processes of convection conduction and radiation. An estimate of power losses can therefore be made by measuring the heat flow from the bearing. The amount of heat carried away by convection i.e by the oil, can therefore be calculated from oil flow rate through the bearing and the difference between the oil inlet temperature and outlet temperature

Heat Flow (convected) = $Q \rho C_v (T_{out} - T_{in})$

For high speed journal bearings, this accounts for approximately 85 - 95 % of the heat flow and so, in this study, chosen as the power loss of the bearing

In experiment the oil inlet temperature was the temperature of the oil just before entering the housing and oil outlet temperature was the temperature of the oil in the drain to the return pump.

During experiments it was observed that the bearing inlet temperature flactuated as much as $1 \pm C^{o}$ about the mean.

APPENDIX E

COORDINATE TRANSFORMATION X,Z TO R,S COORDINATES

Coordinate X and Z are related to R, S coordinate as follows :

$$R = X\cos\alpha + Z\sin\alpha$$

$$S = X\cos\alpha - Z\sin\alpha \qquad \text{(E.1)}$$

$$\frac{\partial}{\partial X} = \frac{\partial}{\partial R}\frac{\partial R}{\partial X} + \frac{\partial}{\partial S}\frac{\partial S}{\partial X}$$

$$\frac{\partial}{\partial Z} = \frac{\partial}{\partial R}\frac{\partial R}{\partial Z} + \frac{\partial}{\partial S}\frac{\partial S}{\partial Z} \qquad \text{(E.2)}$$

$$\frac{\partial}{\partial X} = \cos\alpha\frac{\partial}{\partial R} + \sin\alpha\frac{\partial}{\partial S}$$

$$\frac{\partial}{\partial Z} = \sin\alpha\frac{\partial}{\partial R} - \cos\alpha\frac{\partial}{\partial S} \qquad \text{(E.3)}$$

$$\begin{bmatrix}\frac{\partial}{\partial X}\\ \frac{\partial}{\partial Z}\end{bmatrix} = \begin{bmatrix}\cos\alpha & \sin\alpha\\ \sin\alpha & -\cos\alpha\end{bmatrix}\begin{bmatrix}\frac{\partial}{\partial R}\\ \frac{\partial}{\partial S}\end{bmatrix} \qquad \text{(E.4)}$$

The Reynolds equation (4.1) in X and Z coordinate can be written as

$$\frac{\partial}{\partial X}\left(-\frac{H^3}{\mu 12}\frac{\partial P}{\partial X}+\frac{1}{2}UH\right)+\frac{\partial}{\partial Z}\left(-\frac{H^3}{\mu 12}\frac{\overline{\partial P}}{\partial Z}\right)+\frac{dH}{dt}=0 \quad \text{(E.5)}$$

To converting in to R and S coordinate equation (E.5) become

$$\left(\cos\alpha\frac{\partial}{\partial R}+\sin\alpha\frac{\partial}{\partial S}\right)\left[\frac{-H^3}{\mu 12}\left[\cos\alpha\frac{\partial \overline{P}}{\partial R}+\sin\alpha\frac{\partial \overline{P}}{\partial S}\right]+\frac{1}{2}UH\right]$$

$$+\left(\sin\alpha\frac{\partial}{\partial R}-\cos\alpha\frac{\partial}{\partial S}\right)\left[\frac{-H^3}{\mu 12}\left[\sin\alpha\frac{\partial \overline{P}}{\partial R}-\cos\alpha\frac{\partial \overline{P}}{\partial S}\right]\right]+\frac{dh}{dt}=0 \quad \text{(E.6)}$$

$$Q_r=-\frac{H^3}{\mu 12}\frac{\partial \overline{P}}{\partial R}+\frac{1}{2}U_rH\cos\alpha \quad \text{(E.8)}$$

$$Q_s=-\frac{H^3}{\mu 12}\frac{\partial \overline{P}}{\partial S}+\frac{1}{2}U_sH\sin\alpha \quad \text{(E.7)}$$

The Reynolds equation in R and S coordinates is as follows

$$\frac{\partial Q_s}{\partial S}+\frac{\partial Q_r}{\partial R}+\frac{dH}{dt}=0 \quad \text{(E.9)}$$

APPENDIX F

TRANSFORMATION OF COORDINATES FROM R,S COORDINATES TO X,Z COORDINATE

The R and S coordinates are related to coordinates X and Z as follows

$$X = R \cos \alpha + S \sin \alpha$$

$$Z = R \sin \alpha - S \cos \alpha \qquad \text{(F.1)}$$

$$\frac{\partial}{\partial R} = \frac{\partial}{\partial X}\frac{\partial X}{\partial R} + \frac{\partial}{\partial z}\frac{\partial z}{\partial R} \qquad \text{(F.2)}$$

$$\frac{\partial}{\partial S} = \frac{\partial}{\partial X}\frac{\partial X}{\partial S} + \frac{\partial}{\partial Z}\frac{\partial Z}{\partial S}$$

$$\frac{\partial}{\partial R} = \cos \alpha \frac{\partial}{\partial X} + Sin\ \alpha\ \frac{\partial}{\partial Z} \qquad \text{(F.3)}$$

$$\frac{\partial}{\partial S} = Sin\ \alpha \frac{\partial}{\partial X} - Cos\ \alpha\ \frac{\partial}{\partial Z}$$

The Reynold's equation for smoothed pressure in R and S coordinates is given as:

$$\frac{\partial}{\partial s}\left[\frac{1}{I\_3}\ \frac{\partial p}{\partial S} + \frac{1}{2}\ U_s\ \frac{I\_2}{I\_3}\sin\alpha\right] + \frac{\partial}{\partial r}\left[-I_3\ \frac{\partial p}{\partial R} + \frac{1}{2}\ U_r\ I_1\cos\ \alpha\right] + \frac{\partial h}{\partial t} = 0 \qquad \text{(F.4)}$$

$$(\sin\alpha\frac{\partial}{\partial X} - \cos\alpha\frac{\partial}{\partial Z})\left[\frac{1}{I\_3}\sin\alpha\frac{\partial p}{\partial X} - \cos\alpha\ \frac{\partial p}{\partial Z} + \frac{1}{2}\ u_s\sin\alpha\frac{I\_2}{I\_3}\right]$$

$$(\cos\alpha\frac{\partial}{\partial x}+\sin\frac{\partial}{\partial z})\left[-I_3\cos\alpha\frac{\partial p}{\partial x}+\sin\alpha\ \frac{\partial p}{\partial z}+\frac{1}{2}u_r\cos\alpha I_1\right]+$$
$$\frac{\partial h}{\partial t}=0$$

Expanding last two equations and denoting the constants

$$A = Sin\ \alpha^2\ \frac{1}{I\_3} + I_3\ Cos\alpha^2$$

$$E = Cos^2\ \alpha\ \frac{1}{I\_3} + I_+3\ \sin^2\alpha$$

$$F = Cos\ \alpha\ \sin\alpha\left[I_+3 - \frac{1}{I\_3}\right]$$

$$G_1 = \left[Sin^2\ \alpha\frac{I_-2}{I\_3} + Cos\ \alpha^2\ I_1\right]$$

$$G_2 = Sin\ \alpha\ \cos\ \alpha\left[I_+1-\frac{I\_2}{I\_3}\right]$$

$$q_x = -A\frac{\partial p}{\partial x} - E\ \frac{\partial p}{\partial z} + \frac{1}{2}\ U_x\ G_1$$

$$q_z = -E\ \frac{\partial p}{\partial x} - F\ \frac{p}{z} + \frac{1}{2}\ U_z\ G_2 \qquad \text{(F.6)}$$

APPENDIX G

TO CALCULATE INTEGRALS I_{-3}, I_{+3} ,I_{-2} ,I_{+1}

The equations to calculate integerals I_{-3} ,I_{+3} ,I_{-2} ,I_{+1} for the groove of rectangular shape Figure 4.3. Assuming the groove depth h_g is constant, and h_r is the film thickness for a ridge, r is the ratio of ridge width to groove width and b is the combined width of a agroove ridge pair,

$h= h_r + h_g$

The equations to calculate the integrals are given as [16]:

$$I_{-3} = \frac{1}{1+r}\left[\frac{r}{h_r^2}+\frac{1}{h^3}\right]$$

$$I_{+3} = \frac{1}{1+r}\left[rh_r^3+h^3\right]$$

$$I_{-2} = \frac{1}{1+r}\left[\frac{1}{1+h_r^2}+\frac{1}{h^2}\right]$$

$$I_{+1} = \frac{1}{1+r}\left[rh_r+h\right]$$

APPENDIX H

STABILITY PARAMETER

The bearing stiffness and damping coefficients are used in the stability analysis of a bearing. The equations of motion [43,44,45] can be written as

$$M\ddot{x} + A_{xx}X + A_{xy}Y + B_{xx}\dot{X} + B_{xy}\dot{Y} = 0$$

$$M\ddot{y} + A_{yx}X + A_{yy}Y + B_{yx}\dot{X} + B_{yy}\dot{Y} = 0 \qquad \text{(H.1)}$$

If we assume a small perturbation of the shaft so that the oil film forces act as linear spring dampers. The stability of equation (H.1) can be assessed by assuming a solution

$$X = \bar{x}e^{\lambda t}$$
$$Y = \bar{y}e^{\lambda t} \qquad \text{(H.2)}$$

X and Y are small displacements of the shaft about the equilibrium position.

$$\lambda = p + J\Omega \quad J = \sqrt{-1} \qquad \text{(H.3)}$$

and Ω is frequency of vibration

At the threshold of instability p = 0 , i.e

$$\lambda = J\,\Omega \qquad \text{(H.4)}$$

and

$$x = \bar{x}e^{J\Omega t}$$
$$Y = \bar{x}e^{J\Omega t} \qquad \text{(H.5)}$$

Substituting expression (H.5) into equation (H.1), we get in the matrix form,

$$\begin{matrix} (-M\Omega^2+A_{xx}+J\Omega B_{xx}) & (A_{xy}+J\Omega B_{xy}) \\ (A_{yx}+J\Omega B_{yx}) & (-M\Omega^2+A_{yy}+J\Omega B_{yy}) \end{matrix} \begin{bmatrix} x \\ y \end{bmatrix} = 0 \qquad (F.6)$$

For a non-trivial solution the determinat of the coefficient matrix must be equal to zero i.e.

$$\begin{matrix} (-M\Omega^2+A_{xx}+J\Omega B_{xx}) & (-M\Omega^2+A_{yy}+J\Omega B_{yy}) \\ -(A_{yx}+J\Omega B_{yx}) & (A_{xy}+J\Omega B_{xy}) \end{matrix} = 0 \qquad (H.7)$$

Expanding the above equation and separating the real and imaginary parts, we get

$$Re=\Omega^2 (B_{xy}B_{yx}B_{xx}B_{xy}) + (A_{xx}-M\Omega^2) (A_{yy}-M\Omega^2) - A_{xy}A_{yx}$$

and an imaginary part (H.8)

$$\Omega J(A_{xx}B_{yy}+A_{yy}B_{xx}-A_{xx}B_{yx}-A_{yx}B_{xy}) - M\Omega^2 (B_{xx}+B_{yy}) \Omega J$$

Hence for the onset of the stability real and imaginary parts are equal to zero.

$$\Omega^2 = \frac{(A_{xx}-M\Omega^2) (A_{yy}-M\Omega^2) - A_{xy}A_{yx})}{(B_{xx}B_{yy}-B_{xy}B_{yx})} \qquad (H.9)$$

$$M\Omega^2 = \frac{(A_{xx}B_{yy}+A_{yy}B_{xx}-A_{xy}B_{yx}-A_{yx}B_{yx})}{(B_{xx}+B_{yy})} \qquad (H.10)$$

In the dimensionless form the response coefficients are given as:

$$K_{I,J} = \frac{A_{I,J}\times C}{W_b}$$
$$C_{I,J} = \frac{B_{IJ}C\omega}{W_b} \qquad (H.11)$$

Multiplying both the numerator and denominator of the RHS of equation (H.9)by C/w_b and both side by $1/\omega^2$, we have

$$\left(\frac{\Omega}{\omega}\right)^2 = \frac{\left(K_{xx}-\frac{M\Omega^2C}{W_b}\right)\left(K_{yy}-\frac{M\Omega^2C}{W_b}\right)-(K_{xy}K_{yx})}{C_{xx}C_{yy}-C_{xy}C_{yx}} \quad \text{(H.12)}$$

Multiply both the numerator and denominator of RHS of F.10 by $C\omega^2/w_b$ and both sides by C/w_b

$$\frac{M\Omega^2C}{W_b} = \frac{K_{xx}C_{yy}+K_{yy}C_{yx}-K_{xy}C_{yx}-K_{yx}C_{xy}}{C_{xx}+C_{yy}} \quad \text{(H.13)}$$

From equation (H.12)

$$\left(\frac{\Omega}{\omega}\right)^2=\left[\frac{(K_{xx}-K_o)\,(K_{yy}-K_0)-K_{xy}K_{yx}}{C_{xx}C_{yy}-C_{xy}C_{bx}}\right]= \overline{\Omega}^2$$

From equation (H.13)

$$\frac{M\Omega^2C}{W_b} = K_0$$

$$\frac{M\overline{\Omega}^2\omega^2C}{W_b} = K_0$$

$$\frac{M\omega^2C}{W_b} = \frac{K_0}{\overline{\Omega}^2}=S_p$$

$\frac{MC\omega^2}{W_b}$ is called stability parameter and is also known as the critical

M = Mass of housing [kg]

ω^2 = Speed of Journal (rad /sec)

C = Radial clear m

Ω = Whirl speed (rad/sec)

W_b = Bearing load at the threshold of instability [N]

K_0 = Effective bearing stiffness (N/m)

$\overline{\Omega}$ = whirl speed ratio

APPENDIX I

Computer programm list follows after this page

```
C       PROGRAMME TO ANALYISE STEADY STATE AND DYNAMIC CHARACTERSTICS.
C       OF HELICAL GROOVE JOURNAL BEARING.

        REAL KXX,KXY,KYX,KYY,LASQ,LASQ2,L ,MCR
        INTEGER TA,SW,ELE,COUNTER
        REAL DG(432)
        REAL NEWATT,NEWPRESS,IPRESS,LMIN


        COMMON/NODES/NN,N,COORD(432,2)
        COMMON/ELEMEN/NEL,TA(792,4),THETA(432),HS(432),H(432)
        COMMON/BC/SW(432),PIDS(432)
        COMMON/PRESET/PR(432),NRN,IN(432)
        COMMON/BR/L,R,ATNGLE
        COMMON/INLET/PH1,PH2,DIA,LMIN
        COMMON/ROTATE/VIS,SPEED,OMEGA
        COMMON/SPIRAL/ALFA,HO,GAM
        COMMON NC,NL,C,IPRESS,BPRESS ,X,Y
        DATA PI/3.1415926/

        READ(5,*) L,R,C, X,Y,ATNGLE
        PRINT *,L,R,C, X,Y,ATNGLE
        READ(5,*)VIS,SPEED
        PRINT *,VIS,SPEED
         READ(5,*) ALFA,HO,GAM
        PRINT *, ALFA,HO,GAM
        READ(5,*)NC,NL
        PRINT *,NC,NL
        READ(5,*)IPRESS,BPRESS
        PRINT *, IPRESS,BPRESS

        OMEGA=(2.*PI*SPEED)/60.
        OLDPRESS=0.0
        COUNTER=0
        DO 30 ITER=1,10
        COUNTER =COUNTER+1
        OLDATT=ATNGLE
        print*, 'oldatt'
        print*,oldatt
        XX=X/C
        YY=Y/C
        VX=0.0
        VY=0.0
         CALL FINITE(DG,XX,YY,VX,VY,COUNTER)
         CALL FORCE(DG,FX,FY)
         NEWATT=ATAN(-FY/FX)
         ATDIF=ABS(NEWATT-OLDATT)
         PRINT*,'ATDIF'
         PRINT*,ATDIF
         NEWPRESS=0.0
        DO 40 I =1,NN
        NEWPRESS=DG(I)+NEWPRESS
40      CONTINUE
         PRDIF=ABS((NEWPRESS-OLDPRESS)/NEWPRESS)
         PRINT*,'PRDIF'
         PRINT*,PRDIF
        IF(((PRDIF.LE..0001).AND.(ATDIF.LE..0001))
     1  .OR.(ITER.EQ.10))THEN
         GO TO 144
                                                    ELSE
         OLDPRESS=NEWPRESS
         ATNGLE=NEWATT
         ENDIF
 30      CONTINUE
144     RESULT=SQRT(FX**2+FY**2)
        FO=(12.0*VIS*OMEGA*R**4)/C**2
        PRINT*,'FO'
        PRINT*,FO
        FX1=FO*FX
        FY1=FO*FY
        WTO=SQRT(FX1**2+FY1**2)
        SUMF=((VIS*SPEED*L*2.*R)/(60.*WTO))*(R/C)**2
        EX=SQRT(XX**2+YY**2)
        WRITE(6,16) L,R,C
16      FORMAT(///,1X,'LENGTH=',F6.1,4X, 'RADIUS=',F6.1,4X,
     1  'CLEARANCE=',F10.6)
        WRITE(6,17)ALFA,HO,GAM
17      FORMAT(///,1X,'GROVE ANGLE=',F8.3,4X,'GROOVE DEPTH='
     1  ,F6.2,4X,'GAB=',F6.2)
```

```
      WRITE(6,18) NC,NL
18    FORMAT(///,1X,'NUMEBER OF ELEMENT ALONG CIRCUMFERENCE=',
     1 I7,4X,' NUMBER OF ELEMENT AXIAL=',I7)
      WRITE(6,21)FX,FY
      WRITE(6,22)RESULT
      WRITE(6,25)  ITER,PRSDIF,ATDIF
      WRITE(6,26)  FX1,FY1,ATNGLE
      WRITE(6,27)SUMF,WTO,SPEED ,EX
      WRITE(6,28)VIS
21    FORMAT(///,1X,'FX=',F10.3,4X,'FY=,' F10.3)
22    FORMAT(///,1X,'RESULT=',F12.3)
25    FORMAT(///,1X,'ITER=',I5,4X,'PRESDIFF=',F12.7
     1 ,4x,'ATTDIFF=',F12.7)
26     FORMAT(///,1x,'FX1=',F12.3,4x,'FY1=',F12.3
     1  ,4X,'ATNGLE=',F8.3)
27    FORMAT(///,1X,'SUMF=',F12.4,4X,'LOAD=',F15.2,4X,
     1 'SPEED=',F10.2,4x,'EC=',F10.4)
28    FORMAT(///,1X,'VIS=' ,F12.7,'REYNES')
```

```
      do 111 i =1,nn
      write(6,112) COORD(I,1) ,DG(I),H(I)
112   format(3F8.4)
111   continue
        WT=150

       XX=X/C
       print*,'XX'
       print*,XX
       YY=Y/C
       print*,'YY'
       print*, YY
       PTBN=.0001
       XPDX=XX+PTBN

       CALL FINITE(DG,XPDX,YY,0.0,0.0,COUNTER)
       CALL FORCE(DG,FXPX,FYPX)

       XPDX=XX-PTBN
       CALL FINITE(DG,XPDX,YY,0.0,0.0,COUNTER)
       CALL FORCE(DG,FXNX,FYNX)
```

```
       YPDX=YY+PTBN
       CALL FINITE(DG,XX,YPDX,0.0,0.0,COUNTER)
       CALL FORCE(DG,FXPY,FYPY)
       YPDX=YY-PTBN
       CALL FINITE(DG,XX,YPDX,0.0,0.0,COUNTER)


       CALL FORCE(DG,FXNY,FYNY)


       DFXX=(FXPX-FXNX)/(2.*PTBN)
       DFYY=(FYPY-FYNY)/(2.*PTBN)
       DFXY=(FXPY-FXNY)/(2.*PTBN)
       DFYX=(FYPX-FYNX)/(2.*PTBN)

C
       PTBN=.0001*OMEGA
       XX=X/C
       YY=Y/C
       CALL FINITE (DG,XX,YY,PTBN,0.0,COUNTER)
       CALL FORCE(DG,CXPX,CYPX)
       CALL FINITE (DG,XX,YY,-PTBN,0.0,COUNTER)
       CALL FORCE(DG,CXNX,CYNX)
       CALL FINITE (DG,XX,YY,0.0,PTBN,COUNTER)
       CALL FORCE(DG,CXPY,CYPY)
       CALL FINITE (DG,XX,YY,0.0,-PTBN,COUNTER)
       CALL FORCE(DG,CXNY,CYNY)
       CFXX=(CXPX-CXNX)/(2.*PTBN)
       CFYY=(CYPY-CYNY)/(2.*PTBN)
```

```
      CFXY=(CXPY-CXNY)/(2.*PTBN)

      CFYX=(CYPX-CYNX)/(2.*PTBN)

C     CALCULATE STIFFNES DIMENSIONLESS

      KXX=-DFXX

      KXY=-DFXY

      KYX=-DFYX

      KYY=-DFYY



      AXX=KXX*FO/C
      AXY=KXY*FO/C
      AYX=KYX*FO/C
      AYY=KYY*FO/C

C     DIMENSIONAL DAMPING COEFFICIENT


C      CALCULATE DAMPINGS

      CXX= -CFXX

      CXY=-CFXY

      CYX=-CFYX

      CYY=-CFYY
      CXX1=CXX/C
      CXY1=CXY/C
      CYX1=CYX/C
      CYY1=CYY/C
      BXX=(CXX1*FO)/OMEGA
      BXY=(CXY1*FO)/OMEGA
      BYX=(CYX1*FO)/OMEGA
      BYY=(CYY1*FO)/OMEGA

      WRITE(6,300)
300   FORMAT(///,1X,'DIMENSIONLESS   CHARACTERSTICS')

      WRITE(6,350) KXX,CXX,KXY,CXY

      WRITE(6,400) KYY,CYY,KYX,CYX

      WRITE(6,401)
401   FORMAT(///,1X,'DIMENSIONAL CHARACTERSTICS')
      WRITE(6,450)AXX,BXX,AXY,BXY

      WRITE(6,550) AYY,BYY, AYX,BYX

350   FORMAT(////,1X,'KXX=,'F10.4,4x,'CXX=,'F10.4
     1 ,4X, 'KXY=,'F10.4,4X, 'CXY=,'F10.4)
400   FORMAT(///,1X,'KYY=,'F10.4,4X,'CYY=,'F10.4
     1 ,4X, 'KYX=,'F10.4,4X, 'CYX=,'F10.4)

450   FORMAT(///,1X,'AXX=,'F12.2,4X,'BXX=,'F12.2
     1 ,4X, 'AXY=,'F10.2,4X, 'BXY=',F10.2)

550   FORMAT(///,1X,'AYY=,'F12.2,4X,'BYY=,'F12.2
     1 ,4X, 'AYX=,'F12.2,4X, 'BYX='F12.2)



C
C       CALCULATE STABILITY PARAMETER

        D1=(KXX*CYY+CXX*KYY-CXY*KYX-CYX*KXY)/
     1    (CXX+CYY)
        D2=(AXX*BYY+BXX*AYY-BXY*AYX-BYX*AXY)/
     1     (BXX+BYY)
         LASQ2=((AXX-D2)*(AYY-D2)-AXY*AYX)/
     1         (BXX*BYY-BXY*BYX)
        Print*,'LASQ2'
```

```
      Print*,LASQ2

      LASQ=((KXX-D1)*(KYY-D1)-KXY*KYX)/
     1  (CXX*CYY-CXY*CYX)

       print*,'LASQ'
        print*,LASQ
      Q=D1/LASQ
      print*,'Q'
      print*,Q

      IF(Q.LT.0.0) GOTO 644

      OMS=SQRT(Q)
      OM1=SQRT(WT*(C/386.)*1./WTO)*9.55
      THRES=OMS/OM1


      WRITE(6,600) D1
      WRITE(6,601) D2

600   FORMAT(/////,1X,'EFFECTIVE BEARING STIFFNESS =,' F10.4)
601   FORMAT(//,1X,'EFFECTIVE BEARING STIFFNESS D2=,' F15.2)

644   WRITE(6,650)WH


650   FORMAT(////,1X,'WHRIL FREQUENCY =,' F10.3)

      WRITE(6,700)OMS

700   FORMAT(////,1X,'STABILITY PARAMETER=,'F12.6)

      WRITE(6,750)

750   FORMAT(////,1X,'STABILITY PARAMETER UNBOUNDED')

      WRITE(6,800) THRES
800   FORMAT(//,1X,'THRES HOLD SPEED=',F10.2)
      STOP
       END
C*************************************************************
      SUBROUTINE FINITE(DG,XX,YY,VX,VY,COUNTER)
      REAL  KG(432,432),UG(432),VG(432)
      REAL  KR(432,432),PG(432),PRE(432)
      REAL  DG(432),DR(432),RG(432)

      REAL NEWPRESS,NEWATT ,IPRESS,L,LMIN
      INTEGER TA,SW,ELE


      COMMON/NODES/NN,N,COORD(432,2)
      COMMON/ELEMEN/NEL,TA(792,4),THETA(432),HS(432),H(432)
      COMMON/BC/SW(432),PDIS(432)
      COMMON/PRESET/PR(432),NRN,IN(432)
      COMMON/BR/L,R,ATNGLE
      COMMON/INLET/PH1,PH2,DIA,LMIN
      COMMON/ROTATE/VIS,SPEED,OMEGA
      COMMON/SPIRAL/ALFA ,HO,GAM
      COMMON NC,NL,C,IPRESS,BPRESS,X,Y

      DATA PI/3.1415926/
      CALL INPUT (XX,YY,VX,VY,COUNTER,NT,NR,PG)

      CALL ASMB(NT,KG,UG,VG)
      CALL REDUCER (NT,NR,KG,PG,KR,PRE,UG,VG)
      CALL SOLVER(NR,KR,DR,PRE)
      CALL PRESS(NT,NR,DR,DG)
      RETURN
      END

      SUBROUTINE INPUT(XX,YY,VX,VY,COUNTER,NT,NR,PG)
      INTEGER SW

      REAL PG(432),L,IPRESS,LMIN


      COMMON/NODES/NN,N,COORD(432,2)
      COMMON/ELEMEN/NEL,TA(792,4),THETA(432),HS(432),H(432)
      COMMON/BC/SW(432),PDIS(432)
```

```
      COMMON/PRESET/PR(432),NRN,IN(432)
      COMMON/BR/L,R,ATNGLE
      COMMON/INLET/PH1,PH2,DIA,LMIN
      COMMON/ROTATE/VIS,SPEED,OMEGA
      COMMON/SPIRAL/ALFA,HO,GAM
      COMMON NC,NL,C,IPRESS,BPRESS,X,Y


      DATA PI/311414/

      CALL MESH(XX,YY,VX,VY,COUNTER)
      NT=NN
      DO 10 I=1,NT
      PG(I)=0.0
      SW(I)=0
10    PDIS(I)=0.0

      NR=NT

      DO 20 J=1,NRN
      K=IN(J)
      SW(K)=1
      PDIS(K)=PR(J)
20    NR =NR-1
      RETURN
      END

C
      SUBROUTINE MESH(XX,YY,VX,VY,COUNTER)
      REAL IPRESS,L,LMIN
      REAL ZOUT(432),ZIN(432),NCR,NLR
      REAL  LINE(432) ,IPRESS
      INTEGER TYPE(432),TYPA(432),ELE,TA ,SW,COUNTER

      COMMON/NODES/NN,N,COORD(432,2)
      COMMON/ELEMEN/NEL,TA(792,4),THETA(432),HS(432),H(432)
      COMMON/PRESET/PR(432),NRN,IN(432)
      COMMON/BR/L,R,ATNGLE
      COMMON/INLET/PH1,PH2,DIA,LMIN
      COMMON/ROTATE/VIS,SPEED,OMEGA
       COMMON NC,NL,C,IPRESS,BPRESS,X,Y
       DATA PI/3.1415926/
print *,'nc'
print *,nc
print *,'nl'
print *, nl
print *,'ipress'
print *,ipress
print *,'bpress'
print *,bpress
 print *,'l'
 print *,l
 print *,'r'
 print *,r
 print *,'c'

 print *,c
 print *,'ec'
 print *,XX
 print *,YY


 print *,'COUNTER'
 print *,COUNTER
IF(COUNTER.EQ.1)THEN
NCR=NC*1.0
NLR=NL*1.0
DX=(2.*PI)/NCR
DL=L/R
DZ=DL/NLR
IF(LMIN.LT.L/2.0)THEN
POSN1=(LMIN/2.0-DIA/2.0)
POSN2=(LMIN/2.0+DIA/2.0)
                     ELSE


POSN1=(L/2.0-DIA/2)
POSN2=(L/2.0+DIA/2.0)
ENDIF
```

```
      IF(PH1.LE.0)THEN
      PH1=PH1+2.0*PI

      ENDIF
          APOX=PI/360
          IR=0
       DO 10 I=1,(NC+IR)
       LINE(I+IR)=(I-1)*DX
10     CONTINUE
       NEL=(NC+IR)*NL
       NN=(NC+IR)*(NL+1)


       DO 20 I=1,(NL+1)
          ZOUT(I)=(I-1)*DZ

 20    CONTINUE
       NOS=0

       DO 30 I=1,(NL+1)
        DO 40 J=1,(NC+IR)
        NODE=((I-1)*(NC+IR))+J
        COORD(NODE,1)=LINE(J)
        COORD(NODE,2)=ZOUT(I)
        IF(TYPE(J).EQ.1)THEN
        IF(TYPA(I).EQ.1)THEN
        NOS=NOS+1
        IN(NOS)=NODE
        PR(NOS)=IPRESS
       ENDIF
       ENDIF

       IF((I.EQ.1).OR.(I.EQ.(NL+1)))THEN
       NOS=NOS+1
       IN(NOS)=NODE
       PR(NOS)=BPRESS
       ENDIF
40     CONTINUE
30     CONTINUE
       NRN=NOS
       DO 50 I=1,NL
          DO 60 J=1,(NC+IR)
          ELE=((I-1)*(NC+IR))+J
         TA(ELE,1)=((I-1)*(NC+IR))+J
         TA(ELE,4)=(I*(NC+IR))+J
       IF(J.EQ.(NC+IR))THEN
        TA(ELE,3)=(I*(NC+IR))+1
        TA(ELE,2)=((I-1)*(NC+IR))+1
                  ELSE
        TA(ELE,3)=TA(ELE,4)+1
        TA(ELE,2)=TA(ELE,1)+1

       ENDIF
60     CONTINUE
50     CONTINUE
       CALL SPLIT
       ENDIF
       PRINT *,'NL'
       PRINT *,NL
       PRINT *,'NC'
       PRINT *,NC
       print *,XX
       print *,YY
       print *,'VY'
       print *,Vy
       print *,'VX'
       print *,VX
       print *,'ATNGLE'
       print *,ATNGLE
       DO 70 I=1,(NL+1)
        DO 80 J=1,NC
             NODE=(I-1)*NC+J
       THETA(NODE)=LINE(J)-ATNGLE
       HS(NODE)=-VX*COS(THETA(NODE))-VY*SIN(THETA(NODE))
       H(NODE)=1.0- XX*COS(THETA(NODE))- YY*SIN(THETA(NODE))
80     CONTINUE
70     CONTINUE
       RETURN
       END
```

```
      SUBROUTINE  OUTPUT
      INTEGER TA,ELE,SW

      COMMON/NODES/NN,N,COORD(432,2)
      COMMON/ELEMEN/NEL,TA(792,4) ,THETA(432),HS(432),H(432)
      COMMON/PRESET/PR(432),NRN,IN(432)
      COMMON/BC/SW(432),PDIS(432)
      WRITE(6,40)
      WRITE(6,60)NN
      WRITE(6,80)NEL
40    FORMAT(///,10X,'****GENERATED MESH DATA****',//)
60    FORMAT(1H0,10X 'NUMBER OF NODAL POINTS=',I6)
80    FORMAT(1H0,14X, 'NUMBER OF ELEMENTS=',I6)
      WRITE(6,100)
      WRITE(6,120)
 100  FORMAT(1H0,4X,'NODAL POINTS COORDINATES')
 120  FORMAT(1H0,2X,'NODES NO',10X,'X-COORD',10X,'Z-COORD')
      DO 10 NP=1,NN
  10  WRITE(6,140)NP,(COORD(NP,ID),ID=1,2)
 140  FORMAT(I10,2F15.5)
      WRITE(6,160)
      WRITE(6,180)
 160  FORMAT(//,4X,'ELEMENTS NODAL CONNECTION')
 180  FORMAT(//,4X,'ELEMENTS',4X,'NODAL POINTS',7X,'CONNECTION NO')

      DO 20 ELE=1,NEL
   20 WRITE(6,220)ELE,(TA(ELE,N),N=1,3)
 220  FORMAT(1x,10i5)
      WRITE(6,240)
  240 FORMAT(//,4X,'NODES NO WITH KNOWN PRESSURE',6X,'PRESSURE VALUE')
      RETURN
      END
C
      SUBROUTINE SPLIT
       INTEGER LEN(4),TA,ELE

      COMMON/NODES/NN,N,COORD(432,2)
      COMMON/ELEMEN/NEL,TA(792,4),THETA(432),HS(432),H(432)

      KOUNT=0
      DO 10 ELE=1,NEL
      NOTAL=NEL+ELE
      DO 10 INODE=1,4
   10 TA(NOTAL,INODE)=TA(ELE,INODE)
      DO 40 ELE=1,NEL
      NOTAL=NEL+ELE
      DO 20 INODE=1,4
      INDEX=TA(NOTAL,INODE)
      LEN(INODE)=INDEX
    20 CONTINUE

C
c     GO TO 15

C     DIVIDE ACROS THE SHORTEST DIAGONAL
C     DIAG1=SQRT((CORD(1,1)-COR(3,1))**2+(CORD(1,2)-CORD(3,2))**2
c     DIAG2=SQRT(CORD(2,1)-CORD(4,1))**2+(CORD(2,2)-CORD(4,2))**2
c     DIFER=DIAG1-DIAG2
c     IF(DIFER.GT.1.0E-09)GOTO 30
      KOUNT=KOUNT+1
      TA(KOUNT,1)=LEN(1)
      TA(KOUNT,2)=LEN(2)
      TA(KOUNT,3)=LEN(3)

      KOUNT=KOUNT+1
      TA(KOUNT,1)=LEN(1)
      TA(KOUNT,2)=LEN(3)
      TA(KOUNT,3)=LEN(4)
      GO TO 40
   30 KOUNT=KOUNT+1
      TA(KOUNT,1)=LEN(1)
      TA(KOUNT,2)=LEN(2)
      TA(KOUNT,3)=LEN(4)
      KOUNT=KOUNT+1
      TA(KOUNT,1)=LEN(2)
      TA(KOUNT,2)=LEN(3)
      TA(KOUNT,3)=LEN(4)
```

```
   40 CONTINUE
      NEL=2*NEL
      RETURN
      END

C ***************************************************************************

C     SUBROUTINE ASMBLER

      SUBROUTINE ASMB (NT,KG,UG,VG)
      REAL KG(432,432),UG(432),VG(432)
      REAL KE(3,3),XE(3),ZE(3)
      REAL UE(3),VE(3)
      INTEGER TA

      COMMON/NODES/NN,N,COORD(432,2)
      COMMON/ELEMEN/NEL,TA(792,4),THETA(432),HS(432),H(432)

      DATA PI/3.1415926/
      DO 5 I=1,NT
         DO 5 J=1,NT
         KG(I,J)=0.0
   5  CONTINUE
      DO 6 I=1,NT
         UG(I)=0.0
         VG(I)=0.0
   6  CONTINUE
C
      DO 10 IE =1,NEL
      N=3
      IF(((TA(IE,3)-TA(IE,1)).EQ.1).OR.
     +   (TA(IE,3)-(TA(IE,2)-1)+TA(IE,1)).EQ.TA(IE,3))THEN
      DO 7 I=1,N
      IF(((I.EQ.2).OR.(I.EQ.3)).AND.COORD(TA(IE,I),1).EQ.0.0)THEN
      XE(I)=2.*PI
      ZE(I)=COORD(TA(IE,I),2)
                                          ELSE
      XE(I)=COORD(TA(IE,I),1)
      ZE(I)=COORD(TA(IE,I),2)
      ENDIF
   7  CONTINUE
                                        ELSE
      DO 8 I=1,N
      XE(I)=COORD(TA(IE,I),1)
      ZE(I)=COORD(TA(IE,I),2)
   8  CONTINUE
      ENDIF
      IF(IE.LE.NEL/2)THEN
      CALL ELEMENT1(IE,N,XE,ZE,KE,UE,VE)
                                                ELSE
      CALL ELEMENT2(IE,N,XE,ZE,KE,UE,VE)
      ENDIF
C
      DO 30 I=1,N
      IL=I
      IG=TA(IE,I)
      UG(IG)=UG(IG)+UE(IL)
      VG(IG)=VG(IG)+VE(IL)

      DO 40 J=1,N
         JL=J
      JG=TA(IE,J)
      KG(IG,JG)=KG(IG,JG)+KE(IL,JL)
  40  CONTINUE
  30  CONTINUE
  10  CONTINUE
      RETURN
      END

C ***************************************************************************
      SUBROUTINE ELEMENT(IE,N,XE,ZE,KE,UE,VE)
      REAL KE(3,3),UE(3),VE(3)
      REAL XE(3),ZE(3),B(3),C(3),HE(3),HSE(3)

      INTEGER TA
      REAL L

      COMMON/ELEMEN/ NEL,TA(792,4),THETA(432),HS(432),H(432)
      COMMON/BR/L,R,ATNGLE
 /
```

```
      COMMON /ROTATE/VIS,SPEED,OMEGA
      DATA PI/3.1415926/

      CALL PROP1(XE,ZE,B,C,AE)
      Do 3 I=1,N
      DO 3 J=1,N
        KE(I,J)=0.0
3     CONTINUE
      DO 4 I=1,N
         UE(I)=0.0
         VE(I)=0.0
4     CONTINUE
       OM=(2.0*PI*SPEED)/60.0
      U=OM*R
      RP=U/(OM*R)
      DO 50 I=1,N
      HE(I)=H(TA(IE,I))
      HSE(I)=HS(TA(IE,I))
50    CONTINUE
      HI=HE(1)
      HJ=HE(2)
      HK=HE(3)

      HA=(HI+HJ+HK)/3.0

      HSI=HSE(1)
      HSJ=HSE(2)
      HSK=HSE(3)

      HSA=(HSI+HSJ+HSK)/3.0
C
      DO 60 I=1,N
      DO 70 J=1,N
       KE(I,J)=KE(I,J)+(HA**3)/(4.0*AE)*(B(I)*B(J)+C(I)*C(J))
 70    CONTINUE
       UE(I)=UE(I)+ ((RP*HA)/4.0)*(B(I))
       VE(I)=VE(I)+(HSA*AE)/3.0
 60    CONTINUE
       RETURN
       END
C*******************************************************************
      SUBROUTINE PROP1(XE,ZE,B,C,AE)

      REAL XE(3),ZE(3),B(3),C(3)

      B(1)=ZE(2)-ZE(3)
      B(2)=ZE(3)-ZE(1)
      B(3)=ZE(1)-ZE(2)

      C(1)=XE(3)-XE(2)
      C(2)=XE(1)-XE(3)
      C(3)=XE(2)-XE(1)

      AE=(XE(2)*ZE(3)+XE(3)*ZE(1)+XE(1)*ZE(2)-XE(2)*ZE(1)
     +  -XE(3)*ZE(2)-XE(1)*ZE(3))/2.0
      RETURN
      END
C 451 ********************************************************************
      SUBROUTINE REDUCER (NT,NR,KG,PG,KR,PRE,UG,VG)
      INTEGER NT,NR
      REAL KG(NT,NT),KR(NR,NT),PG(NT),PRE(NT)
      REAL UG(NT),VG(NT)
      INTEGER SW

      COMMON/BC/SW(432),PDIS(432)


      IR=0
      DO 5 I=1,NR
      DO 6 J=1,NR
      KR(I,J)=0.0
 6    CONTINUE
 5    CONTINUE
      DO 10 I=1,NR
      PRE(I)=0.0
10    CONTINUE
      DO 20 I=1,NT
      IF(SW(I).NE.1)THEN
      IR=IR+1
      PRE(IR)=PG(I)+UG(I)-VG(I)
```

```
      JR=0
      DO 30 J=1,NT
      IF(SW(J).EQ.1)THEN
      PRE(IR)=PRE(IR)-(KG(I,J)*PDIS(J))
      ELSE
      JR=JR+1
      KR(IR,JR)=KG(I,J)
      ENDIF
   30 CONTINUE
      ENDIF
   20 CONTINUE
      RETURN
      END
C 481 ************************************************************
      SUBROUTINE SOLVER (N,A,X,Y)
      REAL A(N,N),X(N),Y(N),SUM,Q
      DO 10 K=1,(N-1)
      IF(A(K,K).EQ.0.0) THEN
      PRINT*,'GAUSS FAILED!!'
      ENDIF
      DO 20 I=(K+1),N
      Q=A(I,K)/A(K,K)
      Y(I)=Y(I)-(Q*Y(K))
      DO 30 J=(K+1),N
       A(I,J)=A(I,J)-(Q*A(K,J))
   30 CONTINUE
   20 CONTINUE
   10 CONTINUE


      DO 50 I=N,1,-1
      SUM=Y(I)
      DO 60 J=(I+1),N
      SUM=SUM-(A(I,J)*X(J))
   60 CONTINUE
      X(I)=SUM/A(I,I)
   50 CONTINUE
       RETURN
       END
C 505 ************************************************************
      SUBROUTINE PRESS(NT,NR,DR,DG)
      REAL DG(432),DR(432)
      INTEGER SW

      COMMON/NODES/NN,N,COORD(432,2)
      COMMON/BC/ SW(432),PDIS(432)

      IR=0
      IG=0
      DO 20 I=1,NN
      IG=(IG+1)
      IF(SW(IG).EQ.1)THEN
      DG(IG)=PDIS(IG)
                                ELSE
      IR=IR+1
      DG(IG)=DR(IR)
      ENDIF
   20 CONTINUE
      RETURN
      END
C  525 ***********************************************************
        SUBROUTINE  FORCE (DG,FX,FY)
      REAL XE(3),ZE(3),THE(3)
      REAL DG(432),PRES(3)
      REAL FTT(3),FRR(3)
      INTEGER TA
      COMMON/NODES/NN,N,COORD(432,2)

      COMMON/ELEMEN/NEL,TA(792,4) ,THETA(432),HS(432),H(432)
      DATA  PI/3.1415926/

      FY=0.0
      FX=0.0
      DO 90 IE=1,NEL
      N=3
      IF(((TA(IE,3)-TA(IE,1)).EQ.1).OR.
     +  (TA(IE,3)-(TA(IE,2)-1)+TA(IE,1)).EQ.TA(IE,3))THEN
      DO 6 I=1,N
      IF(((I.EQ.2).OR.(I.EQ.3)).AND.COORD(TA(IE,I),1).EQ.0.0)THEN
      XE(I)=2.0*PI
```

```
      ZE(I)=COORD(TA(IE,I),2)
                                    ELSE
      XE(I)=COORD(TA(IE,I),1)
      ZE(I)=COORD(TA(IE,I),2)
      ENDIF
6     CONTINUE
                                              ELSE
      DO 7 I=1,N
      XE(I)=COORD(TA(IE,I),1)
      ZE(I)=COORD(TA(IE,I),2)
7     CONTINUE
      ENDIF
      AE=ABS((XE(2)*ZE(3)+XE(3)*ZE(1)+XE(1)*ZE(2)-XE(2)*ZE(1)
     +   -XE(3)*ZE(2)-XE(1)*ZE(3))/2.0)

      FYVE=0.0
      FXVE=0.0
      DO 95 I=1,N
      IF(DG(TA(IE,I)).LT.0.0)THEN
      PRES(I)=0.0
                                         ELSE
      PRES(I)=DG(TA(IE,I))
      ENDIF
95    CONTINUE
      DO 98 I=1,N
      THE(I)=THETA(TA(IE,I))
98    CONTINUE
     DO 97 I=1,N
      FTT(I)=PRES(I)*(SIN(THE(I)))
      FRR(I)=PRES(I)*(COS(THE(I)))
97   CONTINUE
      FYVE=FYVE+AE*(FTT(1)+FTT(2)+FTT(3))/3.0
      FXVE=FXVE+AE*(FRR(1)+FRR(2)+FRR(3))/3.0
      FY=FY-FYVE
      FX=FX-FXVE
 90   CONTINUE
      RETURN
      END
C     ***********************************************************************
      SUBROUTINE FLOW (NT,KG,DG,PG,RG,UG,VG)
      REAL KG(432,432),DG(432),PG(432),RG(396)
      REAL UG(432),VG(432)

      COMMON/NODES/NN,N,COORD(432,2)


      PRINT *,NN
      PRINT *,NT
      IG=0

      DO 10 I=1,NT
      RG(I)=0.0
10    CONTINUE

      DO 100 I=1,NN
      IG=IG+1
      RG(IG)=-PG(IG)-UG(I)+VG(I)
      DO 120 JG=1,NT
      RG(IG)=RG(IG)+(KG(IG,JG)*DG(JG))
120   CONTINUE
100   CONTINUE
      RETURN
      END

C ***********************************************************************
      SUBROUTINE ELEMENT1(IE,N,XE,ZE,KE,UE,VE)

      REAL KE(3,3),UE(3),VE(3)
      REAL XE(3),ZE(3),B(3),C(3),HE(3),HSE(3)

      INTEGER TA
      REAL L

      COMMON/ELEMEN/ NEL,TA(792,4),THETA(432),HS(432),H(432)
      COMMON/BR/L,R,ATNGLE
      COMMON /ROTATE/VIS,SPEED,OMEGA
      COMMON/SPIRAL/ALFA,HO,GAM
      DATA PI/3.1415/
```

```
      CALL PROP1(XE,ZE,B,C,AE)
      DO 3 I=1,N
      DO 3 J=1,N
        KE(I,J)=0.0
3     CONTINUE
      DO 4 I=1,N
         UE(I)=0.0
         VE(I)=0.0
4     CONTINUE
      OM=(2.*PI*SPEED)/60.0
      U=OM*R
      RP=U/(OM*R)
      DO 50 I=1,N
      HE(I)=H(TA(IE,I))
      HSE(I)=HS(TA(IE,I))
50    CONTINUE
      HI=HE(1)
      HJ=HE(2)
      HK=HE(3)

      HA=(HI+HJ+HK)/3.0

      HSI=HSE(1)
      HSJ=HSE(2)
      HSK=HSE(3)

      HSA=(HSI+HSJ+HSK)/3.0

      CALL SPIRL1(HA,CT11,CT12,CT22,BT11,BT12)

      DO 60 I=1,N
      DO 70 J=1,N
       KE(I,J)=KE(I,J)+(HA**3)/(4.0*AE)*(CT11*(B(I)*B(J))+
     +    + CT12*(B(I)*C(J))+CT12*(C(I)*B(J))+CT22*(C(I)*C(J)))
 70    CONTINUE
       UE(I)=UE(I)+(RP*HA*.25)*(BT11*B(I)+BT12*C(I))
       VE(I)=VE(I)+(HSA*AE)/3.0
60    CONTINUE
      RETURN
      END
C *****************************************************************
      SUBROUTINE ELEMENT2(IE,N,XE,ZE,KE,UE,VE)

      REAL KE(3,3),UE(3),VE(3)
      REAL XE(3),ZE(3),B(3),C(3),HE(3),HSE(3)

      INTEGER TA
      REAL L

      COMMON/ELEMEN/ NEL,TA(792,4),THETA(432),HS(432),H(432)
       COMMON/BR/L,R,ATNGLE
       COMMON /ROTATE/VIS,SPEED,OMEGA
       COMMON/SPIRAL/ALFA,HO,GAM
      DATA PI/3.1415926/

      CALL PROP1(XE,ZE,B,C,AE)

      DO 3 I=1,N
      DO 3 J=1,N
        KE(I,J)=0.0
3     CONTINUE
      DO 4 I=1,N
         UE(I)=0.0
         VE(I)=0.0
4     CONTINUE
      OM=(2.*PI*SPEED)/60.0
      U=OM*R
      RP=U/(OM*R)
      DO 50 I=1,N
      HE(I)=H(TA(IE,I))
      HSE(I)=HS(TA(IE,I))
50    CONTINUE
      HI=HE(1)
      HJ=HE(2)
      HK=HE(3)

      HA=(HI+HJ+HK)/3.0

      HSI=HSE(1)
      HSJ=HSE(2)
```

```
      HSK=HSE(3)

      HSA=(HSI+HSJ+HSK)/3.0
       CALL SPIRL2 (HA,CT11,CT12,CT22,BT11,BT12)
      DO 60 I=1,N
      DO 70 J=1,N
       KE(I,J)=KE(I,J)+(HA**3)/(4.0*AE)*(CT11*(B(I)*B(J))+
     +    + CT12*(B(I)*C(J))+CT12*(C(I)*B(J))+CT22*(C(I)*C(J)))
   70   CONTINUE
        UE(I)=UE(I)+(RP*HA*.25)*(BT11*B(I)+BT12*C(I))
        VE(I)=VE(I)+(HSA*AE)/3.0
   60   CONTINUE
        RETURN
        END
C*******************************************************************
        SUBROUTINE SPIRL1(HA,CT11,CT12,CT22,BT11,BT12)
        COMMON/SPIRAL/ALFA,HO,GAM

        HGR=1.0+HO/HA
        HGR3=HGR**3
        A=1.0+GAM
        A1=HGR3+GAM
        A2=HGR3+GAM*HGR3
        A3=1.0+GAM*HGR3
        A4=HGR+GAM
        A5=HGR+GAM*HGR3


        CT11=(A1/A)*(COS(ALFA))**2+(A2/A3)*(SIN(ALFA))**2
        CT12=((A1/A)-(A2/A3))*(SIN(ALFA))*(COS(ALFA))
        CT22=(A1/A)*(SIN(ALFA))**2+(A2/A3)*(COS(ALFA))**2

        BT11=(A4/A)*(COS(ALFA))**2+(A5/A3)*((SIN(ALFA))*(COS(ALFA)))
        BT12=((A4/A)-(A5/A3))*(SIN(ALFA))*(COS(ALFA))

        RETURN
        END
C*******************************************************************
        SUBROUTINE SPIRL2(HA,CT11,CT12,CT22,BT11,BT12)
        COMMON/SPIRAL/ALFA,HO,GAM

        ALFA1=3.1415926- ALFA

        HGR=1.0+HO/HA
        HGR3=HGR**3
        A=1.0+GAM
        A1=HGR3+GAM
        A2=HGR3+GAM*HGR3
        A3=1.0+GAM*HGR3
        A4=HGR+GAM
        A5=HGR+GAM*HGR3


        CT11=(A1/A)*(COS(ALFA1))**2+(A2/A3)*(SIN(ALFA1))**2
        CT12=((A1/A)-(A2/A3))*(SIN(ALFA1))*(COS(ALFA1))
         CT22=(A1/A)*(SIN(ALFA1))**2+(A2/A3)*(COS(ALFA1))**2

        BT11=(A4/A)*(COS(ALFA1))**2+(A5/A3)*((SIN(ALFA1))*(COS(ALFA1)))

        BT12=((A4/A)-(A5/A3))*(SIN(ALFA1))*(COS(ALFA1))

        RETURN
        END
```